b
UNIVERSITÄT
BERN

Measuring the Neutron Electric Charge with High-Visibility Grating Interferometry

Inaugural dissertation
of the Faculty of Science,
University of Bern

presented by
Marc Persoz
from Saules (NE)

Supervisor of the doctoral thesis:
Prof. Dr. Florian M. Piegsa
Albert Einstein Center for Fundamental Physics
Laboratory for High Energy Physics
Physics Institute

This thesis work was performed in the Fundamental Neutron and Precision Physics Group at the University of Bern.

Measuring the Neutron Electric Charge with High-Visibility Grating Interferometry

Inaugural dissertation
of the Faculty of Science,
University of Bern

presented by
Marc Persoz
from Saules (NE)

Supervisor of the doctoral thesis:
Prof. Dr. Florian M. Piegsa
Albert Einstein Center for Fundamental Physics
Laboratory for High Energy Physics
Physics Institute

Accepted by the Faculty of Science.

Bern, Tuesday 21st January, 2025 The Dean

"It is a profound and necessary truth that the deep things in science are not found because they are useful; they are found because it was possible to find them."

J. Robert Oppenheimer

Abstract

The neutron is a fundamental particle bound in atomic nuclei and is traditionally considered electrically neutral. However, any minuscule deviation from zero charge could provide insights into new physics beyond the Standard Model of particle physics. Precise neutron property measurements are essential for advancing fundamental physics and improving the performance of neutron-based experimental techniques. This dissertation presents a comprehensive study on the design, development and characterization of the QNeutron apparatus, a cold neutron time-of-flight Talbot-Lau interferometer. To improve the current best upper limit on the neutron electric charge, this instrument must be optimized for high-precision measurements, focusing particularly on neutron beam deflections induced by a sample or an externally applied electric field. The apparatus can operate in two distinct regimes: ballistic and diffraction. Both have been meticulously characterized in order to find the most sensitive setup with the given experimental conditions.

This work involves simulations and extensive experimental characterizations at leading neutron research facilities, including the Paul Scherrer Institute and the Institut Laue-Langevin. These efforts culminated in a first-of-its-kind measurement of the neutron electric charge, achieving a statistical sensitivity of

$$\sigma(Q_n) = 1.06 \times 10^{-19} e$$

in about 84 hours of data taking, where e is the elementary charge. Although not yet competitive with the current best limit, this result demonstrates the potential of the QNeutron apparatus for high-precision measurements.

Acknowledgements

First of all, I would like to express my deepest gratitude to Florian Piegsa, my supervisor in the Fundamental Neutron and Precision Physics Group. You trusted me for this challenging project and hired me as a PhD student four years ago to initiate and conduct the QNeutron experiment. Your guidance, profound expertise and precious feedbacks have been precious and I particularly appreciate how you gave me such freedom of action during the development and characterization phases of the project, while always suggesting improvements and brilliant ideas. It was sometimes crazy how we were struggling about a problem during beam times and you could solve it with just a quick phone call... But I really enjoyed that as it always felt like being in good hands as a PhD student in your group. Thanks for all the opportunities and the support during this journey.

A special acknowledgment goes to my colleagues from the group. To you Gjon and Phillip, with whom I shared approximately 80 days of intense and exhausting beam time at PSI and to every member of the group, Anastasio, Ciro, Ivo, Jacob, Jakob, and Luca, who joined then at the ILL as additional support for these two long beam times representing another 50 days. These periods were quite demanding and the working days felt sometimes like an eternity, often lasting until late into the night. Thanks to you all, the humor and friendship was always *au rendez-vous* with improvised fondue, grillade or just shared laughter that help to keep us all sane. Those beam time experiences have left me with stories and memories that will last long after this thesis is done.

I also wish to express my gratitude to Torsten Soldner, our colleague from ILL. Your constructive feedback and your unconditional help during our longest beam times at Institut Laue-Langevin were also extremely appreciated, and I deeply thank you for this. I remember taking data during the beam time at PF1B and seeing you coming to the instrument from the cabin. I knew that you would almost always have unexpected but very relevant questions about our measurements and I particularly appreciated how you involved yourself in this project and how you challenged me with these very constructive inputs.

To all my other colleagues from the university of Bern, I thank you for your assistance during this thesis. Roger, Jan, Lorenzo, Silas and Vasco from the workshop, we could come to you with strange or urgent requests and you were always extremely arrangeful

for the design and construction of our mechanical parts. Thanks to you Marcella, you helped me doing the administrative work during my PhD and always in a wonderful atmosphere.

I would also like to acknowledge the generous funding provided by the Swiss National Science Foundation, and the facilities made available by Institut Laue-Langevin and Paul Scherrer Institute, which were crucial in enabling this research.

C'était pas gagné d'avance... Après avoir eu la chance de visiter et terminer l'école d'ingénieur en 2014 et fait mon service militaire l'année suivante, j'ai trouvé un poste de travail agréable qui m'offrait tout ce dont j'avais besoin pour vivre très convenablement. Et pourtant... J'avais ce petit titillement qui me disait qu'il fallait que j'étudie la physique. Après deux ans, ce sentiment est devenu trop fort et il était temps de se lancer. À ce moment-là, la décision pouvait sembler un peu farfelue et déraisonnable en vue des nombreuses années que ça représentait... Mais j'ai la chance énorme d'avoir eu le soutien de ma famille et de mes amis tout au long de cette histoire.

À mes parents, Claude-Alain et Sophie, merci infiniment pour tout ce que vous avez fait pour moi et tout ce que vous êtes et représentez. Vous m'avez poussé et soutenu tout au long de ma vie et n'avez jamais douté de mes capacités. Vous avez aidé à me forger, mes idées, mes valeurs et mes convictions et sans vous, c'est clair que je n'en serais pas là où j'en suis aujourd'hui. Ce parcours n'était pas toujours super facile mais votre soutien ne s'est jamais affaibli et m'a aidé à aller jusqu'au bout. Merci pour tout papa et maman. Merci aussi à mon frère Jeremy et à Camille. Même si on ne se le dit pas beaucoup, je sais que vous me soutenez et je vous remercie d'être vous et d'être présents.

Pendant ces années à étudier le master de physique à Grenoble, mon pied-à-terre était chez toi, Grand-Maman Martine. Je te remercie pour ces trois ans de colocation où tu m'as hébergé pendant les périodes où j'étais de retour à Neuchâtel et pour tout le reste. À toi aussi Grand-Maman Annette, un grand merci. Pouvoir présenter ma thèse de doctorat à vous deux représente une chance incroyable et j'en suis très reconnaissant. À toi Grand-Papa René, je sais ce que tu pensais avant de t'en aller et je suis fier de pouvoir te présenter ce travail.

À tous les potes avec qui j'ai partagé des discussions profondes à propos du cosmos qui souvent menaient nulle part à cause d'une absinthe de trop, je vous remercie. Être entouré par vous tous est vraiment d'une importance énorme et m'a permis de rester léger et sain d'esprit durant mon parcours.

Finally, to everyone who has been part of this journey, whether through direct contributions or by simply being there to listen and offer support, I express my deepest appreciation. This work is as much a testament to your support as it is to my efforts.

Marc Persoz

Contents

Preface

Measuring the neutron electric charge touches on aspects ranging from theoretical particle physics to real-world applications in technology, along with notable technical advancements. This thesis addresses the challenging and nuanced task of developing a high-precision instrument for fundamental research and applications. This work represents a significant advancement in the field of neutron physics, providing not only a complete description of this novel instrument but also assessing its achievable performances. The contributions presented in this thesis are expected to refine the accuracy of neutron charge studies, offering valuable insights for both fundamental physics and targeted applications in experimental techniques.

The work is structured around several key topics:

Theoretical Foundations and Motivations: The thesis begins with a discussion of the neutron's properties and the theoretical significance of its charge from experimental observations. It is further described how potential deviations from charge neutrality could indicate new physics, especially in the context of atom and bulk matter neutrality.

Neutron Production and Interferometry: The methods for neutron production at spallation sources and nuclear reactors are addressed, followed by a short explanation of neutron cooling techniques essential for creating low-energy neutrons for precision measurements. Neutron interferometry and particularly the formalism of the Talbot-Lau interferometer are described in detail, including its operational modes and applications.

Experimental Setup: An overview of the entire experimental apparatus, including the beam chopper and the neutron detection system, is documented. This section also covers the alignment procedures, measurement strategies, and the importance of precise grating positioning to ensure high visibility of interference patterns.

Development and Characterization: Results of the characterization from multiple beam times at the Paul Scherrer Institute and the Institut Laue-Langevin are presented.

The findings confirm the feasibility of detecting tiny deflections of a neutron beam. To maximize the sensitivity of the instrument for this task, all aspects and parameters of the experimental components had to be optimized.

Neutron Electric Charge Measurement: The core of the thesis is the actual measurement of the neutron electric charge. The methodology involves observing the deflection of a cold neutron beam in an electric field using the optimized apparatus. Specifically, the measurement was conducted in the ballistic mode, which provides greater sensitivity to beam deflections. The results are then compared with theoretical expectations and previous experimental limits.

Conclusion and Future Directions: The thesis concludes by summarizing the findings and outlining potential improvements to the experimental setup, suggesting directions for future research.

1. Introduction

The neutron is a fundamental subatomic particle and constitutes a building block of matter along with the proton and the electron. It played an important role in defining elemental abundances in the universe during primordial nucleosynthesis [1–3] and, since then, contributed to the evolution of the cosmos [4, 5]. Today, the neutron is studied and used in a wide range of applications, some of which will be discussed in this chapter. Its unique properties make it essential for our understanding of particle physics and cosmology and, therefore, it is particularly interesting to study its fundamental characteristics with high accuracy.

In the Standard Model of particle physics (SM), the neutron is electrically neutral ($Q_n = 0$) (Particle Data Group (PDG) [6]). However, some considerations following experimental observations linked to neutrinos have been made to revisit the SM, with the consequence of potentially modifying the neutron properties [7, 8]. These assumptions leading to a non-zero electric charge for the neutron are discussed in this introductory chapter.

Apart from its significance as a fundamental object of study, neutrons can be controlled and utilized over a wide range of energies. From traveling at thousands of kilometers per second when produced during nuclear reactions [9] to moving at just a few meters per second when cooled to ultracold temperatures [10], they serve as a versatile tool for experimental investigations in fundamental physics and beyond.

The development of an instrument capable of probing the fundamental properties of the neutron, such as its electric charge, with high precision is the central theoretical and technical motivation for the QNeutron experiment presented in this thesis. While the primary focus is on precision measurements for particle physics research, the potential for applications in other scientific and technological fields will also be explored. The methods for producing and moderating neutrons, which are critical for conducting these high-precision experiments, will be addressed later in this chapter, along with examples of practical applications.

1.1 The Neutron

Discovered in the 1930s by James Chadwick [11], the neutron has never ceased to be an object of rigorous investigation. Numerous experiments and measurements have established its fundamental properties. The most up-to-date numerical values for these properties are sourced from the PDG [6]:

- **Composition:** Neutrons are baryons composed of three quarks udd (one up quark and two down quarks) bound together by the strong nuclear force.
- **Mass (m_n):** With a mass of approximately 1.675×10^{-27} kg (939.565 MeV/c^2), neutrons are slightly heavier than protons. This mass difference arises not only from the heavier down quark but also from the dynamics of the strong interaction and binding energy contributions [12]. The mass of a neutron cannot be directly measured by mass spectrometry since it has *a priori* no electric charge (according to the SM). However, it can be deduced by determining the proton mass m_p, the deuteron mass m_d and the deuteron binding energy $E_{B,d}$ [13]:

$$m_n = (m_d - m_p) + E_{B,d}/c^2 \tag{1.1}$$

- **Spin (S_n):** With a spin of $S_n = \frac{1}{2}$, the neutron is a fermionic particle with intrinsic angular momentum [14]. Despite having no electric charge, the neutron possesses a magnetic moment of $-1.913\,\mu_N$ (nuclear magnetons), due to the motion of its internal quarks and the strong interaction [12, 15].
- **Lifetime (τ_n):** Neutrons are unstable particles with a lifetime of $\tau_n = (878.4 \pm 0.5)$ s, as recommended by the PDG since 2019. This value represents the weighted average of results from eight bottle experiments using ultracold neutrons [16–23]. However, a significant discrepancy exists when compared to beam experiments. For instance, the NIST BL1 experiment, currently the most precise beam experiment for determining the neutron lifetime, measured a value of $\tau_n = (887.7 \pm 1.2[\text{stat}] \pm 1.9[\text{sys}])$ s [24, 25]. This difference, known as the neutron lifetime puzzle, presents intriguing challenges to our understanding of nuclear stability and decay processes [4, 26–28].
- **Electric Charge (Q_n):** The SM states that the neutron electric charge is the result of the combined charges of its constituent quarks. Composed of two down quarks each carrying a charge of $-\frac{1}{3}e$ and one up quark with a charge of $+\frac{2}{3}e$, the neutron must have a net charge of zero. This can be expressed

mathematically as:

$$Q_n = 2\left(-\frac{1}{3}e\right) + \frac{2}{3}e = 0 \tag{1.2}$$

This theoretical result is supported by numerous experimental measurements, which have consistently failed to detect any deviation from a zero charge [29–31]. However, several extensions to the SM motivated by experimental observations suggest that this may not be the case after all. An example of such an observation is given later in this chapter.

- **Electric Dipole Moment (EDM):** The neutron electric dipole moment (nEDM) is a crucial parameter for studying CP violation and physics beyond the SM. The SM predicts an extremely small nEDM of around 10^{-31} e·cm. However, theories beyond the SM, such as supersymmetry or certain baryogenesis scenarios, predict significantly larger values [4]. Among several experiments aiming for this measurement, the nEDM collaboration at PSI have placed an upper bound of $|d_n| < 1.8 \times 10^{-26}$ e·cm (90% C.L.) [32].

1.2 Applications with Neutrons

As stated before, neutrons are used in a wide range of fundamental and societal applications. Due to their particular interactions with nuclear structures and their electromagnetic properties, they represent a particularly interesting tool for performing elastic and inelastic scattering [33, 34], imaging experiments [35, 36] or studying fundamental particle phenomena with high precision and detail [37]. Below are several examples of scientific fields where neutrons are used as probes to investigate specific phenomena.

Medical Therapy

A promising medical application using neutrons is the Boron Neutron Capture Therapy (BNCT). This technique employs neutron beams to selectively destroy cancer cells when combined with boron compounds and offers a novel and effective therapy option [38–40]. Additionally, neutrons play a crucial role in the production of medical radioisotopes, which are essential for various diagnostic procedures and treatments in nuclear medicine [41, 42].

Archaeology

Neutron activation analysis is used in archaeology to identify materials and trace elements in artifacts. By analyzing elemental compositions, it is possible to determine the origin and authenticity of ancient pottery, metalwork, and other artifacts, contributing to cultural preservation efforts [43].

Biology and Material Sciences

Neutron scattering techniques are crucial for studying biological molecules and cellular structures. These techniques allow the analysis of protein structures at the atomic level, giving information about biological mechanisms and facilitating the design of novel drugs targeting specific enzymes or receptors [44–46]. In material science, neutron diffraction, scattering and imaging reveal the atomic structure and properties of materials, advancing applications involving metallurgy, polymers, magnetic systems, superconductors and semiconductors [34, 47, 48].

Energy Production

Nuclear fission is driven by neutron interactions and is a powerful source of energy playing a significant role in global electricity generation. By harnessing controlled nuclear reactions, nuclear power plants produce large amounts of heat, which is converted into electricity by steam turbines [49, 50].

Fundamental Sciences

Beyond applied sciences, the neutron itself is a very interesting object of study. Tests of fundamental symmetries and interactions in particle physics can be performed by investigating its properties. Measurements of the neutron electric dipole moment [51, 52], neutron lifetime [53], neutron decay parameters [54], neutron quantum gravitational states [55] and electric charge through electric field interactions [29, 30, 56–58] provide information about the behavior of the neutron at the atomic and subatomic levels, contributing to the understanding of the fundamental forces and laws governing the universe.

1.2.1 Measuring the Neutron Electric Charge

Measuring neutron beam deflections with high precision is key to several of the applications presented previously. This kind of deflection provides critical insights

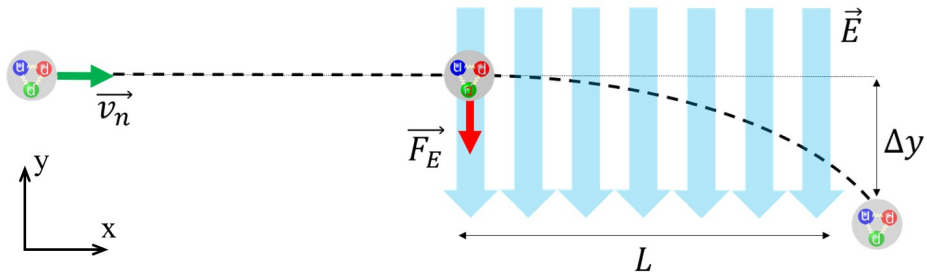

Figure 1.1. Schematic of neutron beam deflection in an applied electric field for measuring the neutron electric charge.

into how neutrons interact with other fields and matter. For the specific case of measuring the neutron electric charge depicted in Fig. 1.1, the deflection is induced by an externally applied electric field. If the neutron has a small but non-zero charge, the electric field exerts a force on it, causing a deflection in its path expressed as:

$$\Delta y = \frac{Q_n \cdot E \cdot L^2}{2 \cdot m_n \cdot v_n^2} \tag{1.3}$$

where Δy is the beam deflection, Q_n the neutron electric charge, E the applied electric field, L the interaction length, m_n the neutron mass and v_n its velocity.

Previous experiments, such as those conducted by Shull in 1967, laid the groundwork for measuring this deflection and provided early limits on the neutron charge [29]. This was later improved upon by Baumann et al. in 1988, who set the current best limit using an achromatic neutron optical imaging system with curved mirrors and multislits [30]:

$$Q_n = (-0.4 \pm 1.1) \times 10^{-21}\ e \tag{1.4}$$

In recent years, new approaches have been developed to improve these measurements. For example, Siemensen et al. proposed an experiment using specific mirrors and ultracold neutrons (UCNs) to enhance sensitivity. The slower speed of UCNs allows for longer interaction times in the electric field, increasing the deflection and making

it easier to detect. With sufficient measurement duration and rigorous control of systematic effects, the theoretical sensitivity of this technique could challenge the current best limit on neutron electric charge [56].

Building upon these previous efforts, the objective of the present experiment is to push the sensitivity to the neutron electric charge even further. To achieve this, an instrument capable of detecting neutron beam deflections in the sub-nanometer range is necessary [59]. This is where neutron interferometry emerges as a particularly powerful technique. When combined with time-of-flight measurements, it constitutes a promising approach due to its ability to capture ultra-small deflections and provide detailed insights into the neutron beam velocity distribution. Such a dedicated experimental setup is at the core of the QNeutron experiment, which aims to use intense, cold neutron beams and cutting-edge interferometric techniques either to discover a non-zero neutron electric charge or to set a new upper limit. The success of all these experiments depends on the availability of intense sources of slow neutrons. In the next section, the principle of neutron interferometry as well as the production and cooling methods of neutrons are presented.

1.3 Neutron Interferometry

Following the discussion in the previous chapter on the interests of precision measurements of neutron properties such as the electric charge, neutron interferometry emerges as one of the most advanced techniques to achieve this. It exploits the wave properties of neutrons to create interference patterns, which can be used for high-precision measurements of various neutron interactions. These include measurements of neutron beam deflections, global phase shifts due to external electric or magnetic fields, gravitational effects on neutrons, and material properties at the atomic scale. This makes neutron interferometry particularly well-suited for studying small global effects, such as those potentially caused by an externally applied electric field in the context of the QNeutron experiment.

1.3.1 Classification of Neutron Interferometers by Working Principle

Different types of neutron interferometers have been developed. They can be classified based on their distinct working principles:

- **Grating-Based Interferometers:** Grating-based interferometers, such as the Talbot-Lau interferometer, use periodic gratings to split and recombine neutron beams. These interferometers leverage the Talbot effect to achieve beam coherence [60–62]. They are particularly effective for applications like phase contrast imaging [63, 64] and dark-field imaging [65–67]. The Talbot-Lau interferometer is central to the QNeutron experiment, where its high sensitivity to sub-nanometer deflections enables precise neutron electric charge measurements [59].
- **Spin Interferometers:** Spin-based interferometers, such as Ramsey interferometers, exploit the neutron spin properties. Originally developed to measure molecular beam transitions [68], this technique was later adapted for neutron physics. By applying oscillating magnetic fields, Ramsey interferometers measure interference patterns in neutron spin states. This method is widely used for precision measurements of the neutron electric dipole moment [69–71].
- **Crystal-Based Interferometers:** Perfect crystal interferometers use perfect crystals, such as silicon crystals, to split and recombine neutron beams via Bragg diffraction [72–75]. These interferometers provide precise control over beam paths and are ideal for studying phase shifts and beam deflections caused by external fields or material properties.
- **Gravitation and Quantum Interference Experiments:** These interferometers explore the quantum behavior of neutrons in the gravitational field. By observing neutron interference in gravitational potentials, they enable studies of gravitational quantum mechanics and potential deviations from classical predictions [76, 77].

The Talbot-Lau interferometer is particularly well-suited for experiments involving beam deflections induced by electric fields or other samples modifying the trajectory of neutrons. The next section is dedicated to a deeper exploration of this type of apparatus and its operating regimes.

1.3.2 Talbot-Lau Interferometer

The Talbot-Lau interferometer employed in this project consists of three identical absorption gratings used to create a Talbot-Lau carpet (interference pattern) from

an incoherent neutron beam.[1] This setup allows for high-resolution imaging and sub-nanometer deflection measurements. Each grating plays a specific role:

- **Source grating G_0:** Converts the incoherent neutron beam into coherent line sources.
- **Diffraction grating G_1:** Diffracts the incoming coherent neutron wavefront to form a Talbot carpet.
- **Analyzer grating G_2:** Resolves and records the interference pattern produced by G_1.

The Talbot length L_T, which governs the optimum distance between gratings for interference, is given by the relationship [78]:

$$L_T = \frac{p^2}{\lambda} \tag{1.5}$$

where p is the grating period and λ is the wavelength of the neutron beam. Typically, the analyzer grating G_2 is placed at one Talbot length or higher integer multiples from the diffraction grating G_1. Any disturbance between the two gratings (such as an applied electric field or sample interaction) causes a shift in the interference pattern, allowing for sensitive measurements of neutron deflections.

Regimes of the Talbot-Lau Interferometer

A Talbot-Lau interferometer, e.g. the QNeutron apparatus, can be operated in two distinct regimes depending on the grating period p, the neutron wavelength λ, and the distance between the gratings L_G. These configurations influence the neutron beam behavior and the shape of the resulting intensity modulation. The two main cases, which will be explored in this section, are the **diffraction** regime and the **ballistic** regime. During this project, the QNeutron apparatus has been characterized in both these regimes.

Diffraction Regime:

The interferometer operates with a distance between the gratings L_G that matches the Talbot length $L_T = \frac{p^2}{\lambda}$ (or higher multiples) for the working wavelength of the beam

[1] With a coherent source, the instrument would require one less grating, functioning instead as a Talbot interferometer.

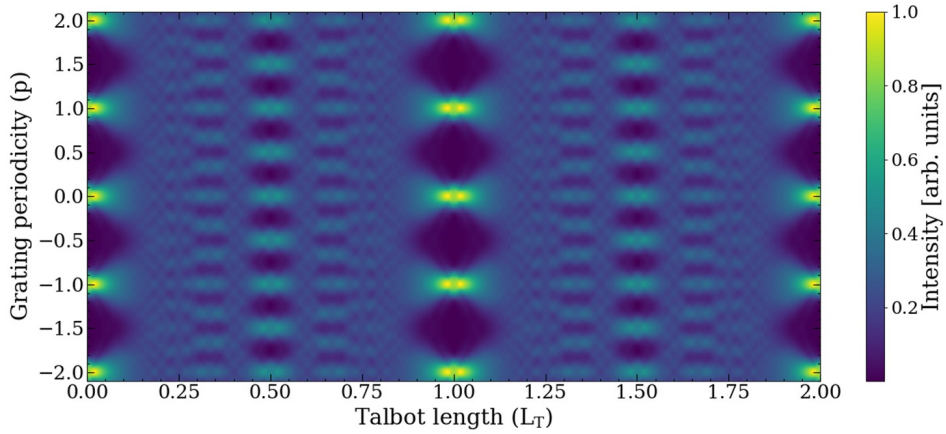

Figure 1.2. Simulation of an interference pattern produced by the diffraction grating G_1 over four periods at $x = 0$. In a classic Talbot-Lau interferometer, the analyzer grating G_2 is placed at a distance $x = L_T$ from G_1. This figure shows the interference pattern spanning two Talbot lengths. For this simulation, the opening fraction of the grating is 20% of the period.

line. As the neutron wavefronts pass through the gratings, they undergo diffraction and interference, resulting in an intensity pattern with high contrast called a Talbot carpet illustrated in Fig. 1.2.

The interference pattern produced is highly sensitive to variations in neutron wavelength, making velocity-dependent measurements necessary. When the analyzer grating G_2 is positioned at one Talbot length from the diffraction grating G_1, the resulting intensity pattern captures interactions taking place in the region between the two gratings. However, with intense, polychromatic cold neutron beams, the broad wavelength distribution poses challenges, as the Talbot length condition is met only for specific wavelengths. Consequently, accurate characterization of the beam's velocity distribution becomes essential to correctly interpret the interference pattern, though this reduces usable flux and leads to a loss in statistics.

While this configuration offers high sensitivity to sub-nanometer deflections due to the diffraction properties, the trade-off comes in the form of a more complex experimental setup. Optimizing this configuration requires balancing the precision of deflection measurements with the practical limitations imposed by setup stabilization

and reduced statistics. These aspects will be further discussed in the next chapter, along with potential strategies to address these challenges.

Ballistic Regime:

The interferometer operates in the ballistic regime when the Talbot length L_T is significantly larger than the distance between the gratings ($L_T \gg L_G$). In this regime, diffraction and interference effects can be neglected, and the trajectories of the neutrons between the gratings are approximated as straight lines. Because of the absence of diffraction, a shadow image of the diffraction grating G_1 forms at the position of the analyzer grating G_2. This occurs due to the collimating effect of the three identical gratings G_0, G_1, and G_2, ensuring that neutrons of all wavelengths overlap to form an image at the same position.

The absence of diffraction in this regime is primarily due to the use of larger grating periods. This also simplifies the system by reducing the sensitivity to misalignment and stabilization challenges. One of the key advantages of the ballistic configuration is that it is well-suited for use with non-monochromatic neutron beams, as it does not require detailed knowledge of the beam velocity spectrum. While the ballistic regime may be less sensitive to beam deflections due to the larger grating periods, it benefits from the use of the full white neutron spectrum, which significantly improve the statistics compared to the diffraction regime.

The following chapters will present how these regimes were explored experimentally, highlighting the practical challenges and advantages encountered in each mode. The instrument will consistently be referred to as an interferometer throughout this thesis, even though, technically, no interference occurs in the ballistic regime.

Simulations and Validation of Regimes

To support the experimental work and validate the behavior of the Talbot-Lau interferometer in both regimes, simulations were conducted. For the diffraction regime, a Python-based implementation was employed to model the interference patterns using the Fourier coefficients of the grating transmittance function [79–81]. This approach allows for the accurate calculation of the interference field at the observation plane (analyzer grating G_2).

In the ballistic regime, Monte Carlo simulations were used to model neutron trajectories, assuming straight-line paths between the gratings. This method focuses on how

neutrons interact with the gratings to produce intensity patterns that can be analyzed for deflection measurements.

Both regimes were compared to experimental data, and key insights were gained regarding the optimal duty cycle of the gratings and the geometry of the setup. More details about these simulations and their results can be found in App. A, where the full derivations of the formulas and detailed behavior of both regimes are provided.

To effectively test and validate both the diffraction and ballistic regimes of the Talbot-Lau interferometer, it is crucial to have access to well-characterized neutron beams with appropriate energy ranges. These beams are typically generated and provided at large-scale research facilities.

1.4 Neutron Production and Cooling

Neutrons are massive, supposedly chargeless subatomic particles with a magnetic moment and interact via the strong force, making them an ideal probe in both fundamental physics and various applications. As seen above, low-energy neutron production and control are useful to conduct experiments exploring the fundamental properties of matter. This kind of research is carried out at national and international large-scale research facilities providing dedicated beam lines [82–88].

Two common techniques are employed to produce neutrons for fundamental research and applications. During this project, the QNeutron apparatus has been characterized with both types of sources detailed below.

Production at Spallation Sources

Spallation sources use high-energy particle accelerators to generate neutrons by bombarding heavy target materials with energetic protons or other charged particles. One of the leading facilities employing this technique is the Paul Scherrer Institute (PSI) in Villigen, Switzerland (Fig. 1.3), which hosts the Swiss Spallation Neutron Source (SINQ). The availability of this neutron source has enabled scientists to make significant contributions to numerous studies and publications in the field of neutron science. A few recent examples can be found here [89–95].

The process by which neutrons are typically produced in a spallation source is described below.

Figure 1.3. Paul Scherrer Institute (PSI) in Villigen, Switzerland. Home of the spallation source SINQ, the PSI offers a wide range of instruments for fundamental research as well as a center for proton therapy. Image taken from [96].

- **Proton acceleration:** A high-energy proton beam, usually obtained from a particle accelerator, is directed onto a heavy metal target, such as tungsten, lead, or uranium [97].
- **Target interaction:** The energetic protons collide with the nuclei of the target material, causing spallation reactions where fragments of the target nucleus, including neutrons, are ejected in every direction [98–100].
- **Neutron moderation:** The fast neutrons produced in the spallation process initially have an energy of a few MeV. They are moderated, or slowed down, by elastic scattering using materials like water or graphite, to achieve lower energies suitable for experiments [101, 102]. The production of UCN involves the use of solid deuterium or superfluid helium as a converter medium. More details are given below.

Production at Nuclear Reactors

Nuclear reactors also serve as sources of neutrons, particularly for continuous neutron beams. The Institut Laue-Langevin (ILL) in Grenoble, France (Fig. 1.4), operates a high-flux research reactor that provides intense neutron beams for a wide range of scientific investigations [103, 104]. The process of neutron production in a nuclear reactor is described below:

- **Fission process:** Nuclear reactors employ controlled nuclear fission of uranium or plutonium isotopes. The fission of these materials releases neutrons among other products [49, 50].
- **Neutron flux and moderation:** The fission reactions within the reactor core generate a flux of fast neutrons [105, 106], which are essential for sustaining the chain reaction. To enhance the probability of further fission events, they are moderated to lower energies [107]. These moderated neutrons can finally be used in scientific research, providing beams suitable for various experiments. In the next section, the different mechanisms to cool neutrons and the achievable energies are presented.

Neutron Moderation

The process described here allows neutrons to be slowed down to low energies (thermal, cold and ultracold neutrons), providing longer observation time for studying particle interactions and performing high-precision measurements [101, 102, 109, 110].

- **Thermal neutrons:** Neutrons produced at high energies are initially thermalized (slowed down) through elastic collisions with nuclei of moderating materials like water, heavy water, or graphite. Thermal neutrons have the peak of their energy spectrum at about 25 meV, corresponding to a velocity of approximately 2200 m/s and a temperature of about 300 K (room temperature).
- **Cold neutrons:** Further cooling is achieved by passing the thermalized neutrons through a moderating material (e.g., liquid deuterium), where they lose energy through repeated collisions. As a result, cold neutrons typically have energies peaking at around 5 meV, with velocities near 1000 m/s and a temperature close to 60 K.
- **Ultracold neutrons (UCN):** Cold neutrons are converted into ultracold neutrons via inelastic processes, such as the creation of a phonon in a converter

Figure 1.4. Institut Laue-Langevin in Grenoble, France is the home of the world's most intense cold neutron beam line: PF1B. The ILL offers a wide range of instruments for fundamental research in neutron sciences. Image taken from [108].

medium at very low temperatures, e.g. superfluid helium or solid deuterium. These inelastic collisions allow the neutrons to lose energy and slow down to very low velocities. UCNs have kinetic energies below 300 neV, velocities less than 7 m/s, and a corresponding effective temperature below 3 mK.

The moderation mediums, energies, velocities, and temperatures of these three categories of neutrons are summarized in Table 1.1. Note, ultracold neutrons don't follow a Maxwell distribution as there is no thermal equilibrium in superthermal sources. For the entirety of this work, the QNeutron apparatus has been operated using **cold neutrons**.

Table 1.1. Energy, velocity, and temperature of neutron categories.

Category	Moderator/Converter	Energy	Velocity	Temp.
Thermal	H_2O or D_2O (300 K)	~ 25 meV	~ 2200 m/s	~ 300 K
Cold	Liquid D_2 (25 K)	~ 5 meV	~ 1000 m/s	~ 60 K
UCN	sD_2 (6 K), He-II (<1 K)	< 300 neV	< 7 m/s	< 3 mK

1.5 Theoretical Considerations About the Neutron Electric Charge

In the process of scientific discovery, discrepancies between experimental results and theoretical predictions often serve as a catalyst for revisiting and refining models of fundamental physics. One such case is the discovery of neutrino oscillations [111, 112], which challenged the assumption of the SM stating that neutrinos are massless [6, 113]. These observations have led to significant revisions in the understanding of particle physics.

In this section, the theoretical explanations for neutrino oscillations are explored. Specifically, the introduction of neutrino mass can lead to modifications in other aspects of particle physics, such as the electric charge of the neutron. This exploration will highlight how efforts to incorporate neutrino mass into the SM could influence the properties of the neutron, potentially giving rise to a small but measurable electric charge.

Representation in the Standard Model

The description of the universe at the most fundamental level is possible by understanding its symmetries [114, 115]. In physics, a symmetry refers to the property that a physical system remains invariant under a given transformation. These transformations can include operations like rotations, reflections, translations, or can impact more abstract properties such as time reversal (T) or the electric charge of an elementary particle (C) [116, 117]. In the SM, the possible transformations of a particle are described by gauge symmetries. The mathematical formulation of the SM involves three specific groups $SU(3)_C \times SU(2)_L \times U(1)_Y$ responsible for the interactions between fundamental particles.

- $SU(3)_C$ is the symmetry group of quantum chromodynamics (QCD), which describes the strong interactions between quarks and gluons.
- $SU(2)_L$ describes the weak interaction, responsible for processes like β-decay.
- $U(1)_Y$ corresponds to the hypercharge, which is related to the electromagnetic interaction after spontaneous symmetry breaking.

The fermions (quarks and leptons) are assigned to specific representations under these groups, which dictate their interactions with the gauge fields. In general, the symmetries of these groups are expected to be conserved for a given physical system [118]. However, in the case of subatomic particles, certain quantum effects, known as anomalies, can break these symmetries [119–121]. To maintain the consistency of the theory, the total contribution of these anomalies across all particles must cancel out to zero [122].

This anomaly cancellation condition plays a crucial role in defining the hypercharges of particles, which in turn determine their electric charges [123]. For example, the charge assignments of quarks and leptons in the SM are derived to ensure this cancellation. However, any modification to the particle content, such as the introduction of new particles, would require a re-evaluation of these conditions by extending the model. The anomaly cancellation conditions could potentially be altered and lead to subtle changes in the predicted charges of fundamental particles, including the neutron.

A Neutrino Mass for a Neutron Electric Charge

The discovery of neutrino oscillations [111, 112], during which a neutrino changes its flavor as it propagates, has provided unambiguous evidence that they must have mass. This property requires a reconsideration of the massless neutrino assumption and an exploration of modifications to the SM that could accommodate these findings.

One of the most natural and straightforward extensions involves the introduction of right-handed neutrinos [7, 124, 125]. Unlike their left-handed counterparts, right-handed neutrinos do not interact via the weak force. The introduction of these particles allows for the inclusion of a Majorana mass term, which could explain the small observed neutrino masses [126]. Importantly, the presence of right-handed neutrinos alters the anomaly cancellation conditions, as the new particle content must satisfy these constraints.

Revisiting the anomaly cancellation conditions in light of right-handed neutrinos may slightly modify the predicted electric charges of particles. This opens the possibility that the neutron, traditionally considered electrically neutral, might have a small non-zero charge. While a precise theoretical value for this deviation is not predicted, even a tiny deviation from zero would have profound implications for our understanding of atomic neutrality and charge quantization beyond the SM [127–130].

Baryon Asymmetry of the Universe

When observing the universe on large scales, objects such as galaxies and galaxy clusters appear to be distributed uniformly and isotropically [131]. Current understanding indicates that these objects, as well as smaller structures like asteroids, planets, and stars, are composed of ordinary matter, known as baryonic matter, consisting of protons, neutrons, and electrons. While the SM provides the most precise framework for describing the behavior of these subatomic particles, it cannot explain the origin of baryonic matter itself [132].

When particles are created from high-energy collisions, a fundamental symmetry exists between matter and anti-matter. If a given number of baryons is created, the exact same number of anti-baryons is also produced. This symmetry is consistently confirmed in experiments, such as those conducted by the BASE collaboration [133]. However, astronomical observations reveal a different reality, as no anti-galaxies or even large amounts of antiparticles have ever been observed. This discrepancy suggests that, during the early universe, a process must have violated this symmetry, leading to the predominance of matter over antimatter.

In 1967, Andrei Sakharov published three conditions that a baryon-generating mechanism should fulfill to account for this discrepancy. The Sakharov conditions for generating a baryon-antibaryon asymmetry are [134]:

1. **Baryon Number Violation:** There must be processes that violate baryon number conservation, enabling a net imbalance between the number of baryons and antibaryons, which is essential for explaining the observed dominance of matter over antimatter.
2. ***C* and *CP* Violation:** There must be violations of charge conjugation (C) and combined charge conjugation-parity (CP) symmetries, which are crucial for creating a net baryon excess in the early universe.

3. **Departure from Thermal Equilibrium:** Relevant processes must occur out of thermal equilibrium to enable the accumulation of a baryon asymmetry over time.

Considering these conditions, an exciting avenue for exploring baryon number violation is brought by the potential existence of neutron-to-antineutron oscillations [135–138]. However, if the neutron possesses a small non-zero electric charge, such oscillations would be forbidden, as electric charge is a conserved quantity in particle transformations and reactions.

Thus, the QNeutron experiment not only refines our understanding of neutron properties but also broadens our knowledge in other areas of fundamental physics. By achieving high-precision measurements of the neutron electric charge, this experiment aims to place tighter constraints on possible deviations from the SM. Such measurements are crucial for investigating potential mechanisms behind baryon asymmetry and exploring the implications of charge quantization at the subatomic level. Furthermore, detecting even a small deviation from neutron charge neutrality could provide insights into new physics beyond the SM, offering a deeper understanding of fundamental forces and particle interactions that govern the universe.

1.6 Summary

This chapter has presented the foundational context of the neutron, highlighting its key properties and its critical role in both fundamental and applied sciences. As a baryon, the neutron plays a pivotal part in our understanding of particle physics, cosmology, and nuclear phenomena. While the SM predicts the neutron as being electrically neutral, experimental evidences, such as the discovery of neutrino oscillations, suggest the need to revisit certain assumptions within this framework.

The QNeutron experiment seeks to address one of these fundamental questions, which is the possibility that the neutron possesses a small, non-zero electric charge. By developing an instrument capable of detecting ultra-small deflections of a neutron beam in an applied electric field, this experiment aims to achieve unprecedented precision in measuring the neutron electric charge. In doing so, QNeutron not only strives to enhance our understanding of particle physics but also provides insights that could influence future applications in fields where such an instrument is employed.

Overall, this work contributes to the broader goal of probing the limits of the SM, advancing both theoretical and experimental physics while offering potential applications across diverse scientific fields.

2. QNeutron Apparatus

In the previous chapter, the fundamental properties of neutrons, the motivation for measuring their electric charge, and the role of neutron interferometry in achieving the required precision have been presented. To perform these high-sensitivity measurements, the design and operation of a specialized experimental setup are essential. This chapter provides a detailed overview of the QNeutron apparatus, the key instrument used in the project.

The QNeutron apparatus is designed specifically to measure ultra-small deflections of neutron beams caused by external electric fields, with the ultimate goal of setting a new upper limit or finding a non-zero value of the neutron electric charge. Here, the components of the setup, their roles in the experiment, and the methods used for data collection, measurement, and analysis are outlined.

2.1 General components

Figure 2.1 provides a schematic overview of the apparatus, including labeled coordinate axes, rotation angles around the main axes, device names, and key components.

This work adopts the following coordinate system as the standard nomenclature, used consistently to describe the setup, orientations, and measurements. In this system, each axis designation includes both a position variable and a corresponding rotation angle.

- $(\boldsymbol{x}, \boldsymbol{\theta})$: Beam axis. The 0-position is defined at the fixed starting point of the beam line. All subsequent measurements are taken from this origin.
- $(\boldsymbol{y}, \boldsymbol{\varphi})$: Grating scanning axis, oriented perpendicular to the beam axis, following the periodic structure of the gratings.
- $(\boldsymbol{z}, \boldsymbol{\psi})$: Vertical axis.

Each notation pair, such as (x, θ), consistently refers to a position along a given axis and a rotational angle around that same axis.

The gratings are referenced as described in the previous chapter as G_0, G_1 and G_2. The distances between them are labeled L_0 between G_0 and G_1 and L_1 between G_1

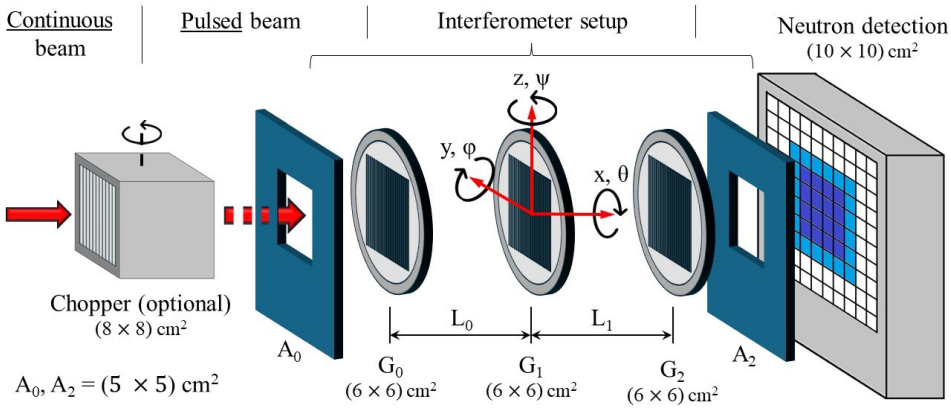

Figure 2.1. Scheme of the QNeutron apparatus. The neutron beam goes from left to right. The optional chopper converts the continuous beam into bunches of neutrons allowing for velocity characterization. The beam goes through the three absorption gratings (G_0, G_1 and G_2), which are positioned between two collimating apertures (A_0 and A_2). The neutron detector is located at the end of the setup.

and G_2, respectively. For the majority of this work, the two distances are equal, and therefore $L_0 = L_1 = L_G$.

2.1.1 Beam Collimation

Adjustable apertures made of borated aluminum (BorAl[1]) are positioned along the setup to match the acceptance limits of each main component (chopper, gratings, detector). These apertures ensure precise collimation and shape the beam to a square profile suitable for typical measurements, with a cross-section small enough to avoid obstruction by any component. The defining apertures are named with the same number as for their respective grating. In Fig. (2.1), only two squared apertures are depicted as A_0 and A_2 (before G_0 and in front of the detector), corresponding to the most common configuration used in Chap. 3 and 4. In Chap. 5, an additional aperture A_1 is added between G_0 and G_1, close to G_1 and the beam shape will be adapted to the two-beam method (Sec. 4.4.5) for the experimental setup.

[1] An aluminum alloy containing up to 4% ^{10}Boron.

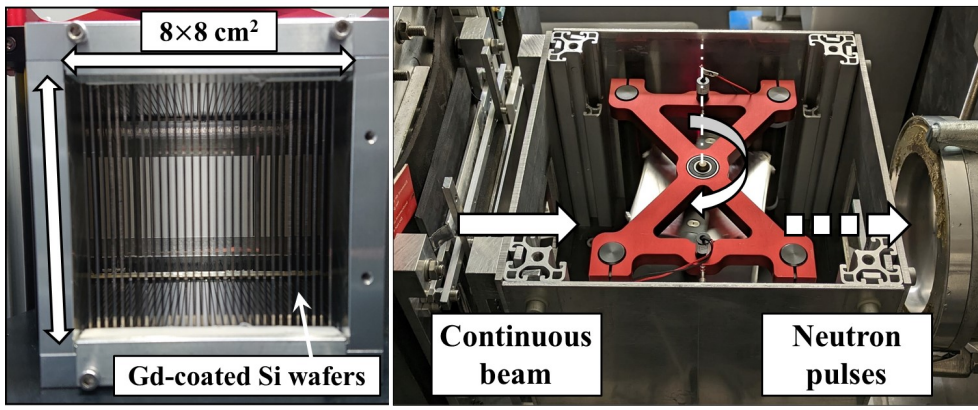

Figure 2.2. Left: Neutron Fermi-type chopper collimator box with TiGd-coated silicon wafers to produce neutron pulses with an adjustable frequency. The acceptance cross-section is a square with sides of 8 cm. Right: Top view of the chopper with the collimator mounted inside. The white arrows represent the direction of the neutron beam. The rotation frequency and the opening time are measured by a laser-photodiode pair.

2.1.2 Chopper

For velocity characterization measurements, a custom-built Fermi-type chopper, shown in Fig. 2.2, is employed. The setup consists of a rotating casket filled with 32×2 silicon wafers coated on both sides with 2 µm of titanium gadolinium. Each pair of wafers has a total thickness of 0.8 mm (2×0.4 mm wafers) and are spaced 2.5 mm apart (center-to-center). This configuration ensures the fitting within the 8×8 cm^2 acceptance limit of this collimator box. When the wafers are aligned with the beam, a hole in the rotating platform allows the light of a fixed laser, mounted on the chopper case, to reach a fixed photodiode positioned below the platform. When the hole passes under the laser, the photodiode detects the signal, triggering an electric pulse which is sent to the central computer. At the same time, a corresponding neutron pulse propagates downstream to the detector.

The chopper can be operated in three modes:

- **Closed:** Chopper not rotating, wafers positioned perpendicular to the neutron beam, fully blocking transmission.

- **Open:** All 32 wafers installed, chopper not rotating. The wafers are aligned with the neutron beam direction and provide a continuous transmission. Then the neutron intensity is typically about 65% of the full beam intensity without the chopper.
- **Measurement:** Chopper rotating at a chosen frequency. For velocity-dependent characterizations (Chap. 4), a neutron pulse repetition frequency of $f_{ch} = 25$ Hz (rotation frequency of 12.5 Hz) is used, resulting in a reduction of beam intensity by approximately a factor 200 compared to when the chopper is not mounted.[2] The resolution of the chopper in term of neutron wavelength can be determined using the geometry of the collimation box and the rotation frequency.

By measuring the time interval between each chopper pulse and the arrival of neutron counts at the detector, the beam line velocity spectrum can be obtained. Neutron counts are sorted into time bins with a minimum size of 100 ns, allowing for detailed time-of-flight (TOF) analysis. Typical time bins with a duration of 50 µs were used in TOF measurements.

The stepper motor of the chopper is controlled by a custom-built Chopper Control Box (CCB), connected to the central computer, which manages data acquisition through the MIDAS application described in Sec. 2.1.5. The CCB is powered by a Keysight E3634A DC power supply providing 48 VDC [139].

2.1.3 Neutron Detector

The detection of neutrons is achieved using a custom-made Cascade detector (Fig. 2.3) from CDT Cascade Detector Technologies GmbH [140]. This detector employs stacked Gas Electron Multiplier (GEM) foils and coated with thin ^{10}Boron layers that capture neutrons and produce ^{7}Li and alpha particles as fragmentation products. These charged particles ionize the surrounding ARCAL™5 gas mixture (82% CO_2 and 18% argon). The resulting electron cloud is accelerated by a high-voltage toward a readout card, where it generates measurable electronic signals and allows measurement with various time bin sizes in minimum steps of 100 ns. With an active area of 10×10 cm^2

[2] Since direct removal of the chopper causes detector saturation under normal flux conditions (saturation at a neutron count rate of 2×10^7 s^{-1}), this factor has been determined with a reduced beam flux achieved by installing the gratings and the electrode setup beforehand. Hereby, the neutron rate was reduced from about 700×10^3 s^{-1} (chopper not mounted) to 3.5×10^3 s^{-1} (pulse repetition frequency of 25 Hz)

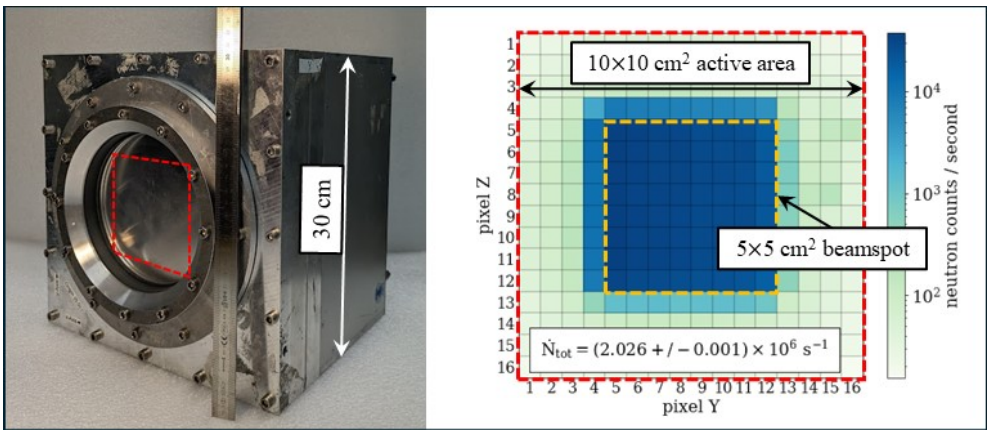

Figure 2.3. Left: Neutron Cascade detector with an active area of 10×10 cm^2. Right: Example of a measurement taken with the detector during 30 s at the PF1B beam line with a resolution of 16×16 pixels. The defining apertures of the apparatus create an active beam spot of 5×5 cm^2 visible in blue tones. Each pixel can be analyzed separately for measurements requiring a spatial characterization of the beam.

and a resolution of 16×16 pixels, it allows a maximum detection rate of 20 MHz with an overall efficiency of around 35% at a neutron wavelength of 0.5 nm.

The neutron detector is powered with two different voltages. A negative high-voltage of around 2700 V provided by a power supply iseg SHQ 226L to feed the detector, and a 5 VDC supply for the electronic read-out by a Keysight E3633A DC power supply. Like the chopper, the detector is connected and read out by the central computer with the application MIDAS (Sec. 2.1.5).

High-Voltage Settings

For optimal detection efficiency, the neutron detector must operate in proportional mode at a high-voltage between −2500 V and −2950 V, with the exact setting depending on the specific ARCAL™5 gas mixture. To determine this setting, a systematic scan is conducted, measuring the detector's response across this voltage range. Plotting the corresponding neutron count rates reveals a "plateau region" where the count rate stabilizes even as voltage increases. This plateau indicates the detector's operational stability, maximizing signal amplification without excess noise or saturation.

Details about this scan are given in the next chapters related to characterization measurements.

Discriminator Sensitivity

Before applying the high-voltage, it is essential to determine the appropriate discriminator setting. This process involves measuring and plotting the count rate against the discriminator setting for each readout channel to identify where the counting noise is minimized. The discriminator value is adjusted via an eight-bit register, allowing variation between −200 mV and 200 mV, with 0 mV corresponding to a register value of 128. Typically, the scan reveals a noise-related peak around a setting of 128. For detectors with negative charges, such as the Cascade detector, the optimal setting is slightly below this peak, at discriminator values of about 108. Examples of such scans can be found in Sec. 4.1.5.

Event-Filter Algorithm

The Cascade DAQ system includes a real-time event filtering algorithm designed to minimize false events caused by issues like sparks or faulty pixels. This algorithm optimizes the detector performance by analyzing event statistics and adjusting parameters to achieve typical operational values. Real neutron events are identified as signals spanning multiple adjacent pixels and multiple time bins with a duration of 100 ns. The event filter consolidates these signals into single events, removing ambiguous data such as simultaneous hits in unconnected regions. The user can disable the filter to transfer raw data for further analysis, offering flexibility in data processing to meet specific experimental needs. In Chap. 3, an unfortunate issue led to a wrong event filter setting. As a consequence, a scaling factor has to be applied to the data to compensate for false events (Sec. 3.2). In Chap. 4 and 5, this problem has been resolved.

2.1.4 Absorption Gratings

A neutron absorption grating is a physical structure that modulates neutron wavefronts through periodic patterns such as alternating lines of absorbing and transparent material. When waves pass through these patterns, they interfere with one another and create diffraction and interference effects.

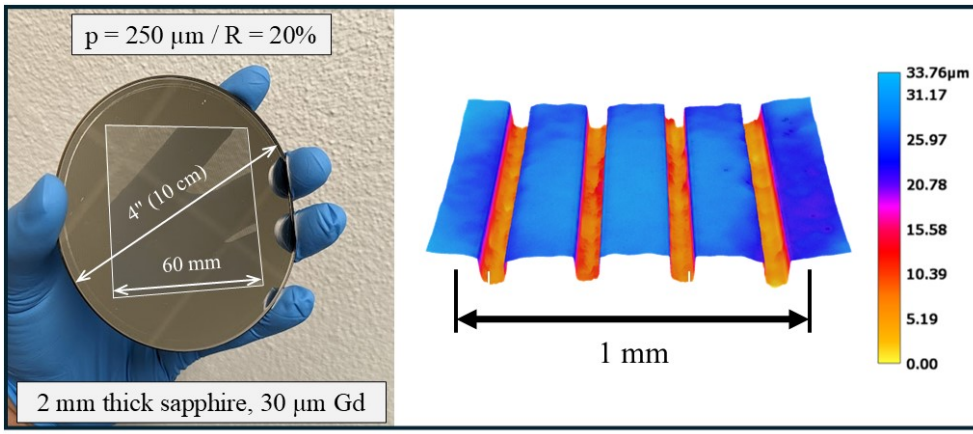

Figure 2.4. Absorption grating with a period $p = 250\,\mu m$ and duty cycle $R = 20\%$ on a 4 in-diameter, 2 mm-thick sapphire substrate. Left: The gadolinium thickness is 30 µm and the line structure is laser-engraved on a 6×6 cm^2 area. Right: Depth map of the same grating under an optical microscope.

Manufacturing

The gratings used in the setup are of two types: one with a 1 mm-thick sapphire substrate coated with a 20 µm gadolinium layer, and another with a 2 mm-thick substrate and a 30 µm gadolinium layer. Both substrate have a diameter of 4 inch. Sapphire was chosen for its transparency and durability, which also enables potential use with visible light. These gratings serve as absorption gratings, using the high neutron absorption cross section of gadolinium of 49 700 b (for 2200 m/s neutrons) [141]. The Sapphire wafers come from the company **Wafer Universe** [142] and the gadolinium coating has been made by **Swiss Neutronics** [143].

Each grating is laser-engraved by the company **PhotonsAtWork** [144] with a specific line pattern covering a 6×6 cm^2 area, ensuring it fully covers the neutron beam profile. The center-to-center distance between two adjacent lines represents the grating period p and the duty cycle R is defined as the ratio between a slit width and the period. Figure 2.4 shows an image of a grating and a depth map captured with an optical microscope.

Design Parameters

For characterization and optimization purposes, multiple sets of gratings have been manufactured:

- **Ballistic regime:** In this configuration, all the gratings have a period p = 250 µm and duty cycles of 10%, 20%, and 40%. The design with 20% features both gadolinium thicknesses of t_{Gd} = 20 µm and 30 µm. Adjusting these parameters helps to optimize the performance of the apparatus in the ballistic setup described in Chap. 3 and extensively in Sec. 4.4.
- **Diffraction regime:** Two sets of gratings have been manufactured with p = 25 µm, R = 20% and t_{Gd} = 20 µm and 30 µm. The results are again presented in Chap. 3 and in more detail in Sec. 4.5.
- **Intermediate regime:** Three other sets were manufactured, two with p = 125 µm (duty cycle of 20% and 40%) and a last one with p = 100 µm and R = 10%. These intermediate-sized sets are useful to understand the transition between the ballistic and the diffraction regime. It also allowed testing a variant of the setup with non-equal distances between the gratings (Sec. 4.4.6).

Gratings Manufacturing Issue

It is important to note that the gratings with a period of p = 250 µm, R = 20%, and t_{Gd} = 30 µm were produced in two separate batches using different laser engraving processes. The absorption characteristics of the first batch did not align with expectations across all wavelengths. A surprisingly high background was indeed noticed in dedicated measurements presented in Chap. 3. A second batch was subsequently produced using an optimized process and tested in Sec. 4.4, resulting in absorption performance that meets expected specifications.

Motorized Positioners

The gratings are mounted on a stack of three motorized precision positioners from the manufacturer Standa [145]. The respective model, working axis and resolution of each stage are listed below:

- **Goniometer 8MG99-80** with a resolution of 10.96” (0.003 °) per step over a range of ±2.5° allowing the rotation of the grating around the beam axis θ.

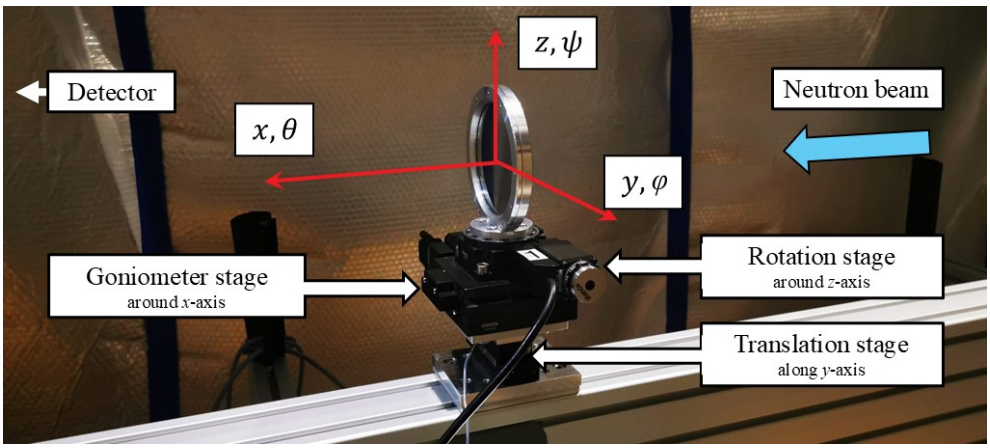

Figure 2.5. Grating with an engraved area of 6×6 cm^2 mounted on the three motorized positioners allowing rotations around the beam axis θ and the vertical axis ψ, and translations along the grating scanning axis y. The neutron beam is traveling from right to left and the detector is mounted downstream, on the left side of the picture.

- **Translation stage 8MT173-30** for scanning the gratings along the y-direction. The maximum range is 30 mm with a full-step resolution of 1.25 µm. The resolution can be increased even further by using the stage in $(1/4)^{th}$-step mode down to 0.313 µm per step.
- **Rotation stage 8MR151** around the vertical axis ψ with a full-circle range and a resolution of 0.01°.

Each of these motorized positioners shown in Fig. 2.5 is controlled *via* a two-axis motor controller 8SMC5-USB-B9-2 from Standa, which allows remote control and automation of the stages. These controllers are themselves connected to MIDAS, as described in the following section, enabling streamlined integration of the positioners within the data acquisition system. The alignment procedure, which can be automated using these controllers, is detailed in App. B.

2.1.5 Data Acquisition System (DAQ)

The QNeutron apparatus uses the MIDAS (Maximum Integrated Data Acquisition System) [146] to control equipment, automate measurement sequences, and collect

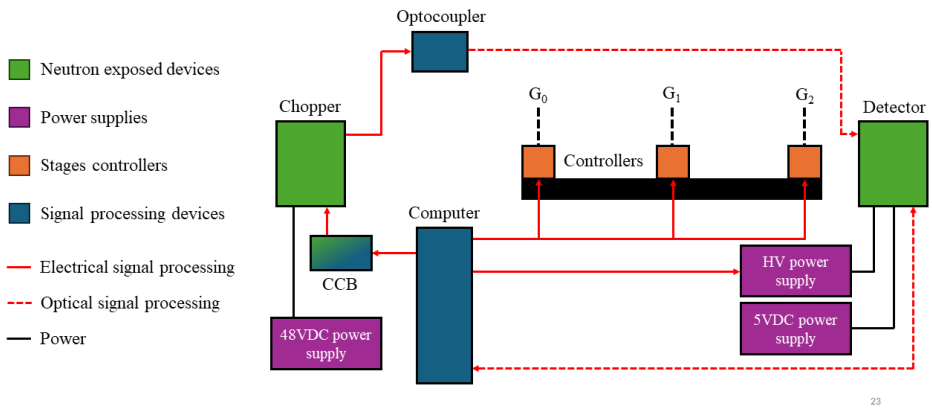

Figure 2.6. Block scheme of the setup depicting the DAQ. The neutron-exposed devices are in green, power supplies in purple, controllers for motorized stages in orange, and signal processing devices in blue. Black and red lines represent electrical and optical connections, respectively.

and process data in real-time. This flexible system, accessible via command-line or web interfaces, supports remote access through SSH and integrates the ROOT framework for data analysis. Figure 2.6 shows the key components and connections within the setup, managed by MIDAS for precise and efficient operation.

The data acquisition process involves the following automated steps:

1. **Initial Setup:** Configurable parameters, such as chopper sweeps, time bin size, and number of bins, are set in MIDAS according to the neutron spectrum under study. The Fermi-type chopper (Sec. 2.1.2) runs at a pulse rate of 25 Hz for most TOF measurements made during this work.

2. **Measurement Start:** With parameters set, the operator can initiate a measurement. MIDAS synchronizes the detector (Sec. 2.1.3) and chopper, monitoring the incoming pulses. The detector is equipped to capture neutron events with temporal resolution down to 100 ns.

3. **Data Collection:** The detector firmware organizes neutron counts into time bins corresponding to distinct arrival times, ensuring accurate velocity spectrum capture. The integration time, set by MIDAS, determines the number of sweeps and timing parameters.

4. **Data Processing and Storage:** After the sweep count is reached, MIDAS stops acquisition and stores data in a binary file. Data is converted into ROOT format and includes time-resolved neutron counts and device settings, such as detector high-voltage or stage positions, for ease of access during further analysis.

5. **Motorized Stage Scans:** MIDAS controls motorized stages (G_2 for example) to move between predefined positions. After each position change, data is recollected, simplifying alignment and facilitating automated scanning sequences.

6. **Final Compilation:** All data from completed runs are compiled into a ROOT sequence file for comprehensive analysis.

The sequencer within MIDAS is a vital tool, enabling automated, continuous measurement sequences by adjusting device parameters automatically and reducing manual intervention. This system improves efficiency and consistency in complex experiments like neutron electric charge measurements performed overnight.

2.2 Measurement Strategy

This section outlines the strategy for optimizing the sensitivity in neutron electric charge detection, focusing on transverse scans (along the y-axis) with G_2 to analyze the resulting oscillating intensity pattern. This pattern is fundamental for characterizing various parameters, such as visibility and setup sensitivity to beam deflection, particularly under time-of-flight conditions to account for varying neutron wavelengths. Prior to these scans, grating alignment is necessary (see App. B).

The sensitivity of a neutron electric charge measurement is given by [59]:

$$\sigma(Q_n) = \frac{4\pi\hbar^2 p}{\eta m_n E L^2 \lambda^2 \sqrt{N_w}} \tag{2.1}$$

where p is the period of the gratings, η the visibility of the oscillating pattern, m_n the neutron mass, E the applied transverse electric field, L the interaction length, λ the neutron wavelength, and N_w the neutron counts measured at the working point w_p. The parameters η and N_w are particularly relevant because they depend heavily on grating geometry and therefore can be tuned. The next sections describe how these parameters are determined and their optimization is detailed in Chap. 3 and 4. The goal of every characterization campaign is to minimize $\sigma(Q_n)$ in order to operate

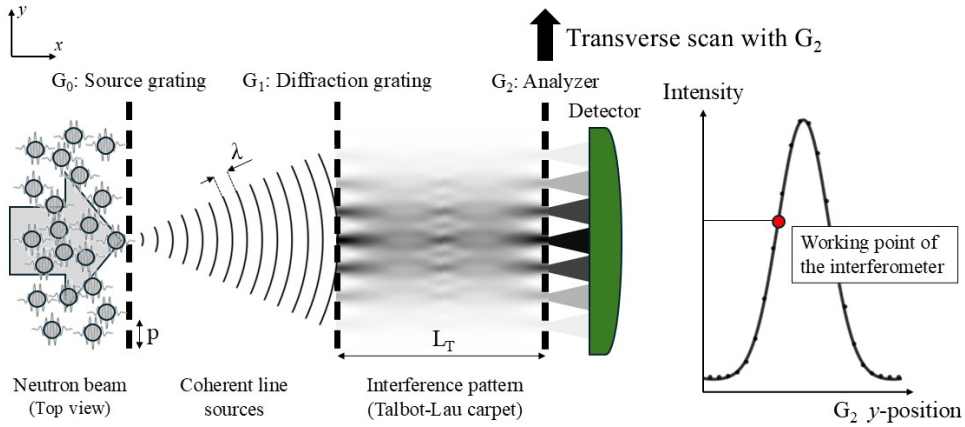

Figure 2.7. Schematic top view of the apparatus. On this example, neutrons enter from the left as a monochromatic beam of wavelength λ. The grating period is denoted as p. In the diffraction configuration, G_0 produces coherent line sources that illuminate G_1. An interference pattern forms at one Talbot length $L_T = \frac{p^2}{\lambda}$, where G_2 is placed as an analyzer. The detector is positioned behind G_2 and is depicted in green. By performing a transverse scan with G_2 along the y-axis over one grating period, an intensity modulation is obtained. This allows for determination of the setup's visibility and working point w_p, indicated by the red point.

with the best possible instrument during the neutron electric charge measurement presented in Chap. 5.

2.2.1 Oscillating Intensity Pattern

The oscillating intensity pattern mentioned above is recorded by moving G_2 step by step perpendicularly to the neutron beam and across several periods while counting the neutrons at each position for a given time. A scheme of the setup view from above is shown in Fig. 2.7 where the transverse scan is illustrated. On the right is the corresponding intensity modulation obtained over one grating period and the red point represents the y position of G_2 with the steepest slope of the modulation, constituting the most sensitive arrangement of the apparatus.

This pattern is essential for characterizing the visibility (η), working point of the instrument (w_p) and the relative position of the interference fringes along the y-

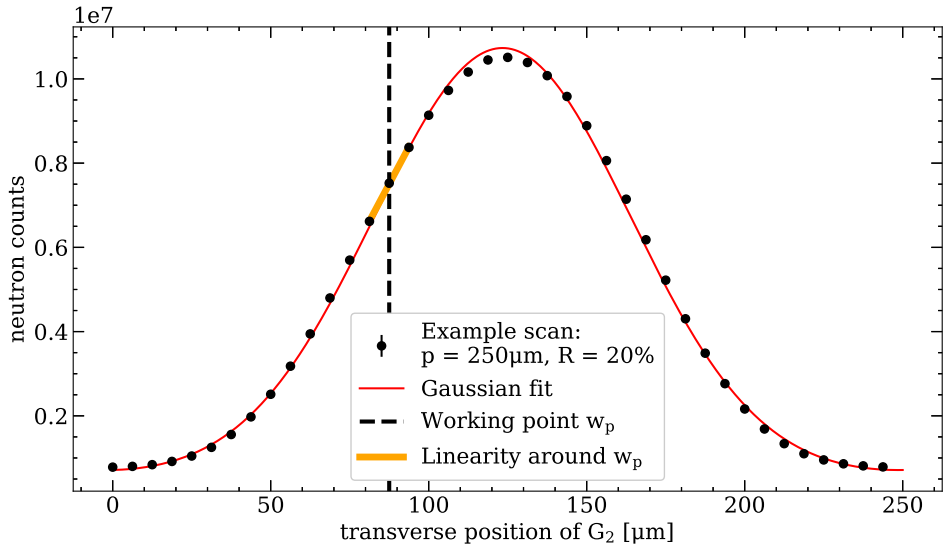

Figure 2.8. Example of a transverse scan with G_2 conducted at the PF1B beam line at the ILL with an exposure time of 20 s per point across one period of 250 µm, using a step size of 6.25 µm. The red line shows a Gaussian fit, while the black dashed line marks the data point with the steepest slope, designating the working point w_p. The thick yellow line indicates a linear fit across three data points, centered around w_p.

axis. By combining these transverse scans with time-of-flight data, a comprehensive wavelength-dependent analysis of these properties is possible. Details regarding their importance and application follow in the next sections.

Interferometer Visibility

The visibility η is a critical parameter in neutron grating interferometry. It describes the contrast in the intensity modulation observed during transverse scans and is defined as:

$$\eta = \frac{I_{\max} - I_{\min}}{I_{\max} + I_{\min}} \tag{2.2}$$

where $I_{\max}$ and $I_{\min}$ represent the maximum and minimum intensities within one grating period. High visibility indicates well-defined intensity peaks, enhancing sensitivity to beam deflections caused by test samples or, crucially, by an externally applied electric field assuming a non-zero neutron electric charge. Maximizing this visibility through optimized grating parameters and alignment is thus a central task of the project considering the main objective of the QNeutron experiment.

Working Point w_p

Another essential feature of the oscillating intensity pattern is the working point, w_p, defined as the position with the steepest slope. Monitoring the intensity at this point helps to quantify the stability of the apparatus, since an intensity change suggests potential alignment drifts or other experimental inconsistencies. For the experiment's objective of measuring beam deflections caused by an externally applied electric field and a non-zero neutron electric charge, w_p is crucial. By using the slope at w_p, it is possible to translate intensity changes into relative shifts in the oscillating pattern's position. The slope at w_p is calculated using a linear fit across three data points centered on w_p.

To differentiate between a true beam deflection (induced by a sample or an applied electric field) and an unintentional setup drift, the two-beam method will be employed. This method, involving splitting the beam into two distinct spots, will be detailed in Sec. 4.4.5. It enables a comparative analysis to distinguish genuine deflections from alignment fluctuations and drifts.

2.2.2 Signal Characterization

The intensity patterns observed during the experiment vary depending on the design and duty cycle of the gratings, as well as the specific regime (ballistic or diffraction) under investigation. To accurately model these patterns, different fitting functions were employed based on the characteristics of the signal.

Ballistic Regime: Periodic Gaussian fit

For the gratings used in the ballistic regime ($p = 250\,\mu\text{m}$), the intensity patterns typically show periodic modulation, resembling a series of Gaussian peaks that vary slightly in shape and amplitude depending on the grating's duty cycle. To capture these variations, the data were fitted with a model of multiple Gaussian functions at

fixed periodic intervals. This approach allows flexibility in accommodating different signal shapes while enabling the extraction of essential fitting parameters.

The model is mathematically represented as:

$$I(y) = A \cdot \sum_{i=-1}^{j+1} \exp\left(-\frac{(y - \mu - i \cdot p)^2}{2\sigma^2}\right) + B \tag{2.3}$$

where $I(y)$ is the intensity at position y along the scanning axis, A represents a common Gaussian amplitude, μ the center of the first peak, p the fixed period, σ the standard deviation, and B a constant offset for background intensity. The value j depends on each measurement, indicating the number of periods included. Two additional Gaussian peaks beyond the primary modulation range help account for periodic boundary effects, improving fit accuracy across the full intensity modulation range. The visibility of the oscillating intensity pattern is calculated either using the fitting parameters A and B or the maximum and minimum values of the fit, while the relative position of the pattern is determined via the parameter μ.

Diffraction Regime: Sum of Two Sine Waves

In the diffraction case, the interference patterns are more complex, requiring a more sophisticated model to fit the data. Here, the intensity pattern is best described by the sum of two sine waves, with the first one having a period corresponding to the grating period ($p_1 = 25\,\mu\text{m} = p$) and the second one half that period ($p_2 = p/2$). The fitting function for this case is given by:

$$I(y) = A_1 \sin\left(\frac{2\pi}{p} y - \varphi_1\right) + A_2 \sin\left(\frac{4\pi}{p} y - \varphi_2\right) + B \tag{2.4}$$

where A_1 and A_2 are the amplitudes, p is the period of the main sine waves and is a fixed parameter corresponding to the period of the grating, φ_1 and φ_2 are the phases, and B is a constant offset.

Robustness of Fitting Routine

To ensure consistency across varying grating designs and duty cycles, a bootstrap approach is applied to the fitting process [147]. This method becomes particularly interesting when comparing data from different grating configurations, especially

when the fit parameters alone do not allow for the direct extraction of the visibility. For example, in high-duty cycle configurations (e.g., 40%), Gaussian fits can represent the modulation pattern but may fail to capture the true signal offset. Bootstrap analysis generates varied data samples, refitting each to derive a range of maximum and minimum values. Averaging over these fits yields an overall visibility with error bars, supporting comparisons and enhancing interpretation in both ballistic and diffraction configurations.

2.3 Conclusion

This chapter introduced the QNeutron apparatus, detailing its components, signal analysis methods, and data acquisition strategies. Each part, from the absorption gratings to the chopper and detector, contributes to precise measurements, especially in detecting deflections from external samples or potentially electric fields. The setup's design, along with calibration procedures like transverse scanning and wavelength-specific analysis, establishes a solid framework for measurement optimization. The next chapters will explore the determination of these experimental parameters and present the full characterization of the apparatus, optimizing it for the experimental campaign during which the neutron electric charge has been measured (Chap. 5).

3. Technical Developments at the Paul Scherrer Institute

The development of the QNeutron apparatus involved extensive optimization and characterization efforts spanning across multiple beam times at the Paul Scherrer Institute (PSI) over nearly three years. This chapter details the journey from initial setup challenges to the determination of critical components characteristics and their implications for future measurements.

Starting from scratch, numerous aspects of the setup required refinement and investigation. Key areas and parameters included:

- Determining the optimal length and configuration of the experimental setup
- Developing precise alignment techniques for the neutron gratings to ensure interference conditions
- Establishing effective measurement techniques to capture and analyse neutron intensity patterns in both the ballistic and diffraction configuration
- Optimizing the components design such as the gratings for enhanced performances

Each aspect underwent iterative improvements and adjustments through numerous investigations and analyses. In the next pages, a summary of each beam time conducted at PSI is presented with the corresponding reached milestone. Each time, the focus has been put on a specific aspect of optimization. These beam times were conducted at the Beam line for neutron Optics and other Approaches (BOA) at PSI [148].

3.1 BOA beam line at PSI

The following description is taken from the PSI website [149]: ”BOA is an 18 m long instrument located at the beam channel 51 looking on the SINQ cold source. The primary polarization element (polarizing bender) of the former design was kept because research with polarized neutrons is of key interest in the neutron scattering community. The position of BOA close to the cold source is crucial for the performance of the instrument: the measured polarized flux is around 1×10^8 n cm^{-2} s^{-1} mA^{-1}. The

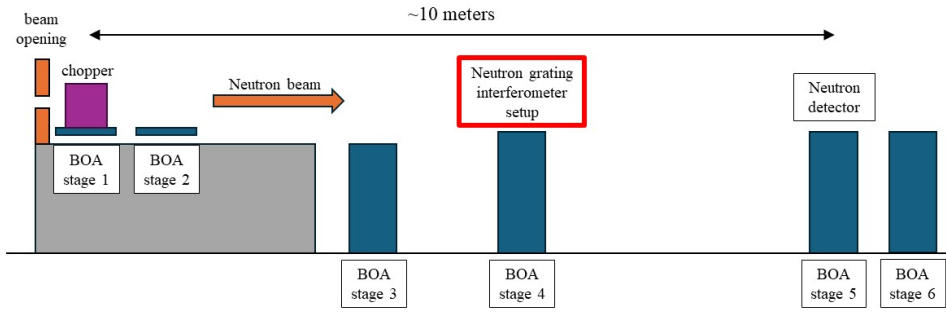

Figure 3.1. Implementation of the BOA beam line at PSI. The neutron beam is traveling from left to right with a measured polarized flux of around 1×10^8 n cm^{-2} s^{-1} mA^{-1}. For the QNeutron experiment, the grating interferometer is installed on stage 4, and the neutron detector on stage 5. Different opening sizes can be set at the beam opening, and BorAl apertures acting as defining apertures are installed before and after the interferometer setup. The optional chopper to record time-of-flight measurements can be installed on stage 1.

secondary instrument consists of a highly flexible geometry. It is equipped with three rotating axes with flexible translation tables and several aperture units. The maximum available free space is around 12 m, which allows new experiments presently not possible at SINQ, and an area-sensitive CCD camera system and optionally an ^{3}He neutron counter are available for data acquisition". A scheme of the beam line is presented in Fig. 3.1.

3.2 Detector Characterization and Normalization Process

At the beginning of each beam time, it is necessary to characterize the detector to determine optimal operating parameters, such as high-voltage (HV) and discriminator threshold, as described in Sec. 2.1.3. During initial phases of the project, an issue with the algorithm filter affected the detector settings, resulting in incorrect neutron count measurements. This issue was identified by examining high-voltage scan curves: a

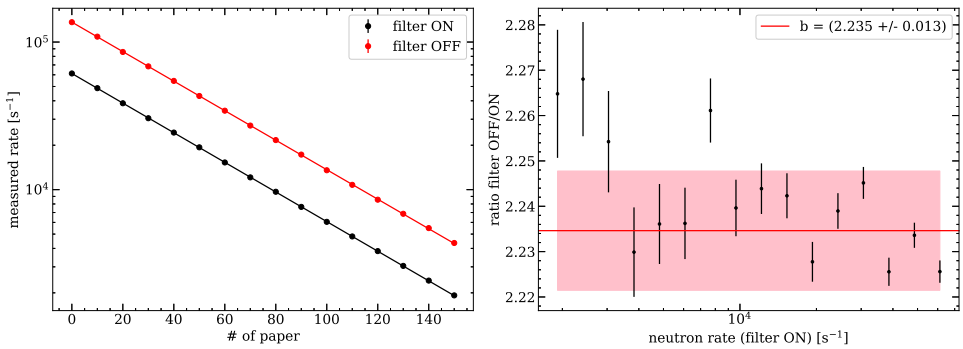

Figure 3.2. Left: Effect of the algorithm filter on the neutron rate as a function of the number of attenuating sheets of paper. Right: Scaling factor determined as a function of the neutron rate when the filter is enabled for an detector voltage $U_{det} = -2600\,\mathrm{V}$ and $U_{discriminator} = -26.67\,\mathrm{mV}$. A factor of 2.235(13) is considered for scaling down every further measurements taken with a wrong algorithm filter setting.

correct scan should show a plateau in neutron counts over a range of HV values, indicating the optimal operating range. The absence of this plateau signaled that the filter was not functioning correctly.

Once the filter algorithm issue was identified in June 2023, tests were conducted at BOA to assess its impact. By attenuating the neutron flux through varying numbers of paper sheets placed in front of the detector, measurements were taken with and without the event filter enabled. Results showed that neutron counts were consistently scaled by a factor of 2.235(13) across different neutron rate levels. This factor was subsequently used to correct all affected measurements, ensuring accurate normalization for further analysis and qualitative comparisons. Figure 3.2 illustrates the relationship between the scaling factor, detector settings, and neutron flux for a fixed detector voltage ($U_{det} = -2600\,\mathrm{V}$) and discriminator threshold ($U_{th} = -26.67\,\mathrm{mV}$), which are the standard settings used for all beam times after December 2021. This threshold voltage corresponds to a register value set to 108.

To address the filter algorithm issue and ensure consistent neutron count data, the following normalization and scaling procedure is applied to every measurements:

- Record one or several measurement runs (neutron counts over a defined time). For each measurement, the total number of events (incorrect neutron counts)

N_{event} is recorded, along with the normalization monitor detector values $N_{monitor}$.

- Divide the total number of events N_{event} by the previously determined scaling factor of 2.235(13) for each measurement run. This provides an estimate closer to the true count of neutrons, without applying normalization. The uncertainty on the scaling factor is neglected in this step to avoid confusion, as including it would add error bars that reflect conversion uncertainty rather than count uncertainty.
- Divide the resulting value by the corresponding $N_{monitor}$ to account for beam instabilities or fluctuations in proton beam power.
- Compute the average $\langle N_{monitor} \rangle$. The previously obtained values are then multiplied by this average to align the results with the typical intensity, yielding values close to the actual neutron counts.

This procedure generates values approximating the true neutron counts while accounting for beam intensity normalization. The deviation from the true count is proportional to the error on the scaling factor, estimated to be about 0.5%. However, since these measurements were taken during development beam times, the neutron intensities are reported in arbitrary units (arb. unit), as they do not directly represent absolute neutron counts. Consequently, it is not possible to assign error bars to the neutron counts directly, as the process does not involve a pure counting method due to the disabled filter algorithm. However, when fitting the data, errors on the fit parameters can be extracted, allowing for the calculation of visibility with associated uncertainties.

At the end of this chapter in Sec. 3.10, a table summarizes all measurements, listing the fitting parameters and corresponding visibility values for each setup. This provides a comprehensive overview of the results obtained and the impact of various configurations on the visibility.

3.2.1 Time-of-Flight Spectrum

To determine the neutron spectrum at the BOA beam line, a time-of-flight measurement has to be conducted before each beam time. The actual spectrum depends on experimental parameters such as the beam collimation, the detector position with respect to the chopper (for scattering in air) and parameters related to the detector

characteristics. A typical measurement of the time-of-flight spectrum at the BOA beam line is shown in Fig. 3.3.

For this measurement of approximately one hour taken during the beam time in November 2022, the chopper was installed on stage 2 and set to a neutron pulse repetition frequency of 20 Hz. With all the wafers installed in the collimation box (Sec. 2.1.2), the opening fraction of the rotating chopper is equal to 0.5%. The resulting spectrum was recorded with 2500 time bins of 20 µs each, over 75000 chopper sweeps. This allows the observation of wavelengths up to 3.5 nm with a time bin size of 0.0014 nm and a resolution of 0.036 nm given the chopper-to-detector distance of 5.63 m during this beam time. However, the plot only depicts wavelengths up to 2 nm for statistical reasons.

Due to the previously mentioned issue with the algorithm filter, the neutron intensity is reported in arbitrary units. While these units approximate the actual neutron counts, they have been adjusted using the scaling method outlined earlier to maintain consistency in data analysis. To achieve a broad measurable wavelength range by limiting background intensity, in this beam time, an extensive shield of iron, PVC, and BorAl materials was installed around the beam opening at the start of the beam line. Iron absorbs high-energy gamma rays and fast neutrons, PVC moderates fast neutrons through hydrogen scattering, and BorAl captures stray thermal and cold neutrons, collectively reducing background and enhancing the signal-to-noise level of the time-of-flight measurement.

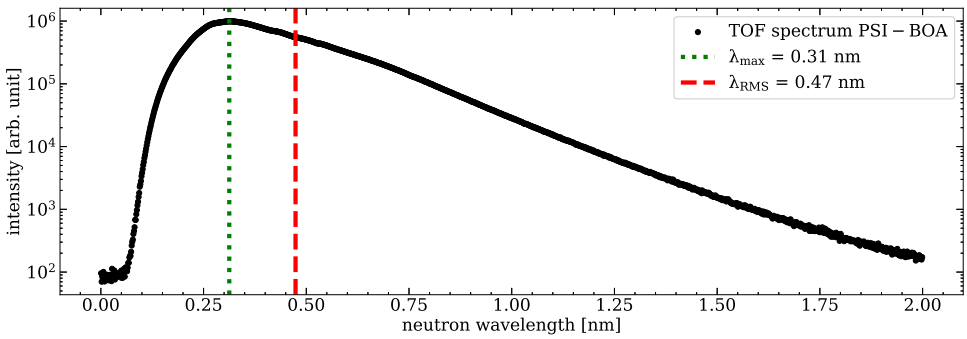

Figure 3.3. Accessible time-of-flight spectrum measured over 1 h at the BOA beam line considering the detector wavelength dependent efficiency. Only the 5×5 cm^2 collimating apertures A_0 and A_2 were installed (no grating) before and after the apparatus. The weighted mean wavelength, $\lambda_{RMS} = 0.47$ nm (red dashed line), is defined as the point where the sum $\sum I_i \lambda_i^2$ is balanced on both sides, i being the time bin indices. This value is relevant since the sensitivity to the neutron electric charge scales with λ^2. The wavelength with maximum statistics is $\lambda_{max} = 0.31$ nm (green dotted line).

3.3 Beam time in April 2021

During this beam time of seven days, the first iteration of a neutron grating interferometer setup was tested in a white beam configuration (without having the neutron chopper in operation). The gratings were installed on motorized stages and mounted on a one-meter-long Thorlabs rail on an optical breadboard with threaded holes. The beam had a defined cross section of 5×5 cm^2 and the sapphire filter of the beam line was used to reduce residual fast neutrons. At both ends of the setup, 5×5 cm^2 BorAl apertures were placed to further ensure a good definition of the beam. The gratings have an inner active area of 6×6 cm^2. The corresponding setup is shown in Fig. 3.4.

During this campaign, only one grating design was tested with period $p = 250$ µm, duty cycle $R = 10\%$, and gadolinium thickness $t_{Gd} = 20$ µm. The separation distance was $L_G = 0.42$ m, ensuring the operation in a purely ballistic regime. Therefore, this measurement can be conducted without a chopper, and the only retrievable information is the integrated neutron count over the entire spectrum at the end of each individual run. After the alignment of the gratings, a first oscillating intensity pattern was recorded over five grating periods and is shown in Fig. 3.5.

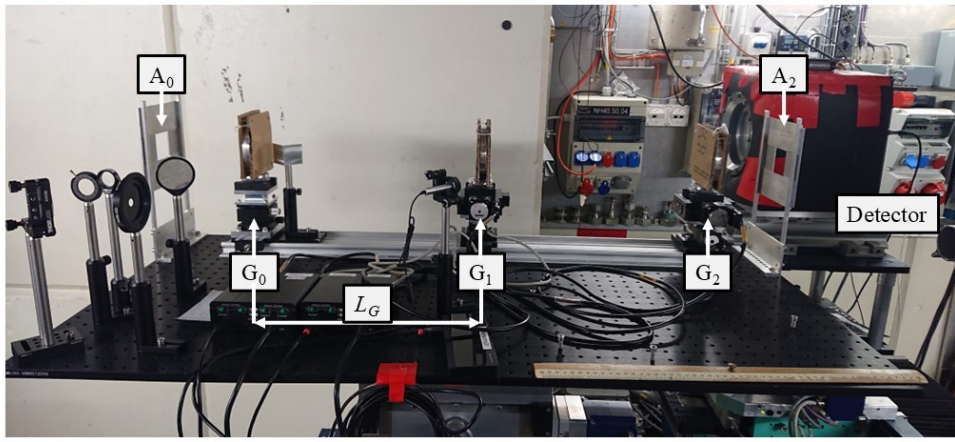

Figure 3.4. Interferometer setup during the first neutron beam time on stage 4 of the BOA beam line at PSI in April 2021. The neutron beam is traveling from left to right, passing through the first defining BorAl aperture of 5×5 cm^2, the gratings, and the second defining aperture. The distance between the grating is L_G = 0.42 m. Some optical components are mounted on the table to facilitate gratings alignment.

Throughout this beam time, methods were established to align the gratings and record the characteristic oscillating intensity pattern. Additionally, it marked the first successful integration of the DAQ system described in Sec. 2.1.5 with the neutron grating setup, facilitating the automatization of subsequent measurements.

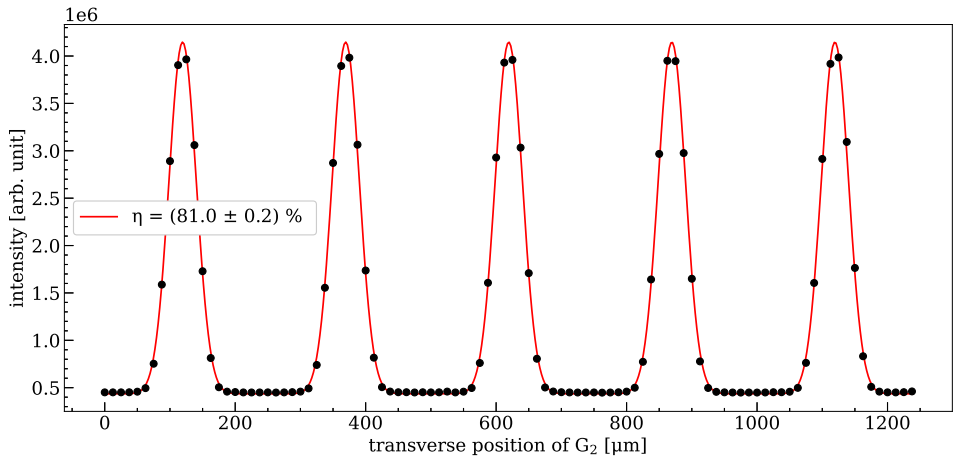

Figure 3.5. First oscillating intensity pattern recorded over five grating periods $p = 250\,\mu\text{m}$, $R = 10\%$, and $t_{Gd} = 20\,\mu\text{m}$ in April 2021. Each data point was taken during a measurement time of $\Delta t \approx 20\,\text{s}$, corresponding to 400 k counts with the normalization detector. The reached visibility with the white beam corresponds to $\eta = (81.0 \pm 0.2)\%$. The solid red lines indicate a periodical Gaussian fit described in the previous section.

3.4 Beam time in August 2021

For the second beam time of eight days, the setup was extended in length using two additional Thorlabs optical breadboards linked together with extruded aluminum profiles. The gratings were mounted on a 2-meters X95 profiled rail, and the distance between them was now $L_G = 95\,\text{cm}$. The whole setup shown in Fig. 3.6 was installed on BOA stage 4 on vibration-damping rubber feet. This stage allows fine longitudinal (y-axis) and angular (θ, φ, ψ) positioning of the apparatus with regard to the neutron beam. The beam cross section was once again set to be $5 \times 5\,\text{cm}^2$ at the very beginning of the beam line and the sapphire filter was used for fast neutron removal.

Two additional sets of gratings were manufactured for this beam time. The first one for a ballistic setup with periods of $p = 250\,\mu\text{m}$ but a new duty cycle of $R = 20\%$, and the second intended for a diffraction regime setup with grating periods of $p = 25\,\mu\text{m}$ and duty cycle $R = 20\%$. For both new sets, the thickness of the gadolinium layer remains unchanged at $t_{Gd} = 20\,\mu\text{m}$. The diffraction setup was still operating using the white

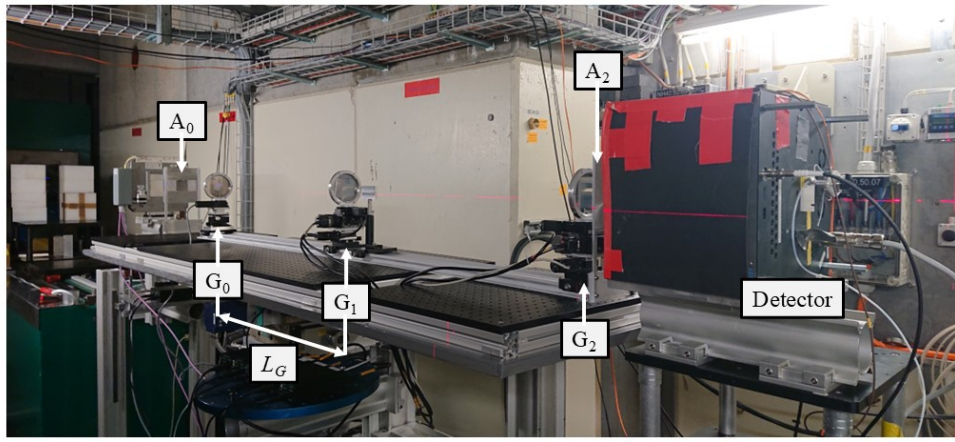

Figure 3.6. Interferometer setup as in August 2021 at the BOA beam line of PSI. The beam opening is defined as the origin for every other distances. The aperture A_0 is at $x = 3.1$ m, the detector sits at $x = 5.51$ m and the grating distance is $L_G = 0.95$ m.

beam, and therefore, the distances between the gratings were not adjusted to be the Talbot length with the RMS wavelength at BOA ($L_T = 1.33\,\text{m} > L_G$). The intensity modulation presented in Fig. 3.7 is consequently of low quality compared to setups in a ballistic configuration. However, the smaller size of the gratings—reduced by a factor of ten—makes their relative precise alignment proportionally more challenging. This beam time served as a demonstration of alignment techniques for these two specific configurations.

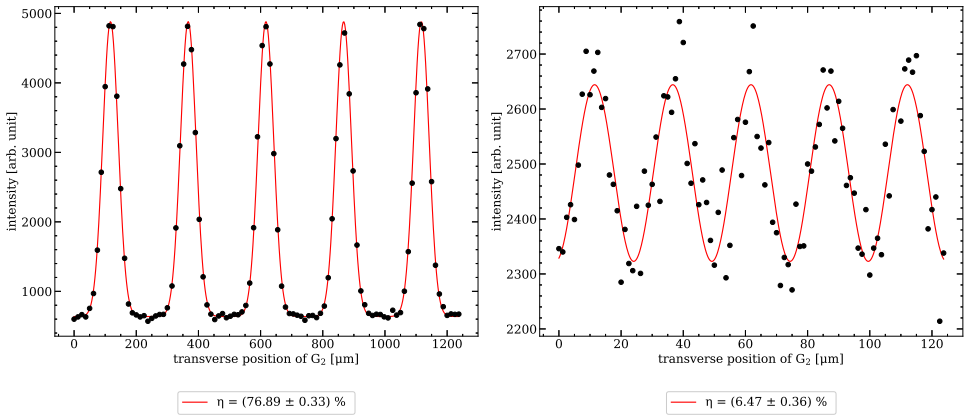

Figure 3.7. Left: Oscillating intensity pattern recorded over five grating periods with p = 250 µm and R = 20%. The distance between the gratings was L_G = 0.95 m, and each data point was taken during an exposure time of approximately 5 s (100 k monitor counts). The visibility of the modulation is η =(76.89 ± 0.33)%. Right: Similar measurement performed with the first diffraction setup using the white beam. The grating period is p = 25 µm and the duty cycle R = 20%. The distance is still L_G = 0.95 m, and each data point was recorded for 10 s (200 k monitor counts). The visibility of the modulation is η =(6.47 ± 0.36)%

3.5 Beam time in December 2021

During the third beam time of ten days, comparison measurements were made to optimize the performance of the apparatus in terms of relative grating alignment and visibility of the intensity modulation. The setup was once again extended with aluminum profiles to have distances between the gratings of L_G = 1.96 m. An additional supporting structure had to be implemented with wire ropes attached to the ends of the apparatus, preventing any bending or torsion of the instrument. Figure 3.8 illustrates the experiment at the BOA beam line during this measurement campaign.

The question about the optimal duty cycle was still open and needed to be addressed. Similarly to the previous beam time, new gratings were ordered (manufacturing according to Sec. 2.1.4) with a duty cycle this time of R = 40%, allowing an extensive comparison between three designs (10%, 20%, and 40%). Moreover, the alignment of the diffraction setup caused difficulties during the previous beam time. To understand these complications, another new set of gratings was ordered with the purpose of

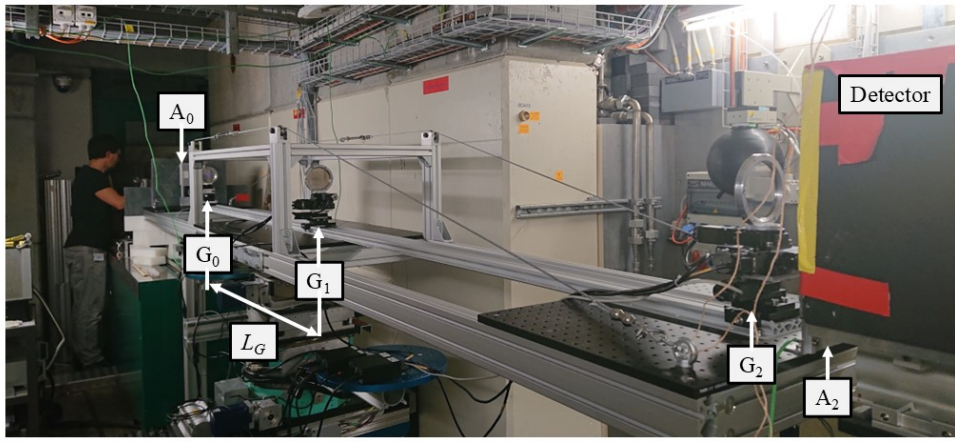

Figure 3.8. QNeutron setup installed at BOA beam line on stage 4 in December 2021. The distance between the gratings is $L_G = 1.96\,\text{m}$. The aperture A_0 is at $x = 1.59\,\text{m}$ from the beam opening and the detector is at $x = 6.11\,\text{m}$.

making the setup intermediate between the ballistic and diffraction regimes. With $p = 100\,\mu\text{m}$ and $R = 10\%$, this intermediate configuration correspond to a Talbot length $L_T = 21.3\,\text{m}$ and offers a valuable step for refining alignment techniques. It is easier to align than the diffraction mode gratings but more challenging than the ballistic ones, providing an ideal training stage for progressively improving alignment precision. The oscillating intensity pattern recorded for the ballistic setup with three duty cycles, as well as the one from the new intermediate setup, are presented in Fig. 3.11. A table summarizing these results can be found at the end of this chapter (Sec. 3.10).

To further investigate the effects of neutron wavelengths on the visibility, measurements with and without a beryllium filter (Be-filter) were conducted. The role of the filter is to remove neutrons below 0.4 nm, as shown in the time-of-flight spectrum in Fig. 3.10. Subsequently, oscillating intensity patterns were recorded for three duty cycles: 10%, 20%, and 40%. It has been found that the visibility is higher with the Be-filter because it removes the low-wavelength neutrons that still pass through the gadolinium to some extent. The filter thereby reduces background and the visibility is increased. However, since the neutron spectrum is most intense below 0.4 nm, removing this part of the spectrum is not ideal due to loss in statistics. This suggests that using a thicker gadolinium layer, *i.e.*, a thicker absorber on the grating, might be

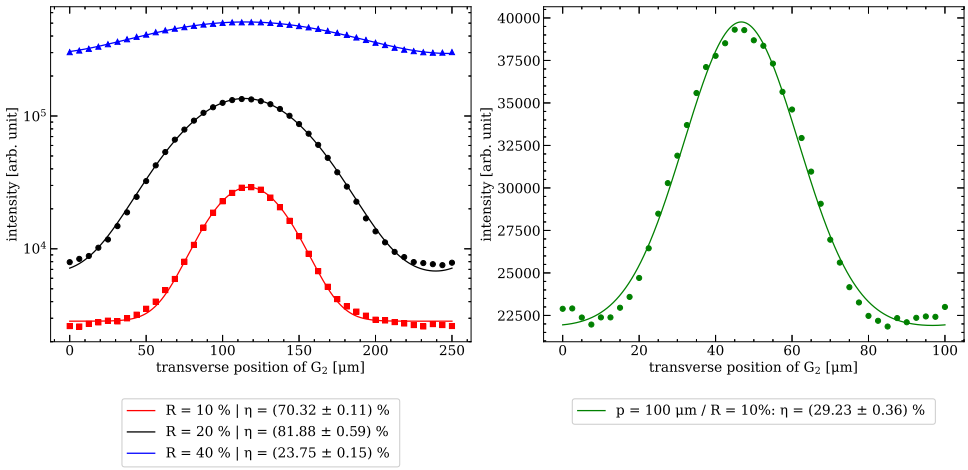

Figure 3.9. Left: Oscillating intensity pattern recorded with a white beam over one grating period of $p = 250\,\mu\text{m}$ and duty cycles $R = 10\%$, 20%, and 40%. The distance between the gratings was $L_G = 1.96\,\text{m}$, and each data point was taken during a time of approximately 10 s (200 k monitor counts). Right: Similar measurement performed with the new intermediate setup and the white beam over approximately 10 s per data point (200 k monitor counts). The grating periods were $p = 100\,\mu\text{m}$, the duty cycle $R = 10\%$ and the grating distance was still $L_G = 1.96\,\text{m}$. The visibility of the modulation is $\eta = (29.23 \pm 0.35)\%$. Due to the emergence of diffraction effects, the modulation is effectively wider than a 10% duty cycle in a purely ballistic regime.

necessary in order to address this issue. This potential improvement is explored in the next section.

In conclusion, the objective is to obtain high visibility and high statistics to decrease the sensitivity in a future neutron electric charge measurement, which is proportional to $1/(\eta \times \sqrt{N_W})$ as seen in Eq. (4.1) in Sec. 4.4 (N_W refers to the counted neutrons at the working point of the apparatus). From the measurements presented above, it is determined that the best compromise is achieved with a duty cycle of 20%. This configuration provides a good balance between visibility and neutron count. However, since these measurements were made using the white beam, it is still necessary to perform time-of-flight measurements with these setups to confirm the results under optimized conditions.

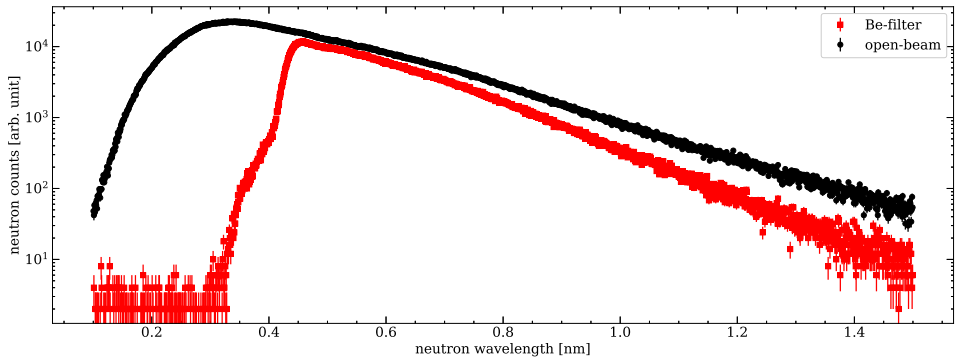

Figure 3.10. Time-of-flight spectrum showing the effect of the Be-filter removing neutrons below 0.4 nm.

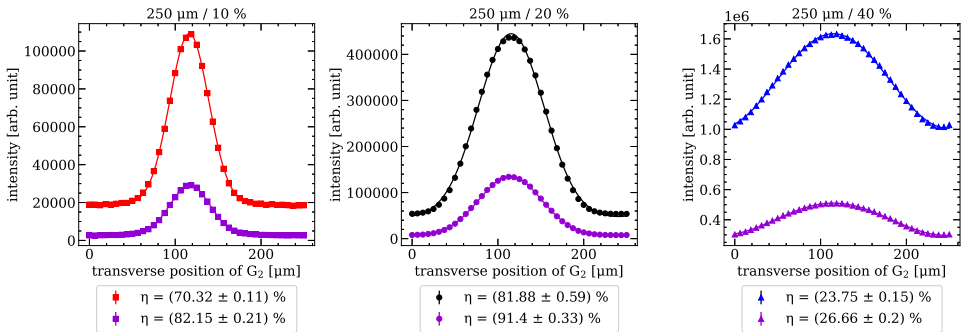

Figure 3.11. Comparison of the oscillating intensity pattern produced with (purple curves) and without (red, black, and blue curves) the Be-filter for $R = 10\%$ (left), $R = 20\%$ (center), and $R = 40\%$ (right). The Be-filter yields better visibilities but also significantly decreases statistics. Increasing the thickness of the Gd layer on the gratings would enhance their ability to replicate the beneficial effect.

3.6 Beam time in May 2022

In May 2022, a beam time of nine days followed, during which measurements were once again conducted without a time-of-flight setup, but by utilizing the white beam. The objective was to understand the effect of air on the oscillating intensity pattern in both configurations: ballistic and diffraction. In the first regime, the gratings period

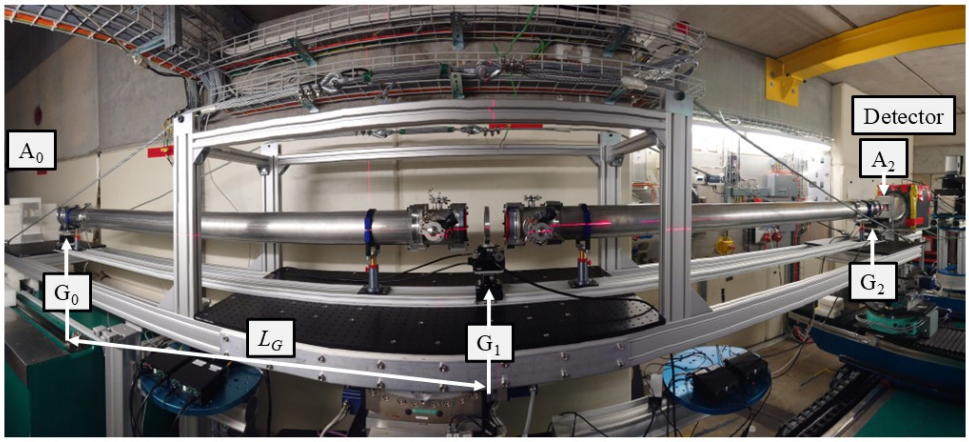

Figure 3.12. QNeutron as of May 2022 with vacuum pipes between the gratings and a distance $L_G = 1.95\,\text{m}$. The aperture A_0 is mounted at $x = 1.52\,\text{m}$ and the detector is at $x = 6.08\,\text{m}$.

was $p = 250\,\mu\text{m}$, while for the diffraction regime, the period was $p = 25\,\mu\text{m}$. Both setups had a duty cycle of $R = 20\%$, as it was determined to be optimum in previous experiments (Sec. 3.5). The distances between the gratings were similar to those in December 2021 ($L_G = 1.95\,\text{m}$). An image of the setup in May 2022 with vacuum pipes installed between the gratings is shown in Fig. 3.12.

Initially, some reference oscillating intensity patterns were recorded with only the gratings installed on the setup. Subsequently, 1.8 m-long vacuum pipes with 2 mm-thick sapphire windows were mounted between G_0 and G_1 as well as between G_1 and G_2, pumped down to a pressure of 1×10^{-2} mbar, and the measurements repeated for comparisons. While the statistics improved due to reduced neutron absorption and scattering (roughly 10%/meter in air), the visibility and modulation width remained essentially unchanged (Summary in Sec. 3.10). This result is illustrated in Fig. 3.13.

This measurement allows understanding of the effects of air and vacuum, which is crucial for future electric charge experiments as applying an electric field is more efficient and straightforward in a vacuum. Overall, a reduction by about 25% in statistics is observed, when the neutrons are traveling in air in both the ballistic and diffraction regimes.

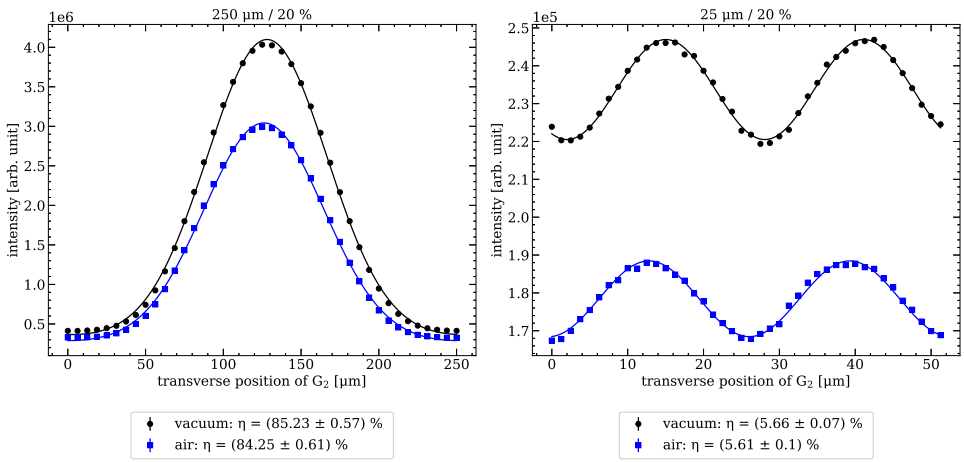

Figure 3.13. Comparison of the oscillating intensity pattern for the ballistic setup (left) with $p = 250\,\mu m$ and the diffraction setup (right) with $p = 25\,\mu m$, measured in vacuum (black) and in air (blue). The measurements indicate that, in the ballistic mode, the intensity is reduced to 74% of its original value in vacuum when measured in air. Similarly, in the diffraction mode, the intensity is reduced to 75%. Despite this reduction in intensity, the visibility remains unchanged in both setups. In both cases, the gratings have a duty cycle of $R = 20\%$.

During the same beam time, other tests were conducted with a double crystal monochromator (DCM). The hypothesis was that aligning the diffraction setup might be easier if a specific wavelength could be selected with the DCM. Time-of-flight measurements were first recorded without the gratings and the DCM to determine the intrinsic spectrum of the beam line. The DCM was then inserted, set to $\lambda = 0.36\,nm$, and the measurements were repeated.

As shown in Fig. 3.14, using the DCM resulted in a significant loss of beam intensity by only allowing neutrons with the set wavelength of 0.37 nm and higher orders through the apparatus. The statistics were affected and reduced by a factor of approximately 50, making it less practical compared to using a pulsed beam. A chopper offers the advantage of accessing a broader range of wavelengths, while the statistical trade-off is comparable.

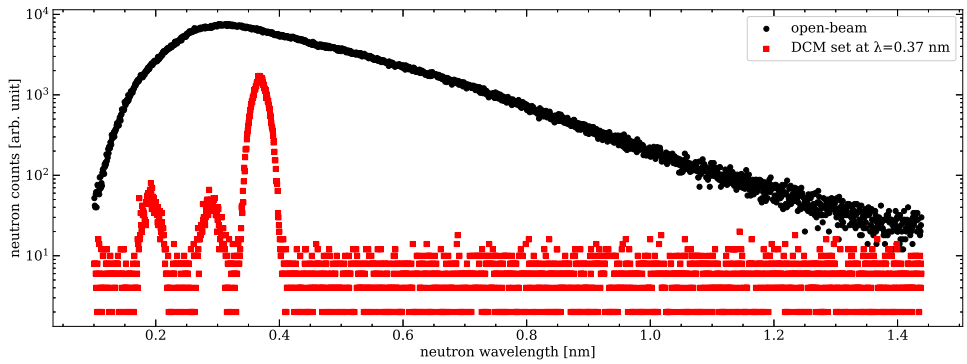

Figure 3.14. Time-of-flight spectrum with and without the DCM set to $\lambda = 0.37$ nm. The use of the DCM resulted in significant loss of beam intensity.

For future diffraction setup measurements, a chopper will be used for measuring in time-of-flight mode to optimize the balance between wavelength selection and neutron statistics. The reason it was not done during this beam time is a lack of measurement time during the campaign. The question of whether it is feasible to characterize the diffraction setup in time-of-flight mode was addressed and answered during the next beam time.

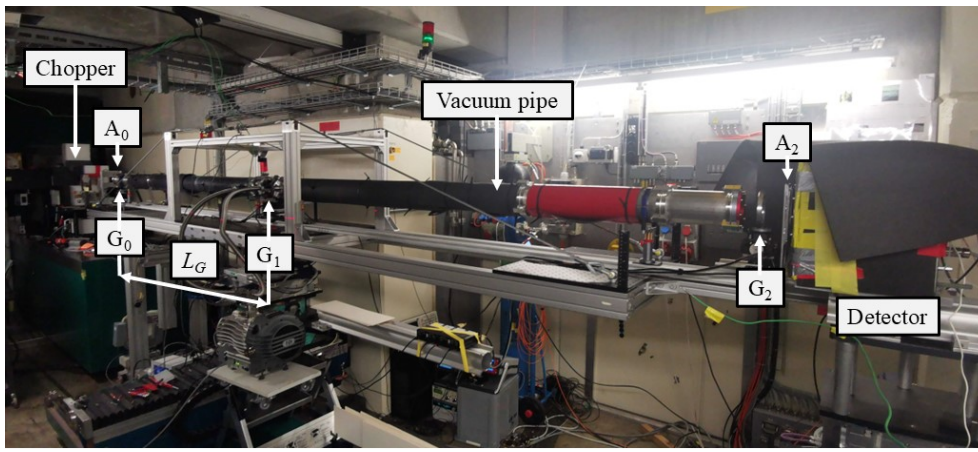

Figure 3.15. QNeutron apparatus installed on BOA stage 4 in August 2022. The distance between the gratings is $L_G = 2.45\,\text{m}$. The chopper is mounted at $x = 0.47\,\text{m}$ from the beam opening, the aperture A_0 is at $x = 0.9\,\text{m}$ and the detector at $x = 6.05\,\text{m}$. Therefore, the chopper-to-detector distance is 5.58 m.

3.7 Beam time in August 2022

During the August 2022 beam time spanning seven days, the setup was extended to increase the distance between the gratings to $L_G = 2.45\,\text{m}$. The primary goals were to investigate the optimal thickness of the absorption layer on the gratings (gadolinium layer, see Sec. 2.1.4) using a ballistic setup with $p = 250\,\mu\text{m}$ and $R = 20\%$, and to implement, for the first time, the time-of-flight technique for the diffraction setup where $p = 25\,\mu\text{m}$ and $R = 20\%$. Figure 3.15 illustrates the apparatus mounted on stage 4 with the chopper installed at the beginning of the beam line, on stage 1.

To support these goals, new gratings with an increased gadolinium layer thickness of $t_{Gd} = 30\,\mu\text{m}$ (compared to the previous $t_{Gd} = 20\,\mu\text{m}$) were introduced in both configurations. Time-of-flight measurements have been performed and the oscillating intensity patterns for both configurations and both thicknesses have been recorded. For the ballistic setup, the visibility of the white beam improves noticeably with the 30 µm gadolinium layer thickness (left plot in Fig. 3.16). This improvement is due to the increased absorption of shorter-wavelength neutrons, which are responsible for background counts. However, an unexpected effect was noted: the visibility dropped drastically above 0.5 nm with the 30 µm thickness (right plot Fig. 3.16). This

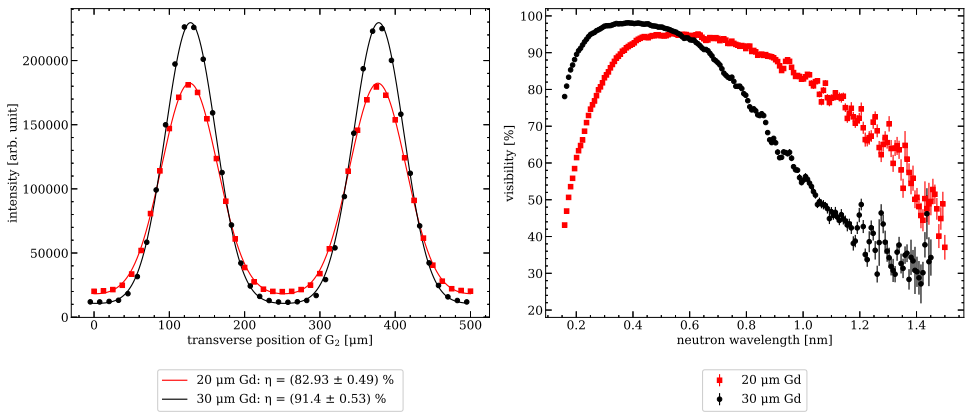

Figure 3.16. Left: Oscillating intensity pattern, recorded with the chopper but integrated over all wavelengths, for the ballistic setup ($p = 250\,\mu m$) with gadolinium thicknesses of 20 µm and 30 µm. Right: Visibility as a function of wavelength for both thicknesses, showing an improvement at shorter wavelength due to better absorption but also a significant drop above 0.5 nm for the 30 µm thickness. This drop is related to a poor manufacturing of the gratings which were reordered for the next chapter.

behavior is linked with the manufacturing process of the grating and this feature has been addressed in Chap. 4.

Similarly, the use of a chopper in the diffraction setup enabled access to the visibility of the oscillating intensity pattern across all wavelengths. By plotting these patterns, peaks of visibility appear at specific wavelengths, consistent with theoretical predictions. With $L_G = 2.45\,m$ and $p = 25\,\mu m$, the first-order working wavelength is calculated as $\lambda_T = p^2/L_G = 0.255\,nm$, with higher-order peaks appearing at multiples of this wavelength.

For this analysis, the bootstrap method described in Sec. 2.2.2 was applied. The fitting function, as described in Eq. (2.4), was a sum of two sinusoidal functions with fixed periods $p_1 = 25\,\mu m$ and $p_2 = p_1/2$, allowing for a more precise analysis of intensity modulations by accounting for higher diffraction orders.

Despite these promising results, measurement time remains a challenge due to a loss in statistics with the chopper by an approximate factor 200 compared to a white beam

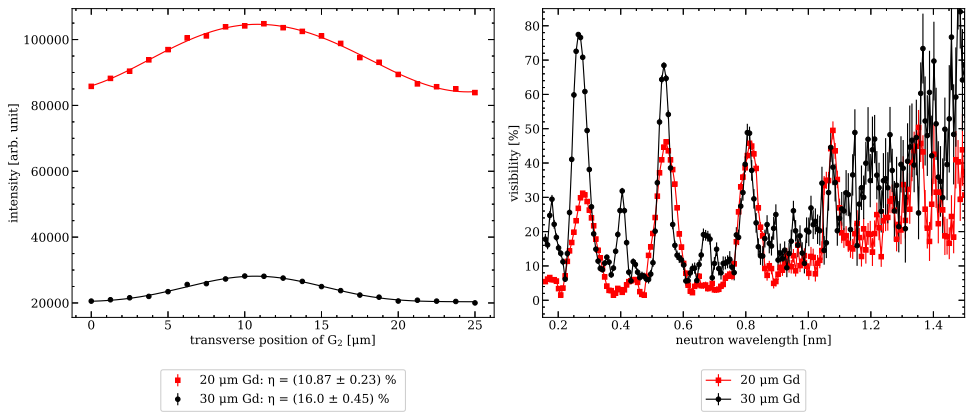

Figure 3.17. Left: Oscillating intensity pattern, recorded with the chopper but integrated over all wavelengths, for the diffraction setup ($p = 25\,\mu m$) with gadolinium thicknesses of 20 µm and 30 µm. This plot shows reduced intensity with increased thickness due to narrower effective slit width and manufacturing imperfections. Nevertheless, the increased visibility indicates the need to investigate this parameter further. Right: Visibility as a function of wavelength for both thicknesses, showing multiple-order interference up to the third order. Secondary peaks at half-order appear only with the 30 µm layer due to better absorption of shorter wavelengths.

without chopper. However, this technique enables the observation of higher-order interference patterns, suggesting the potential for greater distances between gratings if the experimental space at the beam line permits it. Similar to the ballistic regime, the performance of the 30 µm gadolinium layer did not fully meet expectations. While the thicker gadolinium layer ($t_{Gd} = 30\,\mu m$) improved visibility in the white beam by reducing background, visibility declined rapidly for higher-order peaks (by approximately 15% per diffraction order) due to limitations likely related to the manufacturing process of the thicker gratings. Further investigation into this aspect will be necessary to fully understand the impact of these thicker gratings, with characterization data from the Institut Laue-Langevin to be analyzed in the next chapter.

3.8 Beam time in November 2022

In November 2022, a nine days long beam time allowed further measurements in time-of-flight mode to compare the performance of different duty cycles using the FOM approach introduced in Sec. 3.5 (FOM= $1/(\eta \times \sqrt{N_W})$. The experimental setup repeated that of the August 2022 beam time (see Fig. 3.15), with gratings in ballistic mode ($p = 250\,\mu m$) and three duty cycles examined: 10%, 20%, and 40%. For these measurements, the gadolinium layer thickness was fixed at $t_{Gd} = 20\,\mu m$. The oscillating intensity pattern for each duty cycle was recorded and is presented in Fig. 3.18. The left side shows the intensity modulations recorded with the white beam for the three duty cycles, with the corresponding visibility values. On the right, visibilities are plotted as a function of neutron wavelength in time-of-flight mode, demonstrating that the visibility is consistently highest for the 20% duty cycle.

The visibility values for each duty cycle when using the white beam (measurements performed with chopper but integrated over all wavelengths) are:

- $R = 10\%$: $\eta = 77.99(50)\%$
- $R = 20\%$: $\eta = 81.61(39)\%$
- $R = 40\%$: $\eta = 22.98(23)\%$

These results validate earlier conclusion that a 20% duty cycle offers the best balance between visibility and neutron statistics, aligning well with the FOM for optimizing the sensitivity of the apparatus.

Fig. 3.19 further illustrates these findings. On the left, neutron statistics at the peak of the modulation are plotted against the grating duty cycle, while on the right, the FOM is shown as a function of duty cycle. As anticipated, the 20% duty cycle maximizes the FOM within the current experimental constraints, confirming it as the optimum choice to achieve the highest sensitivity for detecting neutron electric charge. It is possible that a duty cycle of 25% or 30% could yield even better results by improving statistics, but this remains to be tested in future experiments.

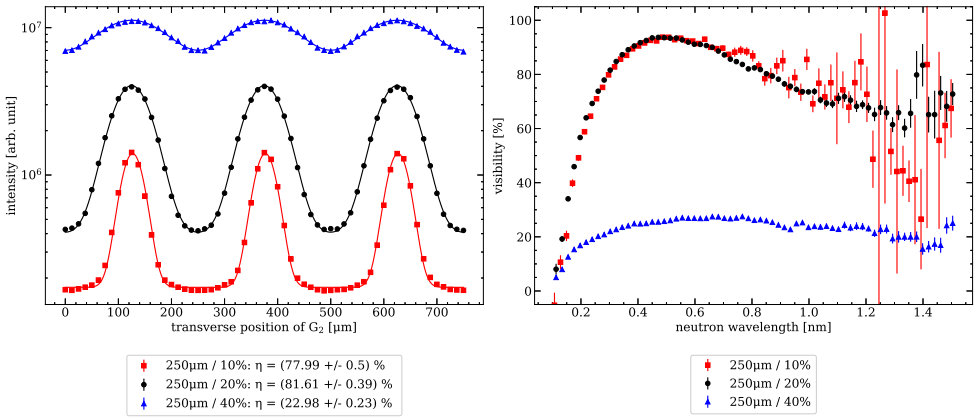

Figure 3.18. Left: Oscillating intensity patterns recorded over three grating periods of p = 250 µm for duty cycles R = 10%, 20%, and 40% with the chopper installed (intensity integrated over all wavelengths). Each data point was recorded over 20 s. Right: Visibility as a function of neutron wavelength for the three duty cycles, measured in time-of-flight mode.

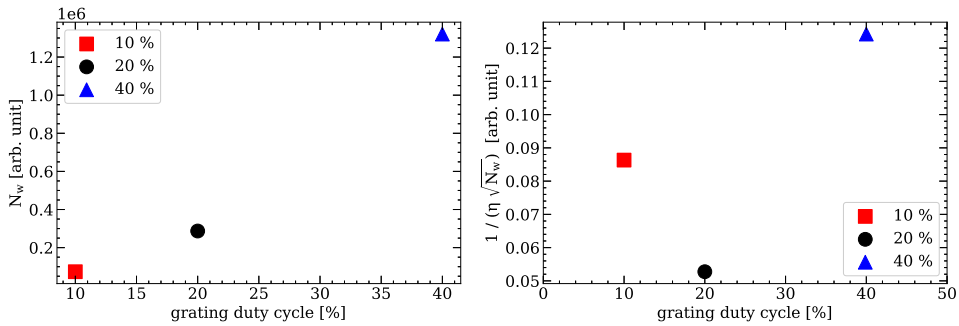

Figure 3.19. Left: Neutron statistics as a function of grating duty cycle. Right: Figure of merit (FOM) as a function of grating duty cycle. The 20% duty cycle optimizes the FOM, reinforcing it as the optimum configuration for future measurements.

3.9 Beam time in June 2023

In June 2023, during eight days the focus was laid on final preparations for a future neutron electric charge measurement, implementing the best configurations identified in previous beam times. The goal was to optimize the setup for an experiment at the Institut Laue-Langevin, which hosts the world's most intense cold neutron source (Sec. 4.2).

It was previously determined that a 20% duty cycle for the gratings was optimum. Additionally, using a 30 µm Gd-layer on the gratings reduced background and improved visibility for the white beam and at short wavelengths, though higher wavelengths did not see the expected improvement. The effect of vacuum on neutron absorption has also been understood. Given the continuous nature of the neutron source at ILL, it can be shown using Eq. (2.1) that utilizing the full statistics of a white beam in a ballistic configuration is advantageous. This choice is due to the fact that continuous sources benefit from the higher statistics available in a white beam setup. The ballistic configuration was preferred for its overall higher statistics, as it utilizes the full spectrum and fits within the limited space at the beam line. If space were not a constraint, the diffraction setup at higher orders could improve sensitivity, though it would reduce neutron flux due to the chopper. Nevertheless, the plan for the charge measurement at ILL is to use the ballistic setup with a white beam, therefore requiring a new design (no mounting stages or tables are available at ILL, the setup must be built up from the floor). A single extruded 6 m long aluminum profile with an 80×160 mm^2 cross section, mounted on rubber feet for stability, was chosen. This one-piece design, unlike previous multi-part setups, is expected to provide better stability against temperature fluctuations due to its solid structure. Additionally, the profile is temperature-stabilized with circulating distilled water regulated at 25 °C. The stability of the setup in this configuration is investigated in Sec. 4.1.4. Figure 3.20 shows the new setup design installed at the BOA beam line for this final characterization beam time.

During this beam time, an alternative setup inspired by Monte-Carlo simulations was explored in the ballistic regime with the hypothesis that an asymmetric configuration could improve sensitivity. In this setup, the distance between the first and second gratings is now half the one between the second and third gratings, while the overall length remains unchanged. Consequently, the period of the first grating must also be halved. This configuration aimed to increase the length over which beam deflection can be measured, thereby enhancing sensitivity.

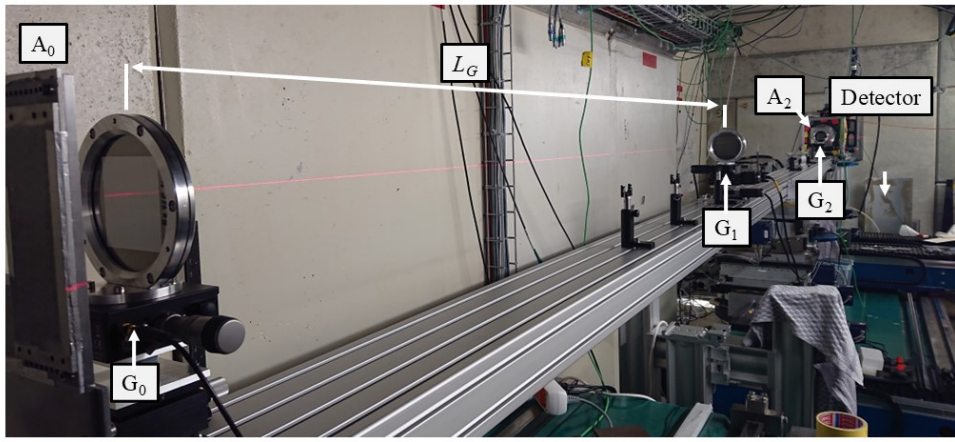

Figure 3.20. New setup installed at BOA beam line at PSI with $L_G = 2.95$ m grating distance and active temperature stabilization. The aperture A_0 is at $x = 1.05$ m from the beam opening and the detector is mounted at $x = 7.07$ m. For this beam time, no chopper was installed.

Measurements confirmed the simulations: the asymmetric setup demonstrated an improvement of the sensitivity to beam deflection by an approximate factor of two compared to the best symmetric setup tested, assuming the electric field extends along the entire distance between gratings. This increased sensitivity applies when beam deflection is measured only between G_1 and G_2. However, if an electric field can be applied additionally between the first and second gratings, a symmetric setup may still offer a better balance between statistics, visibility, and interaction length. Further details on this asymmetric setup, related simulations, and experimental results will be discussed in Sec. 4.4.6.

3.10 Results Summary

The following tables provide a comprehensive summary of the results discussed in this chapter. Depending on the setup configuration, two distinct fitting methods were employed, as described in Sec. 2.2.2.

For the ballistic regime (Table 3.1), the data were fitted using a multi-Gaussian function, which accurately models the intensity peaks resulting from the trajectories of neutrons in this regime.

For the diffraction regime (Table 3.2), a sum of two sine waves was used as the fitting function. This approach accounts for the additional modulation effects, with the second sine wave having half the period of the first, reflecting the diffraction pattern characteristic of this setup.

The uncertainties reported in both tables are not derived from statistical fluctuations but are instead obtained from the fitting routine applied to each dataset.

Table 3.1. Setup in ballistic regime fitted with Eq. (2.3)

Beam time	Grating (p, DC, t_{Gd})	$A \pm \Delta A$ [arb. unit]	$B \pm \Delta B$ [arb. unit]	$\sigma \pm \Delta\sigma$ [µm]	$\eta \pm \Delta\eta$ [%]
April 2021	250µm / 10% / 20µm	3711443 ± 13322	435529 ± 5381	20.9 ± 0.1	81.0 ± 0.2
August 2021	250µm / 20% / 20µm	4244 ± 24	638 ± 11	24.8 ± 0.2	76.83 ± 0.33
December 2021	250µm / 10% / 20µm	90101 ± 206	19017 ± 88	22.8 ± 0.1	70.32 ± 0.11
	250µm / 20% / 20µm	400455 ± 2255	44296 ± 176	38.2 ± 0.3	81.88 ± 0.59
	250µm / 40% / 20µm	627184 ± 3702	1007012 ± 2288	61.5 ± 0.2	23.75 ± 0.15
	250µm / 10% / 20µm (Be-filter)	26240 ± 91	2851 ± 39	23.2 ± 0.1	82.15 ± 0.21
	250µm / 20% / 20µm (Be-filter)	129379 ± 352	6083 ± 255	36.43 ± 0.14	91.4 ± 0.33
	250µm / 40% / 20µm (Be-filter)	214868 ± 1548	392598 ± 956	62.8 ± 0.2	26.66 ± 0.2
	100µm / 10% / 20µm	17990 ± 263	21773 ± 199	15.0 ± 0.3	29.23 ± 0.36
May 2022	250µm / 20% / 20µm (AIR)	2782734 ± 15018	260045 ± 11910	38.61 ± 0.3	84.25 ± 0.61
	250µm / 20% / 20µm (VAC)	3771781 ± 18703	326709 ± 14802	38.5 ± 0.3	85.23 ± 0.57
August 2022	250µm / 20% / 20µm (TOF)	165351 ± 778	17015 ± 587	37.4 ± 0.3	82.93 ± 0.49
	250µm / 20% / 30µm (TOF)	219235 ± 1093	10316 ± 699	33.5 ± 0.2	91.4 ± 0.53
November 2022	250µm / 10% / 20µm (TOF)	15329 ± 759	3005 ± 308	21.0 ± 0.4	78.0 ± 0.5
	250µm / 20% / 20µm (TOF)	61974 ± 227	7263 ± 269	36.8 ± 0.3	81.61 ± 0.39
	250µm / 40% / 20µm (TOF)	116208 ± 1512	193790 ± 550	59.0 ± 0.2	22.98 ± 0.23

Table 3.2. Setup in diffraction regime fitted with Eq. (2.4). The period is fixed to $p = 25$ µm.

Beam time	Grating (t_{Gd})	$A_1 \pm \Delta A_1$	$A_2 \pm \Delta A_2$	$\varphi_1 \pm \Delta\varphi_1$	$\varphi_2 \pm \Delta\varphi_2$	$B \pm \Delta B$	$\eta \pm \Delta\eta$ [%]
August 2021	20µm	128 ± 14	-15.2 ± 1.3	-0.25 ± 0.09	0.48 ± 0.09	2475 ± 10	6.47 ± 0.36
May 2022	20µm (AIR)	-10130 ± 187	-582 ± 19	1.80 ± 0.02	1.8 ± 0.3	178207 ± 130	5.6 ± 0.1
	20µm (VAC)	-13220 ± 308	-247 ± 31	1.32 ± 0.02	-0.5 ± 0.1	233342 ± 216	5.66 ± 0.07
August 2022	20µm (TOF)	-10258 ± 179	-309 ± 18	2.16 ± 0.02	2.4 ± 0.6	94658 ± 125	10.87 ± 0.23
	30µm (TOF)	3878 ± 102	-866 ± 27	-0.92 ± 0.04	-0.25 ± 0.5	23387 ± 36	16.0 ± 0.5

3.11 Conclusion

This chapter has documented and summarized the extensive development and optimization process of the QNeutron apparatus at the Paul Scherrer Institute, spanning nearly three years and involving multiple beam times. From initial challenges in aligning and configuring the setup to fine-tuning detector parameters and exploring various grating designs, each beam time provided valuable insights that gradually improved the setup's performance.

Key findings include the identification of the optimal grating duty cycle of 20%, the benefits of using thicker gadolinium layers ($t_{Gd} = 30\,\mu m$) for reducing background, and the effectiveness of the time-of-flight method for analyzing diffraction setups and characterize the visibilities as a function of the neutron wavelength. These developments culminated in the final design and testing of an extended, actively temperature-stabilized setup, ready for high-precision neutron charge measurements at the Institut Laue-Langevin.

The extensive optimization efforts have not only refined the current setup but also introduced innovative configurations, such as the asymmetric grating arrangement, which indicated possibilities for enhanced sensitivity. With these advancements, the apparatus is now fully prepared for the next phase of experimental campaigns, with the aim of achieving a highly sensitive neutron electric charge measurement.

4. Detailed Characterization of the Apparatus at the Institut Laue-Langevin

The Physique Fondamentale 1B (PF1B) beam line at the Institut Laue-Langevin (ILL) in Grenoble, France, is renowned as the most intense cold neutron facility in the world [150]. Situated in the heart of the French Alps, the ILL has been a pivotal location for neutron research since its creation. The institute hosts a variety of beam lines, each designed to explore different aspects of neutron science. Among them, the PF1B beam line is recognized to produce a high-flux cold neutron beam ideal for precision measurements and fundamental physics research.

Over the years, the PF1B beam line has been instrumental in several groundbreaking experiments. For example, it was used to conduct high-precision measurements related to the neutron lifetime [151], played a significant role in recent studies on the electric dipole moment of the neutron [71, 152, 153] and hosts experiment such as PERKEO designed to study neutron decay and perform precision experiments of the weak interaction [154–157]. These experiments have not only advanced scientific knowledge but also paved the way for the development of new technologies and methodologies in neutron research.

A sketch of the instrument is presented in Fig. 4.1. The PF1B casemate behind the beam exit, made with a reinforced concrete structure to provide protection against neutron and gamma radiation, is designed to house equipment such as neutron choppers or wavelength selectors. The neutron chopper will be mounted inside it during the entirety of the measurements presented in this chapter and therefore, is not shown on the images of the instrument installed at the beam line.

Given its exceptional capabilities in term of cold neutron beam intensity, the PF1B beam line was chosen as the site for the neutron electric charge measurement presented in Chap. 5. The following sections will describe the installation of the experimental apparatus at the PF1B beam line and the subsequent characterization steps.

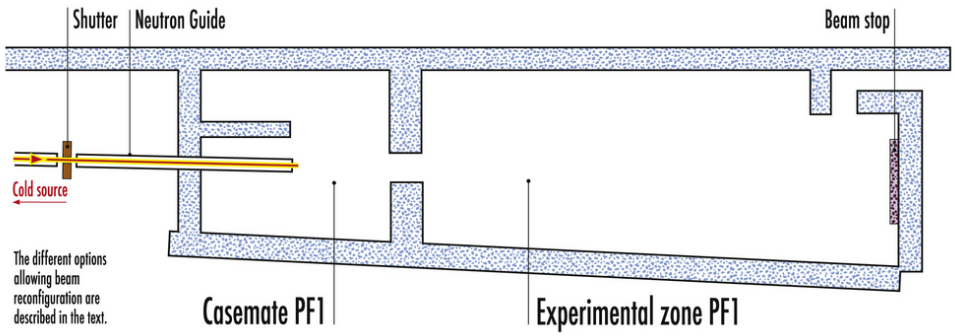

Figure 4.1. Plan of the PF1B beam line at ILL showing the empty casemate and the beam line setup. The neutron chopper, located inside the casemate, provides neutron pulses towards the experimental area. This image is taken from the ILL webpage where the characteristics of the beam line are listed.

4.1 QNeutron at PF1B at the Institut Laue-Langevin

4.1.1 Main structure

After arriving at the PF1B beam line at ILL, the QNeutron apparatus is mounted and aligned with the neutron beam in the experimental area. The apparatus consists of a structure made from extruded aluminum profiles, designed to be positioned accurately at the beam line. A CAD representation of the apparatus installed at the PF1B beam line is shown in Fig. 4.2.

The support structure includes a 400 (length) × 80 (width) × 102 (height) cm^3 frame mounted on ten wheels with adjustable height. Once positioned correctly, the wheels are replaced by fixed rubber feet to dampen vibrations.[1] A single 6-meter-long hollow aluminum profile[2] with a cross-section of 160 × 80 mm^2 is then mounted on top of this base structure using rubber feet with adjustable height, providing fine positioning and best possible alignment with the neutron beam. This setup allows for a distance between the gratings of $L_G = 2.75$ m.

Initial alignment of the setup with the neutron beam was achieved using a theodolite laser and a laser oriented along the neutron beam path. This alignment was further

[1] Jacking Castor D62 120 × 120 0.0.667.44 from Item
[2] Profile 8 160x80 light, natural 0.0.453.32 from Item

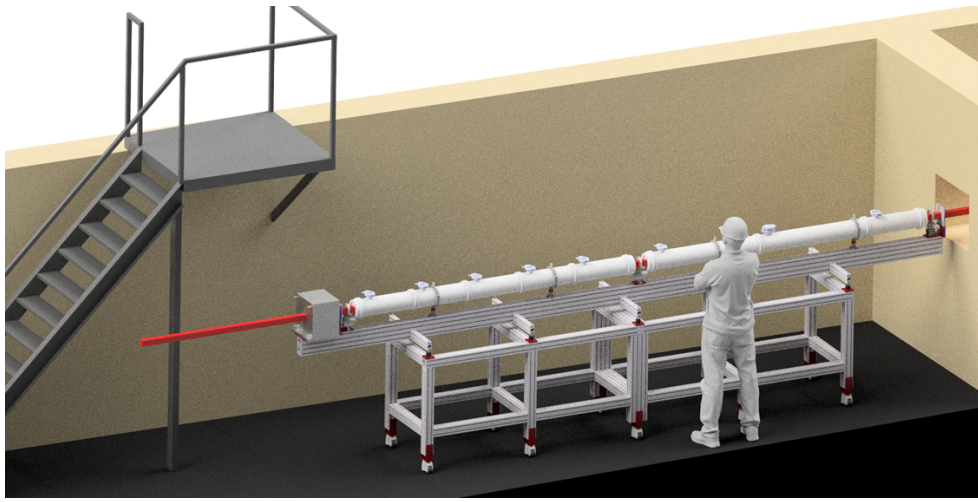

Figure 4.2. CAD representation of the QNeutron apparatus installed in the experimental area of the PF1B beam line at ILL. The neutron beam is represented by the red line and exits through the square hole in the right wall. The casemate is located behind the right wall on this representation.

refined by using the actual neutron beam. A photograph illustrating this alignment process is presented in Fig. 4.3.

4.1.2 Shielding and Safety

When working with intense neutron beams, biological shielding is crucial for both personal safety and the protection of sensitive equipment. To ensure safety and minimize the exposure of the surrounding area to stray radiation, the hole between the casemate and experimental area measuring about 50×50 cm^2 is entirely blocked by lead bricks, leaving only an aperture of 8×8 cm^2 for the neutron beam itself. This feature is presented in Fig. 4.4.

Moreover, the use of gadolinium in the gratings presents another challenge. When gadolinium absorbs neutrons, gamma radiation is produced and can be hazardous. Shielding against these secondary emissions is therefore paramount. During the characterization measurements discussed in this chapter, the neutron flux is significantly reduced by a factor of 200 due to the chopper installed in the casemate upstream of the beam line (Sec. 2.1.2). This reduction allows for sufficiently low radiation levels,

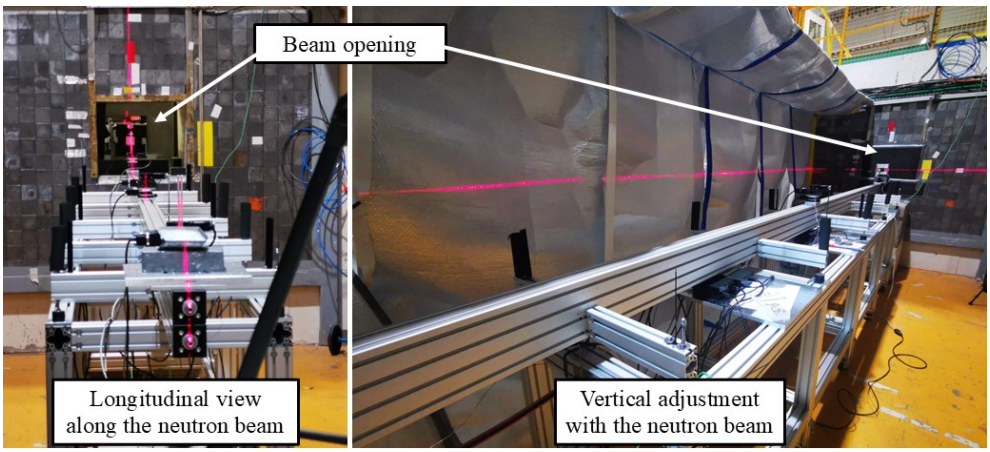

Figure 4.3. Left: Laser beam (red) placed at the beam stop showing the vertical plane parallel to the beam axis. Right: similar with the horizontal axis. These references are helpful for the installation of the components in the neutron beam path (collimating apertures, gratings, vacuum pipes and detector).

meaning that only localized lead shielding around the beam opening is necessary. As a result, samples (gadolinium gratings or aluminum test sample) can be freely installed on the beam without the need for rigorous radiation control procedures at each step. However, the situation will change for the neutron electric charge measurement in Chap. 5. During this phase, the plan to remove the chopper for a higher beam intensity will increase the flux and require significantly more shielding (Sec. 5.1.1).

Additionally, the detector is equipped with shielding around its housing, consisting of a 5 mm-thick B_4C layer surrounding the detector. This shielding helps to reduce potential background signals from other locations within the experimental area.

4.1.3 Further Components Installation

Once the setup itself is in the correct position, the components such as the neutron detector, defining apertures, gratings, and eventual vacuum pipes are placed on top of the extruded aluminum profile. The beam exit has a size of 6×6 cm^2, the defining apertures are chosen to be 5×5 cm^2 and are placed at the very beginning of the setup before G_0, and immediately after G_2, taking the nomenclature A_0 and A_2, respectively.

Figure 4.4. Shielding setup during the characterization measurements at the PF1B beam line. Lead bricks were used to block the beam exit, except for the beam path itself, ensuring safety while allowing the experiment to proceed.

Figure 4.5 illustrates a CAD representation where these components are mounted on the setup.

4.1.4 Temperature Monitoring

Temperature control and stability are essential for maintaining good precision and accuracy during characterization or quantitative measurements. To monitor temperatures across the experimental setup, eight type K thermocouples were installed at various positions around the beam line and the setup:

- Screwed onto the base of the grating holders
- Positioned in the air around the experiment and within the experimental area
- Screwed onto the detector housing
- Screwed onto the temperature-regulated base profile supporting the gratings

These thermocouples were connected via a Picolog TC08 data logger, recording temperature values every second during the entire experiment. The locations of every thermocouple installed for the measurement campaigns are indicated in Fig. 4.6.

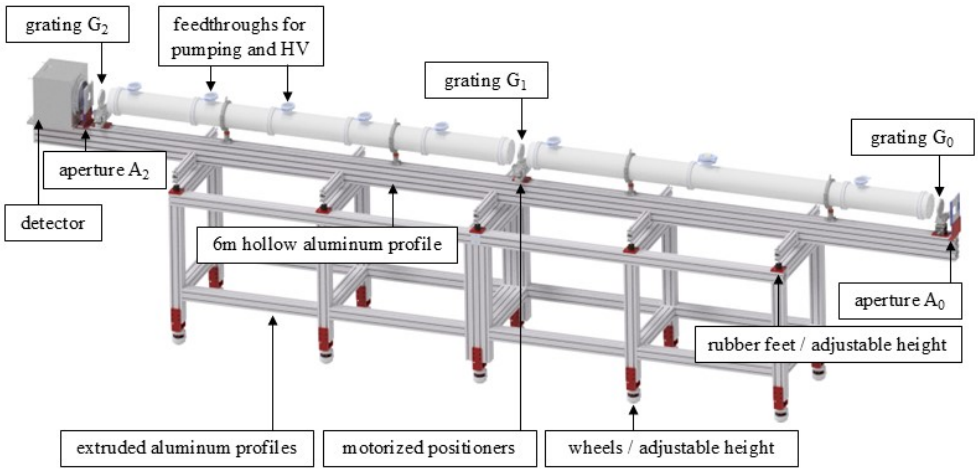

Figure 4.5. CAD representation of the QNeutron apparatus with the relevant components installed. The neutron beam goes from right to left. The neutron Fermi chopper is not represented in this view but sits upstream of A_0. At the beginning of the setup, the neutron beam is defined by A_0. The beam passes the gratings, the vacuum pipes installed in the flight path with 0.5 mm-thick aluminum windows, and the second defining aperture A_2. Finally, neutrons are detected by the Cascade detector.

Temperature Regulation

The profile where the gratings are installed is an extruded, hollow aluminum profile (Sec. 4.1.1). To stabilize the setup temperature, distilled water was circulated continuously through the profile at a constant temperature of 25 °C. The pump is mounted on a temperature-stabilized bath circulator Thermo Scientific ARCTIC A10-SC150. In Chap. 5, during the measurement of the neutron electric charge, a thermal shield made from temperature-protective foil was installed to enclose the entire apparatus [158]. Although this thermal shield is primarily used for the charge measurement described in the next chapter, its performance in terms of stabilizing temperature was investigated here.

An example plot of the recorded temperatures from three thermocouples is shown in Fig. 4.7, along with their respective Allan deviations. The channels highlighted—"G_2", "$profile$", and "$airPF1B$"—are of particular importance during long measurements due to the role of G_2 as analyzer. This plot demonstrates the combined effectiveness

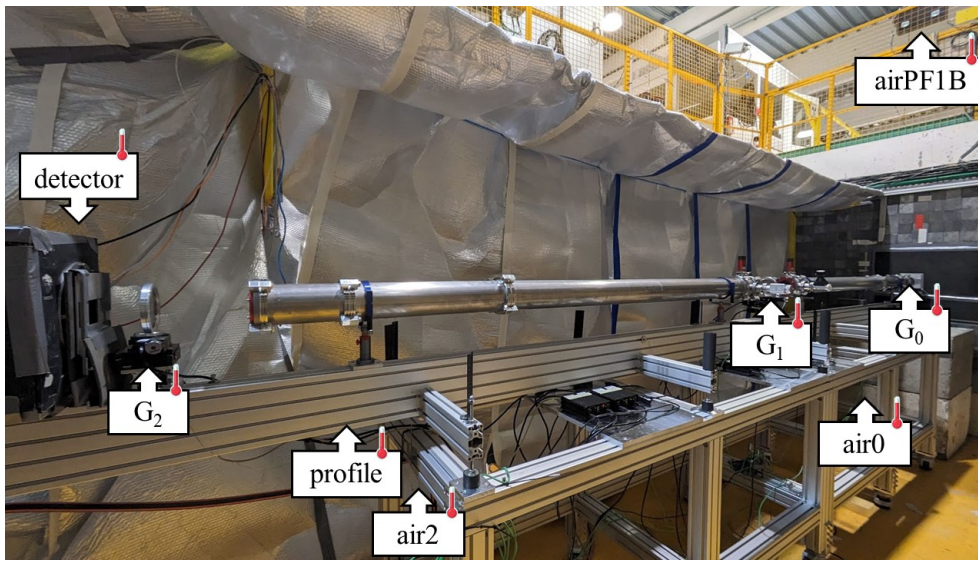

Figure 4.6. Placement of Type K thermocouples around the experiment for temperature monitoring. The sensors labeled "$air0$", "$air2$" and "$airPF1B$" are measuring air temperature while the others are screwed on the indicated components/positions. The temperature is recorded once every second during the experiment.

of the temperature regulation of the profile and the thermal shield in stabilizing the temperature of the grating G_2.

On the plot presented in Fig. 4.7, the efficiency of the regulating method of the profile is demonstrated by looking at the curves of the corresponding channel. On the right plot, it is clear that the profile largely improves the stability of the grating temperature with respect to short-term instabilities. However, at longer timescales, the fluctuations governed by air instability become the main factor impacting temperature changes at the position of G_2. This analysis helps determine an optimal observation time for measurements with the analyzer grating over extended periods, particularly during the electric charge measurement discussed in Chap. 5. Based on the temperature data, the temperature deviation of G_2 is minimized for an observation time of $\tau_{temp} = 260\,\mathrm{s}$.

It is important to note that this optimal time only accounts for temperature fluctuations. The overall stability of the setup, including factors relevant to neutron measurements, is further analyzed in Sec. 4.4.5.

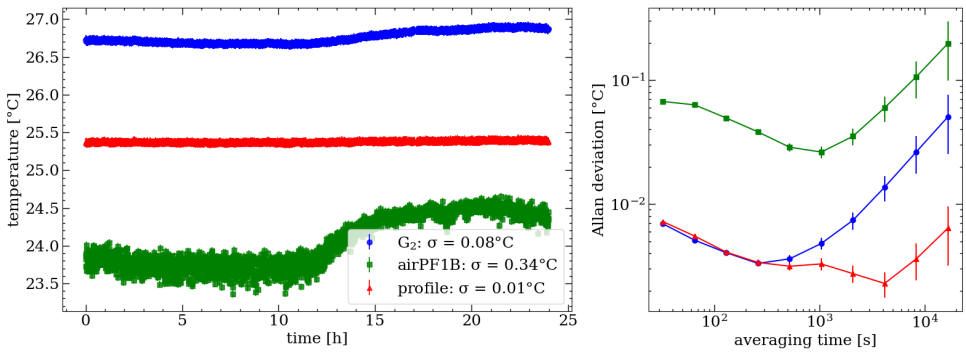

Figure 4.7. Left: Temperature channels "G_2" (blue), "$profile$" (red), and "$airPF1B$" (green) recorded over an observation time of 24 h. Right: Corresponding Allan deviations. The plot shows that for shorter timescales, the temperature of G_2 closely follows the stabilized profile, indicating effective regulation. Over longer timescales, the influence of ambient air fluctuations becomes dominant. This measurement was performed with the thermal shield surrounding the setup, as for the neutron electric charge measurement in Chap. 5.

4.1.5 Detector Settings

In order to operate the neutron Cascade detector in optimal settings, a detector parameters scan has to be conducted at the beginning of each measurement campaign as described in Sec. 2.1.3. The parameters to adjust are the operating voltage of the detector, as well as the voltage threshold of the discriminator.

Discriminator Threshold

The characterization begins by making a discriminator threshold scan without neutron to quantify the sensitivity of the detector to unwanted noise and background. This measurement is shown on the left plot in Fig. 4.8 for several operating voltage of the detector U_{det}. On the right plot, the measurement is repeated with the neutron beam in operation, showing a threshold from which the counts are increasing significantly.

After this preliminary scan, a threshold value of -26.67 mV is selected. First because there are no significant background counts for every tested detector operating voltages (≈ 2 Hz), and second because when the neutron beam is operating, a flat plateau is observed for $U_{det} = -2800$ V. This plateau indicates the operational stability of the

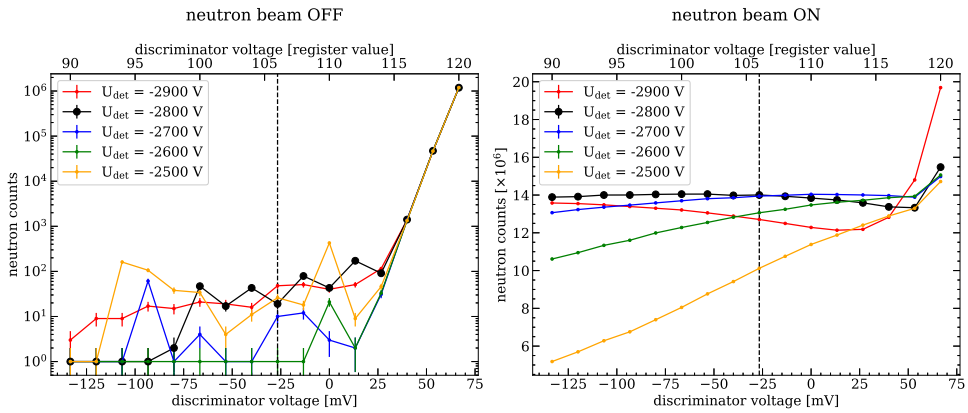

Figure 4.8. Discriminator threshold voltage scan without operating the neutron beam (left). Same measurement while operating the neutron beam (right). For both measurements, each point has been recorded for 10 s. The bottom x-axis shows the voltage, while the top x-axis displays the corresponding register values. The two are related by the conversion: Volt = (Register − 80) × $\frac{20}{3}$ − 200.

detector, maximizing signal amplification without excess noise or saturation. With a higher detector voltage, the count rate is decreasing when the threshold voltage increases and *vice-versa* with lower voltages.

Detector High-Voltage

To confirm these preliminary settings, scans of the detector high-voltage are performed for several values of the discriminator threshold and are shown in Fig. 4.9.

In this plot, the discriminator threshold U_{th} is set to a given value and a detector high-voltage scan is conducted. The count rates show the smallest dispersion for every tested discriminator voltage at a detector voltage $U_{det} = -2800\,\mathrm{V}$. Additionally, a discriminator threshold of $-26.67\,\mathrm{mV}$ presents a flat plateau around this relevant value of U_{det}.

To summarize, a detector voltage of $U_{det} = -2800\,\mathrm{V}$ and a discriminator threshold of $U_{th} = -26.67\,\mathrm{mV}$ (register value of 106) are chosen during the entire beam time of the experiment, guaranteeing the best compromise between high sensitivity to neutron detection and low sensitivity to background or noise signals. Moreover, the

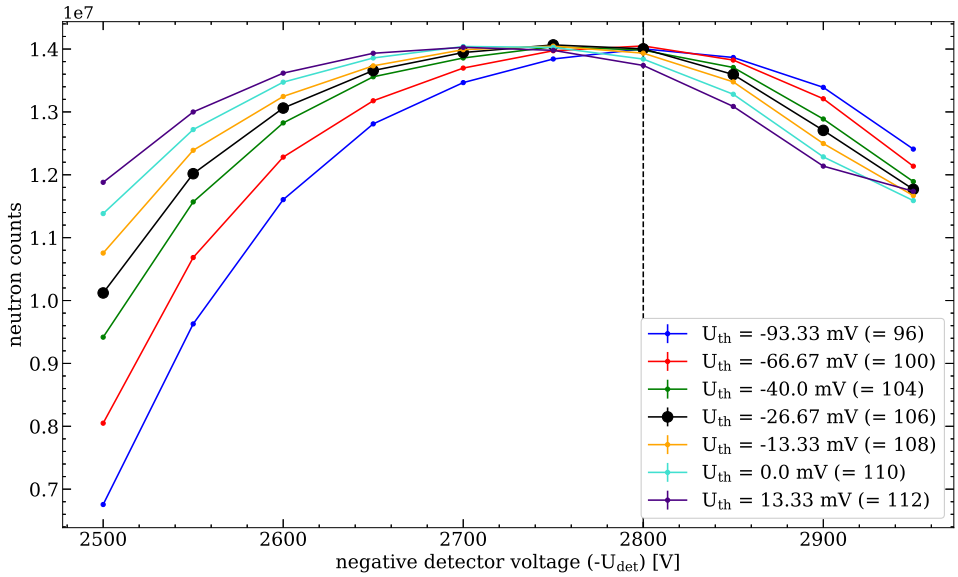

Figure 4.9. Detector high-voltage scan performed before the measurement campaign at ILL with only the 5×5 cm^2 apertures A_0 and A_2 mounted at both extremities of the setup. The chopper was installed and delivered a pulse frequency $f_{ch} = 25$ Hz. Each data point represents 10 s of data acquisition. The discriminator threshold was set to different values (color scheme) while the HV setting varied from -3000 V to -2500 V. Each values of the discriminator threshold investigated are given in Volt with the corresponding register value in brackets. The black dashed line corresponds to the optimal setting where counts are maximized and the discriminator has the least impact.

algorithmic filter described in Sec. 2.1.3 was enabled during these measurements to ensure that any false counts related to multiple detections of the same event were avoided.

4.2 PF1B - Time-of-Flight Spectrum

Before delving into the specific measurements related to the interferometer, it is essential to present the beam line characteristics that directly influence the experiment. The time-of-flight (TOF) spectrum is a critical aspect of these measurements, serving as a reference for further characterizations. The TOF spectrum at PF1B shown in Fig. 4.10 was measured with the beam open, meaning that no other experimental components were installed, aside from the chopper delivering a pulse frequency of 25 Hz (collimator as described in Sec. 2.1.2), detector, and 5×5 cm^2 defining apertures A_0 and A_2 (no gratings).

The characteristics of the PF1B beam line, such as its total flux, weighted-mean wavelength, and the wavelength corresponding to the maximal count rate, are depicted in Fig. 4.10. Understanding these characteristics allows us to optimize the experimental setup by choosing an adequate working wavelength and provides a reference measurement for further characterizations, such as substrate, gadolinium, and grating transmission.

For statistical reasons, in the subsequent sections of this document, the measurements will be presented within the wavelength range of 0.1 nm to 1.5 nm, which corresponds to the region where the relative intensity is above approximately 0.3%. This range was chosen to ensure sufficient statistical accuracy for the fitting procedures while still focusing on the most relevant part of the spectrum.

4.3 Transmission Measurements

This section presents the transmission analysis of different samples, including gratings and grating substrates, as a function of neutron wavelength. Measurements are conducted using the defining apertures A_0 and A_2 shown in Fig. 4.5. First, a reference open-beam time-of-flight measurement is taken for 5 min with a chopper pulse frequency of 25 Hz. Then, the sample under investigation is positioned after A_0, and the measurement is repeated under identical conditions. Transmission spectra are obtained by comparing these measurements, plotted as a function of neutron wavelength.

4.3.1 Substrate Transmission

The transmission properties of the substrate material used for the gratings are evaluated. Five different samples were measured, consisting of three different thicknesses

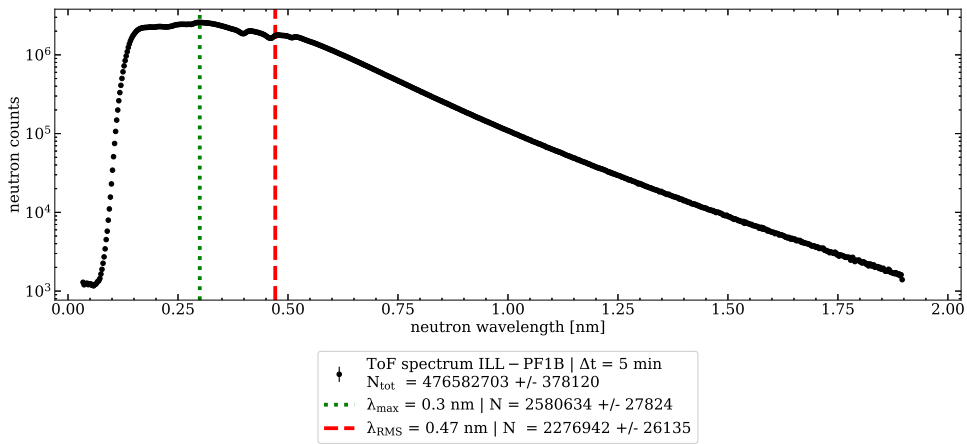

Figure 4.10. Measured time-of-flight spectrum at the PF1B beam line with the beam open, serving as a reference for further measurements. The chopper was set to provide a pulse frequency of 25 Hz. The total observation time of 5 min corresponds to 7500 chopper sweeps. 1000 time bins of 50 µs (0.0024 nm) allow the recording of the spectrum up to a wavelength of 1.89 nm with a resolution of 0.01 nm (chopper-to-detector distance of 8.28 m). The weighted mean wavelength of this spectrum is $\lambda_{RMS} = 0.47$ nm (red dashed line) and the wavelength with maximum statistics is $\lambda_{max} = 0.3$ nm (green dotted line).

of sapphire (1, 2, and $5 \times 2 = 10$ mm), and two additional samples: 1 mm sapphire coated with 20 µm of Gd, and 2 mm sapphire coated with 30 µm of Gd. The results are shown in Fig. 4.11.

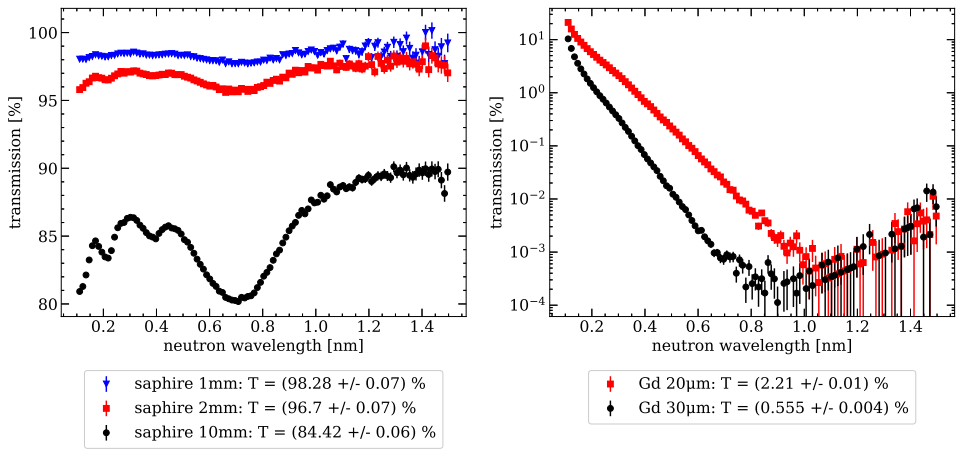

Figure 4.11. Left: Neutron transmission through 1 (blue), 2 (red), and 10 mm of sapphire (Al_2O_3), which constitute the substrate for the gratings. The integrated transmission T over the entire spectrum is shown in the legend. Right: Transmission for 1 mm-thick sapphire coated with 20 µm of Gd (red) and 2 mm-thick sapphire coated with 30 µm of Gd (black). The increase in transmission observed beyond 0.8 nm is attributed to statistical fluctuations, as the neutron flux at these wavelengths is negligible.

4.3.2 Grating Transmission

The same procedure is applied to measure the transmission through the gratings. A reference open-beam measurement is first recorded for 5 min, followed by a measurement with a grating sample placed directly downstream of A_0. The results are grouped either by grating period to compare different duty cycles (top plots in Fig. 4.12) or by duty cycle to compare different absorber thicknesses t_{Gd} (bottom plots in Fig. 4.12).

These measurements are used to calculate the grating transmission as a function of the neutron wavelength for the simulations presented in App. A.

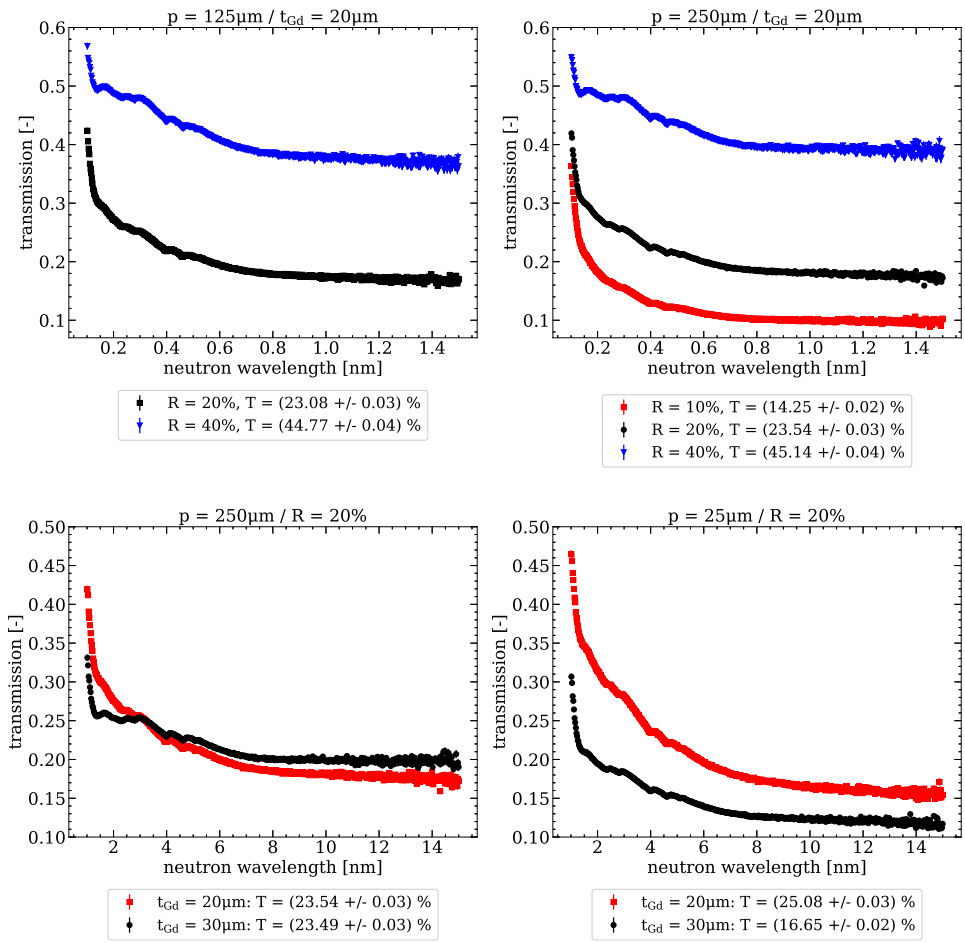

Figure 4.12. Top: Transmission as a function of the neutron wavelength for gratings with $p = 125\,\mu m$ (left) and $p = 250\,\mu m$ (right). Different duty cycles are evaluated: 20% and 40% for $p = 125\,\mu m$, and 10%, 20%, and 40% for $p = 250\,\mu m$.
Bottom: Transmission as a function of the neutron wavelength for gratings with $p = 250\,\mu m$ (left) and $p = 25\,\mu m$ (right). Two absorber thicknesses are investigated: $t_{Gd} = 20\,\mu m$ and $30\,\mu m$. The integrated transmission T over the spectrum is shown in the legend. Note that for gratings, T is slightly higher than the grating duty cycle due to the transmission of shorter wavelengths through the gadolinium. The reduction in transmission observed for the grating with $p = 25\,\mu m$ and $t_{Gd} = 30\,\mu m$ can be attributed to the manufacturing imperfections discussed previously.

4.4 Ballistic Configuration

In this section, different experimental parameters are investigated to maximize the performance of the QNeutron apparatus in a ballistic configuration. The consequences of relative misalignment between the gratings are evaluated, and the grating parameters optimized. The formula used for estimating the sensitivity to a neutron electric charge is [59]:

$$\sigma(Q_n) = \frac{4\pi\hbar^2 p}{\eta m_n E L^2 \lambda^2 \sqrt{N_w}} \tag{4.1}$$

Here, Q_n is the neutron electric charge, p the grating period, η the visibility of the oscillating intensity pattern generated by scanning G_2, m_n the neutron mass, E the transverse electric field, L the interaction length with the electric field, λ the neutron wavelength, and N_w the neutron statistics at the working point w_p (Sec. 2.2.1).

It is important to note that this formula assumes a specific experimental procedure involving opposite deflections of two beams and electric field reversal to enhance sensitivity. The details of this procedure are presented in Sec. 5.2. The following paragraphs focus on optimizing the parameters related to the grating geometry (duty cycle R and thickness of the Gd layer t_{Gd}), which directly influence the factors η and N. This optimization aims to achieve the best compromise between high visibility and high statistics, ensuring enhanced sensitivity to beam deflection measurements and, ultimately, to neutron electric charge determination.

4.4.1 Duty Cycle Optimization

The duty cycle R, defined as the open fraction of the gratings, is a key parameter influencing the visibility η of the intensity pattern observed during transverse scans with G_2. In the ballistic regime, the distance between the gratings ($L_G = 2.75\,\mathrm{m}$) is significantly larger than the Talbot length and neutron trajectories are approximated as straight lines (Sec. 1.3.2). To systematically study the impact of the duty cycle, three sets of gratings were tested with $p = 250\,\mu\mathrm{m}$, $t_{Gd} = 20\,\mu\mathrm{m}$ and $R = 10\%$, 20%, and 40%. For each configuration, transverse scans with G_2 were performed in TOF mode over three grating periods (750 µm). The goal was to optimize the neutron statistics N_w at the steepest point of the intensity oscillations and the visibility η of the modulation. Figure 4.13 shows the recorded intensity modulations for each duty cycle (left) and the corresponding visibility as a function of neutron wavelength (right).

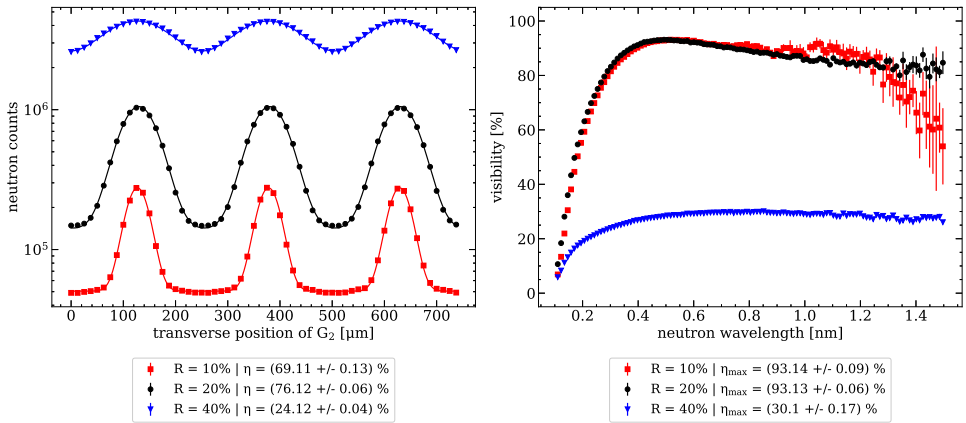

Figure 4.13. Intensity modulation for different duty cycles: integrated over the spectrum (left) and visibility as a function of wavelength (right). For each measurement, the grating period was $p = 250\,\mu m$, $t_{Gd} = 20\,\mu m$ and 750 chopper sweeps were accumulated, corresponding to 30 s per data point ($f_{ch} = 25\,Hz$). Visibilities are comparable for $R = 20\%$ and $R = 10\%$ but significantly lower for $R = 40\%$. When neutron statistics at w_p are considered, a duty cycle of 20% presents the best compromise.

The data, fitted using periodic Gaussian peaks and analyzed with the bootstrap method (Sec. 2.2.2), lead to the following conclusions:

- 10% Duty Cycle: Low neutron flux due to limited open area, resulting in reduced N_w. Although η was high, statistical uncertainties were significant due to low count rates.
- 20% Duty Cycle: Improved neutron flux and N_w, while maintaining high η. This configuration offered a favorable balance between visibility and statistics, enhancing measurement precision.
- 40% Duty Cycle: Highest neutron flux, but reduced η, leading to lower contrast in the interference pattern and diminished sensitivity at the working point of the modulation.

The 20% duty cycle was found to provide the optimal compromise between high visibility and adequate neutron statistics, ensuring precision and reliability for neutron electric charge measurements. It will be adopted as the standard configuration.

4.4.2 Absorber Thickness

The optimization of grating performance requires careful selection of the absorber thickness. The gratings used in this study were fabricated from sapphire wafers coated with gadolinium (Gd) and laser-engraved to form the grating structure (Sec. 2.1.4). For gratings with $R = 20\%$, two Gd thicknesses were investigated: $t_{Gd} = 20\,\mu\text{m}$ and $t_{Gd} = 30\,\mu\text{m}$. The latter gratings are from a new batch, addressing unexpected results from previous measurements (Sec. 3.7).

To evaluate performance, TOF scans were conducted transversally with G_2, recording intensity modulations over three grating periods and for 30 s per data point (750 chopper sweeps at $f_{ch} = 25\,\text{Hz}$). For each thickness, the intensity modulations were analyzed, and the visibility as a function of wavelength was computed. Figure 4.14 shows the intensity modulations recorded for $t_{Gd} = 20\,\mu\text{m}$ and $t_{Gd} = 30\,\mu\text{m}$ with the chopper in operation, but integrating over the full neutron spectrum (left), along with the corresponding visibility as a function of the neutron wavelength (right).

Key observations from these measurements include:

- 20 µm gadolinium: Provides moderate neutron absorption and reasonable visibility. However, higher background, particularly at shorter wavelengths, results in a lower signal-to-noise ratio and reduced sensitivity.
- 30 µm gadolinium: Offers superior neutron absorption, especially at shorter wavelengths, reducing background noise and improving the signal-to-noise ratio. This leads to clearer interference fringes and enhanced visibility. Here, the maximum visibility is (97.0±0.1) % for a neutron wavelength $\lambda = 0.37\,\text{nm}$.

These observations highlight a trade-off between visibility and transmission: increasing the Gd thickness to $t_{Gd} = 30\,\mu\text{m}$ significantly enhances visibility, particularly at shorter wavelengths, while reducing transmission. This improvement in visibility leads to clearer interference fringes and better signal-to-noise ratios, confirming the superior performance of thicker Gd coatings for high-precision neutron measurements. These findings underline the importance of optimizing absorber thickness to achieve the best balance between neutron absorption and intensity modulation, ensuring enhanced sensitivity for neutron electric charge experiments.

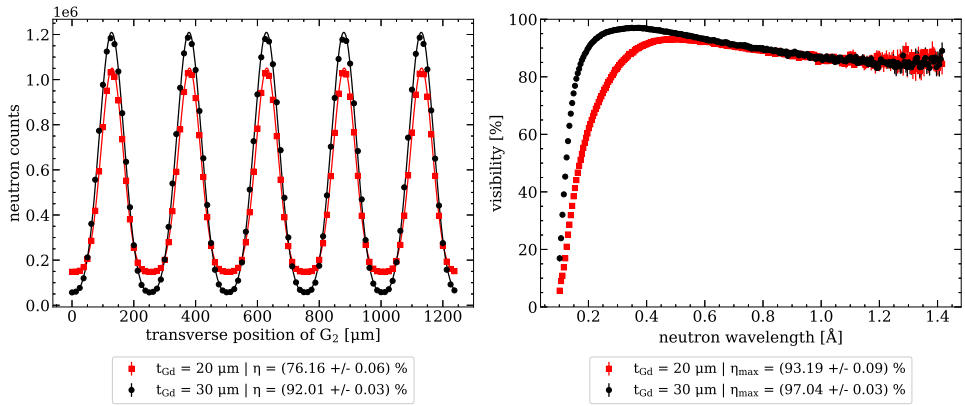

Figure 4.14. Left: White beam measurement of the oscillating intensity pattern recorded with $p = 250\,\mu\text{m}$ and $t_{Gd} = 20\,\mu\text{m}$ (red) and $t_{Gd} = 30\,\mu\text{m}$ (black). Each data point was recorded during 30 s. Right: Visibility of the intensity modulation as a function of neutron wavelength for both thicknesses, showing improved performance with $t_{Gd} = 30\,\mu\text{m}$. A maximum visibility of (97.0±0.1)% is measured for a neutron wavelength $\lambda = 0.37\,\text{nm}$.

4.4.3 Systematic Misalignment

Once the setup was well-aligned, a series of scans were conducted with all the motorized stages to understand the sensitivity of the apparatus to misalignments. These scans were performed around the beam axis (x, θ) and the vertical axis (z, ψ) with G_1 and G_2 using goniometers and rotation stages, respectively. Additionally, G_1 was shifted along the beam axis for longitudinal misalignment.

Rotational Misalignments

To evaluate the sensitivity of the apparatus to rotations around the beam axis (x, θ), goniometers were used to rotate G_1 and G_2 when the setup was at the peak of the intensity modulation. In the left plot of Fig. 4.15, the neutron intensity changes notably with rotations around the beam axis, indicating a significant sensitivity to such misalignments. This sensitivity arises from the formation of Moiré patterns, which occur when two gratings are overlaid with a slight angular or period mismatch, producing interference fringes that reveal misalignments.

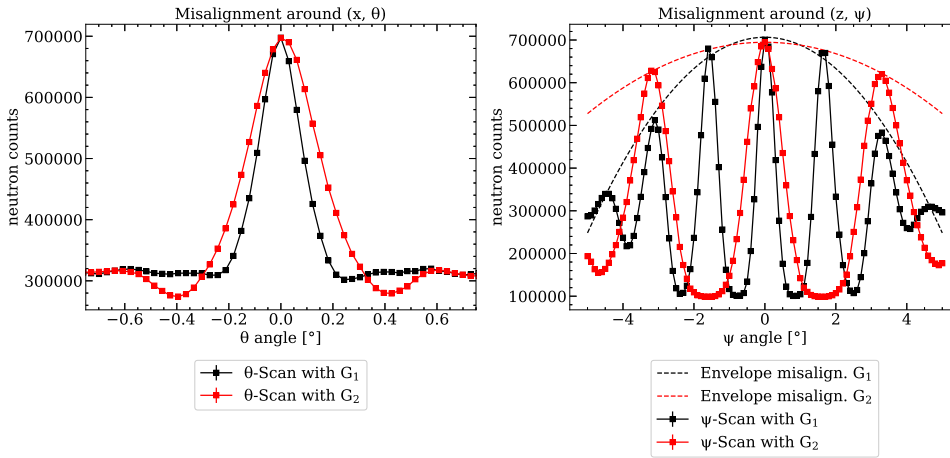

Figure 4.15. Left: Scans performed with the goniometer stages (x, θ) over a range from -1.5° to 1.5° for 30 s per data point (750 chopper sweeps at $f_{ch} = 25$ Hz). Right: Similar scans with the rotation stages of G_1 (black) and G_2 (red) around the vertical axis (z, ψ) over a range from -5° to 5° with respect to the brightest point of the intensity pattern (setup aligned). The fast oscillations are attributed to the non-concentricity between the vertical axis of the grating and the axis of rotation around z, inducing a quasi-transverse scan of the grating.

The right plot in Fig. 4.15 shows the neutron intensity as a function of the misalignment angle around the vertical axis for G_1 (black) and G_2 (red). The fast oscillations with a period of approximately 3 ° are due to a slight misalignment, as the vertical axis of the grating (z-axis) is not concentric with the center of rotation of the stage. As a result, rotating the stage causes a small transverse shift of the grating in the y-direction, inducing a quasi-transverse scan and leading to the observed intensity modulations within the envelope. The dashed lines represent the overall envelope, which arises from the actual misalignment of the grating around the vertical axis. The effect is twice as significant for G_1 compared to G_2, which agrees with expectations.

Figure 4.15 shows that the setup exhibits comparable sensitivity to misalignments around both the x-axis and z-axis, with neutron counts reduced to 99% for a misalignment angle of 0.01°. In the current configuration, the sensitivity to misalignments

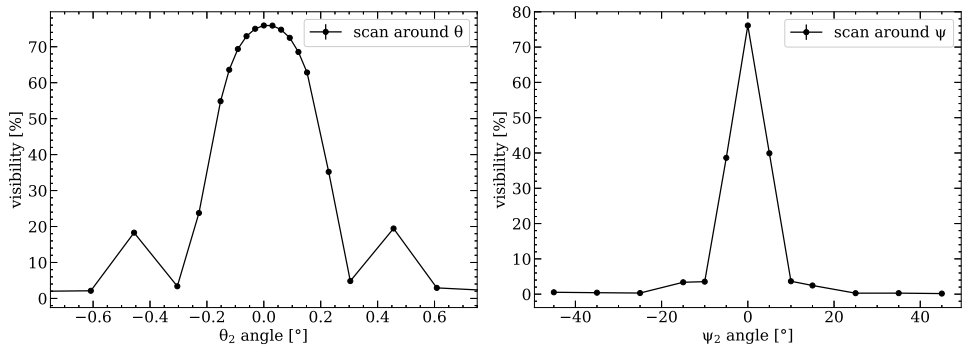

Figure 4.16. Left: Effect of a misalignment angle θ of G_2 on the visibility of the oscillating intensity pattern. Right: Similar measurement with a misalignment angle ψ.

around the z-axis is dominated by the fast oscillations within the envelope.[3] Given that a misalignment of 0.01° corresponds to less than one full step of the stepper motor on the positioners, rotational misalignments have a negligible effect on the measurements within this range.

Additionally, an extensive overnight measurement has been performed for this investigation. An oscillating intensity pattern is recorded transversely with G_2 while being set in several different misaligned positions around the beam axis θ and the vertical axis ψ. The visibility of the intensity modulation can be extracted for each position and is plotted in Fig. 4.16.

The results show that, under ideal conditions, the setup would be significantly less sensitive to misalignments around the vertical axis than around the beam axis. However, due to the non-concentricity between the vertical axis of the grating and the center of rotation of the motorized stage, as described earlier, this reduced sensitivity cannot be fully realized in practice. Consequently, the sensitivity to misalignments around the vertical axis remains comparable to that around the beam axis in the current experimental configuration.

[3] Without the non-concentricity between the z-axis of the grating and the center of rotation of the motorized stage, the sensitivity would be governed by the broader envelope in dashed lines, with neutron intensity reducing to 99% only at a misalignment angle of 1°

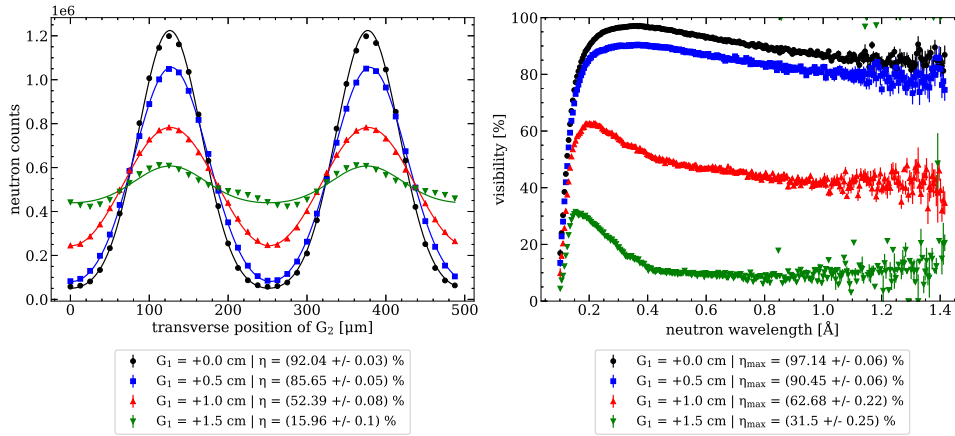

Figure 4.17. Left: Oscillating intensity pattern recorded for the integrated spectrum when the grating G_1 is moved by 0 cm (black, reference), 0.5 cm (blue), 1 cm (red), and 1.5 cm (green) along the x-axis. Right: Visibility as a function of the neutron wavelength for these four configurations, showing a significant loss of performance with increasing longitudinal misalignment.

Longitudinal Misalignment

The susceptibility of the setup to longitudinal misalignments (x-axis) was investigated by shifting G_1 along the beam axis. This adjustment altered the distances between the gratings, creating an asymmetric configuration while keeping the total length of the setup constant. Specifically, the distance between G_0 and G_1 was increased, while the distance between G_1 and G_2 was correspondingly decreased.

Four positions of G_1 were tested, and for each position, an intensity modulation was recorded over two grating period and for 30 s per data point. The results are shown in Fig. 4.17. The left plot depicts the oscillating patterns obtained from the integrated spectrum for shifts of G_1 by 0 cm (black), 0.5 cm (blue), 1 cm (red), and 1.5 cm (green). The right plot shows the corresponding visibility as a function of neutron wavelength.

Figure 4.17 illustrates the high sensitivity of the setup to longitudinal shifts of G_1. As the distance between G_1 and G_2 decreases, the interference pattern becomes increasingly distorted, and visibility is significantly reduced (drop from 92% to 16%

when G_1 is shifted by 1.5 cm). This emphasizes the importance of maintaining equal distances between the gratings for optimal performance.

4.4.4 Beam Deflection Measurement

Neutron grating interferometry, as discussed in Sec. 1.3, provides a precise method for measuring small neutron beam deflections. This section describes the calibration of the beam deflection measurement system using an aluminum prism, demonstrating the high sensitivity of the setup to deflections.

Experimental Setup

The gratings are aligned (App. B), and the baseline oscillating intensity pattern is recorded by scanning G_2 over one period with 30 s per data point (7500 chopper sweeps with a neutron pulse repetition frequency of 25 Hz). Gaussian fitting is used to extract the center position of the intensity modulation (position of the peak).

An aluminum cube is then placed between G_1 and G_2, with its top edge aligned at the mid-height of the gratings (Fig. 4.18). In this configuration, the upper portion of the beam passes unaffected and serves as a reference. The lower portion of the beam interacts with the cube, which, due to its 45° orientation, effectively acts as two "sub-prisms" with a 90° apex angle. This causes the lower part of the beam to split, with the two sections being deflected in opposite directions.

The Cascade detector enables simultaneous analysis of the three beam spots—**left**, **right**, and **top**. With the cube in place, the scan with G_2 is repeated, and the shifted intensity modulation due to the deflection is recorded. An example of the spatial distribution recorded by the detector is illustrated in Fig. 4.19, where the three zones are depicted by colored rectangles.

Measurement

The center positions of the intensity modulations, with and without the cube, are extracted for all three zones. Figure 4.20 shows the results, where a notable shift in the center position is observed for the left and right zones due to the presence of the cube. Additionally, a reduction in intensity is observed due to neutron absorption by the aluminum. The difference between the two measurements yields the beam deflection induced by the two "sub-prisms".

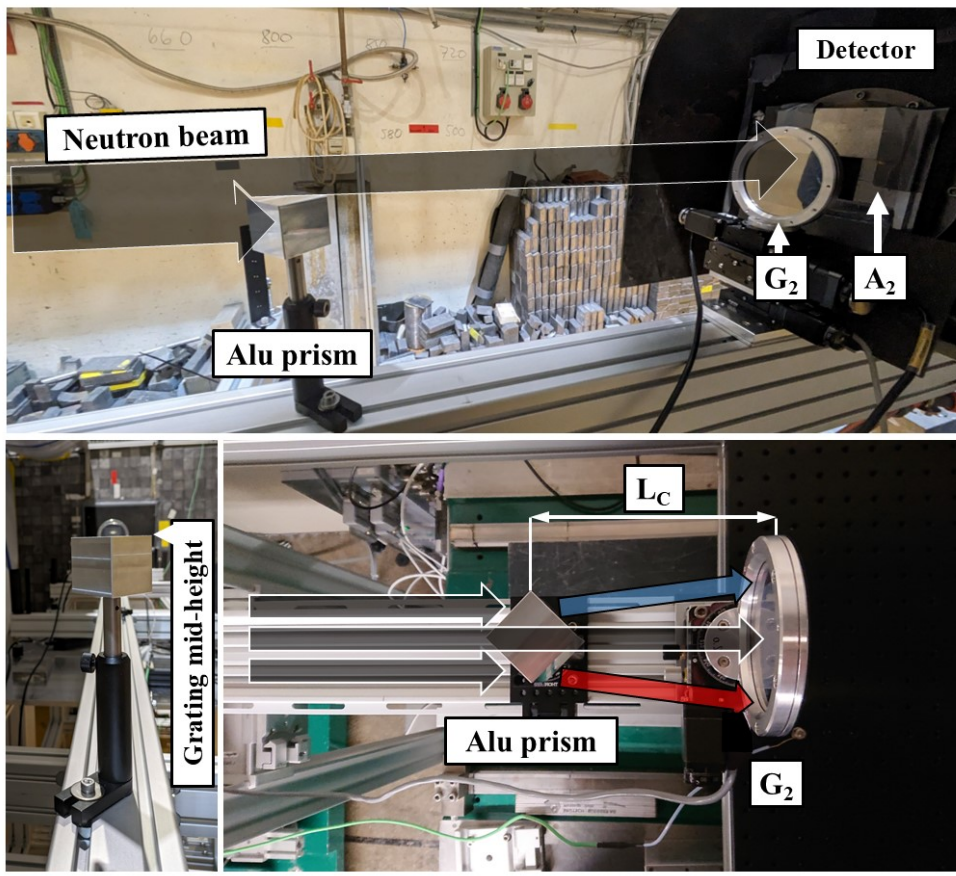

Figure 4.18. Views of the aluminum cube put in the beam under a 45° angle before the analyzer grating G_2. The height of the cube is adjusted so that its upper face aligns with the mid-height of the neutron beam. The colored arrows indicate the unaffected portion of the beam (black) and the two deflected portions of the beam (red and blue) in opposite directions.

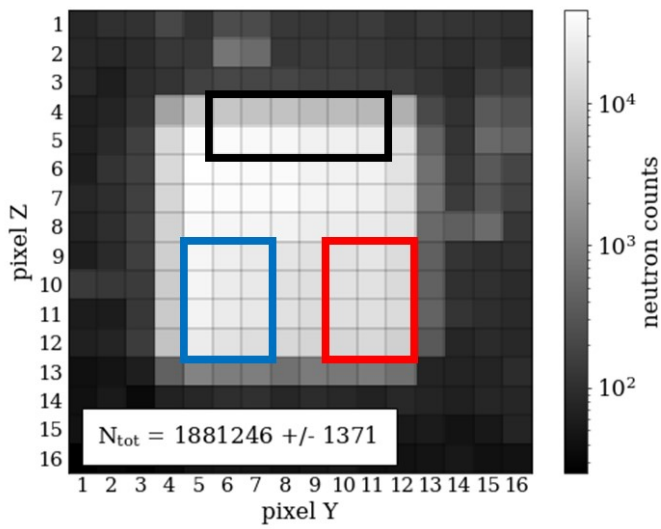

Figure 4.19. A 30 s measurement taken at the peak of the intensity modulation while the cube was mounted on the setup. The left (blue), right (red), and top (black) zones are represented with colored rectangles (compare also Fig. 4.18).

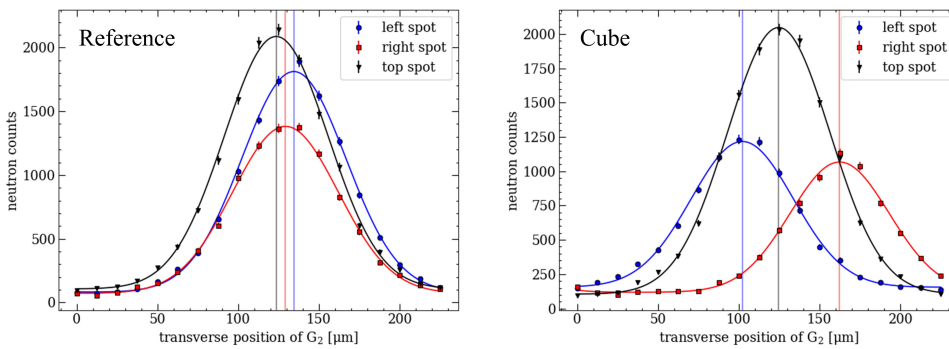

Figure 4.20. Beam deflection measurements with an aluminum cube. The gratings used for these measurement had $p = 250\,\mu\text{m}$, $R = 20\%$ and $t_{Gd} = 20\,\mu\text{m}$. Left: Reference measurement without the cube. Right: Measurement with the cube installed. The horizontal lines indicate the center values of the Gaussian fits for the left, right, and top zones. The measurement have been performed with a chopper, but the neutron wavelength $\lambda = 0.7\,\text{nm}$ is represented for illustrating the deflections of the beam spots. Each data point was recorded over $\Delta t = 1\,\text{min}$ (1500 chopper sweeps at $f_{ch} = 25\,\text{Hz}$).

Results

The beam deflection depends on the neutron wavelength and is measured using the time-of-flight technique. The theoretical deflection is derived from the Snell-Descartes law, which describes wave refraction at material interfaces. For neutrons, the deflection $\delta(\lambda)$ can be expressed as [159]:

$$\delta(\lambda) = \frac{\rho b_c}{\pi} \cdot L_C \cdot \lambda^2 \cdot \tan\left(\frac{\alpha}{2}\right) = A_{th} \cdot L_C \cdot \lambda^2 \tag{4.2}$$

where $\delta(\lambda)$ is the deflection in µm, ρ is the nuclear number density of the material, b_c is the bound coherent scattering length, α is the apex angle of the prism, L_C is the distance between the prism and G_2, and λ is the neutron wavelength. For aluminum ($\rho = 6.02 \times 10^{28}\,\mathrm{m}^{-3}$, $b_c = 3.449\,\mathrm{fm}$) [160], the theoretical constant A_{th} is:

$$A_{th} = 66.12 \times 10^{12}\,\mathrm{m}^{-2} \tag{4.3}$$

The measured deflection as a function of wavelength is shown in Fig. 4.21, with four different cube-to-G_2 distances. The deflection $\delta(\lambda)$ follows a quadratic trend:

$$\delta(\lambda) = K \cdot \lambda^2 \quad \text{with} \quad K = A \cdot L_C \tag{4.4}$$

Here, K is obtained from the fits, and the parameter A is derived by dividing K by the corresponding distance L_C for each measurement.

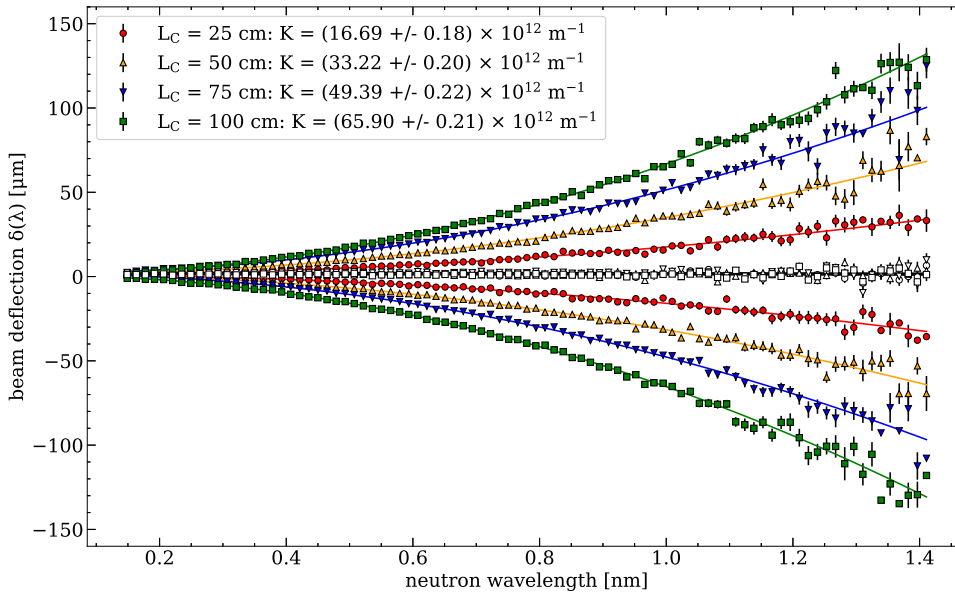

Figure 4.21. Beam deflection for cube-to-G_2 distances of 1 m (green squares), 0.75 m (blue triangles), 0.5 m (yellow triangles), and 0.25 m (red circles). Positive and negative deflections correspond to the **left** and **right** zones, while the **top** zone remains at zero. Solid lines show quadratic fits, confirming the wavelength dependence of deflection.

Goodness of Fit

The Chi-squared values, degrees of freedom (DOF), and reduced Chi-squared values for the quadratic fits are summarized in Table 4.1 for both left and right zones at each distance.

Overall, the χ^2_{red} values indicate that the quadratic model provides a good fit. The few cases where χ^2_{red} deviates (notably $L = 50$ cm, Right and $L = 75$ cm, Right) could hint at minor systematic effects or underestimated uncertainties. These deviations warrant closer examination of the experimental setup, particularly alignment, detector sensitivity, or data processing for those specific configurations.

L_C	Side	χ^2	DOF	χ^2_{red}
L = 25 cm	Left	84	88	0.95
	Right	78.3	88	0.89
L = 50 cm	Left	74.6	88	0.85
	Right	131.2	88	1.49
L = 75 cm	Left	85.4	88	0.97
	Right	115.5	88	1.31
L = 100 cm	Left	86.4	88	0.98
	Right	96.6	88	1.10

Table 4.1. Goodness-of-fit parameters for the quadratic fits applied to the deflection data for different distances and zones.

Measured Deflection Constant

The measured deflection constant, averaged over all four distances, is:

$$A_{\text{meas}} = 66.53(59) \times 10^{12}\,\text{m}^{-2} \tag{4.5}$$

This value agrees well with the theoretical prediction, $A_{th} = 66.12 \times 10^{12}\,\text{m}^{-2}$. Slight deviations at longer wavelengths may arise from factors such as the aluminum purity or a non-perfect positioning of the cube. The agreement between experimental data and theory confirms the validity of the Snell-Descartes law in cold neutron optics. This test measurement demonstrates the capability of the instrument to precisely detect small neutron beam deflections induced by external influences, such as the electric field during the measurement of the neutron electric charge in Chap. 5.

4.4.5 Stability and Sensitivity

The ultimate goal of this study is to measure the neutron electric charge by applying a transverse electric field and detecting any resulting beam deflection. To reduce effects such as beam instability or drifts of the setup (e.g. gratings, motorized stages, beam profile), the two-beam method is employed. This method focuses on the relative positions of two independent beam spots and determining their difference over time. Global drifts, such as those caused by temperature changes or source power

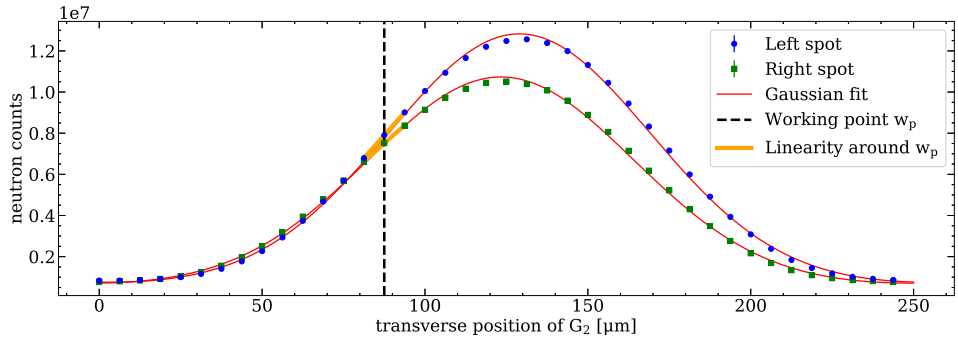

Figure 4.22. Intensity modulations of the left (blue) and right (green) beam spots over one period of 250 µm, $R = 20\%$. The steepest point (common working point w_p) is marked with a dashed black line. The solid red lines represent Gaussian fits, while the thick orange lines show linear fits around the working point. Each point corresponds to 20 s of data acquisition.

fluctuations, affect both beam spots similarly and are canceled out when considering the difference. This section evaluates the effectiveness of this approach.

Two-Beam Method

The setup was divided into two independent beams using a high-voltage electrode, which also serves as a beam separator during the neutron electric charge measurement (Chap. 5). The defining apertures A_0 and A_2 were modified to produce two distinct beam spots, each 50×5 mm^2, and separated by 35 mm center-to-center. The oscillating intensity pattern was recorded by scanning G_2 and identifying the steepest point of the modulation (working point w_p, Sec. 2.2.1). G_2 was then fixed at this position, and repeated measurements were taken for both beam spots during approximately 24 h.

Figure 4.22 shows an example of the intensity modulation for the left and right beam spots recorded for 20 s per data point with the setup used for the neutron electric charge measurement (chopper removed, white beam).

Using the Gaussian fits, the slope at the working point was determined, converting neutron counts into beam spot positions over time. The position difference between the two beam spots was calculated to track the stability of the setup. Figure 4.23 presents a typical 24-hour measurement, showing individual beam spot positions (top) and

their difference (bottom). These measurements were all taken at the working point w_p. The recorded temperatures for the profile and the air near G_2 are also shown, demonstrating the effective stabilization of the profile and suggesting that the drift of the positions of the beam spots is likely caused by temperature fluctuations at G_2.

The average size of the error bars is 15 nm for the left spot, 18 nm for the right spot, and 24 nm for the difference. The standard deviations quoted in the plot reflect the position variation due to temperature drift.

The two-beam method achieves a significant reduction in drift, improving stability by a factor of approximately 20. While individual beam spots exhibit micrometer-scale drifts, their relative difference remains highly stable. This method will be essential for probing beam deflections due to the antiparallel electric fields applied during the neutron electric charge measurement.

Sensitivity Estimation

The Allan deviation [161] was calculated to further evaluate the stability and sensitivity of the system. This statistical tool effectively captures noise and drift characteristics over varying time intervals, providing a robust measure of long-term stability. By focusing on differences between consecutive measurements, Allan deviation reduces the impact of random fluctuations and provides reliable insights into the stability of the system over both short and long timescales.

Figure 4.24 shows the Allan deviation $\sigma(\tau)$ as a function of observation time τ for the difference between the left and right beam spots. The minimum deviation, occurring at $\tau_{R-L} = 2075\,\mathrm{s}$, represents the optimal observation time for achieving maximum stability when comparing two datasets over time. This result is particularly important for the neutron electric charge measurement, where temporal comparisons of deflections between the left and right beam spots are made. For short observation times, the Allan deviation of the beam spot difference is lower than that of the individual left and right spots. This is expected since taking the difference reduces noise between consecutive points.

Conclusion

The characterization measurements confirm that the two-beam method effectively mitigates systematic effects, improving both stability and sensitivity for neutron beam deflection measurements in opposite directions. This method will be systematically

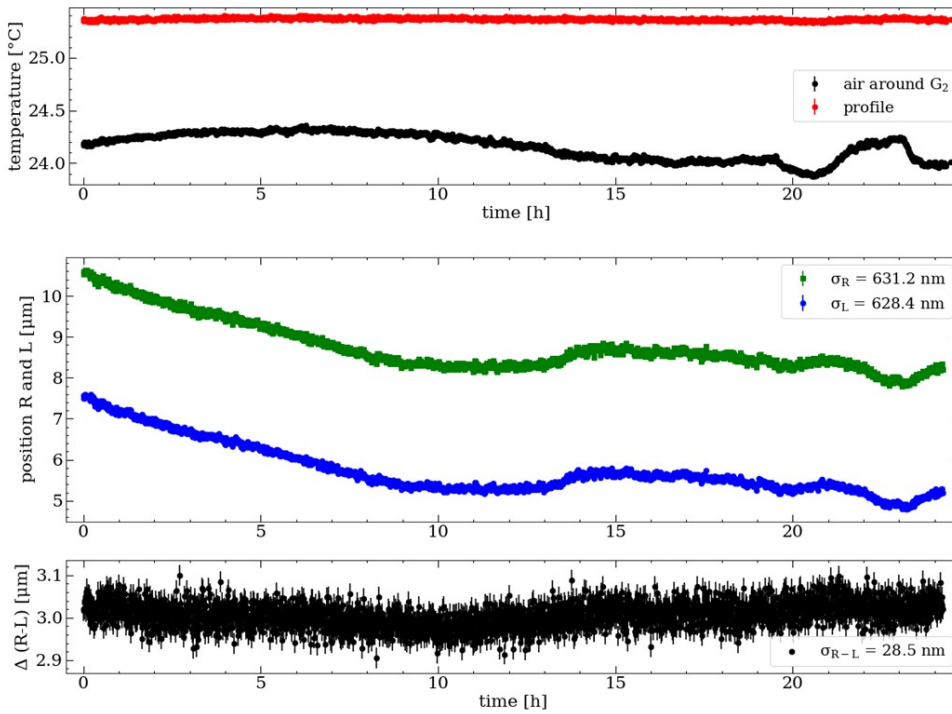

Figure 4.23. Top: Recorded temperatures of the profile (red) and the air near G_2 (black), showing effective stabilization of the profile and indicating that the drift in beam spot positions is likely due to temperature fluctuations at G_2. Center: Position of the left (blue) and right (green) beam spots over 24 h. Each data point represents 20 s of measurement. The observed drift, mainly caused by temperature changes, results in standard deviations of approximately 600 nm. Bottom: Two-beam method showing the difference between the right and left beam spots. The standard deviation is significantly reduced to around 30 nm, an improvement by a factor of 20.

employed in future experiments, including the neutron electric charge measurement detailed in Chap. 5.

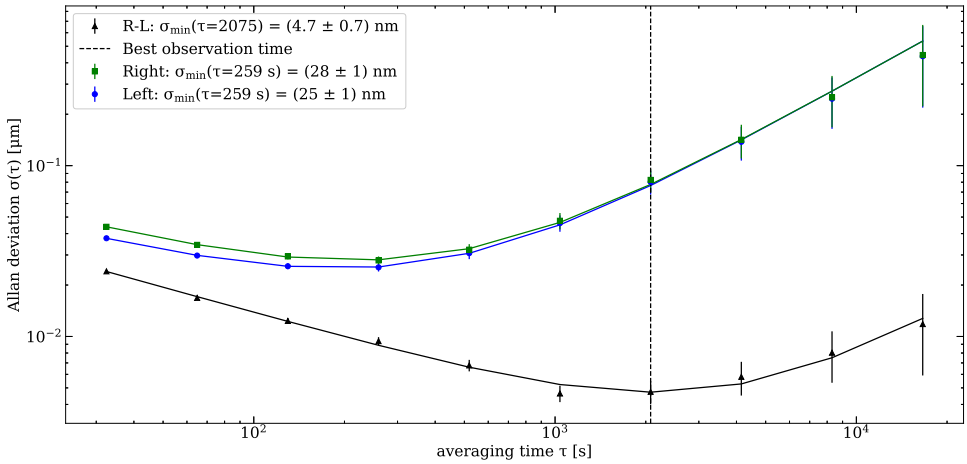

Figure 4.24. Allan deviation of the beam spot positions and the position difference, demonstrating the stability and sensitivity of the setup. The minimum Allan deviation occurs at $\tau_{R-L} = 2075\,\mathrm{s}$ and is equal to (4.7 ± 0.7) nm (dashed black line), indicating the optimal observation time.

4.4.6 Asymmetric Setup

Up to this point, the setup characterized in a ballistic configuration utilized gratings with a period of $p = 250\,\mu\mathrm{m}$ and varying duty cycles. In the previous sections, the gratings were positioned symmetrically, with equal distances of $L_1 = L_2 = L_G = 2.75\,\mathrm{m}$ between G_0, G_1, and G_2. For the following analysis, this symmetric configuration, with all gratings having a duty cycle of $R_0 = R_1 = R_2 = 20\%$, serves as the reference. This setup was identified as optimum for symmetric conditions and will be compared against an asymmetric configuration ($L_1 \neq L_2$) using Monte-Carlo simulations.

The motivation for investigating an asymmetric setup arises from the potential to enhance sensitivity in measuring neutron beam deflections caused by an external electric field applied between G_1 and G_2. By reducing the distance between G_0 and G_1, the interaction length between G_1 and G_2 is increased, which should improve sensitivity. In the asymmetric configuration, the distance between G_0 and G_1 is shortened to $L_1 = 1.83\,\mathrm{m}$, while the distance between G_1 and G_2 is extended to $L_2 = 3.67\,\mathrm{m}$. Additionally, the period of G_0 is halved to $p_0 = 125\,\mu\mathrm{m}$, with duty

cycles modified to $R_0 = R_2 = 40\%$ and $R_1 = 10\%$. The periods of G_1 and G_2 remain at $p_1 = p_2 = 250\,\mu\text{m}$. These adjustments are expected to balance increased statistics from wider grating slits with reduced visibility due to the deviation from the ballistic regime.

Simulation Results

Using Eq. (4.1) introduced earlier, the Monte-Carlo simulations indicate that the asymmetric setup offers higher sensitivity than the symmetric one when considering the key parameters: visibility η, neutron counts at the working point N_w, and the interaction length L. To quantify this improvement, a figure of merit (FOM) F is computed, defined as:

$$F = \frac{1}{L^2 \cdot \eta \cdot \sqrt{N_w}} \tag{4.6}$$

The sensitivity improvement is expressed by the ratio $R_F = F^{sym}/F^{asym}$, which compares the FOM of the symmetric and asymmetric setups. A value $R_F > 1$ confirms that the asymmetric setup provides better sensitivity.

The simulations yield $R_F = 2.14$, indicating a significant improvement in sensitivity with the asymmetric configuration. This enhancement results from the combination of increased collimation for better visibility, higher neutron counts due to larger grating slits at G_0 and G_2, and an extended interaction length, which increases from $L = 2.5\,\text{m}$ in the symmetric case to $L = 3.5\,\text{m}$ in the asymmetric setup. Figure 4.25 shows the interference pattern obtained from the Monte-Carlo simulation, highlighting the improved performance.

On the left plot in Fig. 4.25, a top view of the apparatus is shown, depicting all the simulated neutron ballistic trajectories. The beam travels from left to right and reaches the detector at the green vertical line on the right of the plot. The right plot shows the corresponding oscillating intensity pattern when G_2 is scanned (green), along with the intensity modulation from the best symmetric setup (black).

It should be noted that the horizontal axis of the left plot does not start at $x = 0$ m, as the simulation accounts for the length of the neutron guide preceding the beam line. This inclusion is crucial for accurately modeling the beam divergence, which is approximately 1 cm per 1 m. By incorporating the neutron guide, the simulation

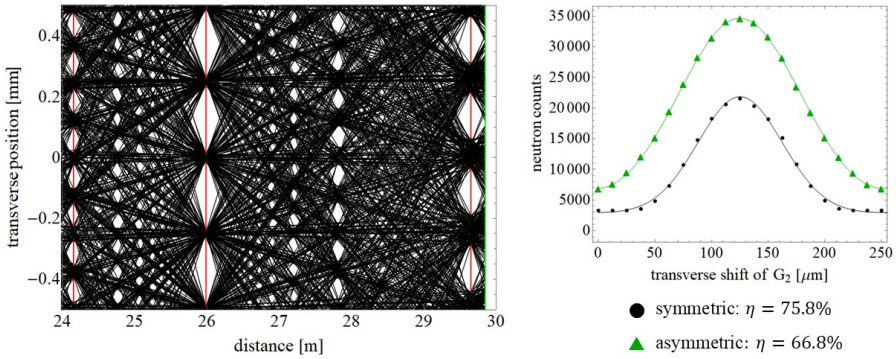

Figure 4.25. Left: Pattern obtained with the Monte-Carlo simulation with the asymmetric setup when $G_0 = 125\,\mu\text{m}/40\%$, $G_1 = 250\,\mu\text{m}/10\%$ and $G_2 = 250\,\mu\text{m}/40\%$ with an initial number of neutrons of 500 k. A similar diamond pattern as for the symmetric setup is visible due to the collimating role of the gratings. Right: Intensity modulations obtained for both the symmetric (black circle) and asymmetric setup (green triangle) with the corresponding computed visibilities. The symmetric setup has three gratings with $p = 250\,\mu\text{m}$ and $R = 20\%$.

realistically captures the divergence effects that influence the collimation of the beam and, consequently, the intensity modulation at the detector.

Experimental Results

New gratings were manufactured to implement this simulated concept and verify once again the validity of the simulation. The experimental comparison is made between the standard symmetric setup and the newly produced asymmetric setup. For both configurations, the gratings have a gadolinium thickness $t_{Gd} = 20\,\mu\text{m}$. The measured oscillating intensity patterns for both configurations are presented in Fig. 4.26 as well as the corresponding plots of the visibility as a function of the neutron wavelength.

As shown in Fig. 4.26, the asymmetric setup exhibits a distinct intensity pattern and altered visibility characteristics compared to the symmetric setup. Specifically, the visibility is lower in the asymmetric configuration (75% at the maximum compared to 92% for the symmetric setup), which can be attributed to the increased distance between G_1 and G_2. Although the setup remains within the ballistic regime, the longer

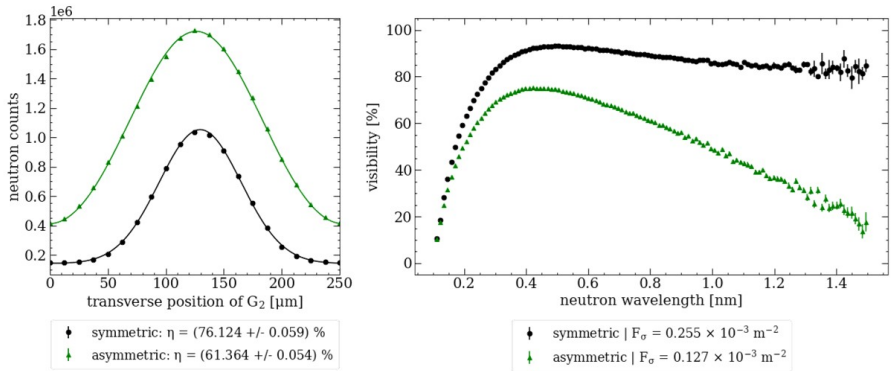

Figure 4.26. Left: Oscillating intensity pattern measured for both the symmetric (black circles) and asymmetric (green triangles) setup. The corresponding visibilities are computed *via* a Gaussian fit and displayed on the plot showing a good agreement with the simulated patterns in Fig. 4.25. Right: Visibility as a function of the neutron wavelength for both setups. A lower visibility is measured with the asymmetric arrangement due to a longer distance between G_1 and G_2. However, the gain of statistics due to higher duty cycles offers in the end a better sensitivity with the asymmetric configuration.

distance brings it closer to the Talbot length, reducing the contrast of the interference fringes. On the other hand, the intensity of the modulation is increased by a factor 1.64 in the asymmetric setup due to the larger duty cycles at G_0 and G_2.

The FOMs of the two configurations are presented in the legend on the plot, with the ratio between them calculated as $R_F = 2.01$, which is in good agreement with the simulated value of $R_F = 2.14$. The slight decrease in this performance factor can be attributed to experimental factors such as small inaccuracies in the distances between the gratings, beam divergence not perfectly implemented in the simulation, or the absorption properties of the gratings.

Discussion

The simulations and experimental results confirm that the asymmetric setup is more sensitive for measuring beam deflection when the electric field is only applied between the second and third gratings. Future work should investigate the potential

for deflection measurements also between G_0 and G_1. If feasible, the symmetric setup may still offer superior sensitivity due to higher visibility. The Monte-Carlo simulation proved again its reliability in terms of predictions for potential future setup designs and for optimization ideas between two measurement campaigns.

Moreover, the observed decrease in visibility with increasing grating distance highlights the importance of maintaining a ballistic configuration for optimal performance. The next section will focus on the effects on the capabilities of the setup when the distance between the gratings is still smaller but becomes comparable to the Talbot length L_T.

4.4.7 Ballistic-to-Diffraction Transition

In the previous section, it has been demonstrated that an asymmetric configuration of the instrument, both through Monte Carlo simulations and experimental measurements, is more sensitive to beam deflection measurements compared to a symmetric setup if the interaction zone is only situated between G_1 and G_2. However, the visibility of the modulation is reduced in the asymmetric setup. This loss in visibility is expected, as the increased distance between the second and third gratings makes the setup "less ballistic" and more susceptible to diffraction effects, approaching the real Talbot-Lau case.

The measurement presented in this section aims to investigate the relationship between visibility and the grating distance L_G, specifically how different percentages of the Talbot length L_T affect the visibility. To explore this, gratings with $p = 125\,\mu\text{m}$, $R = 20\%$ and $t_{Gd} = 20\,\mu\text{m}$ were installed. This choice allows for a wider range of the ratio L_G/L_T, providing greater flexibility in reaching different percentages of the Talbot length. Intensity modulations were recorded for three different distances L_G, and the corresponding visibility was computed from the Gaussian fit.

Using time-of-flight measurements, the visibility of the setup was evaluated as a function of the percentage of the Talbot length, ranging from approximately 2% to 15%.

Grating Distances Variations

The Talbot length L_T for a neutron wavelength λ and grating period p is given by $L_T = \frac{p^2}{\lambda}$ (Sec. 1.3.2). For gratings with a period of $p = 125\,\mu\text{m}$, the Talbot length for the average neutron wavelength $\lambda = 0.47\,\text{nm}$ is calculated as $L_T = \frac{p^2}{\lambda} \approx 33.2\,\text{m}$.

Based on this Talbot length, the three tested distances L_G between the gratings correspond to the following percentages of L_T:

- $L_G = 0.69\,\text{m}$: 2.0% of L_T
- $L_G = 1.72\,\text{m}$: 5.2% of L_T
- $L_G = 2.75\,\text{m}$: 8.3% of L_T

Taking into account the polychromaticity of the spectrum with the TOF measurement, it is possible to access other percentages of the Talbot length by considering other neutron velocities. The visibility as a function of the neutron wavelength is plotted on the left of Fig. 4.27 for all three distances with the previously described bootstrap algorithm employing Gaussian fit (Sec. 2.2.2). The x-axis of this first plot is then rescaled to account for the effective percentage of the Talbot length for the distance L_G and the wavelength considered, allowing for the creation of the right plot using the following conversion:

$$\lambda \longrightarrow \frac{L}{L_T} = \frac{L\lambda}{p^2} \tag{4.7}$$

It is now possible to represent all three measurements in the same plot with an adjusted horizontal axis. The corresponding results are shown in Fig. 4.27.

In the right plot, the visibility is plotted as a function of the effective percentage of the Talbot length (L_G/L_T). For $L_G/L_T < 10\%$ (black dashed line), the visibility remains above 80%, with only a slight decrease. However, beyond this point, the visibility declines more rapidly by roughly 10% for each additional 1% increase in L_G/L_T. This behavior is consistent with the limits of a purely ballistic setup, and can easily be explained with geometrical arguments when considering the diffraction on a single slit presented in Fig. 4.28.

It has been established that if the distance between the gratings exceeds $R/2 \cdot L_T$, the setup no longer operates in a purely ballistic configuration. This occurs because adjacent slits begin to get illuminated. In the presented measurement, a change in the slope of the visibility is observed at around 10% of the effective Talbot length. This result aligns well with the prediction, as the duty cycle of the gratings for this measurement was $R = 20\%$.

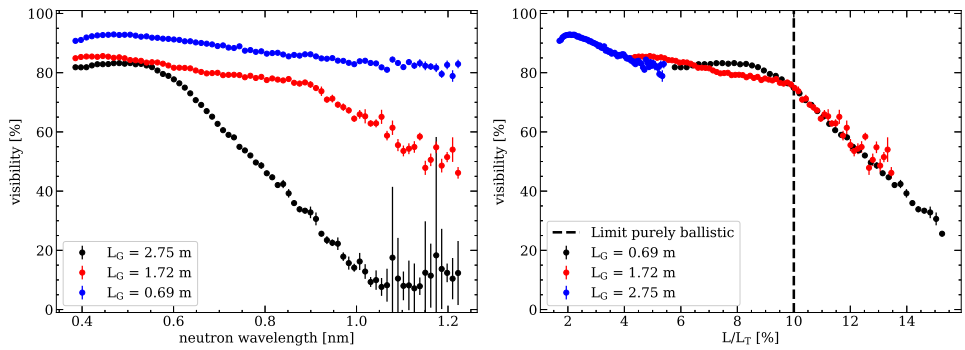

Figure 4.27. Left: Visibility as a function function of the neutron wavelength for gratings with $p = 125\,\mu\text{m}$ and $R = 20\%$ at three different distances L_G. Right: Corresponding plot with x-axis being rescaled to display the percentage of the Talbot length of the corresponding wavelength and distance L_G.

Discussion

The experiments confirm that the visibility of the neutron grating interferometer decreases linearly with increasing percentages of the Talbot length, with a notable change in slope occurring around 10% of L_T. This behavior marks the transition from a purely ballistic regime to one influenced by diffraction effects.

These findings indicate that the grating distance L_G can be increased slightly while remaining in the ballistic regime. This adjustment could enhance sensitivity by extending the interaction length without significantly compromising visibility. For the current best symmetric setup ($p = 250\,\mu\text{m}$, $\lambda = 0.47\,\text{nm}$), where $L_G = 2.75\,\text{m}$ corresponds to only 2% of L_T, there is considerable potential to increase L_G while maintaining close to optimum performance.

This insight provides a pathway for improving the design of the instrument, particularly in experiments requiring longer interaction lengths, such as the measurement of the neutron electric charge.

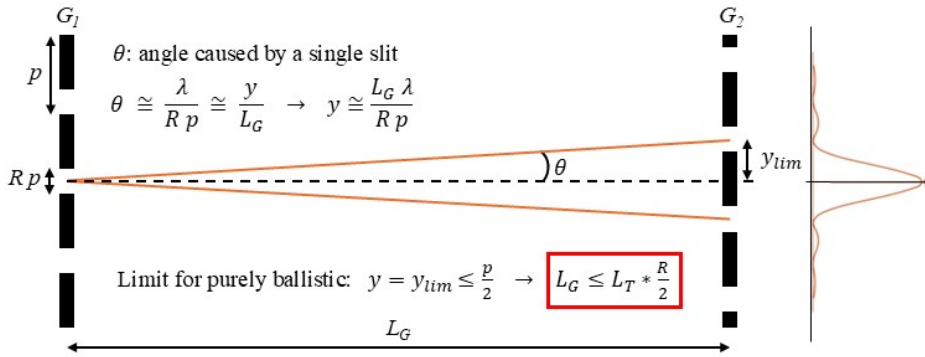

Figure 4.28. Schematics of the setup at the limit between a purely ballistic case and a regime where diffraction effects need to be taken into account. The orange lines represent the first-order minima of the intensity pattern. One can compute the condition for leaving a purely geometric regime, i.e. when the central peak of the intensity pattern starts illuminating two adjacent slits at G_2. In this case where $p = 125\,\mu\text{m}$ and $R = 20\%$, this transition happens when $L_G = 0.1 \cdot L_T = 3.32\,\text{m}$.

4.5 Diffraction Configuration

In this section, the diffraction regime is explored where the distance between the gratings corresponds to multiples of the Talbot length L_T. In this regime, the wave properties of the neutron as a quantum particle result in interferometric phenomena. The corresponding theoretical description of Talbot-Lau interferometry being given in Chap. 1; this section focuses on the experimental results and comparisons made with simulations, not on the phenomenology itself. In the ballistic regime, a wide range of neutron wavelengths enhances contrast. In the diffraction regime, however, only specific wavelengths produce high-visibility interference patterns. This distinction will be explored in the following sections.

4.5.1 Experimental Setup

The experiment was conducted with TOF measurements and neutron gratings with $p = 25\,\mu\text{m}$ and $R = 20\%$. The distance between the gratings was $L_G = 2.75\,\text{m}$,

corresponding to a Talbot wavelength of $\lambda_T = \frac{p^2}{L_G} = 0.227\,\text{nm}$. A Talbot carpet forms, effectively creating a self-image of the diffraction grating G_1 at the position of the analyzer grating G_2 for this wavelength. In total, three setups were characterized with different combinations of gadolinium thicknesses.

In the previous chapter (Sec. 3.7), gratings with $t_{Gd} = 30\,\mu\text{m}$ exhibited unexpected behavior. The visibility of interference patterns decreased at higher wavelengths, despite the increased absorption of the thicker gadolinium layer, which should theoretically reduce background and improve the signal-to-noise ratio. This discrepancy pointed to potential issues in the manufacturing process. Specifically, the gratings of this set were produced using a laser with a smaller beam spot, which likely caused submicrometer-sized ablation structures on the substrate. These fine structures probably lead to neutron small angle scattering and, consequently, reduced visibility.

Further investigations in the ballistic regime with a new set of gratings demonstrated significant improvements (Sec. 4.4.2). For this set, a different laser with a larger beam spot was used, reducing the likelihood of small-scale ablation structures. As a result, the scattering effects were minimized, or at least occurred under smaller scattering angles, leading to enhanced visibility.

Unfortunately, these improved gratings were not yet available for the diffraction measurements discussed here. Therefore, the measurements in this section were conducted with the earlier set, which exhibited the manufacturing defects described above.

Keeping in mind that G_1 is responsible for generating the interference pattern, the three following combinations were tested:

- 1. All gratings with $t_{Gd} = 20\,\mu\text{m}$.
- 2. All gratings with $t_{Gd} = 30\,\mu\text{m}$ (first set).
- 3. Mixed: G_0 and G_2 with $t_{Gd} = 30\,\mu\text{m}$ (first set), G_1 with $t_{Gd} = 20\,\mu\text{m}$.

Following optical alignment, vacuum pipes were installed between the gratings and pumped down to a pressure of 1×10^{-2} mbar to reduce neutron absorption in air. The finer alignment of the gratings with the neutron beam was then carefully conducted using the chopper to produce neutron pulses with a frequency of 25 Hz, allowing for a focus on the wavelengths of interest during the analysis (Talbot wavelength $\lambda_T = 0.227\,\text{nm}$ and higher multiples).

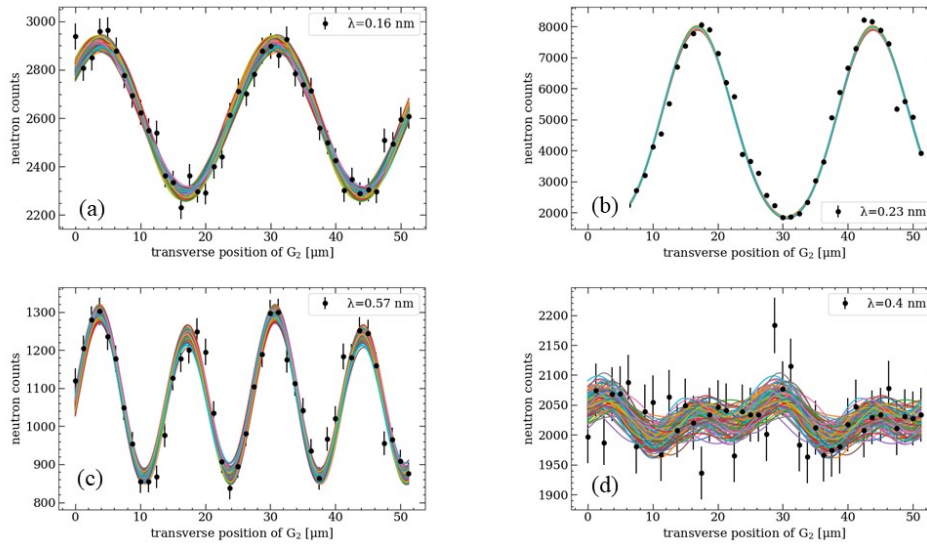

Figure 4.29. Examples of oscillating intensity patterns at four different wavelengths. The solid lines represent the multiple fits from the bootstrap algorithm. (a) showing the effects of the transmission through gadolinium shifting the signal by half a period ($\lambda_T \cdot 0.7$), (b) for first order wavelengths (λ_T) with high visibility, (c) at half-integer multiple ($2.5\lambda_T$) with significantly high visibility and halved period, (d) at a random wavelength (e.g., $1.8\lambda_T$) with low visibility and no modulation.

4.5.2 Interference Patterns

To analyze the neutron interference patterns, transverse scans with G_2 were recorded and, for each wavelength, fitted using the bootstrap method with 100 generated data sets (Sec. 2.2.1). Each data point was recorded for 80 s (2000 chopper sweeps at 25 Hz). Equation (2.4) was used as the fitting function, consisting of a sum of two sine waves with periods p_1 and $p_2 = \frac{p_1}{2}$. This approach accurately captures the complex oscillation patterns and allows for the extraction of the corresponding visibilities. An example of the measured intensity modulations fitted with the bootstrap method is shown in Fig. 4.29 for four exemplary wavelengths.

In the diffractive regime, high visibility is expected at wavelengths corresponding to integer and half-integer multiples of the Talbot wavelength λ_T. This behavior was confirmed through simulations and measurements, showing visibility peaks reaching

90% at $\lambda_T = 0.227$ nm (top right plot in Fig. 4.29) and higher multiples such as $1.5\lambda_T$, $2\lambda_T$, and $2.5\lambda_T$ (bottom left plot in Fig. 4.29).

However, unexpected intensity modulations were observed at certain wavelengths due to the residual transmission of gadolinium in the gratings (Sec. 4.3). One notable case occurs at $\lambda = 0.16$ nm, corresponding to $0.7\lambda_T$, where a shift of half a grating period was visible (top left plot in Fig. 4.29). This wavelength does not correspond to any specific Talbot order and would otherwise not appear in a perfect, fully absorbing grating.

To understand this behavior, modifications were introduced in the simulation to account for the residual transmission through the gadolinium layers (App. A), which were crucial for accurately reproducing the experimental data. The simulations revealed that the observed shift in intensity modulation in fact originates from the partial transmission of the gratings, enabling interference effects at non-Talbot wavelengths. By incorporating these transmission effects, the simulations closely matched the experimental results, highlighting the impact of imperfect grating absorption on the visibility of the interference patterns.

4.5.3 Data and Simulation: Comparisons

To visualize the results and allow for an easier comparison with the simulations, a Talbot-Lau carpet was generated for each of the three grating combinations. This carpet is a 2D density plot where the horizontal axis represents the transverse position of G_2 during a scan, the vertical axis represents the neutron wavelength, and the color scale indicates the intensity normalized to its maximum value (neutron counts for the data and arbitrary units for the simulation). For the simulation, the intensity of the measured TOF spectrum is used as a weighting factor for better comparisons. This carpet is a useful tool to illustrate the periodicity and intensity variations in the interference patterns, making it easier to identify which wavelengths contribute most significantly to the visibility. From the experimental data, the Talbot-Lau carpets for each setup were compared with the simulated carpets. As expected, high visibility peaks appear at the Talbot wavelength $\lambda_T = 0.227$ nm and its multiples. In Fig. 4.30, the results from the simulations (left) and the experimental data (right) are presented for the mixed setup (G_0 and G_2 with $t_{Gd} = 30\,\mu$m, G_1 with $t_{Gd} = 20\,\mu$m), producing the best overall results.

This setup mitigated the unexpected lower visibility at higher wavelengths observed with the pure $t_{Gd} = 30\,\mu$m configuration, likely due to the combined effects of optimal

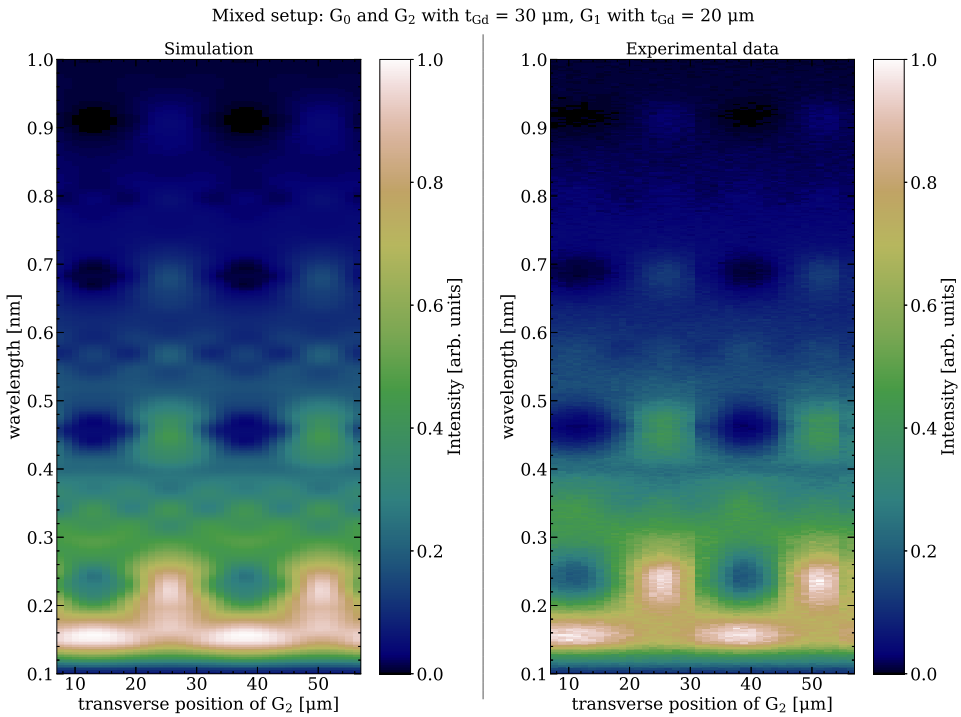

Figure 4.30. 2D density plot (Talbot carpet) showing the neutron intensity as a function of transverse position and neutron wavelength.

absorption and reduced background counts. Similar plots for the two other setups and further analysis and comparisons concerning the oscillating intensity pattern can be found in Appendix C.

Additionally, a plot of the visibility as a function of the neutron wavelength is shown in Fig. 4.31 with both the value of η computed for each wavelength for the simulation (red) and the experimental data (black).

4.5.4 Discussion

The diffraction configuration has been successfully operated, producing high-visibility interference patterns at the Talbot wavelength λ_T and its higher multiples and half-multiples. The experimental results align well with simulations, confirming the

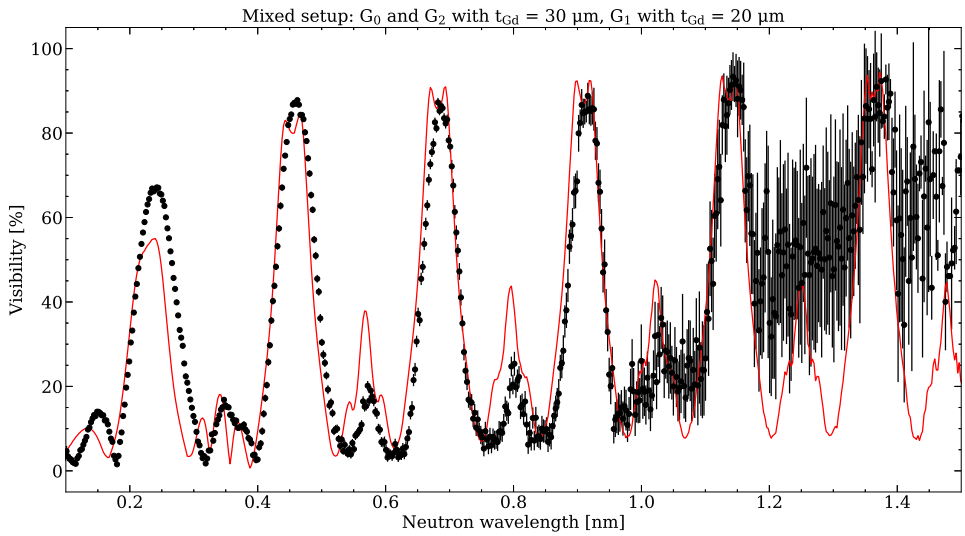

Figure 4.31. Visibility as a function of neutron wavelength extracted from the data (black) and the simulation (red), measured with the mixed setup where G_0 and G_2 have $t_{Gd} = 30\,\mu m$ and G_1 has $t_{Gd} = 20\,\mu m$. For each time bin, the visibility is extracted by evaluating the maximum and minimum of the intensity modulations with the bootstrap algorithm.

validity of the approach. However, the necessity of using a chopper to access time-of-flight measurements significantly reduces neutron intensity, limiting the available statistics.

Despite this drawback, the diffraction setup offers considerable potential for future experiments, particularly when used with a pulsed source and extended interaction lengths. The European Spallation Source (ESS) in Lund, Sweden, which will be the next major neutron facility, would be an ideal location for installing this setup, given its high flux and advanced capabilities.

However, for the current setup at PF1B, the ballistic configuration remains more practical due to the continuous nature of the source and spatial constraints at the beam line. The increased susceptibility of the diffraction regime to instabilities and drifts, due to the smaller grating periods, potentially complicates its use in measurements where long-term stability is required.

4.6 Summary

This chapter presents the detailed investigation of the QNeutron apparatus conducted at the PF1B beam line at ILL, focusing on both ballistic and diffraction configurations to determine the optimal conditions for a neutron electric charge measurement.

Ballistic Configuration: The ballistic setup characterized by gratings with $p = 250\,\mu\text{m}$, $R = 20\%$ and $t_{Gd} = 30\,\mu\text{m}$ was found to offer the best balance between high visibility and sufficient neutron statistics. With a grating distance $L_G = 2.75\,\text{m}$, the setup minimizes diffraction effects and maximizes the usable spectrum. This configuration is ideal for continuous neutron sources like PF1B, where high neutron flux is available within a limited experimental area.

Diffraction Configuration: The diffraction setup, with $p = 25\,\mu\text{m}$, $R = 20\%$ and a Talbot wavelength $\lambda_T = 0.227\,\text{nm}$, was evaluated for its potential to enhance measurement sensitivity. Although it achieves high visibility at specific wavelengths, the reduced neutron flux and selective wavelength usage presents challenges. This configuration shows potential for future applications where space permits extending the interaction length and where a pulsed neutron source allows precise wavelength selection *via* time-of-flight techniques.

Asymmetric Setup: An asymmetric configuration was also investigated, where the grating distances were varied to increase the interaction length between G_1 and G_2. Both simulations and experimental data indicated that this setup could improve sensitivity to beam deflection. Despite a reduction in visibility, the increased interaction length and neutron statistics offers a significant sensitivity improvement.

Key Findings and Conclusions: The chapter emphasizes the importance of carefully balancing grating design, distance, and configuration based on the specific constraints of the experimental setup and neutron source. For the PF1B beam line at ILL, where space is limited and the neutron source is continuous, the ballistic configuration was identified as the most suitable for a high-precision neutron electric charge measurement. The findings provide a strong foundation for the upcoming chapter, where the inaugural neutron charge measurement performed with the QNeutron apparatus is presented.

5. Neutron Electric Charge Measurement

In Chapter 1, the fundamental principles of a non-zero neutron electric charge, neutron production, applications, and neutron interferometry were introduced. Chapter 2 provided a detailed overview of the QNeutron apparatus, followed by its systematic optimization during multiple beam times at PSI (Chap. 3) and ILL (Chap. 4).

Through these extensive experimental campaigns, the setup was continuously refined, culminating in a highly optimized configuration for the neutron electric charge measurement. Key parameters such as grating geometry, absorber properties, and beam line configuration were fine-tuned to maximize sensitivity and stability. This chapter focuses on the charge measurement campaign conducted at ILL, exploiting the optimized setup to perform high-precision measurements at the PF1B beam line.

5.1 Experimental Setup

Given that PF1B is a 10 m beam line at one of the most intense cold neutron sources in the world, the charge measurement was conducted in ballistic regime combined with the two-beam method. Consequently and as described in the next sections, the chopper was removed, vacuum pipes containing the electrodes installed on the setup and extensive shielding of concrete and lead was added around the experiment. This shielding mitigates gamma emission from the absorbed neutrons in the gadolinium of the gratings.

The setup sketched below (without vacuum pipes and ground electrodes for clarity) involves a symmetric configuration with the following parameters:

- **Grating period:** p = 250 µm for purely ballistic regime
- **Duty cycle:** R = 20% for best compromise between visibility and statistics (Sec. 4.4.1)
- **Gd-thickness:** t_{Gd} = 30 µm for better visibility at lower wavelengths (Sec. 4.4.2)
- **Distance between the gratings:** L_G = 2.75 m

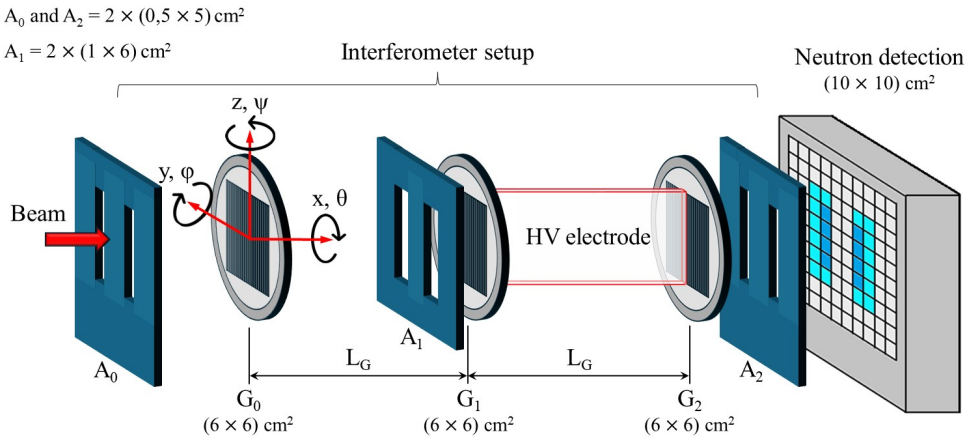

Figure 5.1. Scheme of the apparatus for the electric charge measurement. Neutrons are traveling from left to right, enter A_0 and are defined in two beam spots, pass through G_0 and G_1 and sense an electric field between G_1 and G_2 before reaching the detector. The center-to-center distance between the two beam spots is equal to 35 mm. On this representation, the two ground electrodes surrounding the high-voltage electrode, as well as the vacuum pipes, are not depicted for clarity.

- **Electric field:** $E = 23.33$ kV/cm applied in opposite directions across the two beam spots, with the ability to reverse polarity within the 1.5 cm electrode gaps.
- **Interaction distance (electrode length):** $L = 2.5$ m
- **Neutron count rate** $\dot{N}_w = 3.85 \times 10^5\,\mathrm{s}^{-1}$ at the working point w_p for each beam spot after removing the chopper, requiring additional shielding measures detailed further.

Additionally, an image of this setup operating for the charge measurement is shown in Fig. 5.2. This top-view of the apparatus was taken before installing the radiation and thermal shielding around the experiment. The main components and the beam direction are indicated on the figure.

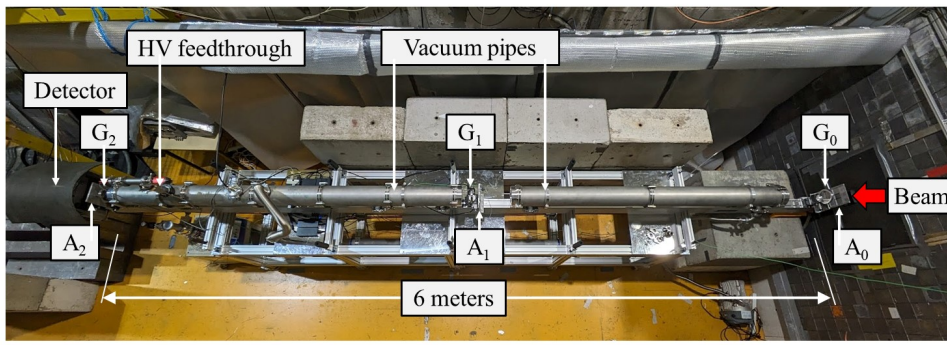

Figure 5.2. Top view of the experimental apparatus employed for the neutron electric charge measurement. The setup is installed at the PF1B beam line at ILL. The neutron beam is coming from right to left through the instrument.

5.1.1 Beam Line Spectrum and Shielding

Figure 5.3 shows the time-of-flight spectrum measured under two conditions: in open beam configuration (no gratings, red) and at the working point w_p of the setup used for the charge measurement (black). The latter includes the two-beam configuration, vacuum pipes with 0.5 mm-thick aluminum windows, and high-voltage electrodes described below. The plotted intensities are therefore the sum over the two beam spots.

After the characterization of the neutron spectrum with the setup for the electric charge measurement, the chopper was remove from the casemate to increase statistics using a white beam. This led to an increase in gamma radiation due to neutron absorption by the gadolinium gratings. To mitigate the radiations, extensive shielding was implemented around the setup. Concrete blocks (30 cm-thick) and lead bricks (10 cm-thick) were installed to reduce radiation levels. Additionally, an integral thermal shield made of temperature-protective foil [158] was added to stabilize conditions and minimize temperature fluctuations during measurements. The temperature stability achieved under these conditions is discussed in Sec. 4.1.4. Images of the setup with radiation (left) and thermal (right) shielding are shown in Fig. 5.4.

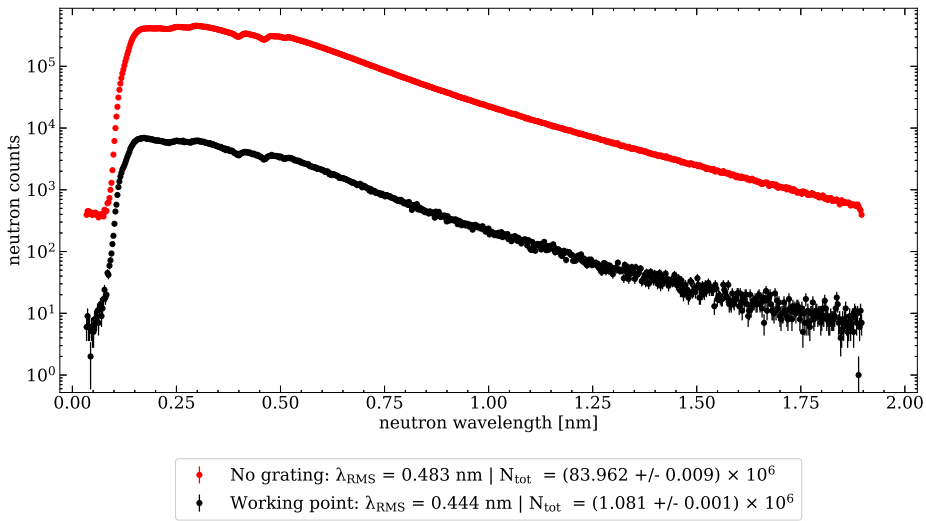

Figure 5.3. Time-of-flight spectrum at the working point of the setup used for the charge measurement (black), showing the weighted RMS wavelength $\lambda_{RMS} = 0.444\,\text{nm}$, compared with the open beam measurement (red) with $\lambda_{RMS} = 0.483\,\text{nm}$. Both measurements were taken during 5 min with a neutron pulse repetition frequency of 25 Hz (7500 chopper pulses) and time bins size of 50 µs (0.024 nm). The chopper-to-detector distance was 8.28 m for both measurements. When the three gratings are installed and G_2 set at w_p, the flux is reduced by a factor of approximately 80 compared to the situation without gratings.

5.1.2 High-Voltage Components

Stainless steel vacuum pipes, each 2.6 m long with an inner diameter of 150 mm and 0.5 mm-thick aluminum windows, were installed between G_0 and G_1, as well as between G_1 and G_2 to enable the application of the electric field using the two-beam method. To produce two distinct beam spots, the 3 mm-thick BorAl apertures A_0 and A_2 (at each end of the beam line) were arranged in two separate rectangles measuring each 50×5 cm^2 and separated by 35 mm center-to-center. An additional aperture A_1 of 60×10 cm^2 was placed just before G_1 to prevent cross-talk and ensure complete separation between the two beams. The effectiveness of this separation was tested by alternately blocking each beam spot with a stack of 5 cm-thick BorAl plates immediately after A_0 and measuring neutron counts at the detector over 5 min. The

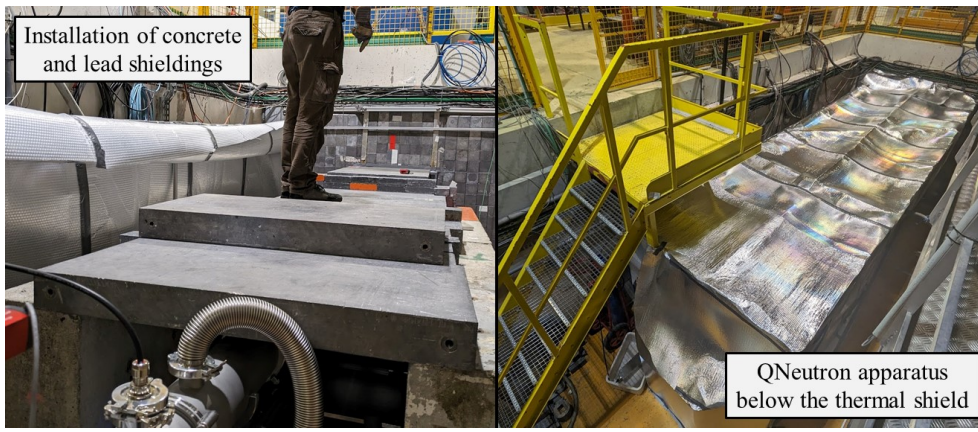

Figure 5.4. Photographs of the experimental setup at PF1B at the ILL, showing the extensive radio protection shielding implemented around the setup, including concrete blocks and lead bricks, as well as the integral thermal shield consisting of temperature-protective foil surrounding the apparatus.

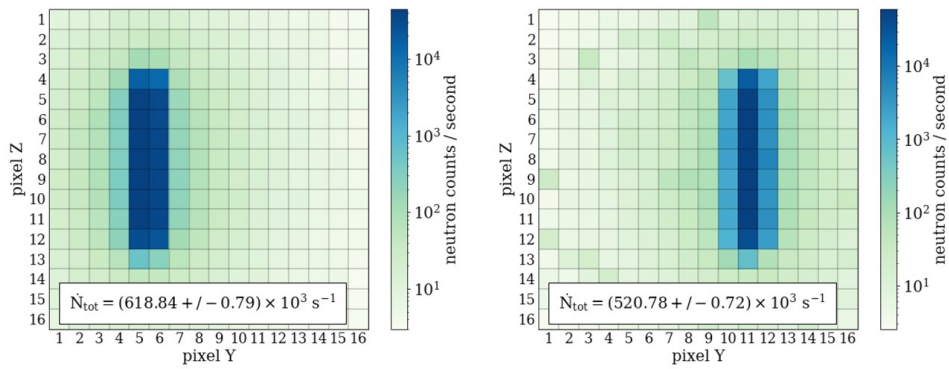

Figure 5.5. Recorded neutron flux of each beam spot at the brightest point of the intensity modulation for the electric charge measurement setup, measured over 5 min. The absence of cross-talk ensures effective separation of the two beams.

results, shown in Fig. 5.5, confirm that cross-talk between the beam spots is negligible, as the blocked beam spot recorded a maximum of only 3 counts per second on average.

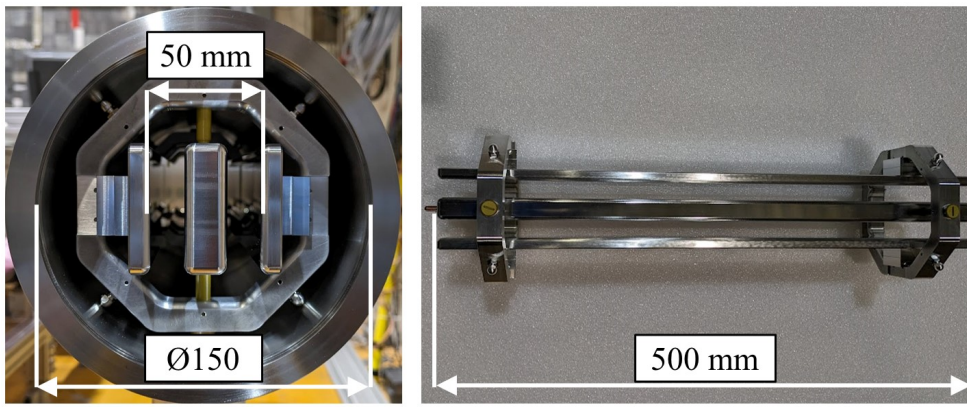

Figure 5.6. Left: Electrode stack installed in the 150 mm-diameter vacuum pipe, showing the high-voltage electrode centered between two ground electrodes. Right: A single 500 mm-long stack outside the vacuum pipe. The HV electrode is 60 mm wide and 20 mm thick, while the ground electrodes are 60 mm wide and 10 mm thick, all with a corner radius of 5 mm. The gap between the electrodes is 1.5 cm. The center-to-center distance of the two beam spots is 35 mm.

The electrode system consists of five electrode stacks, each 50 cm long, with a high-voltage (HV) electrode centered between two ground electrodes. Within each stack, the HV electrode measures 60 mm in width (z-axis) and 20 mm in thickness, while the ground electrodes are also 60 mm wide but 10 mm thick. All electrodes have a corner radius of 5 mm. These stacks are interconnected with copper pins and positioned inside the vacuum pipes between G_1 and G_2, allowing the electric field to be applied in alternating directions over a total interaction distance of $L = 2.5$ m. Figure 5.6 illustrates the electrode stack configuration, both inside and outside the vacuum pipe.

Each beam spot measures 5 cm in height, 0.5 cm in width, with a center-to-center spacing of 3.5 cm. The 1.5 cm gap between the electrodes ensures that the totality of the defined beam passes through the interaction zone. After connecting and aligning the electrodes, a vacuum feedthrough was mounted on the central electrode stack. The system was initially pumped with a scroll pump, followed by a turbopump to achieve a vacuum of 1×10^{-5} mbar. To the high-voltage electrode a 35 kV were applied, with repeated polarity reversals. To minimize systematic effects, a specific polarity sequence was employed: $(+, -, -, +, -, +, +, -, 0)$. The sequence duration was designed to match the optimal observation time τ_{R-L}, as determined by the Allan

deviation analysis in Sec. 4.4.5. Additionally, each polarity within the sequence was held for a time no longer than τ_{temp}, the temperature stability limit of G_2 defined in Sec. 4.1.4. This setup minimizes the effects of mechanical drifts and temperature fluctuations, ensuring stable and consistent conditions throughout the neutron electric charge measurement process.

5.2 Measurement Procedure and Analysis

The measurement process for determining the neutron electric charge involves several distinct phases, each defined by specific terms used consistently throughout this chapter:

- **Run:** A single data acquisition lasting 20 s at a fixed high-voltage polarity
- **Sequence:** A complete set of polarity inversions following the predefined scheme: $+, -, -, +, -, +, +, -, 0$. The sequence duration is designed to be shorter than the optimal observation time $\tau_{R-L} = 2070$ s, as determined in Sec. 4.4.5
- **Cycle:** A continuous repetition of sequences over an extended period, typically 24 h, providing a comprehensive dataset for analysis

Six cycles were conducted, testing two distinct measurement methods: **Single-Point** (cycles 1 to 5) and **Multi-Point** (cycle 6). Each cycle started with a preliminary scan to locate the working point of the instrument.

5.2.1 Preliminary Scan and Working Point Identification

Before initiating each cycle, a preliminary scan of G_2 is performed to locate the working point w_p, where sensitivity to beam deflection is maximized. This scan spans one full grating period of 250 µm, consisting of 41 data points spaced by 6.25 µm, with each point recorded for 20 s.

An example scan is shown in Fig. 5.7, where the intensity modulation for the left and right beam spots is fitted with a Gaussian. The steepest slope of the modulation, marked by the dashed line, defines w_p.

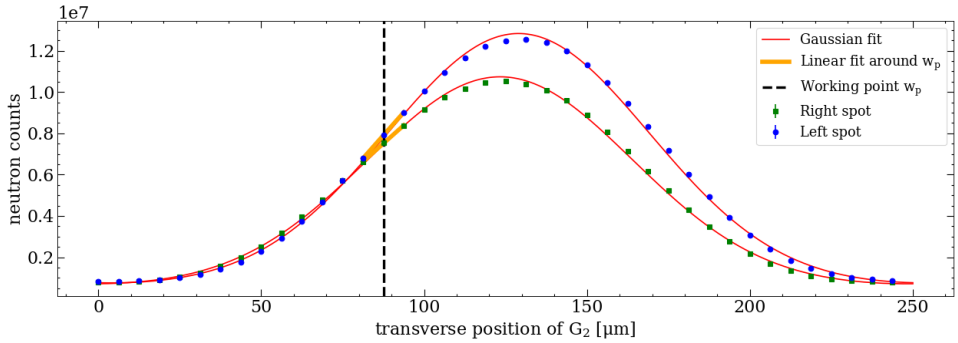

Figure 5.7. Example of intensity modulation recorded for the left (blue) and right (green) beam spots. Each data point represents 20 s of data acquisition. The Gaussian fit (red) identifies the working point w_p at the steepest slope (black dashed line).

5.2.2 Single-Point Mode

In the **Single-Point Mode**, data are collected by fixing G_2 at w_p and recording neutron counts at each polarity over several sequences. For each polarity, 10 consecutive runs (20 s each) are collected, and neutron counts at the working point of each beam spot, N_L and N_R, are extracted. The polarity is then changed according to the HV sequence, and another series of runs is recorded.

Within a sequence, the double ratio $\mathcal{R}$ is calculated for each pair of runs with opposite and adjacent polarities. Specifically, for each polarity inversion, the first run at positive polarity is paired with the first run at negative polarity, the second run with the second, and so on:

$$\mathcal{R} = \frac{(N_L/N_R)^+}{(N_L/N_R)^-} \tag{5.1}$$

This ratio mitigates systematic effects such as mechanical drifts of the setup. Each sequence, following the predefined scheme (+,-,-,+,-,+,+,-,0), includes 4 polarity inversions, resulting in 40 values of the double ratio per sequence. Note, cycles 1 to 4 employed 10 runs per polarity, while cycle 5 acquired only 5 runs (20 s) per polarity.

Figure 5.8 presents the double ratio values $\mathcal{R}$ collected during cycle 1. In total, 2400 runs were performed over 30 sequences, representing a total measurement time

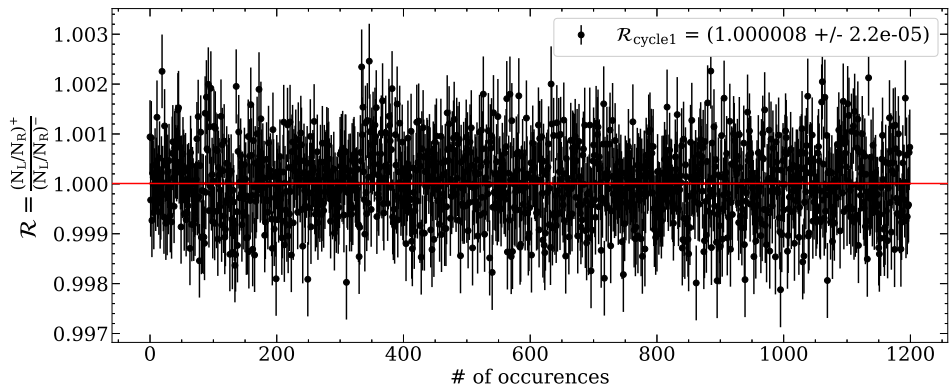

Figure 5.8. Measured double ratios $\mathcal{R}$ for Cycle 1 in single-point mode. The horizontal constant fit provides the weighted mean value of $\mathcal{R}$, which is then converted to the beam deflection Δy.

of 23.55 h with a dead time of 43.4% (13.33 h of effective measurement time). A horizontal constant fit provides the weighted mean value of $\mathcal{R}$. This value is then converted into the beam deflection Δy using a conversion factor obtained through simulation by applying a transverse shift to the preliminary scan and calculating its impact on $\mathcal{R}$. Figure 5.9 illustrates this process for cycle 1, during which a deflection of the neutron beam $\Delta y = (0.093 \pm 0.246)$ nm has been measured. More details about the results from cycles 1 to 5 are given in Sec. 5.3.

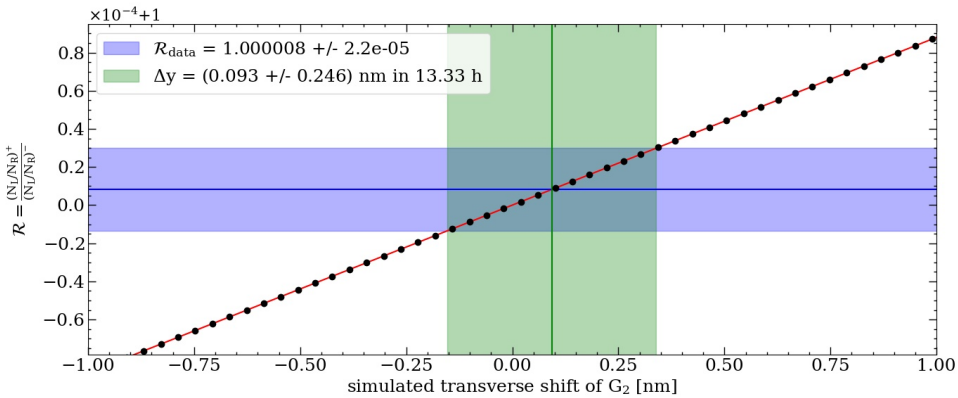

Figure 5.9. Conversion of the combined double ratio $\mathcal{R}$ (blue) to beam deflection Δy (green) by simulating a G_2 shift in the preliminary scans presented in Fig. 5.7 (red line).

5.2.3 Multi-Point Mode

The **Multi-Point Mode**, employed in cycle 6, collects runs at six selected points of the oscillating intensity pattern for each high-voltage polarity: three points centered on w_p on each side of the intensity modulation. These six points are chosen because they correspond to the regions of steepest slope, maximizing sensitivity to beam deflection. The limited number of points ensures that the sequence duration remains within the optimal observation time, τ_{R-L}, preventing systematic effects from long-term drifts.

A Gaussian fit to the preliminary scan provides the fixed parameters A, B, and σ. During the cycle, only the center μ is left as a free parameter in the fit, enabling precise determination of the beam spot position. Figure 5.10 shows an example scan and the resulting intensity modulations for the left and right beam spots, with their corresponding center values μ depicted by the dashed lines, and for both positive and negative polarity.

The deflection difference between the two beam spots, $\mathcal{D}$, is calculated as:

$$\mathcal{D} = (\mu_L - \mu_R)_+ - (\mu_L - \mu_R)_- \tag{5.2}$$

Here, $\mathcal{D}$ represents the combined deflection difference. It accounts for both deflection difference between the left and right beam spots, which introduces a factor of 2, and the

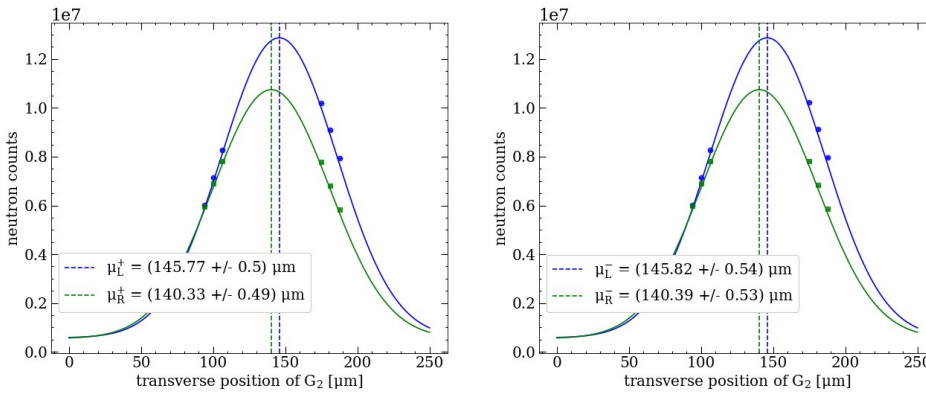

Figure 5.10. Scan with six points around the working point for left (blue) and right (green) beam spots, shown for both positive (left plot) and negative (right plot) polarities. Each data points is recorded over 20 s and a Gaussian fit allows for the extraction of the center values μ.

deflection difference under opposite polarity conditions, introducing another factor of 2. As a result, $\mathcal{D}$ is equal to four times the single-beam deflection Δy, which yields:

$$\Delta y = \frac{\mathcal{D}}{4} \tag{5.3}$$

In total, 74 sequences were recorded during cycle 6, representing 3552 runs of 20 s over approximately 19.73 h of data acquisition (total time of 39.55 h with a dead time of 50.2%) with 296 pairs of polarity (polarity inversions). The deflection results from these sequences are shown in Fig. 5.11 and more details are given in Sec. 5.3.

Unlike the single-point mode, where deflections were inferred via $\mathcal{R}$, the multi-point mode directly measures the Gaussian peak centers. This distinction allows further verification of consistency between the two methods. If both approaches are equally effective, the statistical sensitivity achieved should be comparable for similar measurement durations.

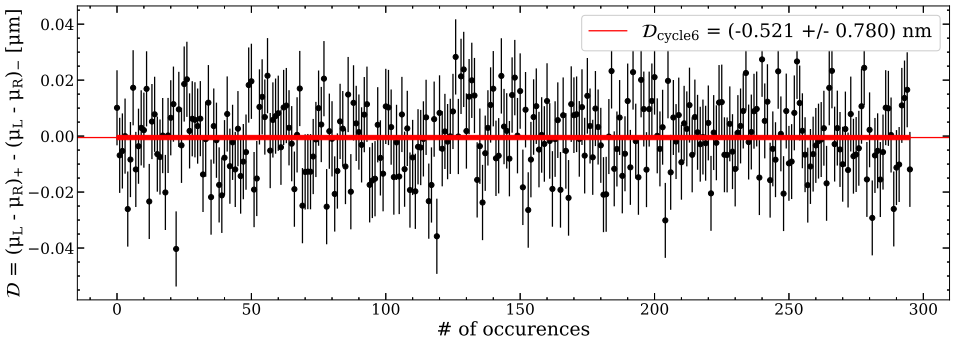

Figure 5.11. Multi-point method results from cycle 6, showing evaluation of $\mathcal{D}$ across 296 polarity inversions.

5.2.4 Conversion to the Neutron Electric Charge

The conversion to neutron charge relies on the fundamental principles of dynamics, considering the Lorentz force in an electrostatic framework and the ballistic deflection Δy of the beam:

$$\Delta y = \frac{Q_n \cdot E \cdot L^2}{2 \cdot m_n \cdot v^2} \tag{5.4}$$

By substituting the de Broglie wavelength $\lambda = \frac{h}{m_n \cdot v}$ into the equation, the expression becomes:

$$Q_n = \frac{2 \cdot h^2}{m_n \cdot E \cdot L^2 \cdot \lambda_{RMS}^2} \cdot \Delta y = P \cdot \Delta y \tag{5.5}$$

Here, P is the proportional constant that links the measured beam deflection Δy to the neutron electric charge Q_n. It encapsulates the influence of experimental parameters and is calculated as:

$$P = \frac{2 \cdot h^2}{m_n \cdot E \cdot L^2 \cdot \lambda_{RMS}^2} \tag{5.6}$$

For the parameters used in this experiment:

- **Electric field (E)**: 23.33 kV/cm
- **Neutron mass (m_n)**: 1.675×10^{-27} kg
- **Average wavelength (λ_{RMS})**: 0.446 nm
- **Planck constant (h)**: 6.626×10^{-34} J s
- **Interaction length (L)**: 2.5 m

the calculated proportional constant is:

$$P = 1.807 \times 10^{-28} \text{ As/m} = 1.128 \times 10^{-18} \text{ e/nm} \tag{5.7}$$

The evaluation of uncertainties associated with the determination of these parameters and their impact on the final results is discussed in the next section.

5.3 Results and Discussion

In this section, the results of the neutron electric charge measurements across the six different cycles are presented. Each cycle is characterized by the total number of runs, measurement time, and dead time. Equation (4.1) introduced in Sec. 4.4 is then used to compare the experimental values with theoretical expectations.

First, the statistical sensitivity of the instrument is extracted from the measurements. The measurement errors and systematic effects also affecting the final result are then estimated. The plots related to the double ratio and the conversion to a beam deflection are presented in App. D for each cycle.

5.3.1 Statistical Sensitivity

Table 5.1 summarizes the properties of each measurement cycle, including the employed methodology:

Cycle	Runs/Polarity	Total Runs	Effective Time	Dead Time
1	10×20 s at w_p	2400	13.33 h	43.4%
2	10×20 s at w_p	2240	12.48 h	43.2%
3	10×20 s at w_p	2320	12.88 h	43.5%
4	10×20 s at w_p	2160	12.0 h	51.5%
5	5×20 s at w_p	2400	13.36 h	45%
6	6×20 s around w_p	3552	19.7 h	50.2%

Table 5.1. Summary of the settings of the cycles and corresponding measurement time. The table shows the number of runs per polarity (not including runs of the sequences at zero voltage), the total number of runs, the total effective measurement time, and the dead time percentage for each cycle.

Using the parameters listed above, the value for the neutron electric charge Q_n and corresponding statistical uncertainty $\sigma_{stat}(Q_n)$ are determined from the measured deflections Δy for each cycle. The results are summarized in Table 5.2.

Cycle	$(\mathcal{R}-1)\times10^5$	Δy [nm]	$Q_n \times 10^{-19}$ [e]	Time [h]
1	0.8 ± 2.2	0.093 ± 0.246	1.05 ± 2.76	13.33
2	5.1 ± 2.3	0.534 ± 0.242	5.99 ± 2.72	12.48
3	-1.1 ± 2.1	-0.127 ± 0.246	-1.42 ± 2.76	12.88
4	1.8 ± 2.3	-0.188 ± 0.242	-2.11 ± 2.72	12.0
5	-1.2 ± 2.1	-0.125 ± 0.237	-1.40 ± 2.66	13.36
6	-	-0.13 ± 0.195	-1.46 ± 2.19	19.7

Table 5.2. Summary of the results from cycles 1 to 6. The table shows the measured ratio ($\mathcal{R}$), beam deflection with associated error (Δy), and the corresponding neutron electric charge Q_n for each cycle.

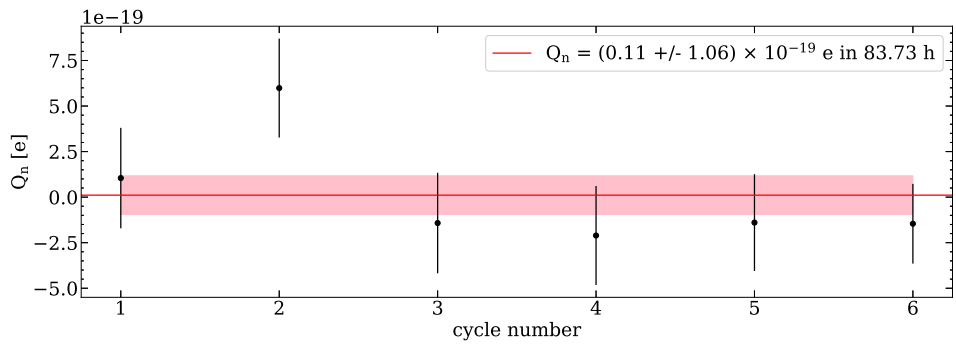

Figure 5.12. Results from cycle 1 to 6 combined together. The red horizontal constant value corresponds to the weighted mean value and the associated statistical uncertainty is shaded, giving a final result of $Q_n = (0.11 \pm 1.06) \times 10^{-19}\ e$.

In Fig. 5.12, the results are combined in a single plot. A horizontal line is fitted in red to determine the weighted mean value of the neutron electric charge, with the associated total statistical error in shaded tone.

The final result is therefore:

$$Q_n = (0.11 \pm 1.06_{stat}) \times 10^{-19}\ e \quad \text{in} \quad 83.73\,\text{h} \tag{5.8}$$

which correspond to a combined beam deflection of:

$$\Delta y = (10 \pm 95)\,\text{pm} \tag{5.9}$$

and concludes the first measurement campaign of the QNeutron apparatus at the PF1B beam line using a white beam in a ballistic configuration.

5.3.2 Comparison with Theoretical Expectations

After the final extraction of this value, it is compared to the expected statistical sensitivity using Eq. (4.1) and employing the following parameter values:

- **Grating period (p)**: 250 µm
- **Average visibility over the entire spectrum (η)**: 88.2%
- **Combined total neutron counts at the working point (N_w) of all cycles**: 219.3×10^9

Note, Eq. (4.1) assumes a sinusoidal shape and may therefore slightly overestimate the sensitivity of the setup. The two sensitivities are compared in Table 5.3.

Cycle	Meas. Sensitivity $\sigma(Q_n)_\text{m}$	Theo. Sensitivity $\sigma(Q_n)_\text{th}$
ALL	$1.06 \times 10^{-19}\,e$	$1.09 \times 10^{-19}\,e$

Table 5.3. Comparison of measured and theoretical sensitivities for the final result combining all cycles 1 to 6.

The close agreement between measured and theoretical sensitivities confirms that the theoretical formula provides a reliable approximation for the sensitivity of the apparatus. This supports the use of theoretical sensitivity calculations for scaling the setup and predicting potential enhancements through future design improvements.

5.3.3 Errors on Experimental Parameters

In Eq. (5.5), used to determine Q_n, the constant P depends on several experimental parameters, each contributing an uncertainty to the final result:

- **Electric Field (E)**: Calculated from the applied voltage and the gap distance, $E = U/d$, with:
  - **Voltage (U)**: 35.00(35) kV, relative uncertainty of 1%.
  - **Gap Distance (d)**: 1.500(75) cm, estimated relative uncertainty of 5%.
- **Interaction Length (L)**: 2.500(25) m, relative uncertainty of 1%.
- **Weighted RMS Wavelength (λ_{RMS})**: 0.446(14) nm, relative uncertainty of 3.2%. This value is determined from the signal of the electric pulses created by the chopper when delivering neutron bunches at a frequency of 25 Hz. The duration of the chopper pulse is 570 µs, which corresponds to approximately 12 time bins of 50 µs (Sec. 2.1.2). Since neutrons can enter the setup at any moment during this time interval, an uncertainty $\sigma(\lambda_{RMS}) = 0.0012$ nm per time bin is assumed. Given 12 time bins, the total uncertainty on λ_{RMS} is 0.014 nm, corresponding to a relative error of 3.2%.

The total uncertainty on the electric field is propagated as follows:

$$\frac{\sigma_E}{E} = \sqrt{\left(\frac{\sigma_U}{U}\right)^2 + \left(\frac{\sigma_d}{d}\right)^2} = \sqrt{(0.01)^2 + (0.05)^2} \approx 0.0515 \tag{5.10}$$

The uncertainty in P is then calculated using the formula for error propagation, considering $P \propto 1/(E \cdot L^2 \cdot \lambda_{RMS}^2)$:

$$\left(\frac{\sigma_P}{P}\right)^2 = \left(\frac{\sigma_E}{E}\right)^2 + \left(2 \cdot \frac{\sigma_L}{L}\right)^2 + \left(2 \cdot \frac{\sigma_{\lambda_{RMS}}}{\lambda_{RMS}}\right)^2 \tag{5.11}$$

Substituting the values:

$$\left(\frac{\sigma_P}{P}\right)^2 = (0.0515)^2 + (2 \cdot 0.01)^2 + (2 \cdot 0.032)^2 = 0.00715 \tag{5.12}$$

Thus, the relative uncertainty on P is:

$$\frac{\sigma_P}{P} = \sqrt{0.00715} \approx 0.0845 \quad \text{(or 8.45\%)} \tag{5.13}$$

Given the combined measured beam deflection over all cycles, Δy =(10 ± 95) pm, the uncertainty on Q_n is primarily driven by the large error on Δy. The relative contribution of the uncertainty from P is negligible in comparison. With $\frac{\sigma(\Delta y)}{\Delta y} \approx 9.5$, the statistical uncertainty is approximately 112 times larger than the uncertainty associated with P.

$$\sigma_{\text{exp}}(Q_n) \approx \frac{\sigma_{\text{stat}}(Q_n)}{112} \approx 0.01 \times 10^{-19}\, e \tag{5.14}$$

5.3.4 Systematic Errors

In the following, systematic effects are considered which can cause a false signal or systematically alter the result of a measurement. It can include, for example, misalignments or drifts of the components resulting in non-uniform electric fields. Effects mimicking a real beam deflection of particles are particularly undesired, and this requires deploying countermeasures such as the two-beam method or the sequence of electric field polarity inversions. Despite being expected to be negligible compared to the statistical sensitivity of the instrument during this measurement, some possible systematic effects and an estimation of their size are listed below.

Non-Uniformity of the Electric Field

In this scenario, the effective electric field is assumed to differ between the two beam spots due to potential non-uniformities such as an uneven electrode gap or a tilt between the electrodes, leading to unequal deflections. To evaluate the impact of this, the deflection formula (Eq. 5.5) was revisited. By analyzing how small differences δE in the electric field affect the deflection, the relation between the electric field error and the deflection error is derived below.

Let Δy_1 and Δy_2 be the deflections for the two individual beam spots, with all other parameters constant for this analysis. The deflections of beam spots 1 and 2 are expressed as:

$$\Delta y_1 = \frac{Q \cdot E \cdot L^2 \cdot m \cdot \lambda^2}{2 \cdot h^2} = C \cdot E \qquad \text{and} \qquad \Delta y_2 = C \cdot (-E) \tag{5.15}$$

where C is defined as:

$$C = \frac{Q \cdot L^2 \cdot m \cdot \lambda^2}{2 \cdot h^2} \tag{5.16}$$

When both beam spots experience the same electric field E, the overall deflection $\delta(\Delta y)$ is given by:

$$\delta(\Delta y) = \Delta y_1 - \Delta y_2 = 2 \cdot C \cdot E \tag{5.17}$$

If the effective electric field for one beam spot changes to $E + \delta E$, the new expressions for the deflections of beam spots 1 and 2, labeled "*sys*," are given by:

$$\Delta y_1^{sys} = C \cdot (E + \delta E) \qquad \text{and} \qquad \Delta y_2^{sys} = C \cdot (-E) \tag{5.18}$$

In that case, the deflection $\delta(\Delta y^{sys})$ becomes:

$$\delta(\Delta y^{sys}) = \Delta y_1^{sys} - \Delta y_2^{sys} = C \cdot (2E + \delta E) \tag{5.19}$$

The deviation on the measured value of the deflection is given by the difference $\delta(\Delta y^{sys}) - \delta(\Delta y)$, taking into account the changes due to the unequal electric field between the beam spots:

$$\sigma(\delta(\Delta y)) = \delta(\Delta y^{sys}) - \delta(\Delta y) = C \cdot \delta E \tag{5.20}$$

And finally, the relative error on the beam deflection $\frac{\sigma(\delta(\Delta y))}{\delta(\Delta y)}$ is linked to the relative error of the value of the electric field between the two beam spots by:

$$\frac{\sigma(\delta(\Delta y))}{\delta(\Delta y)} = \frac{1}{2} \cdot \frac{\delta E}{E} \tag{5.21}$$

For a conservative scenario where a potential deviation of 10% is expected between the electric field of the two beam spots, the corresponding systematic uncertainty on the final charge measurement is given by:

$$\sigma_{sys}^{E}(Q_n) = Q_n \cdot \frac{1}{2} \cdot \frac{\delta E}{E} \tag{5.22}$$

Substituting the values, the systematic uncertainty due to the electric field non-uniformity is:

$$\sigma^{E}_{sys}(Q_n) = 0.006 \times 10^{-19}\, e \tag{5.23}$$

Magnetic Interaction

Another systematic effect linked with the electrodes setup has been previously discussed by Baumann *et al.* and originates from the interaction between the neutron's magnetic moment and a gradient of the electric field in the z-direction due to the relativistic $\mathbf{v} \times \mathbf{E}$-effect [30]. Such an effect can be caused by a slight tilt of the electrode plates relative to one another. The upper limit for the tilt angle α in the case of a fully polarized neutron beam can be estimated by comparing the forces acting on the neutron electric charge and magnetic moment, giving the following condition:

$$\alpha < \frac{Q \cdot c^2 \cdot d \cdot \lambda \cdot m_n}{\pi \cdot \gamma_n \cdot \hbar^2} \tag{5.24}$$

where γ_n is the neutron's gyromagnetic ratio and c the speed of light in a vacuum. Using $Q = 1 \times 10^{-21}\, e$, $d = 1.5\,\text{cm}$, and $\lambda_{RMS} = 0.446\,\text{nm}$, the maximum tilting angle between the electrode plates is found to be in the order of 10 mrad. However, this constraint can be significantly relaxed when assuming an unpolarized neutron beam, like for the present measurement.

Misalignment of the Setup

During the measurement cycle, slight misalignments of the gratings could occur and influence the recorded intensity. A tilt of grating G_2 around the beam axis (the x-axis) is particularly problematic, as it can generate Moiré patterns that impact the two beam spots differently. While the two-beam method mitigates many systematic effects by canceling shared influences on both beam spots when calculating the ratio $\mathcal{R}$, a tilt that creates an asymmetric effect—impacting one beam spot more than the other—could mimic a real beam deflection. In such cases, distinguishing between actual deflection and tilt-induced intensity changes becomes challenging.

To assess this potential systematic effect, the analysis in Sec. 4.4.3 is considered. During those measurements, intensity modulations were recorded for various tilt angles of G_2 around the x-axis. This allowed estimation of the statistical loss as a

function of the misalignment angle. If these tilts are correlated with inversions of the electric field direction, their impact could propagate into the deflection measurement.

The total number of neutrons counted during a polarity inversion reaches 150×10^6, spread across 20 runs for cycles 1 to 4 (10 with positive polarity and 10 with negative polarity). The statistical uncertainty associated with this total is given by $\sqrt{150 \times 10^6}$. Based on results from Sec. 4.4.3, it is possible to determine the degree of tilt required for G_2 to cause a change in neutron counts larger than the statistical sensitivity during a polarity inversion.

The analysis indicates that a tilt of approximately $0.003\,^\circ$, equivalent to one full-step of the stage's stepper motor, could induce a change in neutron counts comparable to the statistical sensitivity. This suggests that even a minor tilt of G_2 could mimic a real deflection signal if it were correlated with the electric field polarity changes. However, such an effect would require strong synchronization with the electric field to have a significant impact, and is therefore not included in the final results. Additionally, since the gratings are mounted outside the vacuum pipes, they benefit from the shielding provided by the vacuum pipes acting as a Faraday cage.

Reflection on Electrodes

Neutrons reflecting off the electrodes could introduce another potential systematic error. In this case, reflected neutrons might scatter and influence the measurements, potentially mimicking or distorting the true beam deflection. However, due to the precision of the collimation system, ensured by the BorAl apertures, any neutron trajectory resulting from reflection would be blocked from reaching the detector.

The apertures precisely define the acceptance angle, allowing only neutrons within the designated trajectory to pass through, while excluding any reflected neutrons outside this range. A schematic illustration in Fig. 5.13 depicts this limitation by showing the maximum reflection angle that is allowed, further demonstrating that the contribution from this type of error is negligible.

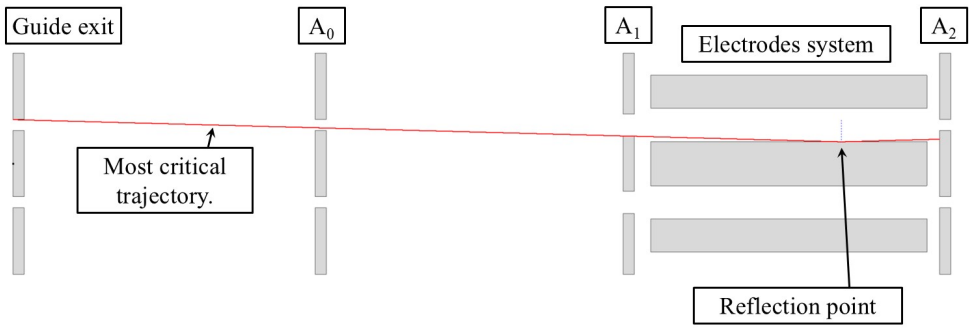

Figure 5.13. Scheme of the apparatus depicting the limit angle possible within the apparatus. As shown by the red line, this trajectory is blocked before reaching the detector. The horizontal distances are scaled down by a factor of 20 for better visualization.

Electrostatic Force Between Electrodes

An additional systematic effect could arise from the electrostatic force between the two electrodes. The electrodes are 2.5 m long, 6 cm high, and separated by a distance of 1.5 cm. The applied voltage is $U = 35\,\text{kV}$. The capacitance C of the system is therefore given by:

$$C = \varepsilon_0 \cdot \frac{A}{d} \approx 90\,\text{pF} \tag{5.25}$$

The electrostatic force F acting between the electrodes is then calculated using:

$$F = \frac{1}{2} \cdot \frac{C \cdot U^2}{d} \approx 4\,\text{N} \tag{5.26}$$

If the electrode configuration were asymmetrical, this force could induce mechanical deformations or shifts, introducing systematic effects into the measurements. However, in the present setup, the high-voltage electrode is symmetrically positioned between two ground electrodes, ensuring balanced forces on either side. This sym-

metrical design minimizes mechanical constraints, allowing the residual electrostatic force to be neglected in the error analysis.

5.3.5 Summary

The final measured value of the neutron electric charge, including statistical and systematic uncertainties, is therefore expressed as:

$$Q_n = (0.11 \pm 1.06_{stat} \pm 0.01_{exp} \pm 0.006_{sys}) \times 10^{-19}\, e \tag{5.27}$$

in 83.73 h of data acquisition. This first campaign was mostly to demonstrate the feasibility of this measurement and the performance of the apparatus, which fulfilled the expectations and allows projections discussed in the next and final chapter.

6. Conclusion and Outlook

6.1 Conclusion

This thesis presents the development, optimization, and application of the QNeutron apparatus, a Talbot-Lau neutron interferometer designed for high-precision measurements of the neutron electric charge. The project involved extensive experimental campaigns at the Paul Scherrer Institute (PSI) and the Institut Laue-Langevin (ILL), with each stage contributing significant advancements in the performance of the instrument.

At PSI, the experimental setup underwent rigorous optimization. Starting from a 1-meter-long prototype, the setup evolved into a 6-meter-long apparatus through seven beam times totaling approximately 80 days. During this phase, various grating configurations, duty cycles, absorber thicknesses, and interaction lengths were systematically tested to identify the optimal parameters. These efforts provided critical insights and prepared the setup for high-precision experiments at ILL.

The first 30-days beam time at ILL focused on refining the instrument in both ballistic and diffraction regimes. The ballistic regime allowed detailed exploration and confirmation of the grating's parameters defined at PSI (duty cycles, absorber thicknesses, and inter-grating distances) optimizing the setup for beam deflection sensitivity. The best setup achieved a visibility of 93% when integrated over all wavelengths using a white beam and reached 97% at the optimal wavelength. A sensitivity assessment demonstrated excellent performance with the two-beam method and enabled the determination of optimal observation times in terms of stability of the setup, providing a solid foundation for a neutron electric charge measurement. Misalignment tests evaluated the impact of grating tilt and shift on the visibility of the intensity modulations, revealing the robustness of the setup under minor deviations or imperfections.

Using a test prism, the experiment successfully verified neutron refraction according to Snell's law, confirming the precision of the instrument in detecting beam deflections. Additionally, an asymmetric grating setup, matching Monte Carlo simulations, was tested, providing further validation of the simulation models. Experiments in an intermediate regime, where the grating separation approached the Talbot length,

demonstrated the versatility of the setup, transitioning smoothly between ballistic and diffraction regimes.

In the diffraction regime, visibility peaks were observed up to the fifth-order Talbot wavelength. These results were consistent with a Python-based wave formalism simulation, accurately capturing the diffraction and interference effects within the setup.

The insights gained from these experiments defined the optimal parameters for the second ILL beam time:

- **Grating Period:** 250 µm
- **Duty Cycle:** 20%
- **Absorber Thickness:** $t_{Gd} = 30\,\mu\text{m}$
- **Interaction Length:** $L = 2.5\,\text{m}$
- **Wavelength Range:** $\lambda = 0.2 - 0.8\,\text{nm}$ (visibilities higher than 90%)

The second ILL beam time spanning 20 days focused on measuring the neutron electric charge. Using the optimized setup and operating in the ballistic regime, the experiment capitalized on the continuous beam and constrained experimental space. Over 83.73 h of data acquisition, six cycles were completed, employing both single-point and multi-point measurement strategies. The two-beam method, combined with a carefully designed polarity inversion sequence, effectively minimized systematic effects by comparing deflections from the two beam spots. Additionally, a study on potential experimental errors in the parameters, along with an analysis of systematic effects related to a non-uniform electric field between the two beam spots, resulted in the following value for the neutron electric charge:

$$Q_n = (0.11 \pm 1.06_{stat} \pm 0.01_{exp} \pm 0.006_{sys}) \times 10^{-19}\ e \tag{6.1}$$

Although this result did not surpass the current best experimental limit, it confirmed the potential of the QNeutron apparatus for high-precision measurements. The second beam time also provided important experimental achievements. The setup demonstrated remarkable high-voltage stability, maintaining a consistent electric field during extended measurement periods. Furthermore, valuable experience was gained regarding the essential shielding required for such sensitive measurements, emphasizing the critical role of lead and concrete shielding in mitigating radiation, as well as ther-

mal shielding for enhanced stability during the measurement. Most importantly, this campaign marked the first successful neutron electric charge measurement using the QNeutron apparatus, establishing a strong benchmark for future investigations into fundamental neutron properties.

6.2 Outlook

This work establishes a robust foundation for future neutron electric charge studies. The QNeutron apparatus has demonstrated its capability for high-precision measurements, and further improvements at advanced facilities such as the European Spallation Source (ESS) could unlock new levels of sensitivity. Increased neutron beam intensity, extended beam lines, and enhanced experimental stability would allow for more precise deflection measurements, potentially achieving a breakthrough in the detection of the neutron electric charge.

Looking ahead, several key topics and activities should be tackled to push the performance of the QNeutron apparatus to its limits:

- **High-Voltage Performance:** Improve the high-voltage system design to achieve higher electric fields and faster ramping times, enhancing sensitivity and increasing the effective measurement time (duty cycle).
- **Detector Design:** Develop an improved detector with high rate capability and increased efficiency to handle larger neutron flux and improved signal-to-noise ratio.
- **Interaction Length:** Investigate the possibility of detecting beam deflections occurring between the first two gratings (G_0 and G_1). This could potentially enhance sensitivity by a factor of four, significantly improving the performance of the instrument.
- **Advanced Gratings:** Explore the use of newly produced gratings with a 25 µm period and 30 µm absorber thickness, fabricated through an improved production process for enhanced performances in the diffraction regime.
- **Larger Grating Cross-Section:** Utilize larger gratings with wafer diameters of 6 inches (active area of 10×10 cm^2) to improve statistics by accommodating a greater number of neutron trajectories.
- **Larger Grating Duty Cycle:** Increase the duty cycle to 25% or possibly 30%, as measurements in the ballistic regime indicate this could be feasible without

departing from the purely ballistic mode. This investigation is worthwhile to improve neutron statistics and enhance measurement precision.

- **Wavelength Modulation Setup:** Develop a new concept for wavelength modulation employing polarized neutrons, specifically designed to match the acceptance of the diffraction regime. This approach could offer increased sensitivity without requiring further experimental complexity.

Future experiments could explore novel configurations, such as extending the diffraction regime analysis to higher Talbot orders or utilizing advanced alignment and stabilization techniques to minimize residual systematic effects and temperature drifts, positioning the QNeutron apparatus as a cutting-edge tool for probing fundamental neutron properties. These developments will not only expand the boundaries of high-precision neutron beam deflection measurements, but also offer valuable insights with significant implications for both theoretical models and experimental techniques in particle physics.

A. Detailed Calculations for Talbot-Lau Interferometer

A.1 Simulation Formalism for the Talbot-Lau Interferometer

This appendix provides a detailed overview of the simulation procedures used for modeling the neutron interferometry setup in both the ballistic and diffraction regimes. Each section is detailed to provide a comprehensive understanding of the methods and calculations used.

A.1.1 Diffraction Configuration Simulation

In the diffraction regime, the Talbot-Lau interferometer was simulated using the formalism developed by Swanson and Leith [79–81,162], which involves the following key steps:

Grating Transmittance Function

The periodic transmittance function $f(y)$ of the gratings is represented in Fig. A.1 and is defined as:

$$f(y) = \begin{cases} \tau & \text{for } -\frac{p}{2} < y < -\frac{Rp}{2}, \\ 1 & \text{for } -\frac{Rp}{2} < y < \frac{Rp}{2}, \\ \tau & \text{for } \frac{Rp}{2} < y < \frac{p}{2} \end{cases} \tag{A.1}$$

where τ is a parameter corresponding to the residual transmission through the gadolinium of the grating and depends on the neutron wavelength, and R is the duty cycle of the grating such that $0 < R < 1$. The function $f(y)$ is periodic, meaning $f(y+p) = f(y)$ for all y.

Fourier Series Representation

The Fourier series of a periodic function $f(y)$ with period p is given by:

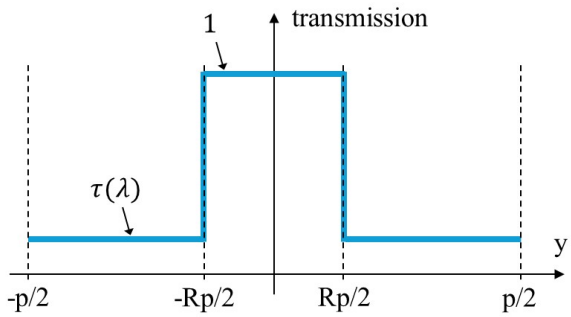

Figure A.1. Plot of the periodic function $f(y)$.

$$f(y) = \sum_{n=-\infty}^{\infty} c_n e^{i\frac{2\pi n y}{p}} \tag{A.2}$$

where the Fourier coefficients c_n are calculated using:

$$c_n = \frac{1}{p}\int_{-\frac{p}{2}}^{\frac{p}{2}} f(y) e^{-i\frac{2\pi n y}{p}}\, dy \tag{A.3}$$

Calculation of Fourier Coefficients

To find the Fourier coefficients c_n, the integral over the period of the function needs to be evaluated. Given that $f(y)$ is piecewise constant, the integral can be splitted into three parts corresponding to the different regions of $f(y)$.

$$c_n = \frac{1}{p}\left(\int_{-\frac{p}{2}}^{-\frac{Rp}{2}} \tau e^{-i\frac{2\pi n y}{p}}\, dy + \int_{-\frac{Rp}{2}}^{\frac{Rp}{2}} 1 \cdot e^{-i\frac{2\pi n y}{p}}\, dy + \int_{\frac{Rp}{2}}^{\frac{p}{2}} \tau e^{-i\frac{2\pi n y}{p}}\, dy\right) \tag{A.4}$$

We compute each integral separately.

First Integral: $-\frac{p}{2} < y < -\frac{Rp}{2}$

For this interval, $f(y) = \tau$:

$$\int_{-\frac{p}{2}}^{-\frac{Rp}{2}} \tau e^{-i\frac{2\pi ny}{p}}\, dy = \tau \left[\frac{p}{-i2\pi n} e^{-i\frac{2\pi ny}{p}} \right]_{-\frac{p}{2}}^{-\frac{Rp}{2}} = \tau \cdot \frac{p}{-i2\pi n} \left(e^{i\pi nR} - e^{i\pi n} \right) \quad \text{(A.5)}$$

Second Integral: $-\frac{Rp}{2} < y < \frac{Rp}{2}$

For this interval, $f(y) = 1$:

$$\int_{-\frac{Rp}{2}}^{\frac{Rp}{2}} e^{-i\frac{2\pi ny}{p}}\, dy = \left[\frac{p}{-i2\pi n} e^{-i\frac{2\pi ny}{p}} \right]_{-\frac{Rp}{2}}^{\frac{Rp}{2}} = \frac{p}{\pi n} \sin(\pi nR). \quad \text{(A.6)}$$

Third Integral: $\frac{Rp}{2} < y < \frac{p}{2}$

For this interval, $f(y) = \tau$:

$$\int_{\frac{Rp}{2}}^{\frac{p}{2}} \tau e^{-i\frac{2\pi ny}{p}}\, dy = \tau \left[\frac{p}{-i2\pi n} e^{-i\frac{2\pi ny}{p}} \right]_{\frac{Rp}{2}}^{\frac{p}{2}} = \tau \cdot \frac{p}{-i2\pi n} \left(e^{-i\pi n} - e^{-i\pi nR} \right) \quad \text{(A.7)}$$

Combining the Results

For $n \neq 0$:

$$c_n = \frac{1}{p} \left[\tau \cdot \frac{p}{-i2\pi n} \left(e^{i\pi nR} - e^{-i\pi nR} - (e^{i\pi n} - e^{-i\pi n}) \right) + \frac{p}{\pi n} \sin(\pi nR) \right] \quad \text{(A.8)}$$

Simplifying given $\sin(\pi n) = 0\ \forall n \in \mathbb{Z}$:

$$c_n = \frac{\sin(\pi nR)}{\pi n} (1 - \tau) \quad \text{(A.9)}$$

DC Component (c_0)

The DC component c_0 corresponds to the average value of the function over one period:

$$c_0 = \frac{1}{p} \int_{-\frac{p}{2}}^{\frac{p}{2}} f(y)\, dy \tag{A.10}$$

Splitting the integral into the three regions:

$$c_0 = \frac{1}{p} \left(\tau \left(\frac{p}{2} - \frac{Rp}{2} \right) + \left(\frac{Rp}{2} + \frac{Rp}{2} \right) + \tau \left(\frac{p}{2} - \frac{Rp}{2} \right) \right) \tag{A.11}$$

$$c_0 = \tau(1 - R) + R. \tag{A.12}$$

Final Results

The Fourier coefficients for the function $f(y)$ are:

- For $n = 0$:

$$c_0 = \tau + R(1 - \tau) \tag{A.13}$$

- For $n \neq 0$:

$$c_n = (1 - \tau) \cdot \frac{\sin(\pi n R)}{\pi n} \tag{A.14}$$

Field at the Observation Plane

Swanson and Leith derived an expression for the field at the observation plane P (position of the analyzer grating G_2 for this setup) resulting from a point source of spatial frequency f_s. The field u_p at P can be written as:

$$\begin{aligned} u_p = & \sum_{n,m} a_n b_m \exp\left[i2\pi (n f_0 + m f_1) y \right] \\ & \times \exp\left[-i2\pi\lambda \left[(x_0 + x_1) n f_0 + x_1 m f_1 \right] f_s \right] \\ & \times \exp\left[-i\pi\lambda \left[x_0 n^2 f_0^2 + x_1 (n f_0 + m f_1)^2 \right] \right] \end{aligned} \tag{A.15}$$

For the case where $f_0 = f_1$ and using the grating period p, where $p_0 = p_1 = p$, and $x_0 = x_1 = L_G$, the expression for u_p simplifies to:

$$\begin{aligned} u_p = \sum_{n,m} a_n b_m \exp\left[i(n+m)k_p y\right] \\ \times \exp\left[-ik_p L_G \lambda\,(2n+m)\,f_s\right] \\ \times \exp\left[-i\pi L_G \frac{\lambda}{p^2}\left[n^2 + (n+m)^2\right]\right] \end{aligned} \tag{A.16}$$

Intensity Calculation

The intensity I_p at the position of the analyzer grating G_2 is given by the square modulus of u_p:

$$\begin{aligned} I_p = u_p u_p^* = \sum_{n,n',m,m'} a_n b_m a_{n'}^* b_{m'}^* \exp\left[i(n-n'+m-m')k_p y\right] \\ \times \exp\left[-ik_p L_G \lambda\,(2(n-n') + (m-m'))\,f_s\right] \\ \times \exp\left[-i\pi L_G \frac{\lambda}{p^2}\left(n^2 - n'^2 + (n+m)^2 - (n'+m')^2\right]\right] \end{aligned} \tag{A.17}$$

Lau Condition and Fourier Modes

The Lau condition is crucial for generating a coherent interference pattern, even when using an incoherent source. This condition ensures that the periodic structures of the two gratings G_0 and G_1 are aligned such that the diffracted beams from the first grating overlap constructively at specific positions after the second grating. This overlap occurs due to a combination of geometric alignment and path-length coherence, allowing interference fringes to form despite the incoherence of the source. For the QNeutron setup, this condition simplifies to:

$$\begin{aligned} x_0 = \frac{x_1}{1 + \left(\frac{p_0}{p_1}\right)\left(\frac{m-m'}{n-n'}\right)} \\ m' = 2(n-n') + m \end{aligned} \tag{A.18}$$

In the context of cold neutron interferometry, maintaining the Lau condition is essential for achieving high visibility of the interference patterns. This forms the basis for

further analysis and optimization of the interferometer setup to enhance sensitivity and accuracy in neutron electric charge measurements.

After simplifications, the expression of the intensity observed at a plane placed at a distance L_G from G_1 allows for the visualization of what the analyzer grating G_2 would record in the experimental setup. This expression becomes:

$$I_p(y) = \sum_{n,n',m,m'=2(n-n')+m} a_n b_m a^*_{n'} b^*_{2(n-n')+m} \exp\left[-ik_p(n-n')y\right] \times \exp\left[i2\pi \frac{\lambda}{p^2} L_G\left[(n-n')(n-n'+m)\right]\right] \tag{A.19}$$

Additionally, the number of Fourier modes considered for generating the interference patterns is determined by the geometry of the grating G_0. This is expressed by the following relation using the single-slit diffraction formula to know how many gratings slits are illuminated at G_1:

$$N(\lambda) = \frac{L_G \cdot \lambda}{p^2 \cdot R} \tag{A.20}$$

When the 1^{st} order working wavelength is considered, where the Talbot length $L_T = p^2/\lambda$ corresponds to the distance between the gratings L_G, the relation becomes:

$$N(\lambda = \lambda_{1^{st}order}) = \frac{1}{R} \tag{A.21}$$

The simulation framework presented here has been utilized to compare experimental data taken with the setup in diffraction regime with the predictions established by Talbot and Lau concerning this type of instrument. These measurements are presented in Sec. 4.5.

A.1.2 Ballistic Configuration Simulation

In the ballistic regime, where diffraction effects are negligible, neutron trajectories are treated as straight lines. The Monte Carlo method was employed to simulate this setup using Wolfram Mathematica. The primary components of the simulation include:

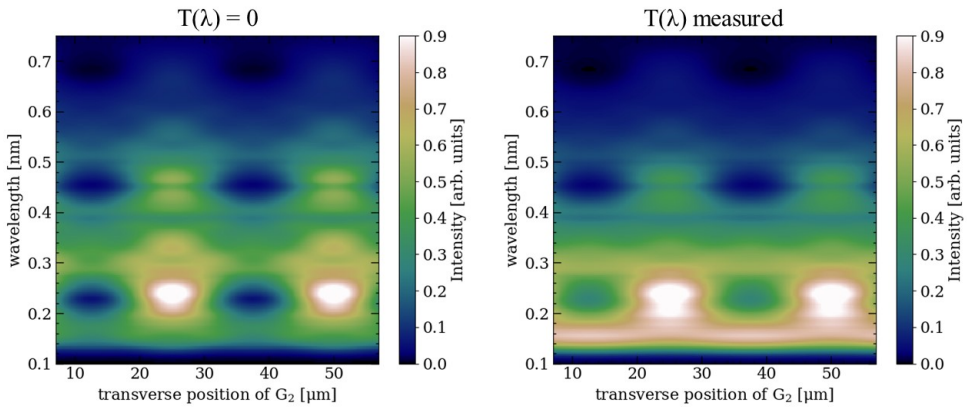

Figure A.2. Simulated intensity pattern at the position of G_2 over two grating periods and a wavelength range from the lowest part of the spectrum to the third-order wavelength. The duty cycle is set to $R = 0.2$.

- **Neutron Source:** Modeled to produce neutrons with random initial positions and directions.
- **Absorption Gratings (G_0, G_1 and G_2):** Characterized by their duty cycles and positioned at specific distances along the beam line.
- **Detector:** Records neutrons that pass through all the gratings without being absorbed.

Simulation Algorithm

The Monte Carlo simulation proceeds through the following steps:

1. **Initialization:** Define the geometry and parameters of the beam line, gratings, and detector.
2. **Random Sampling:** Generate neutron trajectories with random starting points and slopes.
3. **Intersection Testing:** Check if each neutron trajectory intersects any of the gratings.

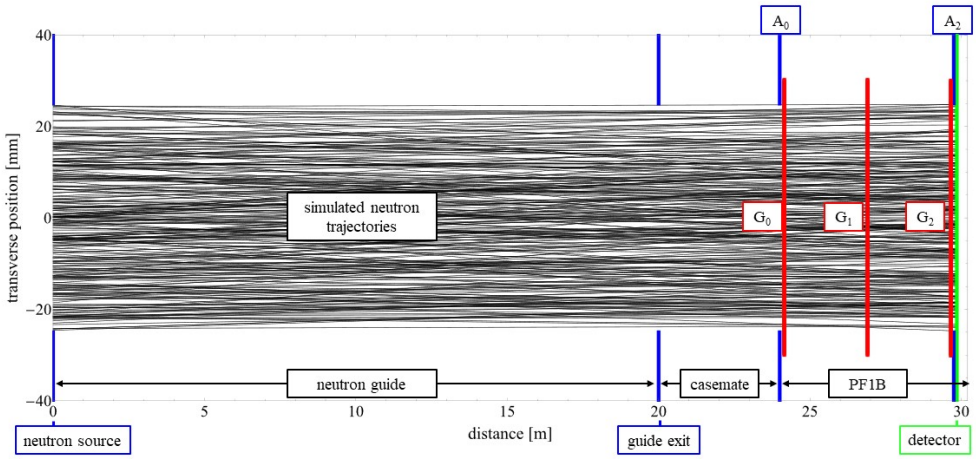

Figure A.3. Monte-Carlo simulation of the Qneutron apparatus operating at the PF1B beam line of the Institut Laue-Langevin in Grenoble, France.

4. **Detection:** Record the number of neutrons that reach the detector without interacting with the gratings.

5. **Transverse Shift Simulation:** Apply a transverse shift to the analyzer grating (G_2) and observe changes in the detected intensity pattern by repeating the simulation.

The neutron trajectories are represented by straight-line equations:

$$y = y_0 + \tan(\theta)(x - x_0) \tag{A.22}$$

where (x_0, y_0) is the starting point and θ is the angle of the trajectory.

Results

The simulation captures intensity patterns by recording the neutrons that reach the detector. When the analyzer grating (G_2) is shifted transversely, the resulting changes in the detected intensity are recorded, producing an oscillating pattern characteristic of neutron grating interferometry in the ballistic regime.

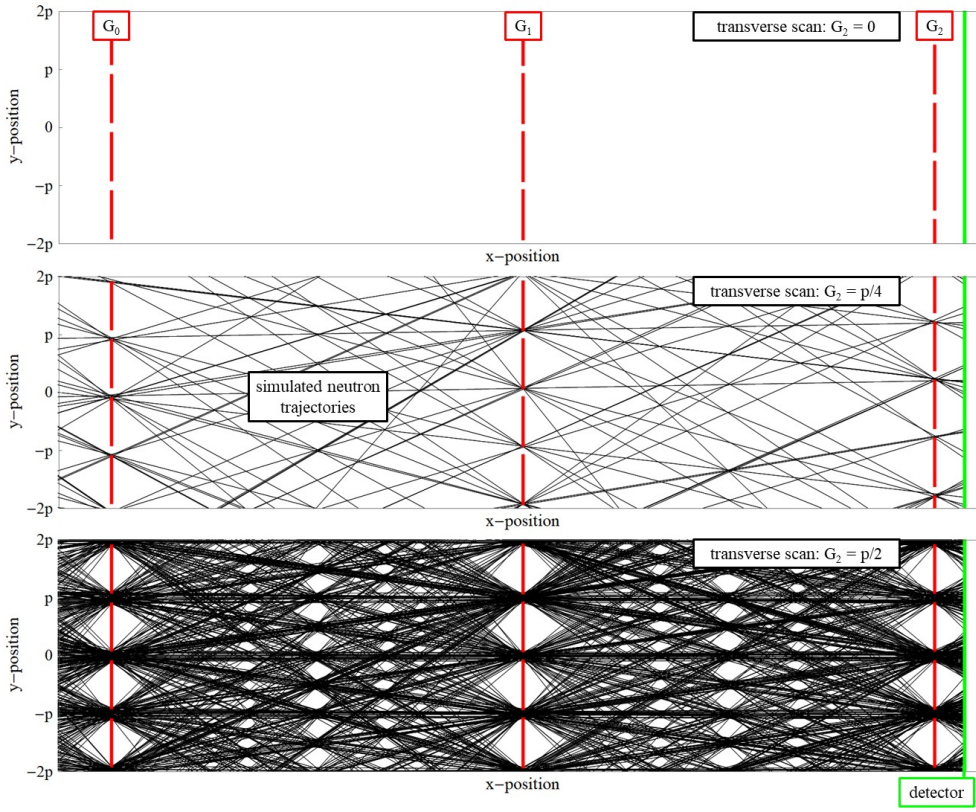

Figure A.4. Example of the Monte-Carlo simulation for the ballistic configuration. Here, the three gratings act as collimators and only allow certain straight-line trajectories. The analyzer grating G_2 is then shifted perpendicularly to the neutron beam axis and neutrons hitting the detector are counted. The simulation is plotted for a transverse shift of G_2 of 0, $p/4$, and $p/2$. The duty cycles of the gratings are set to $R = 20\%$ and 10^6 neutrons are simulated for each G_2 position.

Figure A.3 represent the simulation made for a given position of G_2. By counting how many straight lines reach the detector at each position of G_2, it is possible to obtain a plot of the resulting oscillating intensity pattern. Figure A.4 represent the simulation results for three different position of G_2. A Gaussian fit is then realized in order to extract the visibility, the position of the steepest point, and the neutron counts

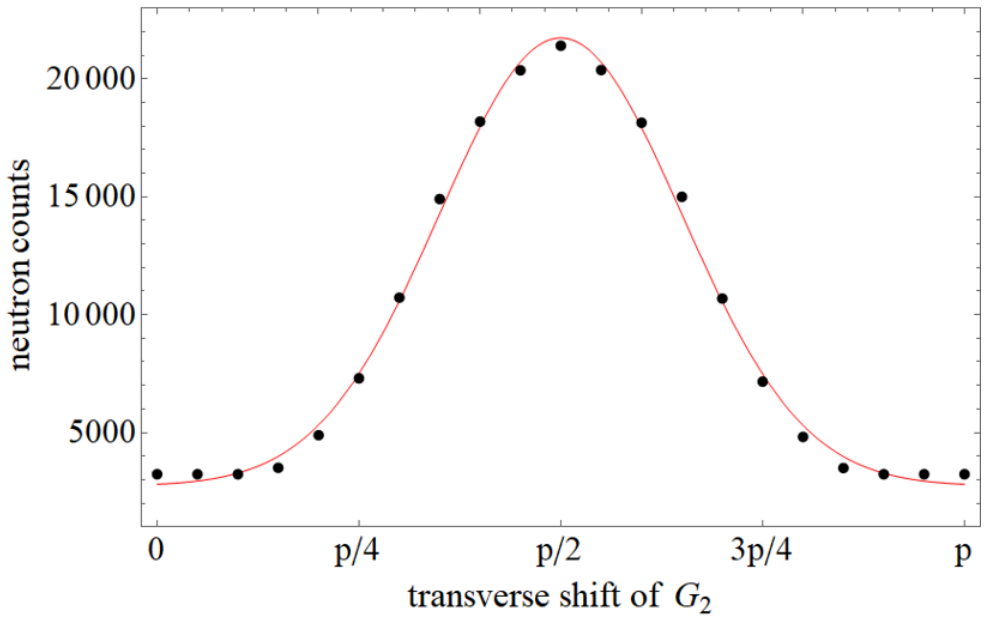

Figure A.5. Oscillating intensity pattern obtained by running the Monte-Carlo simulation in the ballistic configuration over one grating period. The initial number of simulated neutrons is set at 10^6 for every position of G_2. The intensity modulation is fitted with solid lines for the extraction of oscillation's relevant parameters.

at this position, allowing for an estimation of the sensitivity of a given setup. Such an intensity modulation is presented in Fig. A.5 as a specimen result of the simulation.

This pattern can be compared with experimental data to validate the model. By adjusting the beam line design, grating duty cycle, and distances between components, it becomes possible to optimize the setup for specific experimental conditions. The simulation provides insights into how changes in these parameters affect the behavior of the neutron beam and the resulting patterns, helping in the design and interpretation of the experiment. Future enhancements to the simulation could include extending the model to three dimensions for a more accurate representation of neutron trajectories and integrating advanced models of neutron interactions, such as absorption and scattering within samples, to provide more comprehensive insights.

This chapter presented a detailed Monte Carlo simulation of a neutron grating interferometry setup operating in the ballistic regime. By modeling the straight-line trajectories of neutrons and their interactions with absorption gratings, the simulation accurately predicts the resulting intensity patterns. The ability to simulate transverse shifts of the analyzer grating and observe the corresponding intensity oscillations is a significant outcome, demonstrating the potential of Monte Carlo methods in neutron interferometry research.

B. Gratings Alignment Procedure

B.1 Installation and Optical Alignment

The alignment of the three gratings G_0, G_1, and G_2 is a crucial step in the measurement process. These gratings have vertical line structures that must be carefully aligned to ensure optimal performance of the instrument.

B.1.1 Installation and Distance Measurement

Initially, the gratings are installed at their designated positions along the beam line. The distances between the gratings are set with a tape measure to ensure that they are correctly spaced for achieving the desired interference patterns. An analysis has been conducted to understand how the performance of the apparatus in terms of visibility of the intensity modulation decreases when the distances between the gratings are not precisely equal (see Sec. 4.4.3).

B.1.2 Optical Alignment

The optical alignment process begins by placing a laser on the setup along the neutron beam axis. The gratings are then aligned one by one using the reflection of the laser dot against the surface of each gratings. This process ensures alignment around the vertical axis (z, ψ) and the grating scanning axis (y, φ). The laser is directed at the center of each grating, and the gratings are rotated until the reflection hits the laser source.

After aligning the gratings around the z and y axes, the next step involves aligning them around the beam axis. The gratings are illuminated by a laser, not necessarily aligned with the neutron beam axis. This creates a light diffraction pattern along a line perpendicular to the height of the grating slits. A second laser displaying a horizontal line is used as a reference, and the gratings are rotated until the diffraction pattern aligns with the horizontal laser line. This completes the optical alignment of all three gratings. Figure B.1 shows a typical diffraction pattern produced by the grating (green laser) and the horizontality line by the second laser.

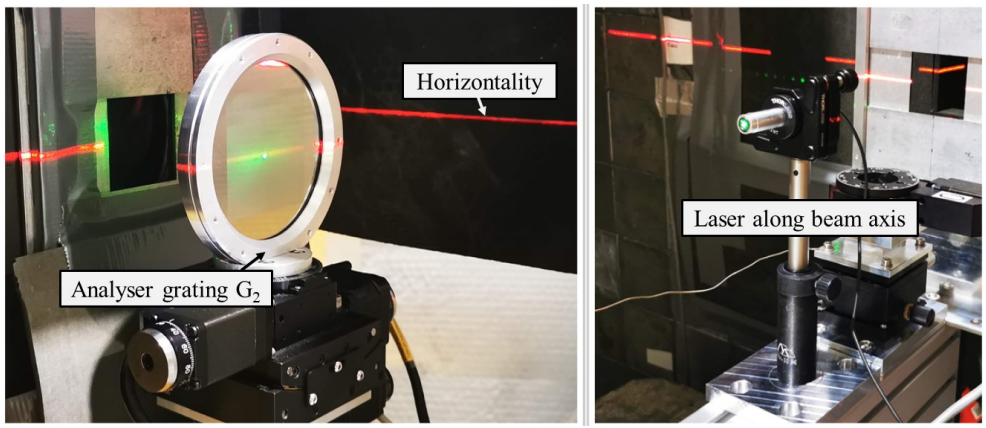

Figure B.1. Left: Analyzer grating G_2 illuminated by the green laser placed along the beam axis. The red line in the background represents the horizontal line. Right: Laser for the optical alignment mounting on a movable plate allowing to match the neutron beam axis and repeat the procedure for all three gratings.

B.2 Neutron Alignment

Once the optical alignment is completed, the neutron beam is turned on, and the neutron alignment procedure begins.

B.2.1 First Alignment Iteration

The first step in the neutron alignment is to perform a transverse scan with G_2 to record an oscillating intensity pattern. The visibility of this pattern is analyzed, and the position of maximum intensity is identified. G_2 is then positioned at this maximum intensity spot.

Next, a scan is performed with G_2 around the beam axis (θ angle). This scan identifies the position where the intensity either peaks or reaches a minimum, corresponding to the optimal angular alignment between the gratings. This alignment is determined by the interference effects of the Moiré patterns formed by two superimposed grids. When the gratings are perfectly aligned, the Moiré pattern vanishes and the intensity reaches an extremum. Positioning G_2 at this optimal point ensures precise relative

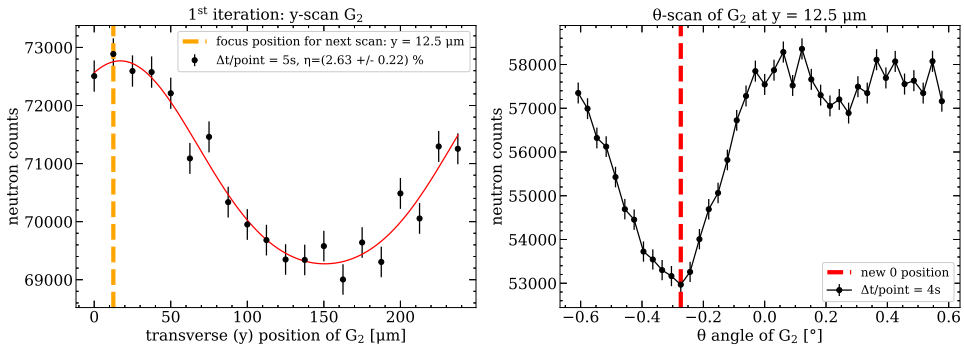

Figure B.2. First Iteration: Transverse scan and angular alignment of G_2.

alignment with G_1. A new zero position is then set for G_2, marking the completion of the first iteration. The corresponding plot for this iteration is shown in Fig. B.2.

B.2.2 Second Alignment Iteration

In the second iteration, another transverse scan with G_2 is conducted to identify the new maximum intensity position. After positioning G_2 at this spot, a simultaneous angular scan is performed with both G_1 and G_2. This step is crucial as it further refines the alignment, ensuring that G_1 and G_2 are now both aligned with G_0.

The scan produces a peak of intensity where no Moiré patterns are visible, indicating optimal alignment. G_1 and G_2 are then positioned at this newly identified spot. This concludes the second iteration, for which the plot is shown in Fig. B.3.

The two steps above are repeated for a total of eight iterations, refining the alignment with each step. On next pages the plots for the remaining iterations are presented (Fig. B.4 and B.5).

After completing all eight iterations, the visibility of the oscillating intensity pattern recorded by scanning G_2 is analyzed as a function of the iteration number. The plot in Fig. B.6 demonstrates that a maximum visibility has been reached. Moreover, after the 7^{th} and 8^{th} iterations, the positions of respectfully G_2 and G_1, G_2 where the intensity is a peak correspond to the preset $zero$ position, indicating one more time that the optimum has been achieved.

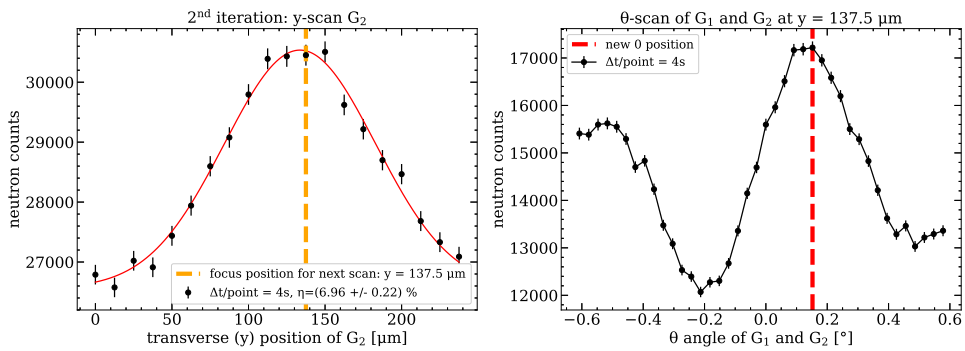

Figure B.3. Second Iteration: Simultaneous scan with G_1 and G_2.

B.2.3 Subsequent iterations (3 to 8)

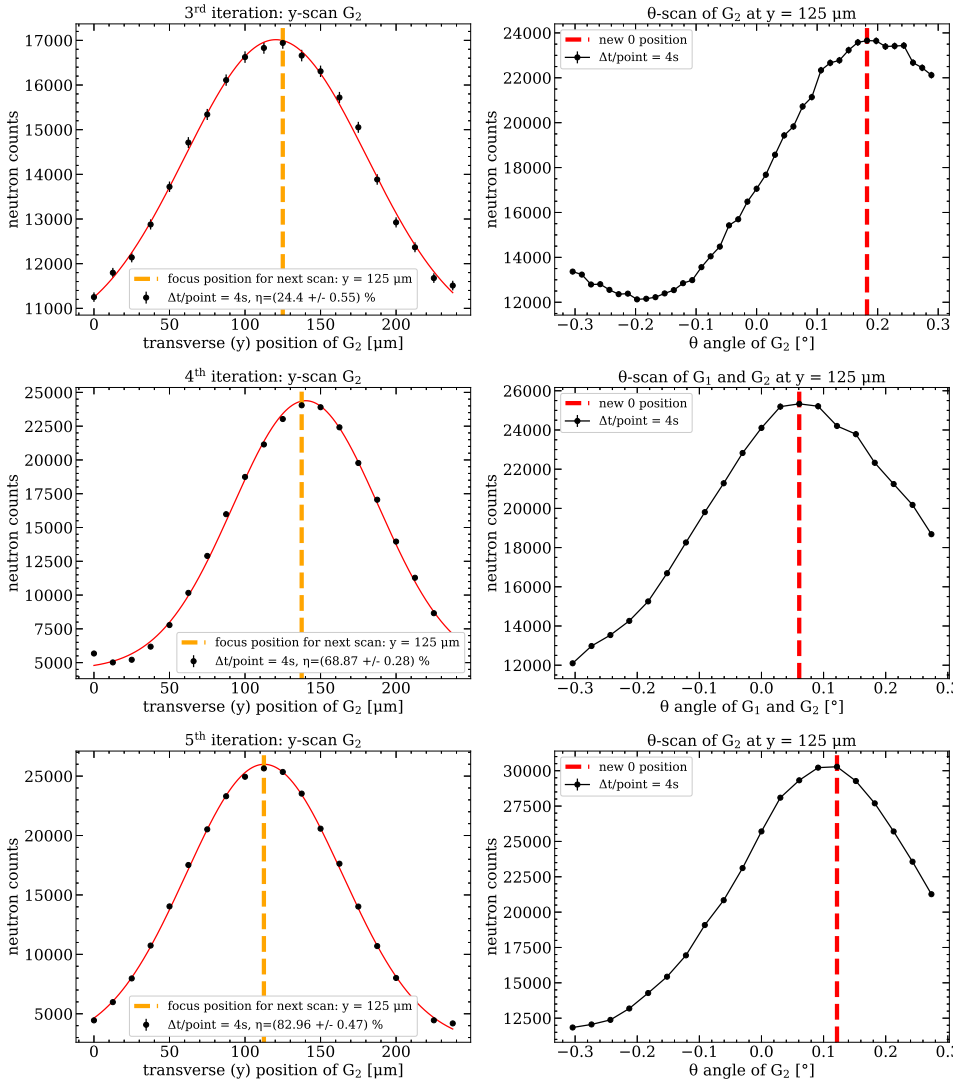

Figure B.4. Third to fifth iteration.

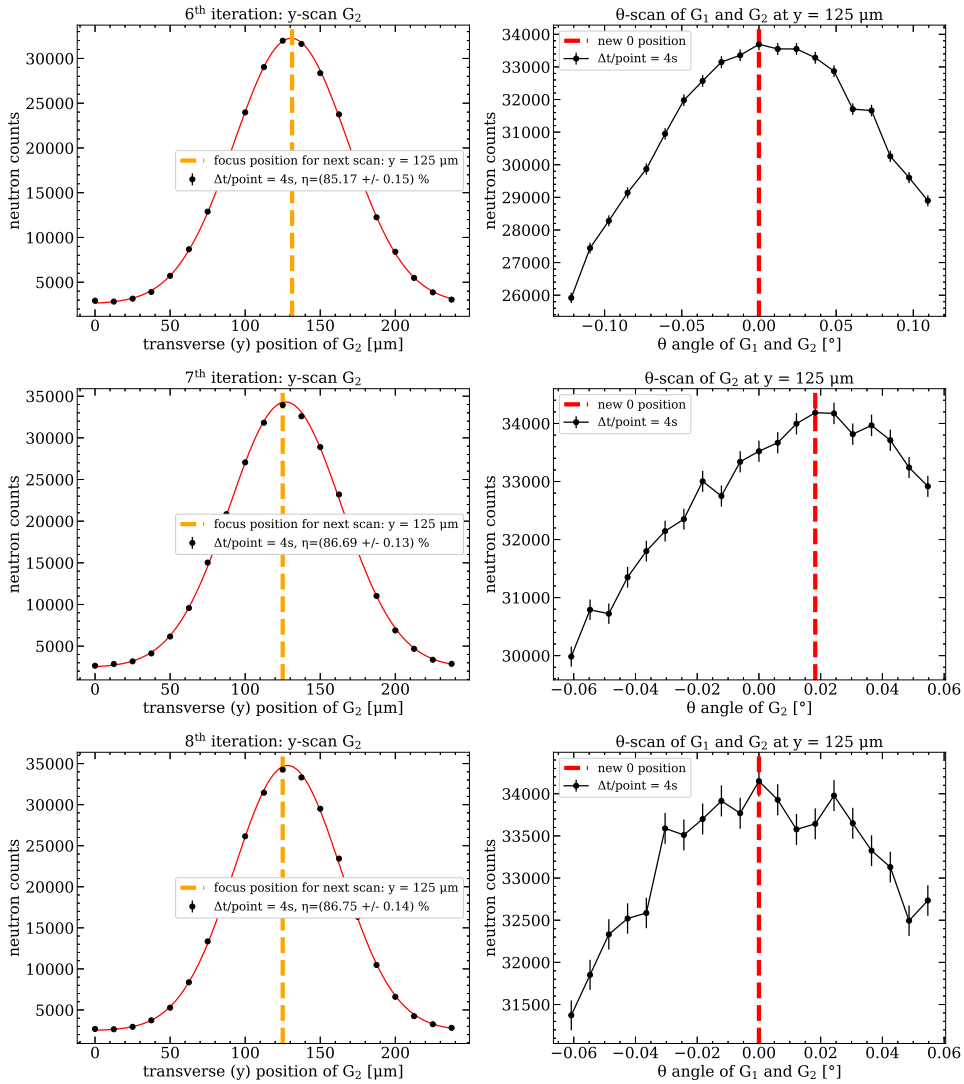

Figure B.5. Sixth to eighth iteration.

B.2.4 Final Visibility

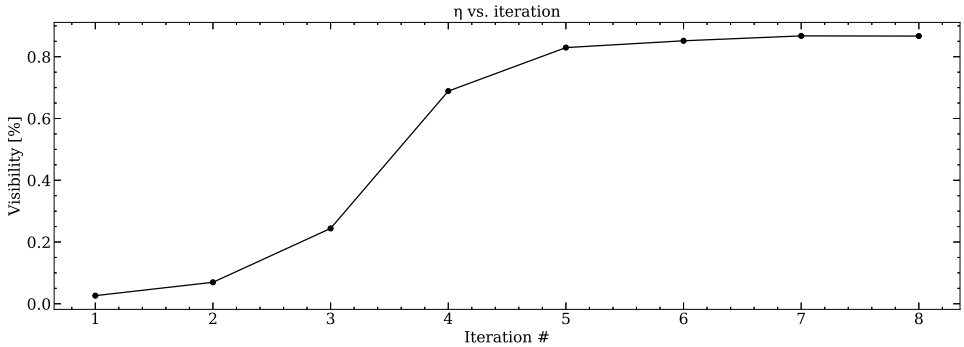

Figure B.6. Visibility vs. Iteration Number.

C. Additional results concerning the diffraction setup

In this appendix, the results from two additional diffraction setups tested at the PF1B beam line are presented. For these measurements, the gratings had a period $p = 25\,\mu m$ and a duty cycle $R = 20\%$. Configurations with two gadolinium thicknesses t_{Gd} of $20\,\mu m$ and $30\,\mu m$ have been investigated. Note, the gratings with $t_{Gd} = 30\,\mu m$ present some manufacturing issues leading to a reduction of the visibility at longer wavelength compare to the setup with $t_{Gd} = 20\,\mu m$.

C.1 Results from the two other setups and comparisons

For these two measurements, every data points constituting the intensity modulations were taken during 80 s (2000 chopper sweeps at 25 Hz). For each setup, the Talbot-Lau carpets resulting from the simulation and the experimental data are presented. A detailed analysis at several remarkable wavelengths is presented in Fig. C.3, confirming once again the reliability of the simulation to accurately reproduce experimental data.

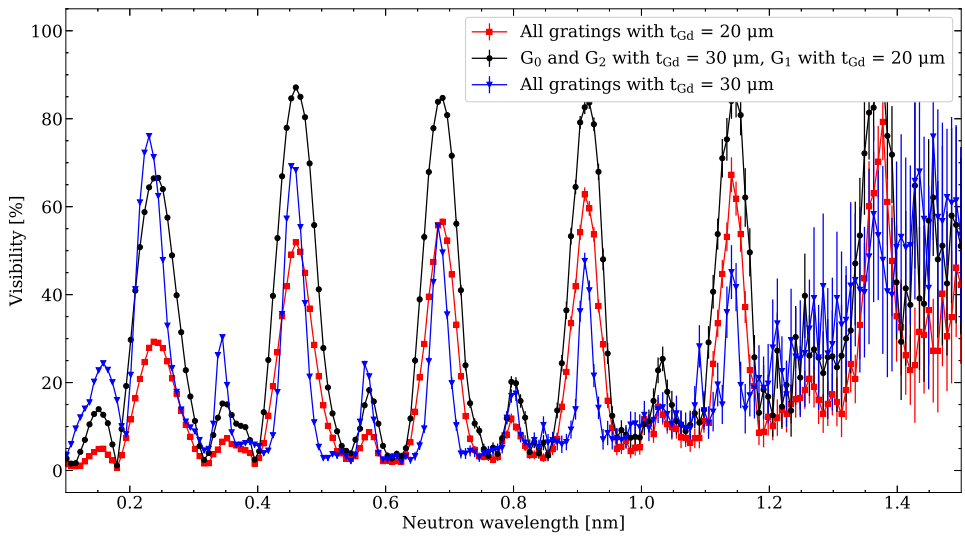

Figure C.1. Visibility of the oscillating intensity pattern as a function of the neutron wavelength for setups in the diffraction regime where $p = 25\,\mu m$ and $R = 20\%$. Three combinations of gadolinium thicknesses were tested: All gratings with $t_{Gd} = 20\,\mu m$ (red), all gratings with $t_{Gd} = 30\,\mu m$ (blue), and a mixed setup with G_0 and G_2 having $t_{Gd} = 30\,\mu m$, and G_1 with $t_{Gd} = 20\,\mu m$ (black).

C.2 Carpet for all setups

C.2.1 All gratings with t_{Gd} = 20 µm

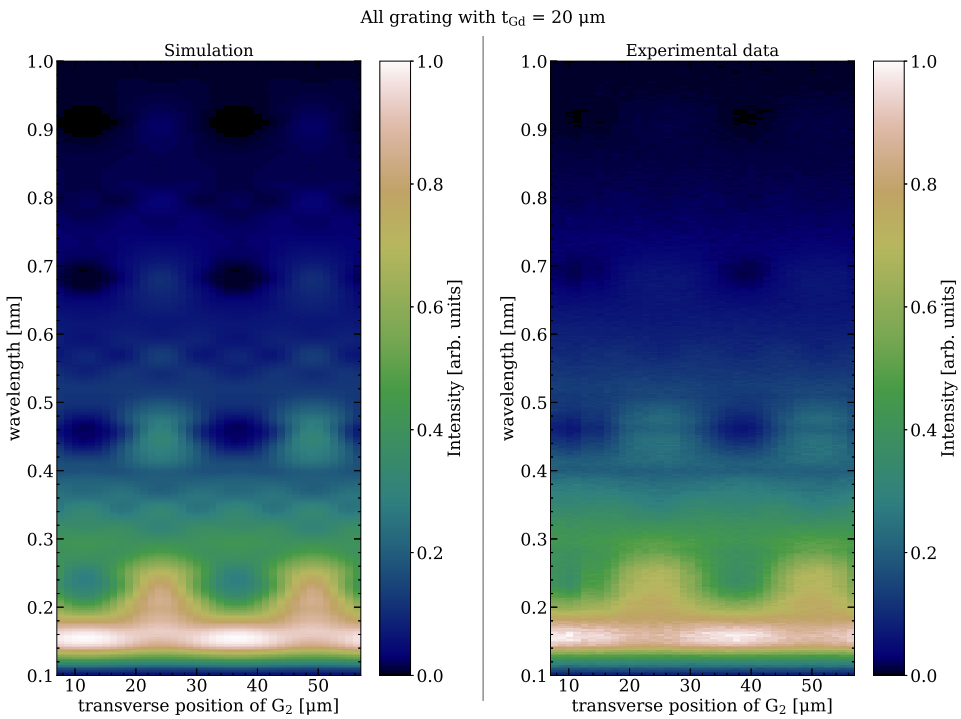

Figure C.2. 2D density plot (Talbot carpet) showing the neutron intensity as a function of transverse position and neutron wavelength.

C.2.2 All gratings with t_{Gd} = 30 µm

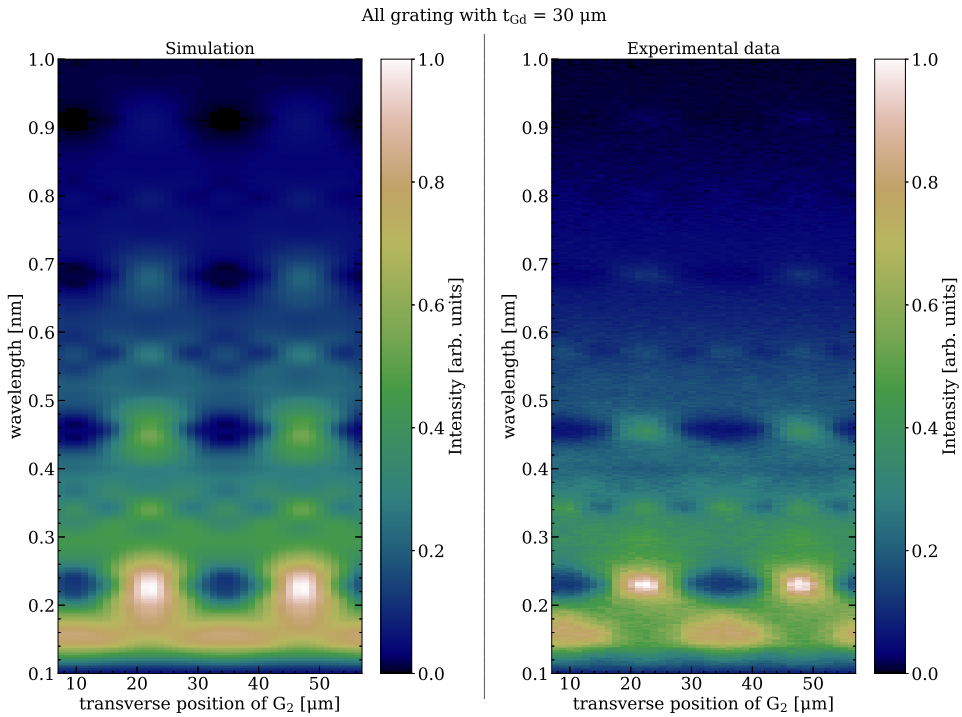

Figure C.3. 2D density plot (Talbot carpet) showing the neutron intensity as a function of transverse position and neutron wavelength.

C.3 Detailed analysis of mixed setup

C.3.1 Talbot wavelength λ_T and $0.67\lambda_T$ with p/2-shift

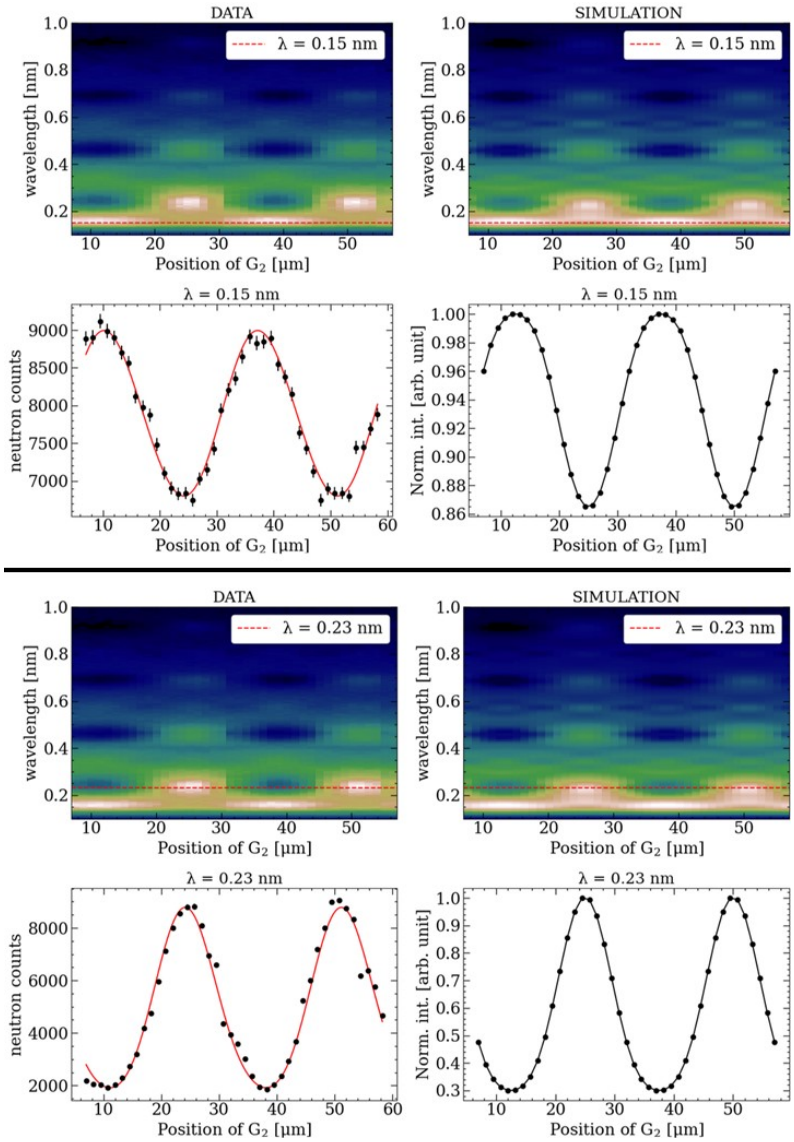

C.3.2 Higher orders $2\lambda_T$ and $3\lambda_T$

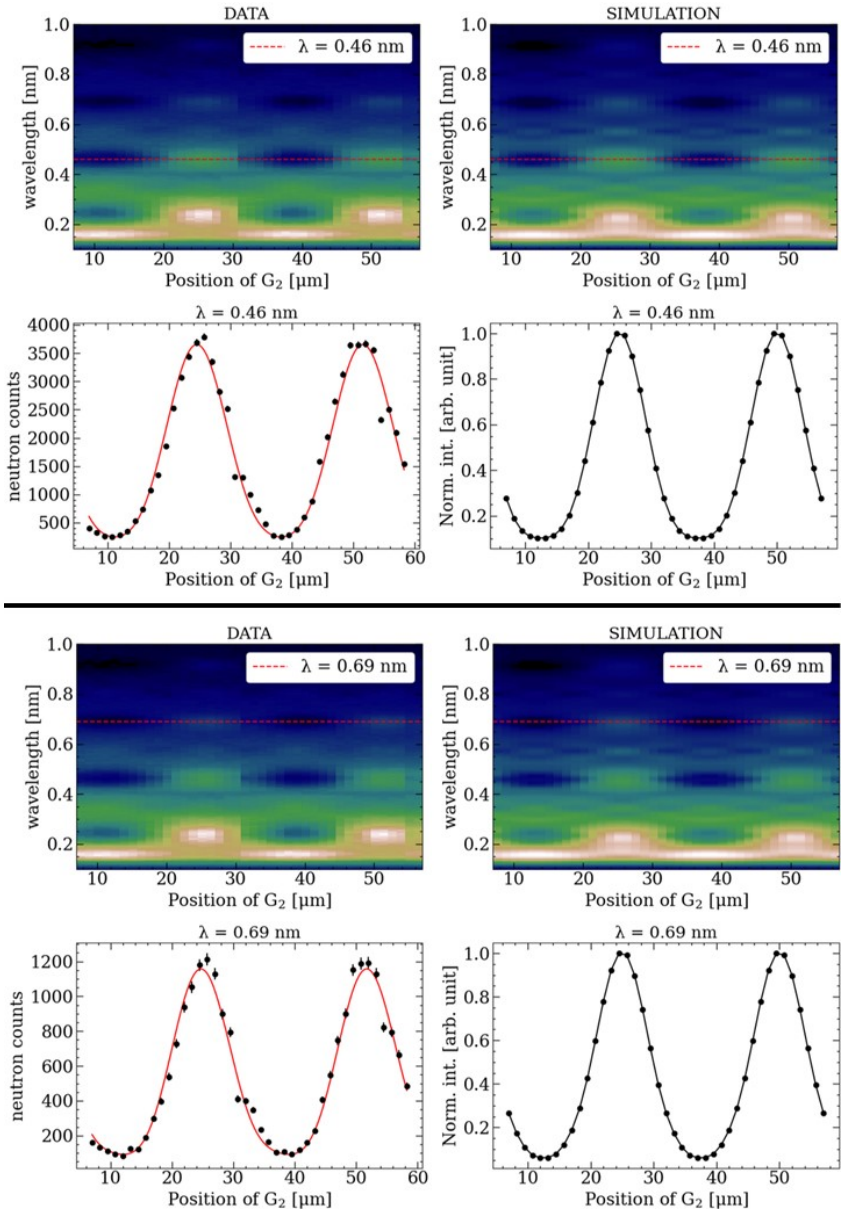

C.3.3 Higher half-orders $1.5\lambda_T$ and $2.5\lambda_T$

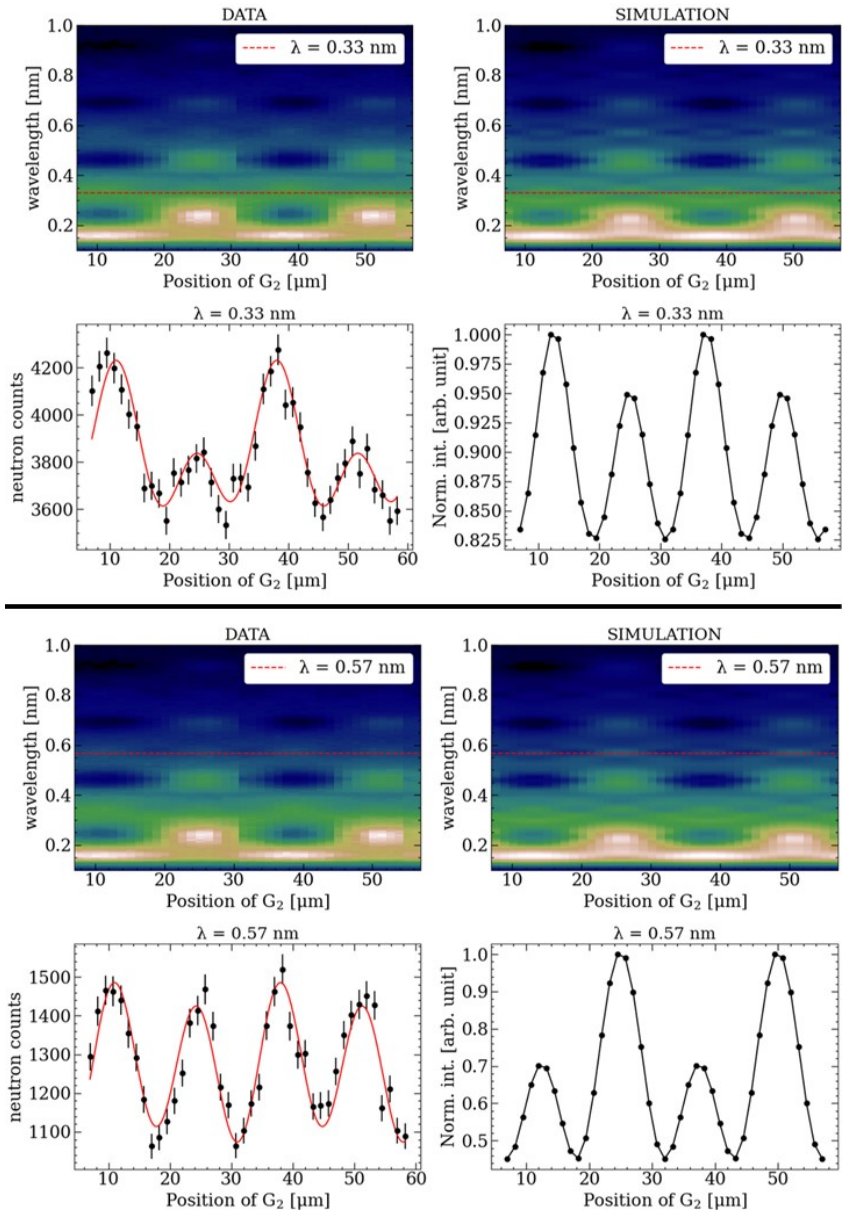

D. Results of neutron electric charge measurement

To complement the analysis provided in the main text, this appendix presents detailed results from each additional cycles of the neutron electric charge measurement. For each cycle, the following key plots are included:

- **Preliminary oscillating intensity pattern and double ratio $\mathcal{R}$:** These plots show the initial oscillating intensity patterns and the measured double ratio $\mathcal{R}$, crucial for assessing the effect of the electric field on the neutron beam.
- **Conversion of $\mathcal{R}$ to beam deflection Δy:** This plot converts the double ratio into the corresponding beam deflection, offering a direct measure of the response of the neutron beam to an electric field.
- **Stability measurement:** The stability of each cycle is assessed through plots of the beam spot positions over time, the difference between them to highlight the effectiveness of the two-beam method, and the corresponding Allan deviation plots.

These additional cycles have significantly enhanced the statistical significance of the results, allowing for a more precise determination of the neutron electric charge. By including multiple cycles, each with detailed analysis of the intensity patterns, beam deflections, and stability metrics, the reliability and repeatability of the neutron charge measurement are ensured. This data collection also helps in identifying and mitigating any potential systematic errors, further solidifying the confidence in the final outcomes of the experiment.

D.1 Cycle 1

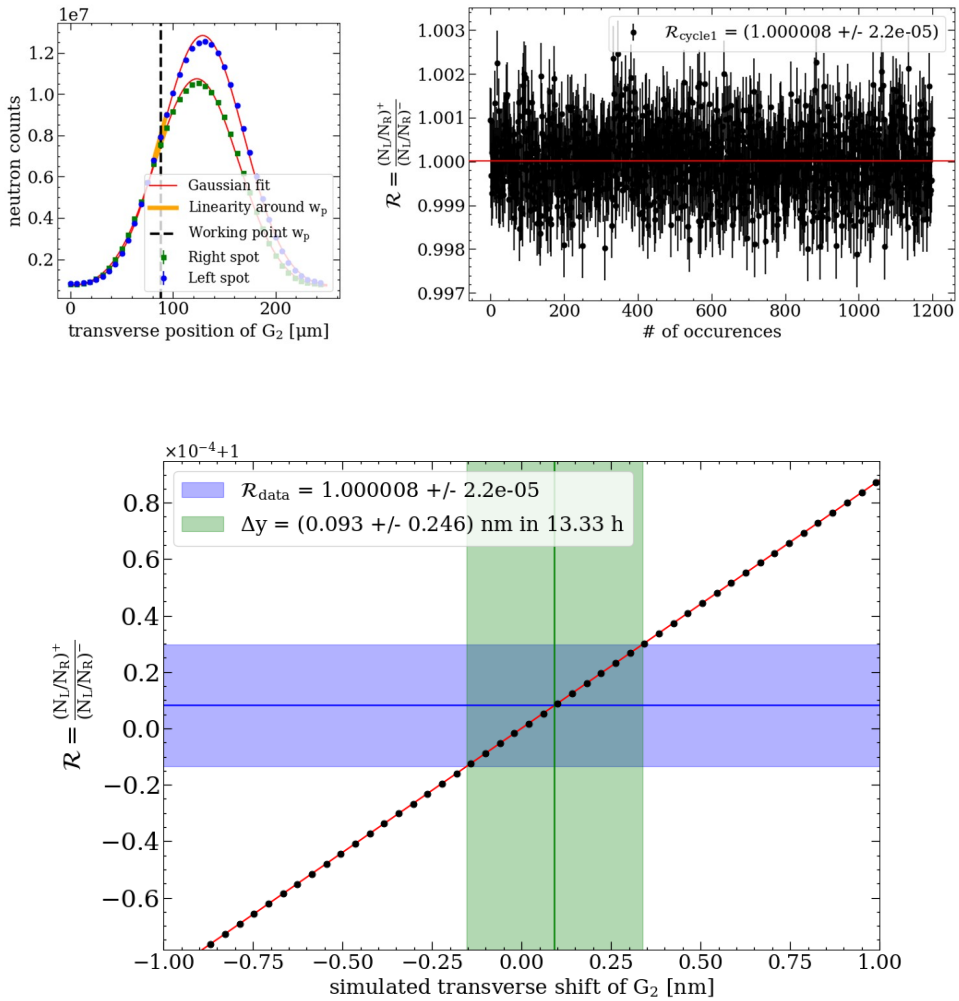

Figure D.1. Top: Intensity pattern before cycle to identify w_p (left). Measured double ratio $\mathcal{R}$ over 1200 polarity inversions. Bottom: Conversion to beam deflection Δy measured in 13.33 hours.

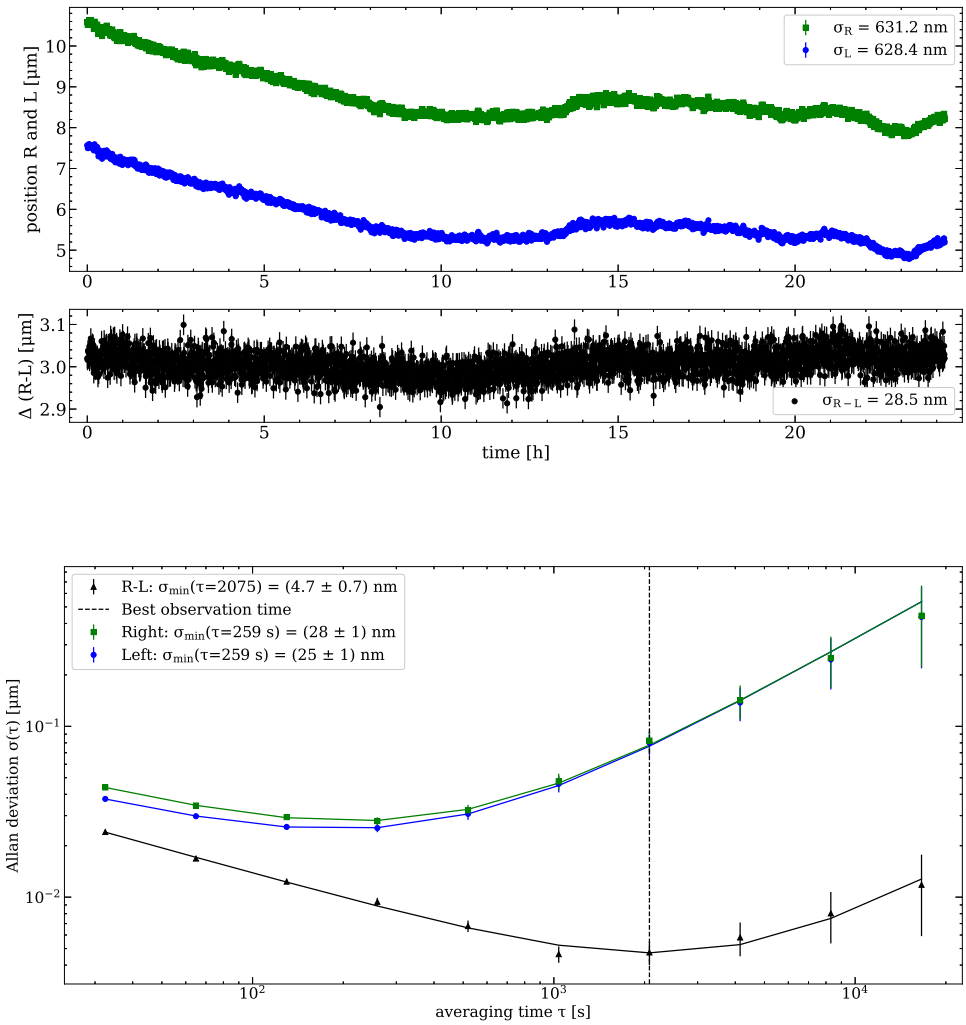

Figure D.2. Top: Left (blue) and right (green) beamspot's position over the cycle. The difference R-L is plotted in black. Bottom: Allan deviation showing an optimal observation time at $\tau = 2075$ s for the difference Δ.

D.2 Cycle 2: 10 points per polarity - 2240 Runs

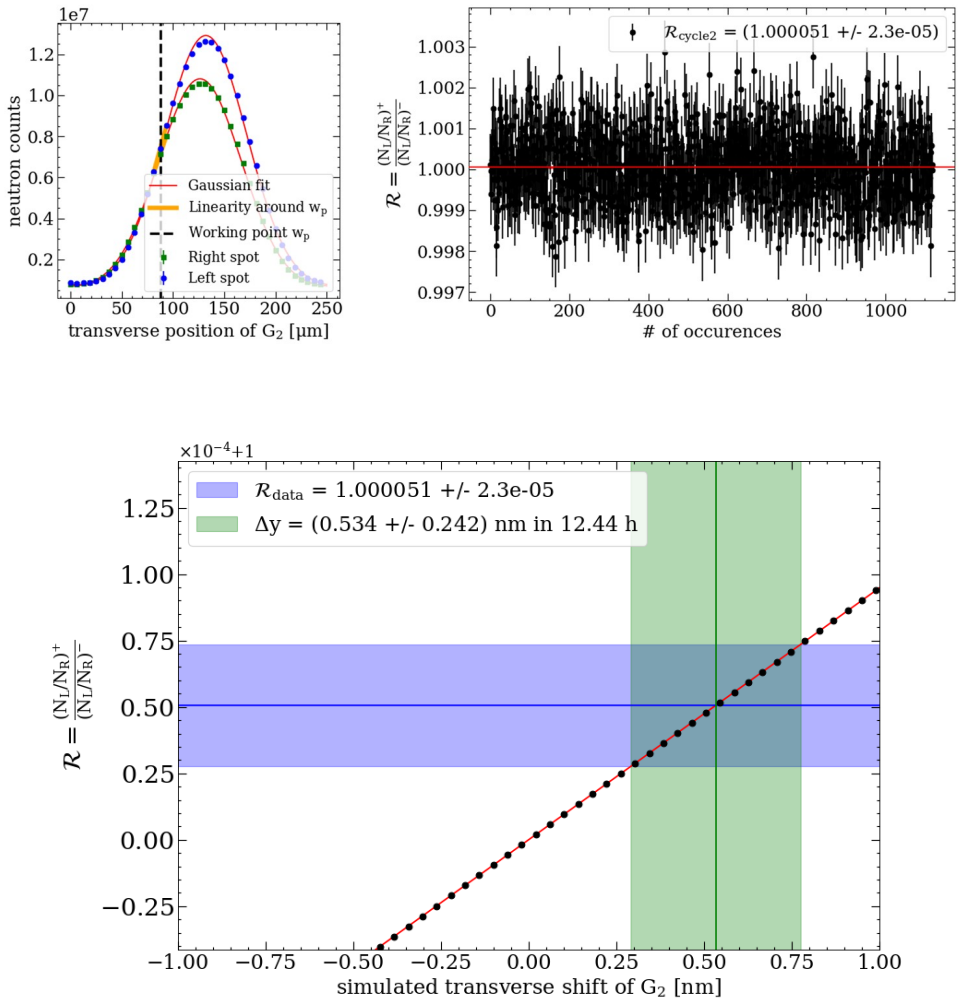

Figure D.3. Top: Intensity pattern before cycle to identify w_p (left). Measured double ratio $\mathcal{R}$ over 1120 polarity inversions. Bottom: Conversion to beam deflection Δy measured in 12.44 hours.

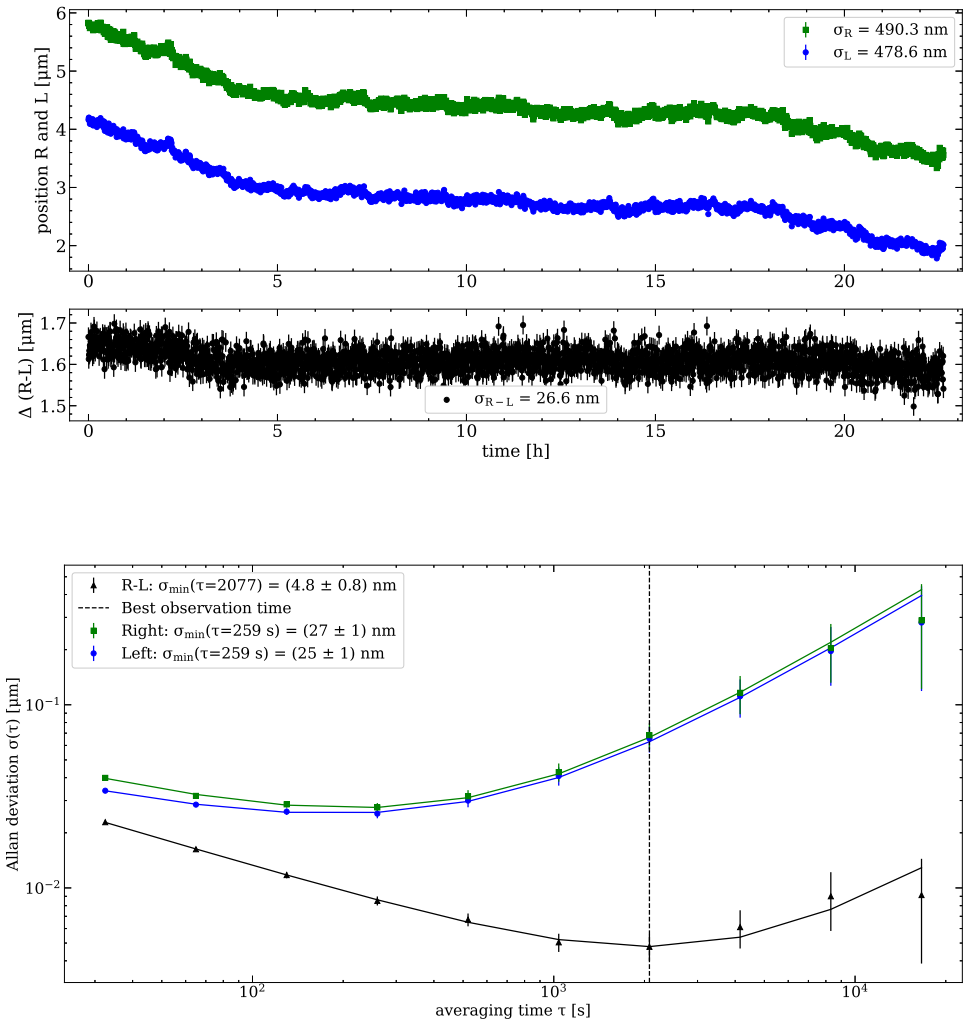

Figure D.4. Top: Left (blue) and right (green) beamspot's position over the cycle. The difference R-L is plotted in black. Bottom: Allan deviation showing an optimal observation time at $\tau = 2075$ s for the difference Δ.

D.3 Cycle 3: 10 points per polarity - 2320 Runs

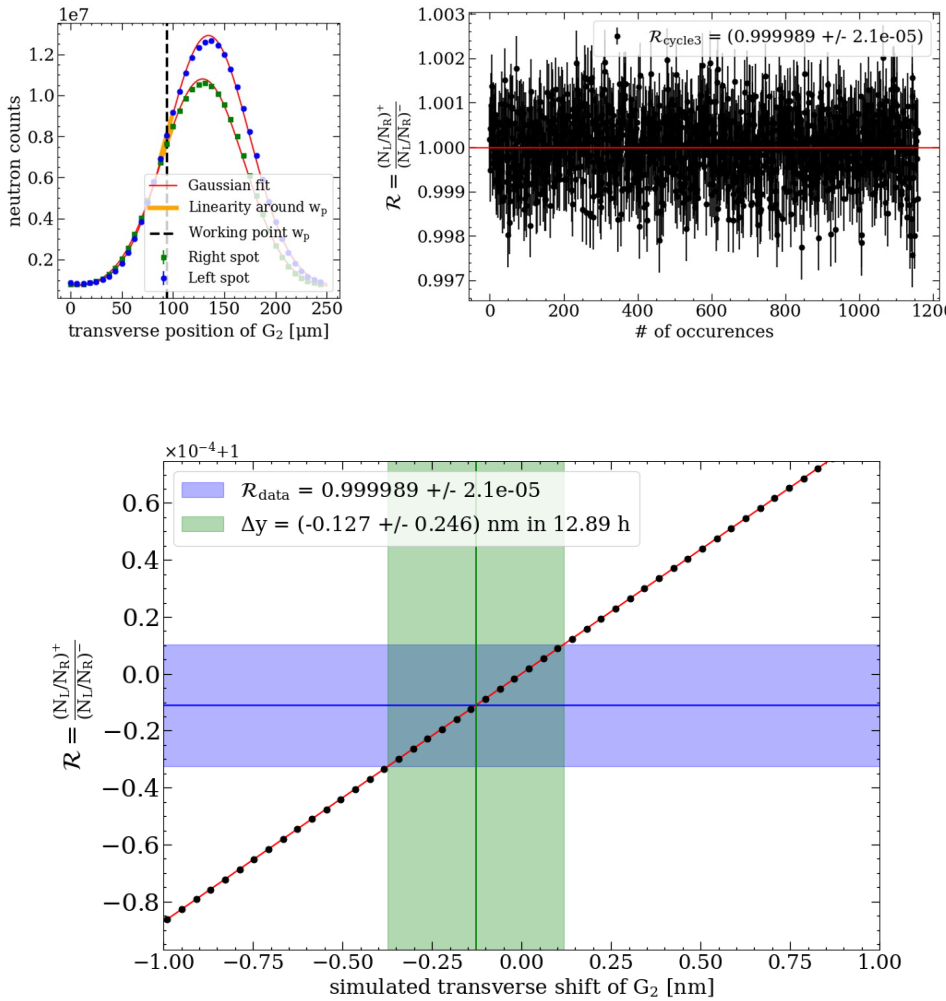

Figure D.5. Top: Intensity pattern before cycle to identify w_p (left). Measured double ratio $\mathcal{R}$ over 1160 polarity inversions. Bottom: Conversion to beam deflection Δy measured in 12.89 hours.

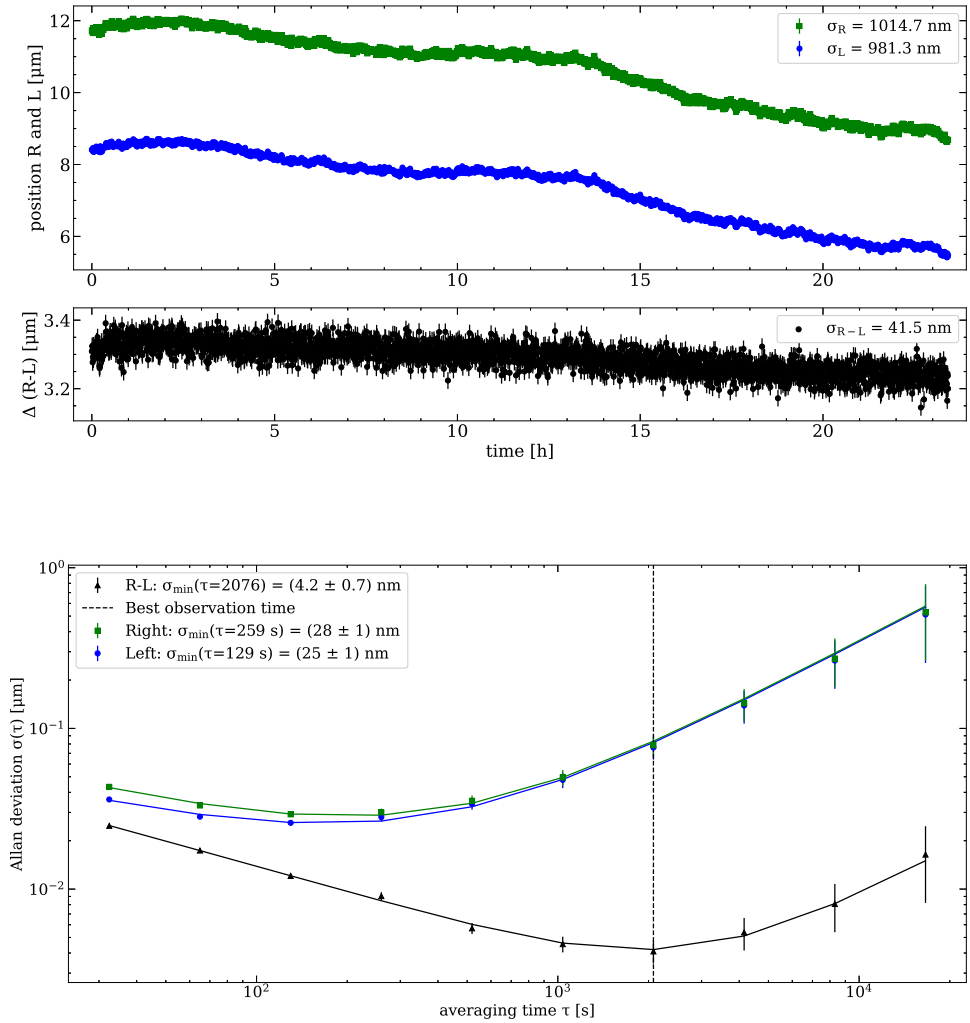

Figure D.6. Top: Left (blue) and right (green) beamspot's position over the cycle. The difference R-L is plotted in black. Bottom: Allan deviation showing an optimal observation time at $\tau = 2075$ s for the difference Δ.

D.4 Cycle 4a: 10 points per polarity - 1440 Runs

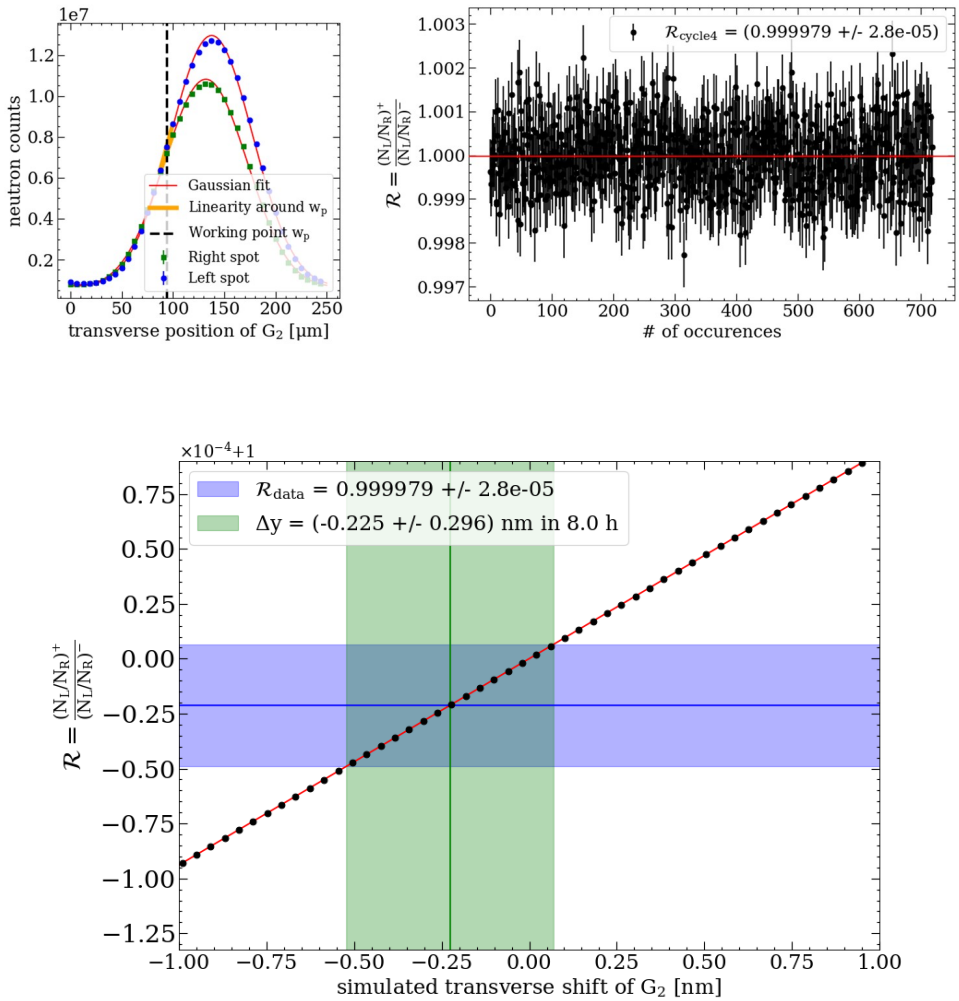

Figure D.7. Top: Intensity pattern before cycle to identify w_p (left). Measured double ratio $\mathcal{R}$ over 720 polarity inversions. Bottom: Conversion to beam deflection Δy measured in 8.0 hours.

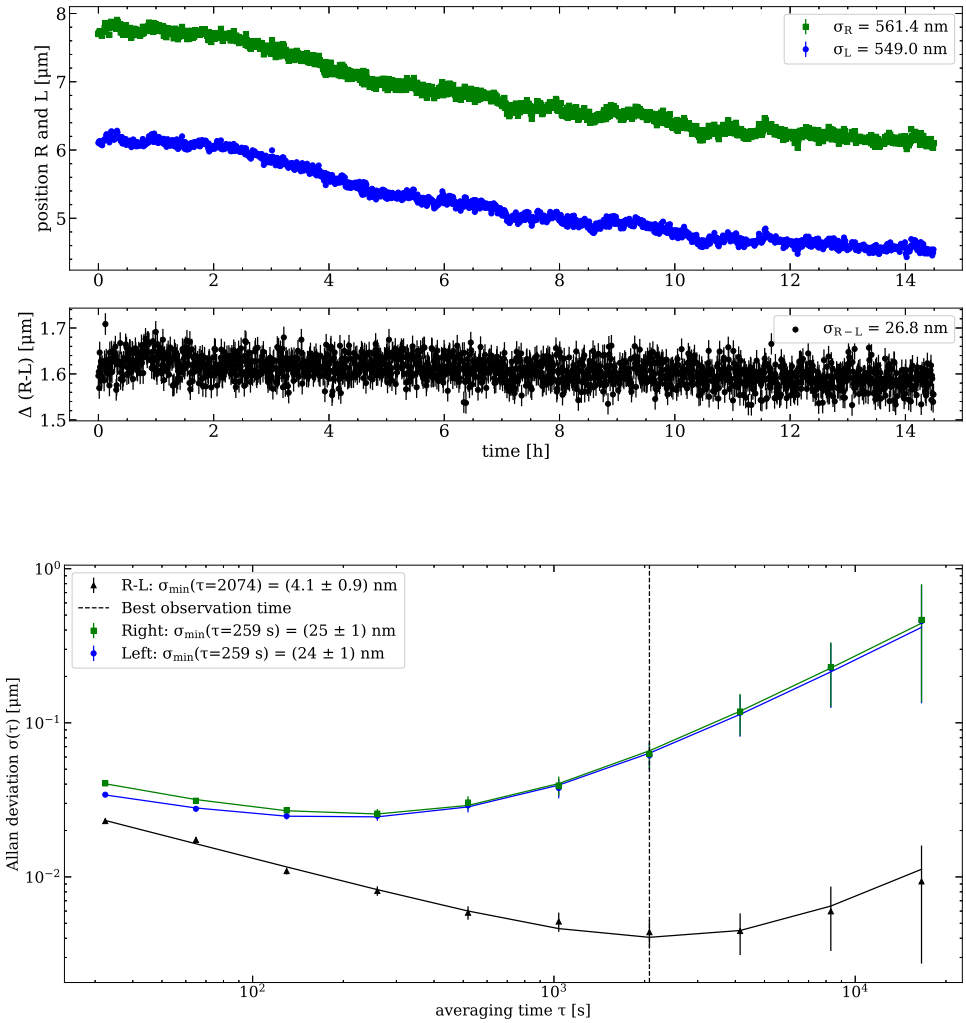

Figure D.8. Top: Left (blue) and right (green) beamspot's position over the cycle. The difference R-L is plotted in black. Bottom: Allan deviation showing an optimal observation time at $\tau = 2075$ s for the difference Δ.

D.5 Cycle 4b: 10 points per polarity - 720 Runs

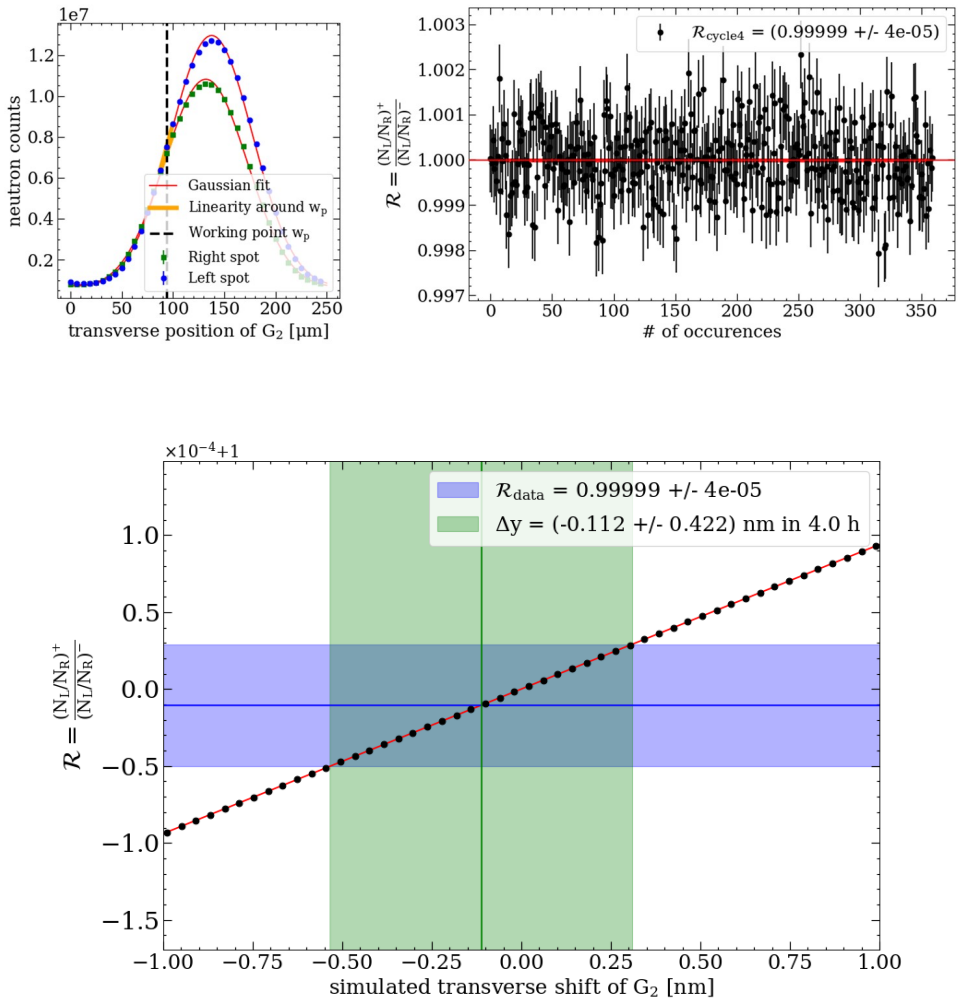

Figure D.9. Top: Intensity pattern before cycle to identify w_p (left). Measured double ratio $\mathcal{R}$ over 360 polarity inversions. Bottom: Conversion to beam deflection Δy measured in 4.0 hours.

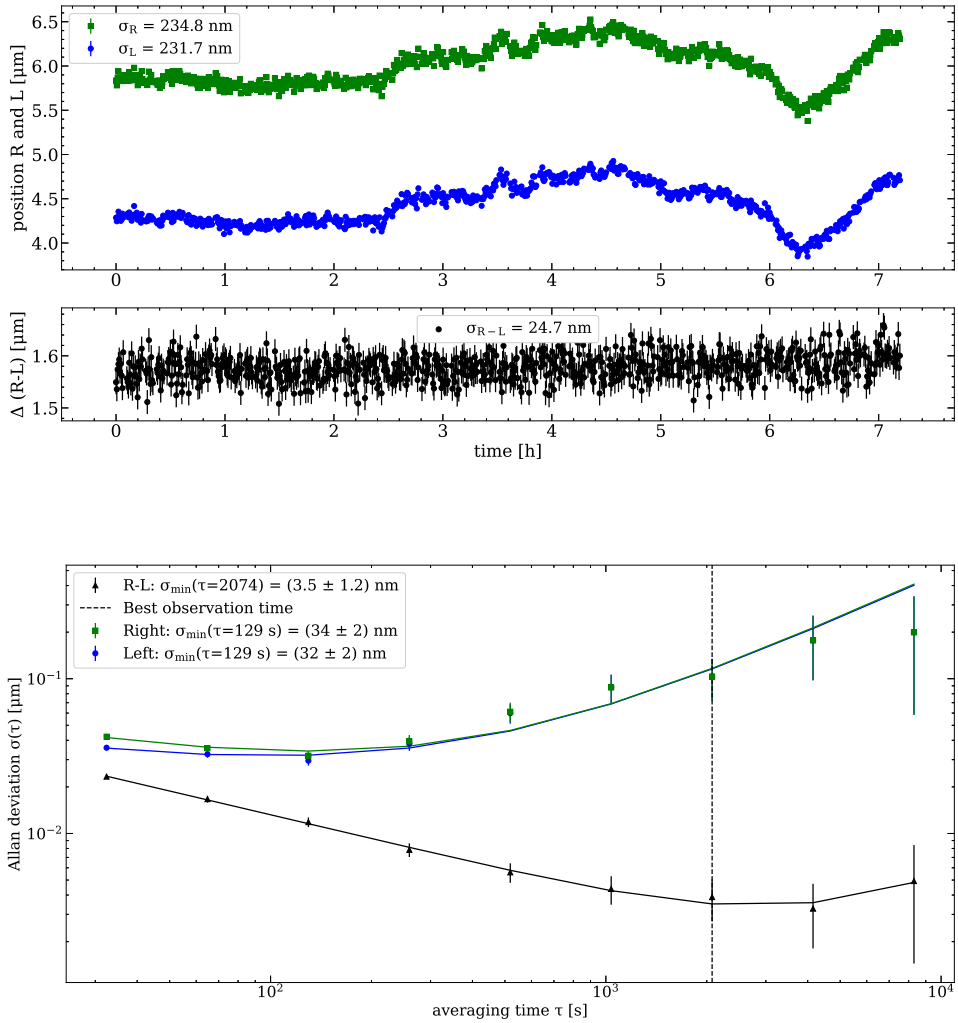

Figure D.10. Top: Left (blue) and right (green) beamspot's position over the cycle. The difference R-L is plotted in black. Bottom: Allan deviation showing an optimal observation time at $\tau = 2075$ s for the difference Δ.

D.6 Cycle 5: 5 points per polarity - 2400 Runs

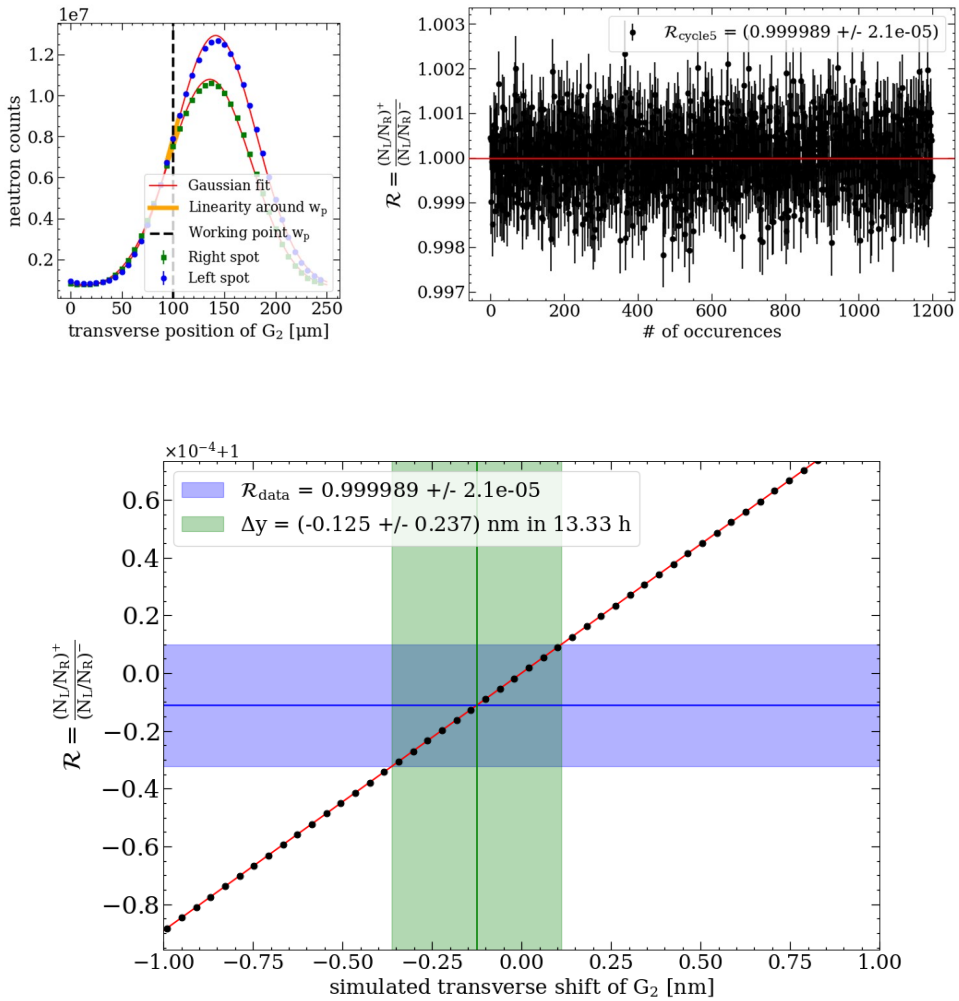

Figure D.11. Top: Intensity pattern before cycle to identify w_p (left). Measured double ratio $\mathcal{R}$ over 1200 polarity inversions. Bottom: Conversion to beam deflection Δy measured in 13.33 hours.

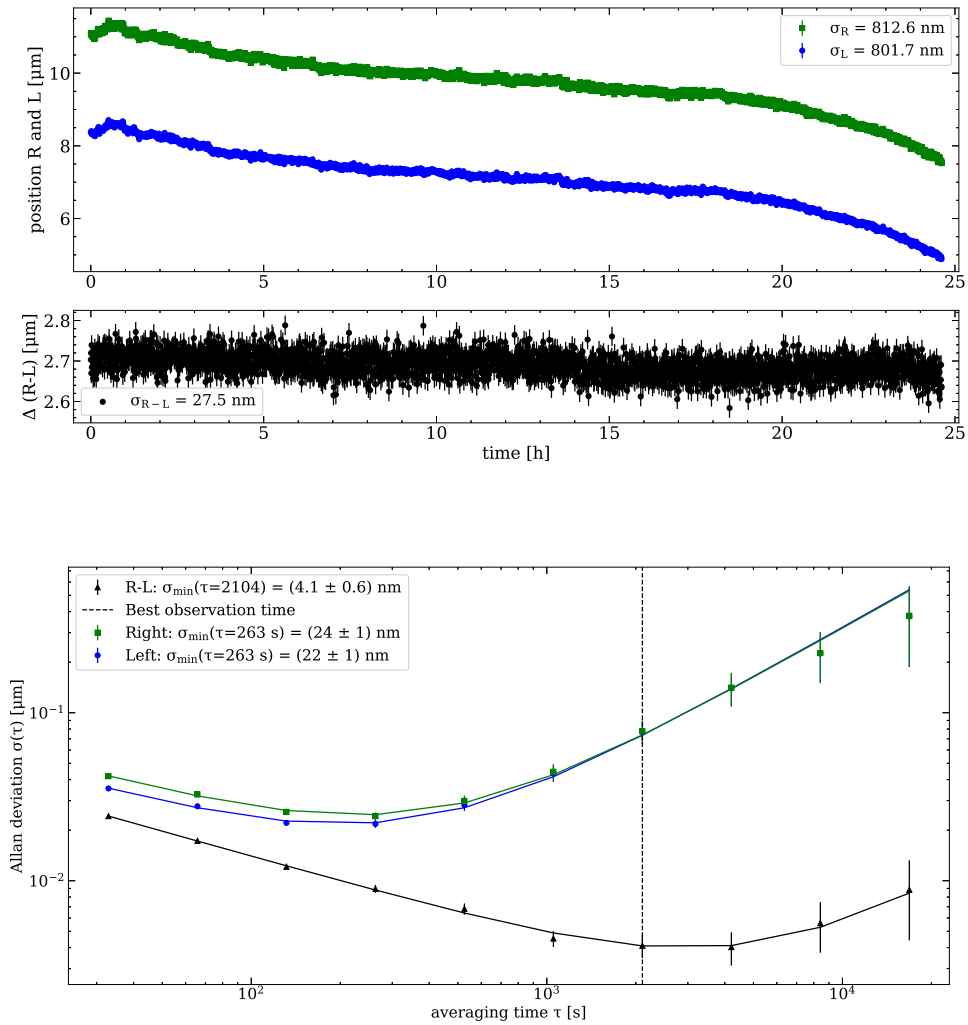

Figure D.12. Top: Left (blue) and right (green) beamspot's position over the cycle. The difference R-L is plotted in black. Bottom: Allan deviation showing an optimal observation time at $\tau = 2075$ s for the difference Δ.

D.7 Results and projections for all cycles

Below, the results from the first QNeutron campaign to measure the neutron electric charge, as well as the detailed predictions and comparisons for each cycle.

Cycle	$(\mathcal{R}-1)\times10^5$	Δy [nm]	$Q_n \times 10^{19}$ [e]	Time [h]
1	0.8 ± 2.2	0.093 ± 0.246	1.05 ± 2.76	13.33
2	5.1 ± 2.3	0.534 ± 0.242	5.99 ± 2.72	12.48
3	-1.1 ± 2.1	-0.127 ± 0.246	-1.42 ± 2.76	12.88
4	1.8 ± 2.3	-0.188 ± 0.242	-2.11 ± 2.72	12.0
5	-1.2 ± 2.1	-0.125 ± 0.237	-1.40 ± 2.66	13.36
6	-	-0.13 ± 0.195	-1.46 ± 2.19	19.7

Table D.1. Summary of results for different run conditions. The table shows the measured ratio ($\mathcal{R}$), beam deflection with associated error (Δy), and corresponding neutron electric charge Q_n for each cycle.

When combining everything together, the final results stands at:

$$Q_n = (0.11 \pm 1.06) \times 10^{-19}\, e \quad \text{in} \quad 83.73\,\text{h} \tag{D.1}$$

Next, the measured value of the sensitivity is compared to the theoretical prediction using the formula introduced previously and by using the remaining parameters and their values in Table D.2:

- **Grating period (p)**: 250 µm.
- **Visibility (η)**: Measured visibility of the interference pattern.
- **Total number of neutron counts at the working point (N_w)**: Summed over the entire measurement period.

Here, the count are evaluated at the steepest of the Gaussian-looking modulation, corresponding to a point slightly higher than the mid-height of the curve. Finally, the two sensitivities are compared and listed in Table D.3.

Cycle	Visibility (η)	Total Neutron Counts (N)
1	0.882	34.18×10^9
2	0.882	30.30×10^9
3	0.882	34.81×10^9
4	0.882	30.91×10^9
5	0.882	35.85×10^9
6	0.882	53.25×10^9
ALL	0.882	219.3×10^9

Table D.2. Visibility and total number of neutron counts for each cycle.

Cycle	Meas. Sensitivity $\sigma(Q_n)_{\mathrm{m}}$	Theo. Sensitivity $\sigma(Q_n)_{\mathrm{th}}$
1	$2.77 \times 10^{-19}\, e$	$2.75 \times 10^{-19}\, e$
2	$2.73 \times 10^{-19}\, e$	$2.92 \times 10^{-19}\, e$
3	$2.77 \times 10^{-19}\, e$	$2.73 \times 10^{-19}\, e$
4	$2.73 \times 10^{-19}\, e$	$2.90 \times 10^{-19}\, e$
5	$2.67 \times 10^{-19}\, e$	$2.69 \times 10^{-19}\, e$
6	$2.20 \times 10^{-19}\, e$	$2.21 \times 10^{-19}\, e$
ALL	$1.06 \times 10^{-19}\, e$	$1.09 \times 10^{-19}\, e$

Table D.3. Comparison of measured and theoretical sensitivities for each cycle.

Bibliography

[1] A. Coc, "Primordial nucleosynthesis", in *Journal of Physics: Conference Series*. 2016, vol. 665, p. 012001, IOP Publishing, Nuclear Physics in Astrophysics VI (NPA6), 19–24 May 2013, Lisbon, Portugal.

[2] Gary Steigman, "Primordial nucleosynthesis in the precision cosmology era", *Annual Review of Nuclear and Particle Science*, vol. 57, pp. 463–491, 2007.

[3] Y. Nagai, K. Takeda, S. Motoyama, T. Ohsaki, M. Igashira, N. Mukai, F. Uesawa, T. Ando, H. Kitazawa, and T. Fukuda, "Neutron capture cross sections of light nuclei in primordial nucleosynthesis", *Nuclear Instruments and Methods in Physics Research Section B: Beam Interactions with Materials and Atoms*, vol. 56-57, pp. 492–495, 1991.

[4] Dirk Dubbers and Michael G. Schmidt, "The neutron and its role in cosmology and particle physics", *Reviews of Modern Physics*, vol. 83, no. 4, pp. 1111–1171, 2011.

[5] H. G. Börner and F. Gönnenwein, *The neutron: a tool and an object in nuclear and particle physics*, World Scientific, Singapore, 2011.

[6] P. A. Zyla and others (Particle Data Group), "Review of particle physics", *Progress of Theoretical and Experimental Physics*, vol. 2020, no. 8, pp. 083C01, 2020.

[7] Robert Foot, Girish C. Joshi, H. Lew, and R. R. Volkas, "Charged neutrinos?", *Modern Physics Letters A*, vol. 5, pp. 95, 1990, Erratum: Mod. Phys. Lett. A 5 (1990) 2085.

[8] Eiichi Akasugi and Minoru Tanaka, "Charged Neutrinos and Atoms in the Standard Model", *Progress of Theoretical Physics*, vol. 87, no. 3, pp. 679–688, 1992.

[9] Weston M. Stacey, *Nuclear Reactor Physics*, Wiley-VCH, 2007.

[10] K. F. Smith, "Ultra-cold neutrons", *Contemporary Physics*, vol. 21, no. 6, pp. 631–650, 1980.

[11] James Chadwick, "Possible existence of a neutron", *Nature*, vol. 129, no. 3252, pp. 312, 1932.

[12] Hartmut Abele, "The neutron: Its properties and basic interactions", *Progress in Particle and Nuclear Physics*, vol. 60, no. 1, pp. 1–81, 2008.

[13] G.L. Greene et al., "New determination of the deuteron binding energy and the neutron mass", *Physical Review Letters*, vol. 56, no. 8, pp. 819–822, 1986.

[14] Th. Sexl, "Spin and statistics of the neutron", *Nature*, vol. 132, pp. 174, 1933.

[15] G. L. Greene, N. F. Ramsey, W. Mampe, J. M. Pendlebury, K. Smith, W. B. Dress, P. D. Miller, and Paul Perrin, "Measurement of the neutron magnetic moment", *Phys. Rev. D*, vol. 20, pp. 2139–2153, Nov 1979.

[16] A. Serebrov, V. Varlamov, A. Kharitonov, A. Fomin, Y. Pokotilovski, P. Geltenbort, J. Butterworth, I. Krasnoschekova, M. Lasakov, R. Taldaev, and et al., "Measurement of the neutron lifetime using a gravitational trap and a low-temperature Fomblin coating", *Phys. Lett. B*, vol. 605, pp. 72–78, 2005.

[17] A. Steyerl, J. Pendlebury, C. Kaufman, S. Malik, and A. Desai, "Quasielastic scattering in the interaction of ultracold neutrons with a liquid wall and application in a reanalysis of the Mambo I neutron-lifetime experiment", *Phys. Rev. C*, vol. 85, pp. 065503, 2012.

[18] V.F. Ezhov, A. Andreev, G. Ban, B. Bazarov, P. Geltenbort, A. Glushkov, V. Knyazkov, N. Kovrizhnykh, G. Krygin, O. Naviliat-Cuncic, and et al., "Measurement of the neutron lifetime with ultra-cold neutrons stored in a

magneto-gravitational trap", *J. Exp. Theor. Phys. Lett.*, vol. 107, pp. 707–711, 2018.

[19] A. Pichlmaier, V. Varlamov, K. Schreckenbach, and P. Geltenbort, "Neutron lifetime measurement with the UCN trap-in-trap MAMBO II", *Phys. Lett. B*, vol. 693, pp. 221–226, 2010.

[20] S. Arzumanov, L. Bondarenko, S. Chernyavsky, P. Geltenbort, V. Morozov, V. Nesvizhevsky, Y. Panin, and A. Strepetov, "A measurement of the neutron lifetime using the method of storage of ultracold neutrons and detection of inelastically up-scattered neutrons", *Phys. Lett. B*, vol. 745, pp. 79–89, 2015.

[21] R.W. Jr. Pattie, N.B. Callahan, C. Cude-Woods, E.R. Adamek, L.J. Broussard, S.M. Clayton, S.A. Currie, E.B. Dees, X. Ding, E.M. Engel, and et al., "Measurement of the neutron lifetime using a magneto-gravitational trap and *in situ* detection", *Science*, vol. 360, pp. 627–632, 2018.

[22] F.M. Gonzalez, E.M. Fries, C. Cude-Woods, T. Bailey, M. Blatnik, L.J. Broussard, N.B. Callahan, J.H. Choi, S.M. Clayton, S.A. Currie, and et al., "Improved neutron lifetime measurement with UCNτ", *Phys. Rev. Lett.*, vol. 127, pp. 162501, 2021.

[23] A.P. Serebrov, E.A. Kolomensky, A.K. Fomin, I.A. Krasnoshchekova, A.V. Vassiljev, D.M. Prudnikov, I.V. Shoka, A.V. Chechkin, M.E. Chaikovskiy, V.E. Varlamov, and et al., "Neutron lifetime measurements with a large gravitational trap for ultracold neutrons", *Phys. Rev. C*, vol. 97, pp. 055503, 2018.

[24] J.S. Nico, M.S. Dewey, D.M. Gilliam, F.E. Wietfeldt, X. Fei, W.M. Snow, G.L. Greene, J. Pauwels, R. Eykens, A. Lamberty, and et al., "Measurement of the neutron lifetime by counting trapped protons in a cold neutron beam", *Phys. Rev. C*, vol. 71, pp. 055502, 2005.

[25] A.T. Yue, M.S. Dewey, D.M. Gilliam, G.L. Greene, A.B. Laptov, J.S. Nico, W.M. Snow, and F.E. Wietfeldt, "Improved determination of the neutron lifetime", *Phys. Rev. Lett.*, vol. 111, pp. 222501, 2013.

[26] Fred E. Wietfeldt, "The neutron lifetime discrepancy and its implications for cosmology and dark matter", *Symmetry*, vol. 16, no. 8, pp. 956, 2024.

[27] Geoffrey L. Greene and Peter Geltenbort, "A puzzle lies at the heart of the atom", *Scientific American*, April 2016.

[28] Fred E. Wietfeldt and Geoffrey L. Greene, "Colloquium: The neutron lifetime", *Rev. Mod. Phys.*, vol. 83, pp. 1173, 2011.

[29] C. G. Shull, K. W. Billman, and F. A. Wedgwood, "Experimental limit for the neutron charge", *Physical Review*, vol. 153, no. 4, pp. 1415–1417, 1967.

[30] J. Baumann, R. Gähler, J. Kalus, and W. Mampe, "Experimental limit for the charge of the free neutron", *Phys. Rev. D*, vol. 37, pp. 3107, 1988.

[31] K. Durstberger-Rennhofer, T. Jenke, and H. Abele, "Probing the neutron's electric neutrality with ramsey spectroscopy of gravitational quantum states of ultracold neutrons", *Physical Review D: Particles, Fields, Gravitation, and Cosmology*, vol. 84, no. 3, pp. 036004, 2011.

[32] C. Abel et al., "Measurement of the permanent electric dipole moment of the neutron", *Physical Review Letters*, vol. 124, no. 8, pp. 081803, 2020.

[33] R. Pynn, "Neutron scattering: A primer", *Los Alamos Science*, vol. 19, pp. 1–31, 1990.

[34] Sven C. Vogel, "A review of neutron scattering applications to nuclear materials", *ISRN Materials Science*, vol. 2013, pp. 1–4, January 2013.

[35] J.S. Brenizer, "A review of significant advances in neutron imaging from conception to the present", *Physics Procedia*, vol. 43, pp. 10–20, December 2013.

[36] U. Garbe, F. Salvemini, and J. J. Bevit, Eds., *Neutron Radiography WCNR-11: 11th World Conference on Neutron Radiography (WCNR-11) Held the 2nd-7th, September 2018 in Sydney, Australia*, Materials Research Forum, 2020.

[37] Jeffrey S. Nico and W. Michael Snow, "Fundamental neutron physics", *Annual*

Review of Nuclear and Particle Science, vol. 55, pp. 27–69, December 2005.

[38] International Atomic Energy Agency, *Advances in Boron Neutron Capture Therapy*, Non-serial Publications. IAEA, Vienna, 2023.

[39] Rolf F. Barth, Zhong Zhang, and Tingting Liu, "A realistic appraisal of boron neutron capture therapy as a cancer treatment modality", *Cancer Communications*, vol. 38, no. 1, pp. 1–7, 2018.

[40] Satoshi Kawabata, Shinichiro Miyatake, Toshihiko Kuroiwa, Katsuyuki Yokoyama, Atsushi Doi, Koji Iida, Satoko Miyata, Naoko Nonoguchi, Hirofumi Michiue, Makoto Takahashi, Tomoyuki Inomata, Yoshitomo Imahori, Masahiro Kirihata, Yoshinori Sakurai, Atsushi Maruhashi, Hiroyuki Kumada, and Koji Ono, "Boron neutron capture therapy for newly diagnosed glioblastoma", *Journal of Radiation Research*, vol. 50, no. 1, pp. 51–60, 2009.

[41] Amirreza Jalilian and Mary Albon, "Neutrons save lives: Research reactors for production of medical isotopes and radiopharmaceuticals", *IAEA Bulletin*, vol. 64, no. 4, December 2023.

[42] World Nuclear Association, "Radioisotopes in medicine", https://world-nuclear.org/information-library/non-power-nuclear-applications/radioisotopes-research/radioisotopes-in-medicine.aspx, 2024.

[43] Michael J. Ashworth and Thomas P. Abeles, "Neutron activation analysis and archaeology", *Nature*, vol. 209, no. 5031, pp. 9–12, 1966.

[44] Sophie Combet, "An introduction to neutrons for biology", *EPJ Web of Conferences*, vol. 236, pp. 01001, 2020.

[45] Benno P. Schoenborn, "A history of neutrons in biology: the development of neutron protein crystallography at BNL and LANL", *Acta Crystallographica Section D: Biological Crystallography*, vol. 66, no. 11, pp. 1262–1268, 2010.

[46] S. Teixeira, G. Zaccai, J. Ankner, M. C. Bellissent-Funel, R. Bewley, M. Blake-

ley, P. Callow, L. Coates, R. Dahint, R. Dalgliesh, N. Dencher, V. Forsyth, G. Fragneto, B. Frick, R. Gilles, T. Gutberlet, M. Haertlein, T. Hauß, W. Häußler, and K. Weiss, "New sources and instrumentation for neutrons in biology", *Chemical Physics*, vol. 345, no. 2-3, pp. 133–151, 2008.

[47] N. Kardjilov, I. Manke, A. Hilger, M. Strobl, J. Banhart, "Neutron imaging in materials science", *Materials Today*, vol. 14, pp. 248–256, 2011.

[48] P. S. Sarkar and Shefali Shukla, "Neutron imaging for material science and engineering", in *Neutron Imaging*, pp. 273–303. Springer, 2022.

[49] Hans Von Halban, Frédéric Joliot, and Lew Kowarski, "Energy of neutrons liberated in the nuclear fission of uranium induced by thermal neutrons", *Nature*, vol. 143, no. 3631, pp. 939, 1939.

[50] Robert Vandenbosch, "Dependence of fission fragment kinetic energies and neutron yields on nuclear structure", *Nuclear Physics*, vol. 46, pp. 129–140, 1963.

[51] S. K. Lamoreaux and R. Golub, "Experimental searches for the neutron electric dipole moment", *Journal of Physics G: Nuclear and Particle Physics*, vol. 36, no. 10, pp. 104002, 2009.

[52] Klaus Kirch and Philipp Schmidt-Wellenburg, "Search for electric dipole moments", *EPJ Web of Conferences*, vol. 234, pp. 01007, 2020.

[53] F. E. Wietfeldt, "Measurements of the neutron lifetime", *Atoms*, vol. 6, no. 4, pp. 70, 2018.

[54] Dirk Dubbers and Bastian Märkisch, "Precise measurements of the decay of free neutrons", *Annual Review of Nuclear and Particle Science*, vol. 71, pp. 139–163, September 2021.

[55] H. Abele, T. Jenke, H. Leeb, and J. Schmiedmayer, "Ramsey's method of separated oscillating fields and its application to gravitationally induced quantum phase shifts", *Phys. Rev. D*, vol. 81, pp. 065019, mar 2010.

[56] C. Siemensen, C. Düsing, P. Geltenbort, C. Giebel, T. Reich, C. Plonka, "Search for an electric charge of the neutron", *Phys. Rev. D*, vol. 97, pp. 052004, 2018.

[57] C. Siemensen, D. Brose, L. Böhmer, P. Geltenbort, and C. Plonka-Spehr, "Improved instrument for the determination of the neutron electric charge", *Nuclear Instruments and Methods in Physics Research Section A: Accelerators, Spectrometers, Detectors and Associated Equipment*, vol. 777, pp. 114–119, 2015.

[58] Joachim Bosina, Hanno Filter, Jakob Micko, and Tobias Jenke, "qBounce: First Measurement of the Neutron Electric Charge with a Ramsey-Type GRS Experiment", 2023.

[59] F. M. Piegsa, "Novel Concept for a Neutron Electric Charge Measurement using a Talbot-Lau Interferometer at a Pulsed Source", *Phys. Rev. C*, vol. 98, pp. 045503, 2018.

[60] H. F. Talbot, "Facts relating to Optical Science", *The London, Edinburgh, and Dublin Philosophical Magazine and Journal of Science*, vol. 9, pp. 401–407, 1836.

[61] S. Buathong, S. Srisuphaphon, and S. Deachapunya, "Investigations of Talbot and Talbot–Lau effects with various light sources", *Applied Physics B*, 2023.

[62] H Lau, "Die Lau-Schattenbilder", *Zeitschrift für Naturforschung A*, vol. 3, no. 5, pp. 371–373, 1948.

[63] Tobias Neuwirth, Alexander Backs, Alex Gustschin, Simon Vogt, Franz Pfeiffer, Peter Böni, and Michael Schulz, "A high visibility Talbot-Lau neutron grating interferometer to investigate stress-induced magnetic degradation in electrical steel", *Scientific Reports*, vol. 10, pp. 1764, 2020.

[64] K. T. A. Assumin-Gyimah, D. Dutta, D. S. Hussey, W. M. Snow, C. Langlois, and V. Lee, "Neutron phase contrast imaging of $PbWO_4$ crystals for G experiment test masses using a Talbot-Lau neutron interferometer", *Classical and Quantum Gravity*, vol. 39, no. 24, pp. 245014, 2022.

[65] Youngju Kim, Jacopo Valsecchi, Jongyul Kim, Seung Wook Lee, and Markus Strobl, "Symmetric Talbot-Lau neutron grating interferometry and incoherent scattering correction for quantitative dark-field imaging", *Scientific Reports*, vol. 9, pp. 18973, 2019.

[66] Youngju Kim, Daeseung Kim, Seho Lee, Jongyul Kim, Daniel S. Hussey, and Seung Wook Lee, "Neutron grating interferometer with an analyzer grating based on a light blocker", *Optics Express*, vol. 28, no. 16, pp. 23284–23293, 2020.

[67] Yoshichika Seki, Takenao Shinohara, Masahiro Hino, Riichiro Nakamura, Tetsuo Samoto, and Atsushi Momose, "Neutron phase imaging by a Talbot-Lau interferometer at kyoto university reactor", *Review of Scientific Instruments*, vol. 94, no. 10, pp. 103701, 2023.

[68] Norman F. Ramsey, "A molecular beam resonance method with separated oscillating fields", *Physical Review*, vol. 78, no. 6, pp. 695–699, Jun 1950.

[69] E. P. Tsentalovich, "The nEDM experiment at the SNS", *Physics of Particles and Nuclei*, vol. 45, no. 1, pp. 249–250, 2014.

[70] C. Abel, N. J. Ayres, G. Ban, G. Bison, K. Bodek, V. Bondar, E. Chanel, P. Chiu, B. Clement, C. Crawford, M. Daum, S. Emmenegger, P. Flaux, L. Ferraris-Bouchez, W. C. Griffith, Z. D. Grujić, P. G. Harris, W. Heil, N. Hild, and G. Zsigmond, "The n2EDM experiment at the Paul Scherrer Institute", in *EPJ Web of Conferences*, 2019, vol. 219, p. 02002.

[71] Florian M. Piegsa, "New concept for a neutron electric dipole moment search using a pulsed beam", *Physical Review C*, vol. 88, pp. 045502, 2013.

[72] Lev Vaidman, "Neutrons and photons inside a nested Mach-Zehnder interferometer", *Physical Review A*, vol. 101, no. 5, pp. 052119, 2020.

[73] D. A. Pushin, M. G. Huber, M. Arif, C. B. Shahi, J. Nsofini, C. J. Wood, D. Sarenac, and D. G. Cory, "Neutron interferometry at the national institute of standards and technology", *Advances in High Energy Physics*, vol. 2015,

pp. 687480, 2015.

[74] Helmut Rauch and Samuel A. Werner, *Neutron Interferometry: Lessons in Experimental Quantum Mechanics, Wave-Particle Duality, and Entanglement*, Oxford University Press, Oxford, UK, second edition, 2015.

[75] H. Lemmel, M. Jentschel, H. Abele, F. Lafont, B. Guerard, C. P. Sasso, G. Mana, and E. Massa, "Neutron interference from a split-crystal interferometer", *Journal of Applied Crystallography*, vol. 55, no. 4, pp. 870–875, August 2022.

[76] Hartmut Abele and Helmut Leeb, "Gravitation and quantum interference experiments with neutrons", *New Journal of Physics*, vol. 14, pp. 055010, 2012.

[77] J. M. Rocha and F. Dahia, "Neutron interferometry and tests of short-range modifications of gravity", *Physical Review D*, vol. 103, no. 12, pp. 124014, 2021.

[78] Liren Liu, "Talbot and Lau effects on incident beams of arbitrary wavefront, and their use", *Applied Optics*, vol. 28, no. 21, pp. 4668–4678, 1989.

[79] G. J. Swanson and E. N. Leith, "Lau effect and grating imaging", *Journal of the Optical Society of America*, vol. 72, no. 5, pp. 552, 1982.

[80] G. J. Swanson and E. N. Leith, "Analysis of the Lau effect and generalized grating imaging", *Journal of the Optical Society of America A*, vol. 2, no. 6, pp. 789, 1985.

[81] William B. Case, Mathias Tomandl, Sarayut Deachapunya, and Markus Arndt, "Realization of optical carpets in the Talbot and Talbot-Lau configurations", *Optics Express*, vol. 17, no. 23, pp. 20966–20974, 2009.

[82] L. Rosta, "Cold neutron research facility at the Budapest Neutron Centre", *Applied Physics A*, vol. 74, no. S1, pp. s52–s54, 2002.

[83] H. J. Prask, J. M. Rowe, J. J. Rush, and I. G. Schröder, "The NIST cold neutron

research facility", *Journal of Research of the National Institute of Standards and Technology*, vol. 98, no. 1, pp. 1, 1993.

[84] A. Anghel, F. Atchison, B. Blau, B. Van Den Brandt, M. Daum, R. Doelling, M. Dubs, P. Duperrex, A. Fuchs, D. George, L. Gültl, P. Hautle, G. Heidenreich, F. Heinrich, R. Henneck, S. Heule, T. Hofmann, S. Joray, M. Kasprzak, and S. Grigoriev, "The PSI ultra-cold neutron source", *Nuclear Instruments and Methods in Physics Research Section A: Accelerators, Spectrometers, Detectors and Associated Equipment*, vol. 611, no. 2-3, pp. 272–275, 2009.

[85] W. Fischer, "SINQ — the spallation neutron source, a new research facility at PSI", *Physica B: Condensed Matter*, vol. 234-236, pp. 1202–1208, 1997.

[86] P. Ageron, "Cold neutron sources at ILL", *Nuclear Instruments and Methods in Physics Research Section A: Accelerators, Spectrometers, Detectors and Associated Equipment*, vol. 284, no. 1, pp. 197–199, 1989.

[87] H. Abele, A. Alekou, A. Algora, K. Andersen, S. Baeßler, L. Barron-Pálos, J. Barrow, E. Baussan, P. Bentley, Z. Berezhiani, Y. Beßler, A. K. Bhattacharyya, A. Bianchi, J. Bijnens, C. Blanco, N. Blaskovic Kraljevic, M. Blennow, K. Bodek, M. Bogomilov, C. Bohm, and Y. Zou, "Particle physics at the European Spallation Source", *Physics Reports*, 2023.

[88] H. Abele, D. Dubbers, H. Häse, M. Klein, A. Knöpfler, M. Kreuz, T. Lauer, B. Märkisch, D. Mund, V. Nesvizhevsky, A. Petoukhov, C. Schmidt, M. Schumann, and T. Soldner, "Characterization of a ballistic supermirror neutron guide", *Nuclear Instruments and Methods in Physics Research Section A: Accelerators, Spectrometers, Detectors and Associated Equipment*, vol. 562, no. 1, pp. 407–417, June 2006.

[89] A. Fratangelo, P. Heil, C. Klauser, G. Markaj, M. Persoz, C. Pistillo, et al., "Frequency-offset separated oscillatory fields technique applied to neutrons", *Physical Review C: Nuclear Physics*, vol. 109, no. 6, pp. 065503, 2024.

[90] Estrid Buhl Naver, M. Bertelsen, Maja Østergaard, D. Battaglia, P. Willendrup,

P. Trtik, et al., "Phase-contrast neutron imaging compared with wave propagation and McStas simulations", *Journal of Applied Crystallography*, vol. 57, no. 3, pp. 707–713, 2024.

[91] M. Nikolic, A. Cesarini, A. J. Saadun, E. R. Carreon Ruiz, A. Borgschulte, P. Trtik, et al., "Operando neutron imaging", *Chimia*, vol. 78, no. 5, pp. 333–338, 2024.

[92] Z. Ma, S. Zheng, Y. Chen, R. Xu, Z. Y. Dong, J. Wang, et al., "Possible gapless quantum spin liquid behavior in the triangular-lattice Ising antiferromagnet $PrMgAl_{11}O_{19}$", *Physical Review B*, vol. 109, no. 16, pp. 165143, 2024.

[93] E. Törnquist, E. T. Wrammerfors, M. Pierantoni, A. Sjögren, A. Tengattini, A. Kaestner, et al., "Exploratory neutron tomography of articular cartilage", *Osteoarthritis and Cartilage*, 2024.

[94] P. Shafabakhsh, B. Cordonnier, A. Pluymakers, T. Le Borgne, J. Mathiesen, G. Linga, et al., "4D neutron imaging of solute transport and fluid flow in sandstone before and after mineral precipitation", *Water Resources Research*, vol. 60, no. 3, pp. e2023WR036293, 2024.

[95] N. M. Alderete, Y. Villagrán-Zaccardi, Y. Shields, P. Van den Heede, M. P. Zappitelli, R. Patel, et al., "Neutron radiography with simultaneous deformation measurements demand rethinking the modelling of imbibition in cement paste", *Cement and Concrete Research*, vol. 179, pp. 107481, 2024.

[96] PSI, "Infrastructure Surrounding at PSI", `https://www.psi.ch/en/guesthouse/infrastructure-general`, 2024.

[97] Hideaki Hotchi, "High-power proton accelerators for pulsed spallation neutron sources", *Review of Accelerator Science and Technology*, vol. 31, pp. Article 23, 2021.

[98] J. Adam, A. R. Balabekyan, V. S. Barashenkov, R. Brandt, V. M. Golovatiouk, V. G. Kalinnikov, K. Katovsky, M. I. Krivopustov, V. Kumar, H. Kumawat, R. Odoj, V. S. Pronskikh, A. A. Solnyshkin, V. I. Stegailov, V. M.

Tsoupko-Sitnikov, and W. Westmeier, "Spallation neutron spectrum on a massive lead/paraffin target irradiated with 1 GeV protons", *The European Physical Journal A*, vol. 23, no. 1, pp. 61–68, 2004.

[99] T. Asano, Y. Asano, Y. Iguchi, H. Kudo, S. Mori, M. Noguchi, Y. Takada, H. Hirabayashi, H. Ikeda, K. Katoh, K. Kondo, M. Takasaki, T. Tominaka, and A. Yamamoto, "Target dependence of charge distributions in spallation reactions of medium-mass nuclei with 12 GeV protons", *Physical Review C*, vol. 28, no. 4, pp. 1718–1724, 1983.

[100] P. J. McNulty, W. G. Abdel-Kader, and G. E. Farrell, "Proton induced spallation reactions", *Radiation Physics and Chemistry*, vol. 43, no. 1-2, pp. 139–149, 1994.

[101] V. D. Rusov, V. A. Tarasov, S. A. Chernezhenko, A. A. Kakaev, and V. P. Smolyar, "Neutron moderation theory with thermal motion of the moderator nuclei", *The European Physical Journal A*, vol. 53, no. 9, pp. 1–13, 2017.

[102] Monica Huerta Parajon, Estefania Abad, and Francico J. Bermejo, "A review of the cold neutron moderator materials: Neutronic performance and radiation effects", *Physics Procedia*, vol. 60, 2014.

[103] "Neutrons for society, continued", *Nature Physics*, vol. 13, pp. 199, 2017.

[104] Institut Laue-Langevin (ILL), "Annual report 2023", `https://www.ill.eu/fileadmin/user_upload/ILL/1_About_ILL/Documentation/Annual_report/AR-23/Annual_report_2023-flip.html`, 2023.

[105] M. Sakanoue and T. Nakanishi, "Measurement of neutron flux in nuclear reactor by means of fission track method", *Journal of the Atomic Energy Society of Japan*, vol. 11, no. 6, pp. 332–339, 1969.

[106] R. L. Fleischer, P. B. Price, and R. M. Walker, "Neutron flux measurement by fission tracks in solids", *Nuclear Science and Engineering*, vol. 22, no. 2, pp. 153–156, 1965.

[107] Pavel V. Tsvetkov and Russell E. Stachowski, "Physics of the fission chain reaction in thermal and fast reactors", in *Encyclopedia of Nuclear Energy*, pp. 172–186. 2021.

[108] Mamet, Laure, "Recherche nucléaire : l'Institut Laue-Langevin de Grenoble célèbre les 50 ans de ses premiers neutrons, Le Dauphiné Libéré", nov 2021.

[109] S. Samothrakitis, M. Bertelsen, P. K. Willendrup, E. B. Knudsen, C. B. Larsen, N. Rizzi, L. Zanini, V. Santoro, and M. Strobl, "Neutron instrument concepts for a high intensity moderator at the european spallation source", *Scientific Reports*, vol. 14, no. 1, pp. 1–10, 2024.

[110] N. Rizzi, B. Folsom, M. Akhyani, M. Bertelsen, P. Böni, Y. Beßler, T. Bryś, A. Chambon, V. Czamler, B. Lauritzen, J. I. M. Damián, V. Nesvizhevsky, B. Rataj, S. Samothrakitis, V. Santoro, H. Shuai, M. Strobl, M. Strothmann, A. Takibayev, and O. Zimmer, "An intense source of very cold neutrons using solid deuterium and nanodiamonds for the european spallation source", *Nuclear Instruments and Methods in Physics Research Section A: Accelerators, Spectrometers, Detectors and Associated Equipment*, vol. 1062, pp. 169215, 2024.

[111] Y. Fukuda et al., "Evidence for oscillation of atmospheric neutrinos", *Physical Review Letters*, vol. 81, pp. 1562–1567, 1998.

[112] Takaaki Kajita, "Atmospheric neutrinos and discovery of neutrino oscillations", *Proceedings of the Japan Academy, Series B, Physical and Biological Sciences*, vol. 86, no. 4, pp. 303–321, 2010.

[113] Vernon Barger, Danny Marfatia, and Kerry Lewis Whisnant, *The Physics of Neutrinos*, Princeton University Press, Princeton, NJ, 2012.

[114] Anthony Zee, *Fearful Symmetry: The Search for Beauty in Modern Physics*, Princeton University Press, 2007.

[115] M. F. Shamir, "Cosmology with Noether symmetry", *The European Physical Journal C*, vol. 80, pp. 115, 2020.

[116] Antonio L. Maroto José R. Peláez Antonio Dobado, Angel Gómez-Nicola, "The symmetries of the standard model", in *Effective Lagrangians for the Standard Model*, pp. 97–123. Springer, 1997.

[117] Gerhart Lüders, "Proof of the TCP theorem", *Annals of Physics*, vol. 2, no. 1, pp. 1–15, July 1957.

[118] R. Jackiw and N. Manton, "Symmetries and conservation laws in gauge theories", *Annals of Physics*, vol. 127, no. 2, pp. 257–273, 1980.

[119] Sinya Aoki, I-Hsiu Lee, and She-Sheng Xue, "The breaking of chiral gauge symmetry", *Physics Letters B*, vol. 224, pp. 441–446, 1989.

[120] H. Georgi and A. Pais, "CP-Violation as a Quantum Effect", *Physical Review D*, vol. 10, pp. 1246–1262, 1974, Report number: COO-2232B-50.

[121] Claudio Bonati, Andrea Pelissetto, and Ettore Vicari, "Breaking of gauge symmetry in lattice gauge theories", *Physical Review Letters*, vol. 127, pp. 091601, 2021.

[122] Enrique Alvarez, José M. Gracia-Bondía, and C.P. Martín, "Anomaly cancellation and the gauge group of the Standard Model in NCG", *Physics Letters B*, vol. 364, pp. 33–40, 1995.

[123] Joseph Hucks, "Global structure of the standard model, anomalies, and charge quantization", *Physical Review D*, vol. 43, pp. 2709–2725, 1991.

[124] R. Foot, "New physics from electric charge quantization?", *Modern Physics Letters A*, vol. 5, no. 2, pp. 95–100, 1990.

[125] U.-J. Wiese, *The Standard Model of Particle Physics*, Institute for Theoretical Physics, University of Bern, 2018.

[126] E. Akhmedov and S. Esposito, "Majorana neutrinos and other majorana particles: theory and experiment", in *The Physics of Ettore Majorana: Theoretical, Mathematical, and Phenomenological*, pp. 303–353. Cambridge University Press, 2014.

[127] Asimina Arvanitaki, Savas Dimopoulos, Andrew A. Geraci, Jason Hogan, and Mark Kasevich, "How to test atom and neutron neutrality with atom interferometry", *Physical Review Letters*, vol. 100, pp. 120407, 2008.

[128] R. Foot, H. Lew, and R. R. Volkas, "Electric-charge quantization", *Journal of Physics G: Nuclear and Particle Physics*, vol. 19, no. 3, pp. 361–372, 1993.

[129] A. Y. Ignatiev and G. C. Joshi, "Can the electric charges of elementary particles change with time?", *Physical Review D*, vol. 48, pp. 4481–4484, 1993.

[130] E. Takasugi and M. Tanaka, "Charge nonconservation and charges of neutrinos, neutron, and atoms", *Physical Review D*, vol. 44, pp. 3706–3714, 1991.

[131] Pavan Kumar Aluri, Paolo Cea, Pravabati Chingangbam, Ming-Chung Chu, Roger G. Clowes, Damien Hutsemékers, Joby P. Kochappan, Alexia M. Lopez, Lang Liu, and Niels C. M. Martens, "Is the observable universe consistent with the Cosmological Principle?", *Classical and Quantum Gravity*, vol. 40, no. 9, pp. 094001, 2023.

[132] John Ellis, "Limits of the Standard Model", *CERN-TH*, , no. 2002-320, 2002.

[133] C. Smorra, K. Blaum, L. Bojtar, M. Borchert, K.A. Franke, T. Higuchi, N. Leefer, H. Nagahama, Y. Matsuda, A. Mooser, and et al., "BASE – the Baryon Antibaryon Symmetry Experiment", *European Physical Journal Special Topics*, vol. 224, pp. 3055–3108, 2015.

[134] A. D. Sakharov, "Violation of CP invariance, C asymmetry, and baryon asymmetry of the universe", *Pisma Zh. Eksp. Teor. Fiz.*, vol. 5, pp. 32–35, 1967.

[135] K. et al. Abe, "Neutron-antineutron oscillation search using a 0.37 megaton-years exposure of Super-Kamiokande", *Phys. Rev. D*, vol. 103, pp. 012008, 2021.

[136] M. Baldo-Ceolin, P. Benetti, T. Bitter, F. Bobisut, and E. et al. Calligarich, "A new experimental limit on neutron-antineutron oscillations", *Zeitschrift für*

Physik C, vol. 63, pp. 409–416, 1994.

[137] DUNE Collaboration and Justin Wheeler, "Neutron-antineutron oscillation sensitivity study at DUNE", Tech. Rep., Fermilab, 2024, Report number: FERMILAB-POSTER-24-0204-LBNF-STUDENT.

[138] Camille Theroine, "A neutron-antineutron oscillation experiment at the European Spallation Source", *Nuclear and Particle Physics Proceedings*, vol. 273–275, pp. 156–161, 2016.

[139] Anastasio Fratangelo, *Search for the Neutron Electric Dipole Moment with the Beam EDM and the n2EDM Experiments and Application of the FOSOF Technique to Neutrons*, Inaugural dissertation, University of Bern, 2024.

[140] CDT CASCADE Detector Technologies GmbH, *CASCADE 2D-200 Operating Manual*, 69123 Heidelberg, Germany, December 2013.

[141] National Institute of Standards and Technology, "Neutron Scattering Lengths and Cross Sections of Elements and Isotopes: Gadolinium (Gd)", https://www.ncnr.nist.gov/resources/n-lengths/elements/gd.html, 2024.

[142] Wafer Universe, "Wafer universe - silicon wafer supplier and manufacturer", https://waferuniverse.com/, 2023.

[143] SwissNeutronics AG, "Swissneutronics - advanced neutron optics solutions", https://www.swissneutronics.ch/, 2023.

[144] Photons at Work GmbH, "Photons at work - experts in laser technology", https://www.photonsatwork.com, 2023.

[145] "STANDA", http://www.standa.lt.

[146] "Maximum Integrated Data Acquisition System", http://https://daq00.triumf.ca/MidasWiki/index.php/Introduction/.

[147] Bradley Efron, *The Jackknife, the Bootstrap, and Other Resampling Plans*, Number 38 in CBMS-NSF Regional Conference Series in Applied Mathematics. Society for Industrial and Applied Mathematics (SIAM), Philadelphia, PA,

1982.

[148] M. Morgano, S. Peetermans, E. H. Lehmann, T. Panzner, and U. Filges, "Neutron imaging options at the BOA beamline at Paul Scherrer Institut", *Nuclear Instruments and Methods in Physics Research Section A: Accelerators, Spectrometers, Detectors and Associated Equipment*, vol. 754, pp. 46–56, 2014.

[149] "BOA: Beamline for neutron Optics and other Approaches", http://https://www.psi.ch/fr/sinq/boa.

[150] "PF1B - polarised cold neutron beam facility", https://www.ill.eu/users/instruments/instruments-list/pf1b/description/instrument-layout.

[151] D. Dubbers, H. Saul, B. Märkisch, T. Soldner, and H. Abele, "Exotic decay channels are not the cause of the neutron lifetime anomaly", *Physics Letters B*, vol. 791, pp. 6–10, 2019.

[152] V. V. Fedorov, M. Jentschel, I. A. Kuznetsov, E. G. Lapin, E. Lelièvre-Berna, V. Nesvizhevsky, A. Petoukhov, S. Y. Semenikhin, T. Soldner, V. V. Voronin, and Y. P. Braginetz, "Measurement of the neutron electric dipole moment via spin rotation in a non-centrosymmetric crystal", *Physics Letters B*, vol. 694, pp. 22–25, 2010.

[153] V. V. Fedorov, M. Jentschel, I. A. Kuznetsov, E. G. Lapin, E. Lelièvre-Berna, V. V. Nesvizhevsky, A. Petoukhov, S. Y. Semenikhin, T. Soldner, F. Tasset, V. V. Voronin, and Y. P. Braginetz, "Measurement of the neutron electric dipole moment by crystal diffraction", *Nuclear Instruments and Methods in Physics Research A*, vol. 611, pp. 124–128, 2009.

[154] B. Märkisch, H. Mest, H. Saul, X. Wang, H. Abele, D. Dubbers, M. Klopf, A. Petoukhov, C. Roick, T. Soldner, and D. Werder, "Measurement of the weak axial-vector coupling constant in the decay of free neutrons using a pulsed cold neutron beam", *Phys. Rev. Lett.*, vol. 122, pp. 242501, jun 2019.

[155] D. Mund, B. Märkisch, M. Deissenroth, J. Krempel, M. Schumann, H. Abele,

A. Petoukhov, and T. Soldner, "Determination of the Weak Axial Vector Coupling $\lambda = g_A/g_V$ from a Measurement of the β-Asymmetry Parameter A in Neutron Beta Decay", *Phys. Rev. Lett.*, vol. 110, pp. 172502, apr 2013.

[156] B. Märkisch, H. Abele, D. Dubbers, F. Friedl, A. Kaplan, H. Mest, M. Schumann, T. Soldner, and D. Wilkin, "The new neutron decay spectrometer Perkeo III", *Nuclear Instruments and Methods in Physics Research A*, vol. 611, pp. 216–218, 2009.

[157] M. Klopf, E. Jericha, B. Märkisch, H. Saul, T. Soldner, and H. Abele, "Constraints on the dark matter interpretation $n \rightarrow \chi + e^+e^-$ of the neutron decay anomaly with the PERKEO II experiment", *Physical Review Letters*, vol. 122, no. 22, pp. 222503–1–222503–4, 2019.

[158] Raja, "Thermo-Luftpolsterfolie - 120 cm x 25 m — Article Number MCB120AL", 2024.

[159] B. Hammouda and D.F.R. Mildne, "SANS Resolution with Refractive Optics", *J. Appl. Cryst.*, vol. 40, pp. 250–259, 2007.

[160] NIST, "Neutron scattering lengths and cross sections", `https://www.ncnr.nist.gov/resources/n-lengths/elements/al.html`.

[161] David W. Allan, "Statistics of atomic frequency standards", *Proceedings of the IEEE*, vol. 54, no. 2, pp. 221–230, 1966.

[162] C Swanson and EN Leith, "Application of the Lau effect to neutron interferometry", *Optics Communications*, vol. 45, no. 4, pp. 213–217, 1983.

Declaration of Consent

On the basis of Article 18 of the PromR Phil.-nat. 19

Name/First Name: Marc Persoz
Registration Number: 11-860-756
Study Program: Dissertation
Title of the thesis: Measuring the Neutron Electric Charge with High-Visibility Grating Interferometry
Supervisor: Prof. Dr. Florian M. Piegsa

I declare herewith that this thesis is my own work and that I have not used any sources other than those stated. I have indicated the adoption of quotations as well as thoughts taken from other authors as such in the thesis. I am aware that the Senate pursuant to Article 36 paragraph 1 litera r of the University Act of September 5th, 1996 and Article 69 of the University Statute of June 7th, 2011 is authorized to revoke the doctoral degree awarded on the basis of this thesis.

For the purposes of evaluation and verification of compliance with the declaration of originality and the regulations governing plagiarism, I hereby grant the University of Bern the right to process my personal data and to perform the acts of use this requires, in particular, to reproduce the written thesis and to store it permanently in a database, and to use said database, or to make said database available, to enable comparison with theses submitted by others.

Bern, Tuesday 21st January, 2025

Marc Persoz